

Quantum Information Enabled Neutron Interferometry

by

Joachim Nsofini

A thesis
presented to the University of Waterloo
in fulfillment of the
thesis requirement for the degree of
Doctor of Philosophy
in
Physics

Waterloo, Ontario, Canada, 2017

© Joachim Nsofini 2017

Examining Committee Membership

The following served on the Examining Committee for this thesis. The decision of the Examining Committee is by majority vote.

External Examiner	Geoffrey Greene Dr.
Supervisor	David Cory Dr.
Internal Member	Kevin Resch Dr.
Internal-external Member	Joseph Emerson Dr.
Other Member(s)	Thomas Jennewein Dr. Dmitry Pushin Dr.

I hereby declare that I am the sole author of this thesis. This is a true copy of the thesis, including any required final revisions, as accepted by my examiners.

I understand that my thesis may be made electronically available to the public.

Abstract

Neutron interferometry with its ability to encode and extract information provides a test bed for quantum mechanics and precise measurement of physical quantities of significant importance in physics. However, this significant key investigative technique is weakened by its very fragile nature; neutron interferometry has proven to be highly sensitive to environmental noise.

Once brought to its optimal state, the use of neutron interferometry enabled with quantum information, represents a milestone. Indeed a realization of high-quality neutron interferometry could pave a way to probe materials research such as probing properties water in proteins and topological materials. Thus understanding and solving the sensitivity of neutron interferometers to noise is a key step toward possible applications. This is the core of the work done in this Thesis.

We incorporated two theoretical techniques developed for quantum information sciences into the construction of a new polarized neutron interferometry beam line: The technique of quantum error correction and the technique of open quantum system. One focus of this work is to report on the design, the construction as well as the characteristic features of this beamline.

This thesis involves experimental data, showing how the neutron beam intensity at the exit of a three-blade neutron interferometer can be controlled by the interferometer blades thickness. Secondly, is also presents an alternative and simplified quantum information approach to dynamical diffraction, based on repeated application of a coherent beam-splitting unitary at coarse-grained lattice sites. Demanding translational invariance added to a computationally tractable number of sites in the coarse-graining reproduced many results typical of standard dynamical diffraction theory and experiments. Building on that, a proposal for a new five-blade neutron interferometer is presented and its robustness to noise, resulting from dynamical diffraction together with low-frequency external mechanical vibration is discussed.

Steps ahead in our work, neutron interferometry may be improved as well as adapted to more applications by incorporating the spin and orbital degrees of freedom to a path-based

interferometer. In this concern, we propose a method to prepare the spin-orbit state by passing a polarized neutron beam through a quadrupole magnetic field. Initially designed for a beam the size of a coherent length, we extend this method to work for spatially displaced beams by using linear magnetic gradients.

Acknowledgements

First, I would like to express my special appreciation and thanks to my supervisor Dr. David Cory, for his guidance during my transformation from a student to a research scientist. Your advices on research and career have been priceless. I would also like to thank Drs. J. Emerson, T. Jenniwein, D. Pushin, K. Resch for serving in my PhD advisory committee, and G. Greene for serving as my external examiner.

I also want to thank the Department of Physics and Astronomy, and the Institute for Quantum Computing at the University of Waterloo for making this research possible. Without your generosity, I wouldn't have made it through this period. Your staff was always there to support me especially Judy McDonnell, the physics coordinator, Carly Turnbull, IQC office assistance, and Jordi Szimenski who read most of my articles and thesis chapters.

I also want to express my gratitude to the members of the Cory group at large (including the host of co-op students); especially H. Hass (my officemate), I. Hincks, M. Nickman, and my interferometry partner D. Sarenac. We have learned to encourage each other during the past few years. To Dr. R. Annabestani, your feedback was always very useful, I really appreciate your effort.

The experiments in this thesis were performed at the National Institute of Standards and Technology (NIST) Center for Neutron Research (NCNR), Gaithersburg, MD, USA. As such, I am thankful to NCNR and my sponsor Dr. M. Arif for hosting me during my many visits. Also, to those I worked with Drs. C. Shahi, D. Pushin, and M. Huber, your patience in teaching me experimental concepts and the various challenges of working in a government laboratory. The support from Drs. D. Jacobson, W. Chen and our machinist R. Shankles is appreciated. My time at NIST will be remembered with fondness.

A special thanks to my family. Words cannot express how grateful I am to my parents and my siblings for all of the sacrifices made on my behalf. Your prayer for me was what sustained me especially in the darkest moments. I'd express my heartfelt gratitude to L. Viban, the lovely queen who sacrificed countless times to call and check on me.

My journey to grad school started from a chat with Dr. C. Akosa, my friend since undergrad days in the University of Buea. I really appreciate the information you have always shared, and your attitude of always pulling me to follow you from Abuja to Waterloo. I would also like to thank all of my friends who supported me in one way or the other throughout my program especially Drs. S. Owerre and E. Ogbe. Some of my friends read all or part of my work. These include D. Djantio and my MDI mentor D Baer. I want to express my heart felt gratitude. To the Cameroon Community in Kitchener-Waterloo, you are a family away from home. The football we played was my main stress therapy during this PhD. I also thank the Anyambot family that always encouraged me to come for a restful weekend in order to recharge.

I must mention that am very lucky to have a very good circle of friends that have been very supportive. It will take me pages to list them and how much they contributed during this perion. I just want to say thank you. To those I might have forgotten to mention, I am grateful for the support gave to me.

Dedicated to my mom, Ernesta Tumi

He gives strength to the weary, and increases the power of the weak.

Isaiah 40:29

Table of Contents

List of Figures	xiv
1 Introduction	1
1.1 Neutron Interferometry	1
1.2 Outline and results	3
1.3 Neutron optics	4
1.3.1 The neutron	4
1.3.2 Wave equation	6
1.3.3 Spin-independent neutron-matter interaction	6
1.3.4 Spin-dependent neutron-matter interaction	8
1.3.5 Phase	10
1.4 Neutron interferometry	13
1.4.1 Wavefront and amplitude division neutron interferometers	13
1.4.2 Neutron spin-interferometry	14
1.4.3 Periodic structure neutron interferometers	17
1.5 Operator representation	20
1.6 Interferometry contrast	23
1.7 Neutron detection	24

2	A New Neutron Interferometry & Optical Facility at NCNR	27
2.1	Introduction	27
2.2	Description of NIOFa beamline	28
2.3	Beam characteristics	32
2.4	Wavelength measurement	35
2.5	Contrast measurement	37
2.6	Neutron polarization	41
3	Dynamical Diffraction in a Perfect Crystal Neutron Interferometer	48
3.1	Introduction	48
3.2	Dynamical diffraction	49
3.3	Three-blade neutron interferometer	55
3.3.1	Case of wavelength spread	57
3.3.2	Case of angular spread	59
3.4	Experimental procedure	60
3.4.1	Contrast variation	62
3.5	Intensities from an interferometer	62
3.6	Data analysis	64
3.7	Conclusion	65
4	Quantum Information Approach to Dynamical Diffraction	66
4.1	Introduction	66
4.2	Quantum information model	68
4.2.1	Formalism of QI model for DD	69
4.2.2	Example: 50:50 beam splitter	74

4.3	Applications	77
4.3.1	Intensity profile of the Borrmann triangle	77
4.3.2	Integrated intensities and Pendellösung oscillations	78
4.4	Extension to a neutron interferometer	81
4.4.1	Beam profiles	82
4.4.2	Output intensities	82
4.4.3	Contrast	85
4.5	Further work and conclusion	86
5	Noise-Refocusing Five-blade Neutron Interferometer	87
5.1	Introduction	87
5.2	Dynamical phase	88
5.2.1	Interferometer geometries	88
5.2.2	Single blade unitary operator	89
5.2.3	Three-blade neutron interferometer	92
5.2.4	Four-blade neutron interferometer	92
5.2.5	Five-blade neutron interferometer	96
5.3	Effects of mechanical vibration	97
5.3.1	X-Noise	98
5.3.2	Y-noise	104
5.4	Future prospects and conclusion	107
6	Spin-Orbit states of a neutron wavepacket	109
6.1	Introduction	109
6.2	Wavefunction	110

6.2.1	Basic characteristics of Laguerre-Gauss beams	112
6.2.2	Internal and external OAM	114
6.3	Generating OAM with a spiral phase plate	115
6.3.1	On-axis SPP	116
6.3.2	Off axis SPP	117
6.3.3	Characterizing OAM using $\langle L_z \rangle$	119
6.3.4	Detection using a neutron interferometer	120
6.4	Spin-orbit states of a neutron wavepacket	121
6.4.1	Generating operator for spin-orbit states	122
6.4.2	On-axis spin-orbit states	124
6.4.3	Charactering spin-orbit states via entanglement	127
6.4.4	Expectation of \hat{L}_z	130
6.5	Ramsey-type experiment with spin-orbit states	130
6.5.1	Spin-Orbit generated from a quadrupole	130
6.5.2	Spin-orbit generated from linear gradients	134
6.6	Spin-orbit states in a neutron interferometer	136
6.7	Conclusion	137
7	Conclusion and Future Prospects	138
	References	141
	APPENDICES	150

A	151
A.1 Selected Publications	151
A.2 Important mathematical relations	152
A.3 Coefficients of a an SPP	153
A.4 Input state expanded in to the LG basis	155
A.5 On-axis quadrupole	157
A.6 Non expanded input state in to the LG basis	159

List of Figures

1.1	Spin-independent reflection	8
1.2	Spin-dependent reflection	9
1.3	Neutron wavefunction through a medium.	11
1.4	Neutron interferometers based on wavefront division.	13
1.5	Spin-path correlation neutron interferometers.	16
1.6	Mach-Zehnder type grating neutron interferometer	17
1.7	One and two blade perfect crystal neutron interferometers	18
1.8	Schematics neutron interferometers in the Laue geometry	20
1.9	Operator formalism of a single crystal diffraction	21
1.10	Neutron detection circuit	25
2.1	A simplistic layout of the NCNR showing the reactor core and	28
2.2	Schematic layout of the NIOFa beamline	29
2.3	Söller collimation	30
2.4	A real view of the NIOFa beamline looking from the guide.	31
2.5	A real view of an interferometer on the NIOFa beamline.	32
2.6	A Bragg angle scan of the NIOFa monochromator	33
2.7	The spectrum for various neutron harmonics $\lambda = (4.4/n) \text{ \AA}$	34

2.8	Schematic setup for wavelength measurement.	36
2.9	The interferometer Bragg angle scan	38
2.10	NI setup to measure contrast and extract the phase, ϕ_s , due to a sample	39
2.11	The O-beam intensities for different table legs	40
2.12	Schematic setup used to measure neutron polarization at the NIOFa.	42
2.13	Tuning voltages in the spin flipper coils	43
2.14	Detector linear and rotation scan for alignment during polarimetry	44
2.15	The spatial dependence of supermirror polarization	45
2.16	Polarization profile for various polarizer and analyzer configurations	46
3.1	Illustration of Bragg diffraction in the Laue geometry	50
3.2	Schematic setup for measuring effect of blade thickness on intensity	56
3.3	Illustration of the wavevector deviation	57
3.4	The Pendellösung oscillations	58
3.5	A colour representation of 2D contrast scan	60
3.6	H-beam contrast against interferometer crystal thickness	61
3.7	The O- and H-beam intensities obtained by tilting an empty NI	63
3.8	The H-beam intensity vs the interferometer tilt angle	64
4.1	A perfect crystal decomposed into various scattering sites	70
4.2	Beam profiles for the reflected and transmitted waves	78
4.3	Transmitted and reflected intensities at the exit of a single crystal	80
4.4	Plot of our simulated Pendellösung oscillation at the exit of the Borrmann fan	81
4.5	The various intensity profiles for a three-blade NI	83
4.6	The intensity of the O-beam and H-beam against the phase difference χ	84

4.7	H-beam contrast as a function of the number of planes in each blade	85
4.8	Depiction of various defects can be studied with the QI model of DD.	86
5.1	Sketch showing the different NI geometries with phase flags ϕ and χ	89
5.2	Wavevector changes during Bragg diffraction in the symmetric Laue geometry	90
5.3	Three-blade NI DD model of a four-blade NI	94
5.4	The DD in a three-blade NI.	95
5.5	The NI intensities against the phase for the X-noise	100
5.6	Decomposition of the five-blade NI into paths	101
5.7	Color plot of the H-beam intensity in the presence of noise	103
5.8	The intensity and contrast for different NIs in the presence of Y-noise	105
5.9	Multipath five-blade NI	108
6.1	Beam profiles of the probability amplitude $ \psi_{n\ell}(\xi, \phi) ^2$	113
6.2	A neutron wavepacket propagating off the center of a phase inducing device	114
6.3	The probabilities for each of the $\ell = 0, 1, -1$ and $n = 0, 1$ states of an SPP	117
6.4	Coefficients of the $\ell = 0$ and $\ell = 1$ OAM for the $n = 0, 1$ subspaces	119
6.5	Normalized 2D intensity with an SPP in an NI	121
6.6	Vector plot of a quadrupole	122
6.7	2D intensity of the neutron after a single quadrupole	124
6.8	The polarization is plotted for $r_c = \sigma_{\perp} = 4$ for a beam through a quadrupole	125
6.9	The coefficients $C_{n,0,\uparrow}$ and $C_{n,1\downarrow}$ of the spin-orbit state for the $n = 0$	126
6.10	Subspace concurrence and probability of the filtered spin-orbit state	128
6.11	Concurrence for the $n = 0$ and $n = 1$ subspaces for various inputs	129
6.12	Concurrence in the spin-orbit states after tracing over the radial subspace	130

6.13 Numerical simulation of the expectation value $\langle L_z \rangle$ for a spin-orbit state	131
6.14 Spin-orbit Ramsey fringe experiment and the resulting intensities	132
6.15 3D spin down Ramsey fringe experiment intensities	133
6.16 Generating OAM using two linear gradients	135
6.17 2D intensity distribution at the unfiltered O-beam of an NI	137

Chapter 1

Introduction

1.1 Neutron Interferometry

Neutron Interferometry is a tool designed to explore the wave-like nature of neutrons. So far, this tool has led to demonstrations of quantum mechanical phenomena, has provided a way of testing the propositions of quantum mechanics, and has allowed the precise measurement of physical quantities of interest in condensed-matter and Standard Model physics. There is a large variety of neutron interferometry implementations, and each may be characterized by the degree of freedom under control, such as momentum, spin, orbit, energy, and path. For instance, the path-based interferometers are designed to split the incident beam into two or more beams where, for example one beam may pass through a sample and the others only through free space. In this case, the interference pattern of different components from different paths reveals information about the examined sample. There are a variety of books and review articles covering the practice and application of neutron interferometry [1, 2, 3, 4].

Closest to the physics of a neutron interferometer, in its description, is an optical Mach-Zehnder interferometer. Relevant key notes to our research are for one that the size of the neutron beam is far broader than the coherent length. As a result, one needs to perform an incoherent averaging over the beam during detection. For this reason, care must be

taken to ensure that the entire beam sees the same components or a spatial incoherence is introduced. Secondly, the neutron beam intensity is generally very low causing most measurements to require days of averaging. Here too, unfortunately time averaging may introduce a temporal incoherence if the phases drift over the measurement. In addition, the neutron travels slowly through the interferometer $\lesssim 2$ km/s. During that time, there is an opportunity for mechanical vibrations, temperature fluctuations, acoustical vibrations, fluctuations in mechanical stress, and finally fluctuating background magnetic fields to introduce decoherence. In this work, we are interested in understanding and controlling these effects.

In previous research, noise from mechanical vibrations was removed by constructing the neutron interferometry facility on a complex custom-made vibration isolation system [5]. In most cases, the custom-made vibration isolation system presented to be very bulky, requiring the experiments to be performed at a significant distance from the beam source. Again this led to unwanted results; by the time the incident beam arrives at the interferometer it loses on needed intensity. An alternative approach can be to incorporate the theoretical techniques developed in quantum information sciences such as quantum error correction and open quantum system to engineer neutron interferometers which exhibit inherent noise robustness. In particular, the notion of decoherence-free subspace (DFS) from quantum error correction formerly adopted to implement a four-blade perfect crystal neutron interferometer (NI) where information is encoded in a specific subspace, thus isolated from external mechanical vibrational noise [6]. The realization of a DFS NI motivated us to construct a compact and sizeable table-top neutron interferometry beamline at the National Institute of Standards and Technology (NIST) Center for Neutron Research (NCNR) [7]. The advantage of the DFS NI setup is its compactness that allow it to be located closer to the neutron source, resulting in only a small loss in the neutron intensity.

The most commonly used type of neutron interferometer is path-base interferometry. However, for certain applications the orbital and the spin degrees of freedom may be incorporated to achieve a composite interferometry with multiple degrees of freedom. Composite neutron interferometry potentially has applications to materials characterization, for example to probe properties of water in proteins, to probe the internal magnetic structures of materials, and also to characterize topological properties of materials. In 2015, the orbital

angular momentum of an unpolarized neutron beam was modified by a spiral phase plate and this change was experimentally detected using a perfect crystal NI [8]. In this thesis, we theoretically show a methodology to realized spin-orbit states of a neutron wavepacket [9].

We focus this thesis on ways to improve the performance of neutron interferometry and to extend its applications. Some of the results presented in this thesis were obtained in collaborations with colleagues from the Cory Lab especially with D. Sarenac.

1.2 Outline and results

In chapter 2, we give a detailed report of the characteristics and features of the new neutron interferometry facility at the NCNR, constructed to work with a DFS neutron interferometry setup. In chapter 3, the theory of dynamical diffraction (DD) [10, 2, 3] is introduced and then applied to demonstrate the effect of NI blade thickness on the phase and intensity of the beam diffracted from a combination of crystals. In chapter 4, we formulate DD from a perfect periodic lattice via a unitary evolution in real space as opposed to the energy eigenstates formalism in momentum space. This relatively simple quantum information approach, which predicts most of the features of DD from a single crystal, is then applied to understand DD in an NI. In chapter 5, we show that despite being a DFS to noise from mechanical vibration, the four-blade NI suffers from noise caused by momentum dependent phases which originate from Bragg diffraction. Further, we provide a design of a five-blade NI and then theoretically show how it refocuses both noise from mechanical vibrations and momentum dependent phases. In chapter 6, we focus on the spin-orbit states of a neutron wavepacket created by a magnetic field with a topological charge [9]. In chapter 7, we present our conclusions and future prospects. Chapters of this thesis are based on the completed projects listed below.

- Design and instrumentation of the new neutron interferometry facility at the NCNR based on the article [7]; joint work with colleagues from the NIST.
- Changes in the intensity and the phase of the beams emerging from an NI when the thickness of the interferometer blades are simultaneously varied.

- Formulation of the quantum information approach to DD and using it to derive various results of DD from perfect periodic lattices [11].
- A proposal of a five-blade NI is presented alongside its ability to decoupled from noise originating from momentum dependent phases and mechanical vibrations [12].
- The process of generation and control of spin-orbit states, using a magnetic topological charge, followed by a Ramsey fringe experiment on the spin-orbit states [9].

1.3 Neutron optics

1.3.1 The neutron

The existence of the neutron was postulated in 1920 [13] and confirmed in 1932 [14]. Neutrons interacts very differently from light as they carry a magnetic dipole moment; and from electrons as they carry no electric charge. A neutron has the ability to penetrate materials deeply; propagate with wavelengths that coincide with material's lattice spacing, exhibit exceptionally strong isotope-dependent scattering in the case of hydrogen; and finally interact with magnetic materials through their magnetic dipole moment. A summary of some important properties of neutrons compared to those of photons is listed in Tab. 1.1.

The de Broglie wave-particle duality [15] associates a wavevector, $\mathbf{k} = m\mathbf{v}/\hbar$, with a neutron propagating through a medium, where \mathbf{v} is the neutron velocity, m its mass, and $\hbar = 1.05457 \times 10^{-34}$ Js is the reduced Planck constant. The wavefunction can be represented as a 3D wavepacket (in Dirac notation),

$$|\Psi(t)\rangle = \int d\mathbf{k} \mu_{\mathbf{k}} e^{-i\omega_{\mathbf{k}}t} |\mathbf{k}\rangle, \quad (1.1)$$

with $\omega_{\mathbf{k}} = E/\hbar$, where E is the energy, $\mu_{\mathbf{k}}$ is the probability amplitude. The state $|\mathbf{k}\rangle$ is a plane wave component with position representation $\psi_{\mathbf{k}} = \langle r|\mathbf{k}\rangle = e^{i\mathbf{k}\cdot\mathbf{r}}$, with wavevector $\mathbf{k} = k_x\hat{e}_x + k_y\hat{e}_y + k_z\hat{e}_z$ and $\mathbf{r} = x\hat{e}_x + y\hat{e}_y + z\hat{e}_z$.

The neutron is a spin one-half particle with a negative magnetic dipole moment (MDM) indicating that the neutron's spin and MDM are anti-aligned. In a magnetic field, the

Property	Photon	Neutron
Mass	0	$m = 1.674928(1) \times 10^{-27}$ kg
Spin	\hbar	$\frac{1}{2}\hbar$
Magnetic Dipole Moment	0	$\mu_n = -9.66237055(71) \times 10^{-27}$ J/T
Equation	$\nabla^2\Psi(\mathbf{r}, t) = \frac{1}{c} \frac{\partial^2\Psi(\mathbf{r}, t)}{\partial t^2}$	$H\Psi(\mathbf{r}, t) = i\hbar \frac{\partial\Psi(\mathbf{r}, t)}{\partial t}$
Energy	$E = \hbar ck$	$E = \frac{\hbar^2 k^2}{2m}$
$n_{(\text{H}_2\text{O})} - 1$	0.33	2.88×10^{-7}
Velocity	c	$v = \frac{3956}{\lambda[\text{\AA}]} \text{ m/s}$

Table 1.1: Properties of neutrons compared to photons. For more detail, a similar table can be found in ref. [16]. The values listed are taken from the PDG summaries of 2014 [17]. $n_{(\text{H}_2\text{O})} - 1$ is the refractive index for water. The calculated values for the neutron uses the thermal neutron wavelength of 1.8 Å.

intrinsic spin is quantized such that the neutron can only occupy two discrete energy states. The total wavefunction for the spin and momentum degrees of freedom is,

$$|\Psi(t)\rangle = \int d\mathbf{k} \mu_{\mathbf{k}} e^{-i\omega_{\mathbf{k}}t} |\mathbf{k}, s\rangle \quad (1.2)$$

where, $|s\rangle$, is the spin state with quantum number s . Other bases of the total wavefunctions are possible, as will be seen in chapter 6 where the wavepacket carries orbital angular momentum.

Many phenomena in neutron optics can be described with the terminology of the coherence function commonly used in quantum optics [18, 3]. The coherence function in this case is defined generally as the autocorrelation function of the wavefunction;

$$\Gamma(\Delta, \tau) = \langle \Psi(0, 0) | \Psi(\Delta, \tau) \rangle, \quad (1.3)$$

where $\Delta = \mathbf{r} - \mathbf{r}_0$, and τ is the time interval. Using the wavepacket description for the neutron wavefunction, the coherence function can be expressed as,

$$\Gamma(\Delta, \tau) = \int p_{\mathbf{k}} e^{i(\mathbf{k} \cdot \Delta - \omega_{\mathbf{k}}\tau)} d\mathbf{k}, \quad (1.4)$$

where, $p_{\mathbf{k}} = |\mu_{\mathbf{k}}|^2$ and $\mathbf{k} \cdot \Delta$ is the phase delay of each component plane wave.

1.3.2 Wave equation

The propagation of a neutron through a medium is governed by the matter-wave Schrödinger equation. In a time independent potential, under steady state conditions, the Schrödinger equation in the position representation is,

$$\left[-\frac{\hbar^2}{2m}\nabla^2 + V(\mathbf{r}) \right] \Psi(\mathbf{r}) = E\Psi(\mathbf{r}), \quad (1.5)$$

where $V(\mathbf{r})$ is the potential energy of the particle, and E is the total energy of the particle. The equation can be written in a form that is similar to the Helmholtz equation in classical optics as,

$$\nabla^2\Psi(\mathbf{r}) + K(\mathbf{r})^2\Psi(\mathbf{r}) = 0, \quad (1.6)$$

with $K(\mathbf{r}) = \sqrt{2m[E - V(\mathbf{r})]}/\hbar$ is the medium dependent wavevector. $V(\mathbf{r})$ can take various forms including electromagnetic, gravitational, and nuclear. Of interest to us is the nuclear and magnetic interaction which will be explored in the next section in detail. One common way to characterize them is via the refractive index, defined as [2, 3],

$$n \equiv \frac{K(\mathbf{r})}{k} = \sqrt{\frac{2m[E - V(\mathbf{r})]}{2mE}} \simeq 1 - \frac{\bar{V}}{2E}, \quad (1.7)$$

where $k = \sqrt{2mE\hbar^{-2}}$ is the wavevector in free space. The approximation in Eq. (1.7) is valid for thermal neutrons as the potential $V(\mathbf{r})$ can be expressed in a form equal to the optical potential, \bar{V} , which for most materials is of the order $10^{-5}eV$.

1.3.3 Spin-independent neutron-matter interaction

Neutron-matter interactions are often dominated by the spin-independent nuclear and spin-dependent magnetic interactions. The nuclear interaction is conveniently represented as a Fermi pseudo-potential [2] that captures the potential of a localized single atom as a delta function. In a bulk material, the effective potential is the collection of pseudo-potentials given by,

$$V(\mathbf{r}) = \sum_j \frac{2\pi\hbar^2}{m} b_j \delta(\mathbf{r} - \mathbf{r}_j), \quad (1.8)$$

where the summation is taken over all the atoms in the bulk. Each of which is located at \mathbf{r}_j and have a scattering coherent length b_j . A neutron scattered by a pseudo-potential gives rise to a wave which can be represented as two components: one along the incident direction and a spherical wave propagating in the radial direction. Their coherent superposition is described by a single wavevector that carries the optical properties of the medium. For example, a material with atom density, N , has an average nuclear potential of,

$$V_O = \frac{2\pi\hbar^2}{m}N\bar{b}, \text{ where } N\bar{b} = \sum_j b_j\delta(\mathbf{r} - \mathbf{r}_j). \quad (1.9)$$

$N\bar{b}$ is the local mean scattering length density, which represents the response of the overall system as multiple copies of a single atom of the same kind. Generally, \bar{b} is complex with typical values in the femtometre scale. Moreover, this value leads to a scattering cross-section defined as $\bar{\sigma}_s = 4\pi|\bar{b}|^2$ and an absorption cross-section defined as $\bar{\sigma}_a = 4\pi\text{Im}[b]^2k^{-1}$, where $\text{Im}[\bar{b}]$ is the imaginary component.

When a neutron beam is shined on an absorbing target of effective thickness D , the intensity of transmitted neutron is related to the incident intensity, I_0 , by [19],

$$I = I_0e^{-\bar{\sigma}_aND}. \quad (1.10)$$

Materials with high $\bar{\sigma}_a$ including lead, cadmium, gadolinium, are commonly used as neutron absorbers. For most materials, $\text{Re}[\bar{b}] > 0$, with the few exceptions of ^2H , ^{48}Ti , and ^{62}Ni

The general form of the complex refractive index from a spin-independent scattering material is [3, 2],

$$n \equiv 1 - \frac{\lambda^2N}{2\pi} \sqrt{\bar{b}^2 - \left(\frac{\bar{\sigma}_r}{2\lambda}\right)^2} + i\frac{\bar{\sigma}_rN\lambda}{4\pi}, \quad (1.11)$$

where $\bar{\sigma}_r = \bar{\sigma}_s k^{-1}$ and for weakly absorbing materials, $\bar{\sigma}_r \rightarrow 0$. Both the refractive index and the scattering linear density are important quantities that are used when calculating the phase or the angle of reflection/refraction when a neutron propagates through a medium.

Shown in Fig. 1.1 is the schematic of a neutron with wavevector k incident onto a planar boundary between air and a material with a refractive index n . Under specular

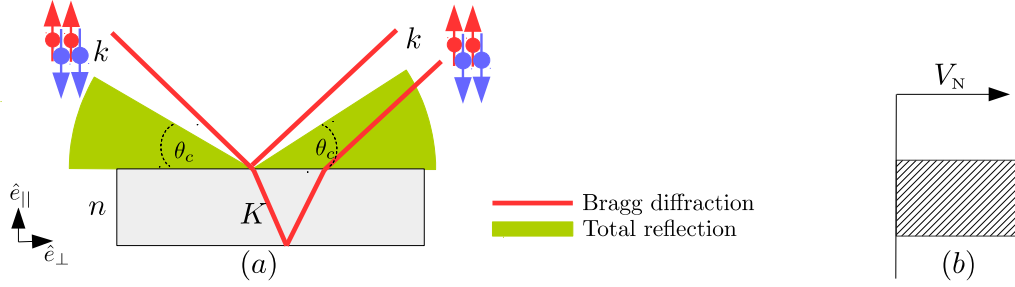


Figure 1.1: Spin-independent reflection from a layer. (a) the neutrons incident at angles less than the critical angle θ^c of the surface are reflected. In (c) is a plot of the nuclear potential, V_N , experienced by a neutron.

reflection where the angle of reflection is equal to angle of incidence, the critical angle is defined as that for which the neutrons are totally reflected. Mathematically, the condition is $E_{\perp} = \hbar^2 k_{\perp}^2 / (2m) = V_N$, where k_{\perp} is the component of the wavevector normal to the surface of the potential, V_N . Given that $k_{\perp} = k \sin \theta$, where θ is the angle of incidence, the critical angle is,

$$\theta^c = \sin^{-1} \sqrt{(1 - n^2)} = \lambda \sqrt{N \bar{b} / \pi}. \quad (1.12)$$

Any neutron incident at an angle $\theta < \theta^c$ is also reflected while the neutron incident at an $\theta > \theta^c$ is transmitted. Materials, with very high critical angle like nickel (for ^{58}Ni , $\theta/\lambda = 2.03 \text{ mrad}/\text{\AA}$) are used to coat the internal surface of neutron guides, to increase the reflectivity of neutrons.

1.3.4 Spin-dependent neutron-matter interaction

In a medium with a static or slowly varying magnetic field $\mathbf{B}(\mathbf{r})$ and electric field $\mathbf{E}(\mathbf{r})$, the neutron magnetic moment interact with the field through a potential [20, 21, 22],

$$V_m(\mathbf{r}) = -\boldsymbol{\mu} \cdot \mathbf{B}(\mathbf{r}) - \frac{\hbar}{mc} \boldsymbol{\mu} \cdot (\mathbf{E}(\mathbf{r}) \times \mathbf{k}) - \frac{\hbar \mu}{2mc} \boldsymbol{\nabla} \cdot \mathbf{E}(\mathbf{r}), \quad (1.13)$$

where $\boldsymbol{\mu}$ is the neutron magnetic moment vector and c is the speed of light. The first term is the Zeemann energy, the second term is the Schwinger spin-orbit, and the third term

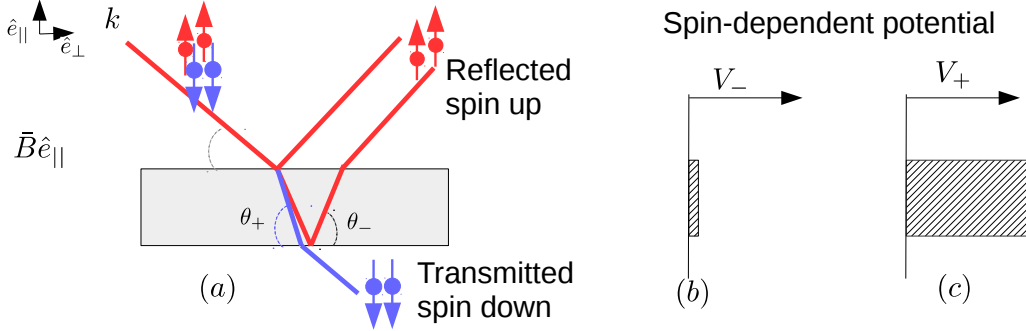


Figure 1.2: Cartoon drawing of spin-dependent reflection (not to scale) from a nonmagnetic/magnetic layer. In (a) \uparrow and \downarrow are the two neutron spin states incident on a magnetic layer. They experience different potentials resulting to \uparrow reflected and \downarrow transmitted. In (b) and (c): the potentials experienced by a neutron of each spin state.

is the Foldy interaction. The main contribution and the one we focus on is the Zeemann term,

$$V_z(\mathbf{r}) = -\boldsymbol{\mu} \cdot \mathbf{B}(\mathbf{r}) = -\mu\boldsymbol{\sigma} \cdot \mathbf{B}(\mathbf{r}), \quad (1.14)$$

where $\boldsymbol{\sigma} = (\hat{\sigma}_x, \hat{\sigma}_y, \hat{\sigma}_z)$ are the Pauli matrices.

Consider a neutron of wavevector k scattered by a Zeemann interaction originating from a magnetic sample with mean magnetic field \bar{B} . The sum nuclear and magnetic potentials is given by,

$$V_\pm = \frac{2\pi\hbar^2}{m}N\bar{b} \pm \mu\bar{B}, \quad (1.15)$$

where the \pm refers to the spin parallel and spin anti-parallel to the magnetic field, respectively. The refractive index corresponding to the potential can be expressed as,

$$n_\pm^2 = 1 - \lambda^2 N \frac{\bar{b} \pm \bar{p}_0}{2\pi}, \quad \bar{p}_0 = -\frac{\mu m \bar{B}}{\pi N \hbar^2} \quad (1.16)$$

where, \bar{p}_0 is the average magnetic scattering length. Magnetic scattering provides an enhancement to the critical angle in the case of $\bar{b} + \bar{p}_0$ and a reduction in the case of $\bar{b} - \bar{p}_0$. Even though, the critical angle for the two neutron spin states when they are reflected by a nonmagnetic material are the same, the situation is very different when they reflect from a planar boundary with two refractive indexes n_\pm . A neutron of one spin emerge at a

smaller angle than a neutron of the opposite spin. Shown in Fig. 1.2a are the trajectories in the spin-dependent potential shown in Fig. 1.2b. These trajectories corresponding to the reflection of the spin parallel and spin anti-parallel are at angles given by,

$$\theta_{\pm} = \sin^{-1} \sqrt{|1 - n_{\pm}^2|} = \lambda \sqrt{N|\bar{b} \pm \bar{p}_0|/\pi}. \quad (1.17)$$

Therefore, by simply controlling \bar{b} and \bar{p}_0 , the potential can be tuned to have neutrons with spin parallel transmitted ($\theta_+ > \theta^c$), and neutrons with spin anti-parallel reflected ($\theta_- < \theta^c$), see Fig. 1.2a. As an example, a layer of Fe:Co:V (49:49:2) in a saturated magnetic field have $N|\bar{b} + \bar{p}_0| = 36.75 \mu\text{rad}^2 \text{\AA}^{-2}$, and $N|\bar{b} - \bar{p}_0| = 0.13 \mu\text{rad}^2 \text{\AA}^{-2}$. Therefore, by selecting the reflected or the transmitted neutrons a polarized neutron beam can be generated. This is the same principle under which polarizing crystal and polarizing mirrors work [23].

1.3.5 Phase

When a neutron propagates through a medium, it can experience a change in a quantum phase. This phase can be represented by an integral over the classical path,

$$\Phi = \frac{1}{\hbar} \int \mathcal{L} dt, \quad (1.18)$$

where \mathcal{L} is the Lagrangian. The Lagrangian can be expressed as a function of the Hamiltonian \mathcal{H} , the canonical momentum \mathbf{p} , and the velocity \mathbf{v} , as,

$$\mathcal{L} = \mathbf{p} \cdot \mathbf{v} - \mathcal{H}. \quad (1.19)$$

The phase is commonly measured when two or more waves are allowed to interfere. Interference phenomenon is a result of adding multiple waves with a definite phase relation between them. An interferometry setting in phase space is shown in Fig. 1.3a where an incident neutron, in a superposition of two states labelled $|\Psi_{\text{I}}\rangle$ and $|\Psi_{\text{II}}\rangle$, evolves through a media picking up phases,

$$\Phi_{\text{I}} = \frac{1}{\hbar} \int \mathcal{L}_{\text{I}} dt, \quad \text{and} \quad \Phi_{\text{II}} = \frac{1}{\hbar} \int \mathcal{L}_{\text{II}} dt, \quad (1.20)$$

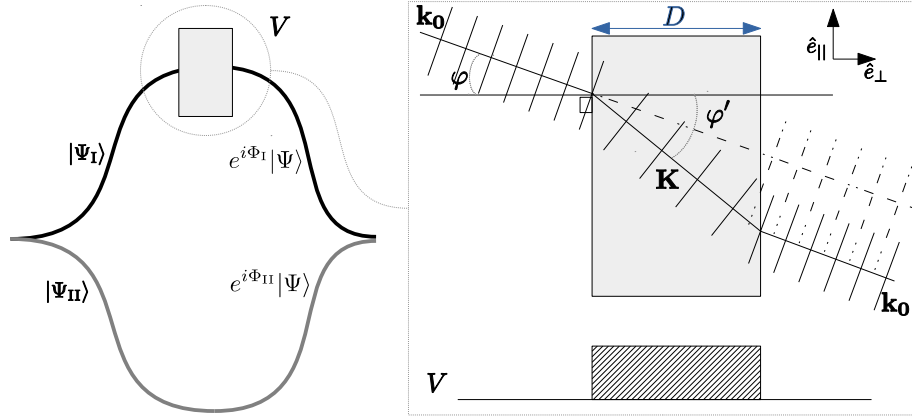


Figure 1.3: The evolution of a neutron wavefunction through a system where one component of the wavefunction goes through a potential V . When the components recombine, they interfere. The refraction of the neutron in the potential is shown in the expanded drawing.

respectively. One phase is introduced by a potential and the other by an empty space. Upon recombination, the resultant phase difference between the two paths is,

$$\Delta\Phi = \Phi_I - \Phi_{II}. \quad (1.21)$$

Under the stationary state conditions, the Hamiltonians $\mathcal{H}_I = \mathcal{H}_{II}$ lead to $\mathcal{L}_I = \mathbf{p}_I \cdot \mathbf{v} - \mathcal{H}_I$ and $\mathcal{L}_{II} = \mathbf{p}_{II} \cdot \mathbf{v} - \mathcal{H}_I$. As a result the phase difference may be expressed exclusively in terms of the momentum as,

$$\Delta\Phi = \frac{1}{\hbar} \left(\int_{\text{path I}} \mathbf{p}_I \cdot \mathbf{dr} - \int_{\text{path II}} \mathbf{p}_{II} \cdot \mathbf{dr} \right) = \oint (\mathbf{k}_I - \mathbf{k}_{II}) \cdot \mathbf{dr}, \quad (1.22)$$

where we have used $\mathbf{v} = \mathbf{dr}/dt$.

In Fig. 1.3b, a neutron of wavevector $\mathbf{k} = k(\sin \varphi \hat{e}_{||} + \cos \varphi \hat{e}_{\perp})$ is incident at an angle φ onto a sample of thickness D . The wavevector inside the potential can be decomposed to $\mathbf{K} = K(\sin \varphi' \hat{e}_{||} + \cos \varphi' \hat{e}_{\perp})$. In other forms, it can be expressed in terms of the refractive index n of the medium and using Snell's law $\sin \varphi = n \sin \varphi'$, we get

$$\mathbf{K} = K \sin \varphi' \hat{e}_{||} + k \sqrt{n^2 - \sin^2 \varphi} \hat{e}_{\perp}, \quad (1.23)$$

Interaction	Potential	Phase shift $[\Delta\Phi]$	Reference
Nuclear	$2\pi\hbar^2 b\delta(\mathbf{r})m^{-1}$	$-Nb\lambda D$	[24]
Magnetic	$-\boldsymbol{\mu} \cdot B(\mathbf{r})$	$\pm\mu Bm\lambda D(2\pi\hbar^2)^{-1}$	[24]
Gravitational	$m\mathbf{g} \cdot \mathbf{r}$	$m^2g\lambda A \sin(\alpha)(2\pi\hbar^2)^{-1}$	[25]
Coriolis	$-\hbar\boldsymbol{\omega}_e \cdot (\mathbf{r} \times \mathbf{k})$	$(2m/\hbar)\boldsymbol{\omega}_e \cdot \mathbf{A}$	[26]
Aharonov-Casher	$-\boldsymbol{\mu} \cdot (\mathbf{v} \times \mathbf{E})c^{-1}$	$\pm\{2\mu/(\hbar c)\}\mathbf{E} \cdot \mathbf{D}$	[27]
Scalar Aharonov-Bohm	$-\boldsymbol{\mu} \cdot \mathbf{B}(t)$	$\pm\mu Bt/\hbar$	[28]
Berry	$i\langle\psi(\xi) \nabla_\xi\psi(\xi)\rangle$	$\Omega/2$	[29]

Table 1.2: The phase shift when the associated neutron interaction potential is placed in one arm of an NI. g is the gravitational strength, \mathbf{A} is the normal area enclosed by the interferometer, α is the angle between the transverse vertical to the beam and the area \mathbf{A} , $\boldsymbol{\omega}_e = 7.27 \times 10^{-5} s^{-1}$ is the angular rotation of the earth, \mathbf{E} is the electric field, ω is the solid angle subtended by the closed loop parametrized by ξ on a Bloch sphere. (Table reproduced from [16])

where $n = K/k$. The phase difference is obtained to be;

$$\Delta\Phi = (\mathbf{K} - \mathbf{k}) \cdot D\hat{e}_\perp = (K_\perp - k_\perp)D = \left(\sqrt{n^2 - \sin^2\varphi} - \cos\varphi \right) Dk. \quad (1.24)$$

Using $n = 1 - N\bar{b}(\lambda^2/2\pi)$, and a first order approximation we obtain,

$$\Delta\Phi \simeq -Nb\lambda D', \quad (1.25)$$

where D' is the effective path length traversed by the neutron inside the sample, and is related to the thickness by, $D' = D(\hat{k} \cdot \hat{e}_\perp)^{-1} = D/\cos\varphi$. If instead of a nuclear potential, the neutron is in a constant magnetic field and with neutron spin aligned parallel or anti-parallel to the field, the phase shift is:

$$\Delta\Phi = \pm \frac{\mu B l}{\hbar v} = \pm \frac{\mu m \lambda B D}{2\pi\hbar^2}, \quad (1.26)$$

where D , is the length of the region containing the field.

Besides the magnetic and nuclear interactions, which are of primary interest to us, a list of neutron interaction potentials and the associated phase shift when the potential is placed in one arm of an NI as compiled in ref. [16] is presented in Table 1.2.

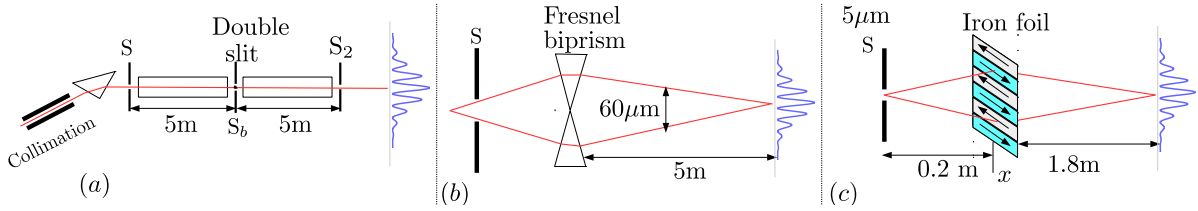


Figure 1.4: Schematic drawings of NI based on wavefront division. (a) is a double slit type NI [30]. A collimated beam through a source slit S propagates as a spherical wave onto a double slit S_d , which acts as a two-slit secondary source to separate the wavefront into two spherical waves. The two waves recombine on a position sensitive detection scheme located 5 m away. Schematic setup in (b) is similar to (a) but the double slit is replaced by a SiO_2 Fresnel biprism [31]. The biprism, through refraction, refocuses the wavefront onto a screen where interference occurs. In (c) is a spin-path based NI which is similar to (b), but the refraction is achieved by Frenel diffraction of neutron by a ferromagnetic domain boundary [32].

1.4 Neutron interferometry

1.4.1 Wavefront and amplitude division neutron interferometers

In wavefront division, the propagating wavefunction is split into two macroscopically distinct wavefronts in analogous to the Young slit experiment in optics [18]. Experimental realizations include the Fresnel biprism, implemented by Maier-Leibnitz and Springer [31], the double slit NI of Zeilinger et al [30], and the ferromagnetic crystal spin-path based NI of Klein and Opat [32], each shown in Fig. 1.4. In Fig. 1.4a, a monochromatic neutron beam emerging from a collimator is incident onto a source slit S , to generate a spherical wave. The spherical wave propagates onto a double slit S_d , located 5 m away, which acts as a secondary source with two slits to separate the wavefronts into two secondary spherical waves. These waves converge and interfere on a screen located 5 m away. Shown in Fig. 1.4b is an NI setup that is similar to Fig. 1.4a, but the double slit is replaced by a SiO_2 Fresnel biprism [31]. The biprism, through refraction, refocuses the whole wavefront onto a screen

where interference occurs. In Fig. 1.4c, the wavefront division is realized through a spin-dependent interaction. In addition, the refocusing is achieved due to the spin-dependent Fresnel diffraction of neutron by a ferromagnetic domain boundary. In most cases, the advantages of wavefront division NIs include less susceptibility to mechanical and thermal disturbances, and a long beam path (10 m) that greatly enhances its sensitivity. On the other hand, their limitations include the small separation of the two wavefronts which is typically around $60 \mu\text{m}$ [31]. Small separations offer less flexibility in experiments as the detection of the neutron is best achieved mostly by position sensitive detector. In addition, a smaller separation makes it very difficult to resolve the beam and to place a sample in one arm for a phase difference measurement. These factors limit the range of experiments that can be performed and also render the implementation very challenging.

We focus on amplitude division NI where the amplitude of the wavefunction is coherently split through partial reflection and partial transmission from beam splitters. An efficient way of realizing a neutron beam splitter is through diffraction from a periodic structure. Another implementation method is through unitary spin evolution under a direct-current (DC) or a radio-frequency (RF) magnetic field.

1.4.2 Neutron spin-interferometry

Spin-interferometry is achieved by controlling the neutron spin via a spin-dependent interaction. With stationary or time-dependent magnetic fields, the neutron spin can be arbitrarily rotated. The associated polarization vector found by the expectation values of the Pauli spin-matrices, $\mathbf{P} = (\langle \hat{\sigma}_x \rangle, \langle \hat{\sigma}_y \rangle, \langle \hat{\sigma}_z \rangle)$, may be used to describe the dynamics of a neutron spin. Along any axis it is defined by the ratio of the difference in the intensities of neutrons with opposite spins to the incident beam. When a neutron beam is exposed to a stationary magnetic field the spin evolution is described by the Bloch equation

$$\frac{d\mathbf{P}}{dt} = \mathbf{P} \times \gamma \mathbf{B}. \quad (1.27)$$

The precession frequency of \mathbf{P} is called the Larmor frequency, expressed as $\omega_L = \gamma |\mathbf{B}|$, where $\gamma = 2\mu/\hbar$ is the gyromagnetic ratio. The Larmor-precession angle solely depends on the magnitude of the applied magnetic field and the time τ spent in the magnetic

field; this angle is given by, $\alpha = \omega_L \tau$, for spin perpendicular to the field. A neutron with spin orientation perpendicular to an axis along $\hat{\mathbf{n}} = \mathbf{B}/|\mathbf{B}|$, and rotated by an angle α is described by the unitary operator,

$$R_{\mathbf{n}}(\alpha) = e^{i\frac{\alpha}{2}\boldsymbol{\sigma}\cdot\hat{\mathbf{n}}} = \cos(\alpha/2)\mathbb{1} + i\boldsymbol{\sigma}\cdot\hat{\mathbf{n}}\sin(\alpha/2). \quad (1.28)$$

For example, if a neutron with spin oriented along the +z axis, denoted as $|\uparrow\rangle$ is incident onto a field of strength α , and with orientation along the +x-axis, $\hat{\mathbf{n}} = (1, 0, 0)$, the neutron spin state transforms to,

$$R_x(\alpha)|\uparrow\rangle = \cos(\alpha/2)|\uparrow\rangle + i\sin(\alpha/2)|\downarrow\rangle. \quad (1.29)$$

A 50:50 spin rotation is achieved by setting $\alpha = \pi/2$, while a spin flip is achieved by setting $\alpha = \pi$. Standard DC driven precession spin flippers [33, 34] for time independent fields operate under this principle and completely reverse the spin of a neutron with nearly 100% efficiency.

Figure 1.5a presents a Ramsey-type NI which makes use of two $(\pi/2)_x$ spin rotators. The first spin rotator, $(\pi/2)_x$, rotates the incident state $|\uparrow\rangle$ to the state $|\psi_R\rangle = (|\uparrow\rangle + |\downarrow\rangle)/\sqrt{2}$, which is further rotated by a second spin rotator, $(\pi/2)_x$, before spin sensitive measurement.

In Fig. 1.5b, the input states given by $|\psi_+\rangle = (|\uparrow\rangle + |\downarrow\rangle)/\sqrt{2}$ is prepared along the x-axis. The beam splitter is achieved by passing the neutron through a Walleston prism, whose fields are oriented along the z-axis. The Walleston prism provides a field in which the two neutron spin states experience different magnetic gradients. As a result of the magnetic gradient, the spins are deflected in analogous to the deflection of light through a glass prism. A second Wollaston prism with a reversed field configuration redirects the spin-path correlated states to propagate parallel to each. The state after the assembly is denoted by,

$$|\psi_{\text{SP}}\rangle = \frac{|\uparrow\rangle|\text{I}\rangle + |\downarrow\rangle|\text{II}\rangle}{\sqrt{2}}. \quad (1.30)$$

The separation between the two states is determined by the strength of the field, and the time spent in the Walleston prism. With a bigger separation, a sample can be introduced before the state is refocused by another pair of Wollaston prisms. A study with this setup has revealed existing properties of some samples [35].

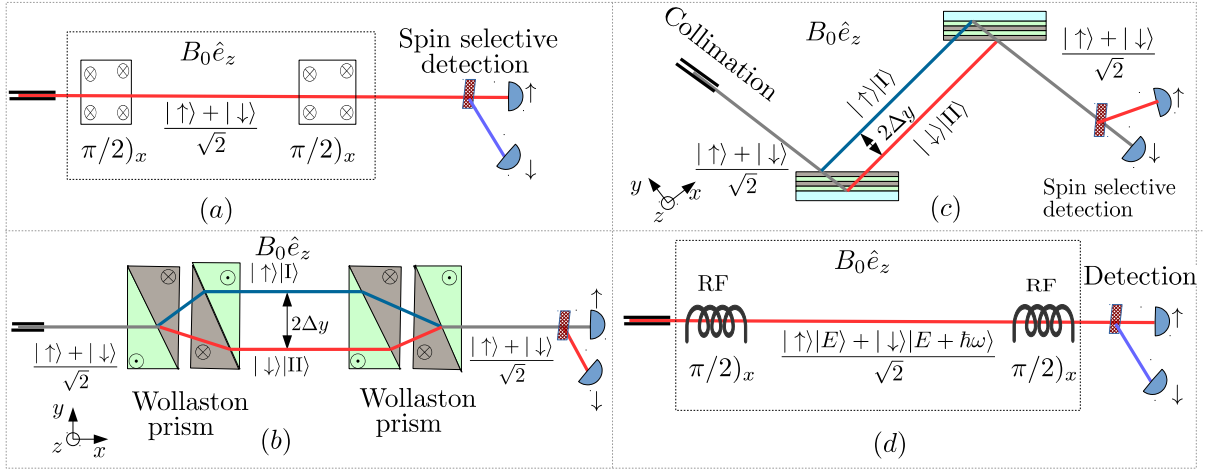


Figure 1.5: Schematic of spin-path based neutron interferometry. (a) Ramsey-type spin NI implemented with two $\pi/2)_x$ spin rotators oriented perpendicular to the incident spin state (the +z-axis), followed by spin sensitive measurement [33]. In (b), the input state $|\psi_+\rangle = (|\uparrow\rangle + |\downarrow\rangle)/\sqrt{2}$ is prepared along the x-axis. The beam-splitting is achieved by passing the neutron through a pair of Wollaston prisms, the action of which produces a state that is correlations in the spin and path DOFs. The state is further recombined by another pair of Wollaston prism before spin selective measurement [35]. In (c) an input $|\psi_+\rangle$ sent through a beam splitter implemented using magnetic multilayer. The spin-path correlated state is then passed through another magnetic multilayer where they recombine and interfere [36]. In (d), an RF field is used to create a superposition spin-energy entangled state [34].

Figure 1.5c presents an interferometry setup similar to (a) with an input state $|\psi_+\rangle$, but the beam-splitting is achieved by reflection from a magnetic/nonmagnetic layer. A spin-path correlated state emerging from the first beam splitter is then passed through another magnetic multilayer where they recombine and interfere [36, 37].

Figure 1.5d presents an incident state $|\uparrow\rangle|E\rangle$, where E is the total energy, propagating through an RF coil [38] with a time-dependent magnetic fields. In an RF flipper, the neutron spin flip is accompanied by an energy exchange leading to a non conserved total energy of the neutron. After the RF field, the spin anti-parallel to the field has energy

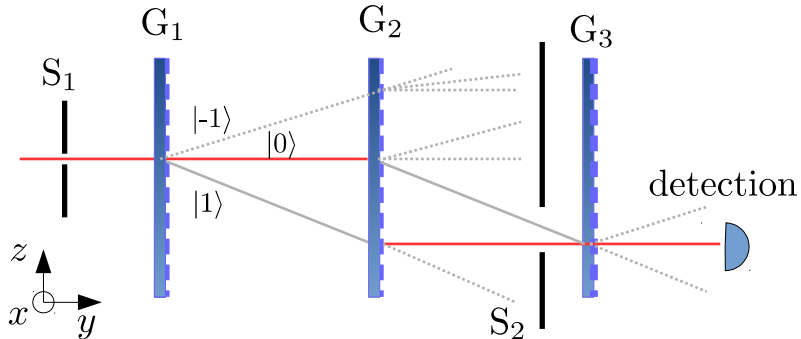


Figure 1.6: Mach-Zehnder type grating NI with the first grating, G_1 , acting as a beam splitter. The second grating, G_2 , refocuses the wavefunction so that they recombine and interfere on G_3 . See [41] for more details and applications of grating neutron interferometry.

$E - \hbar\omega$, while that along the field remain with energy E , where ω is the frequency of the excitation. The correlated spin-energy state then given by [39],

$$|\psi_{SE}\rangle = \frac{|\uparrow\rangle|E\rangle + |\uparrow\rangle|E - \hbar\omega\rangle}{\sqrt{2}}. \quad (1.31)$$

In an interferometry setup, the state can coherently recombine and interfere on the next RF field. Other spin-base implementations of neutron interferometry are possible, for more information see ref. [16].

1.4.3 Periodic structure neutron interferometers

Periodic structure neutron interferometers have been implemented with either gratings [40] or perfect crystal [3]. For a grating NI, a schematic is shown in Fig. 1.6. The first grating, G_1 , coherently splits the incident neutron wavefunction into various orders. The second grating, G_2 , is geometrically oriented to refocus the selected orders, by use of a slit, onto the third grating, G_3 , where they interfere. For more details on functionality and applications, see ref. [41].

A greater part of this thesis is based on perfect crystal NI. Therefore, prior to giving a detailed description, we first introduce some geometries that have been used over the

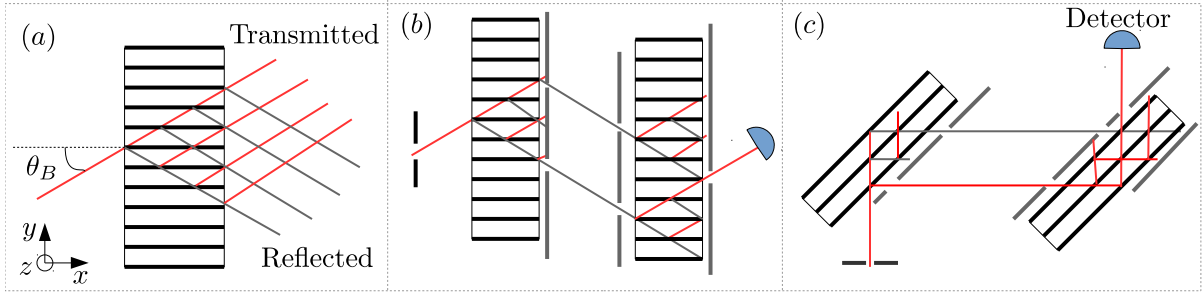


Figure 1.7: Perfect single crystal NIs. a) Single crystal NI with Pendelösung oscillations [43]. (b) Double crystal NI in the Laue geometry [44]. (c) Double crystal NI in the Bragg geometry [45]. The first crystals of the double crystal NI is a beams splitter, to create a coherent superposition state which then recombine and interfere on the second crystal.

years. One reason for the use of Si is the availability of pure monocrystalline ingots originally provided by the semiconductor industry. These NIs are macroscopic devices with a characteristic dimension typically of a few centimeters. In most cases, they consist of one or more parallel crystal blades machined on a common crystal base. This ensures an arcsecond alignment of the lattice planes of each blade relative to each other, which is a stringent requirement to observe interference from Bragg diffraction. In addition, their operation principle is based on the undisturbed arrangement of atoms in a single crystalline silicon crystal. When a neutron beam is incident on a perfect crystal such that the Bragg condition given by,

$$2d_{hkl} \sin \theta_B = n\lambda, \quad \text{with, } n = \pm 1, \pm 2, \dots, \quad (1.32)$$

is satisfied, the beam splits coherently into two components. d_{hkl} , is the crystal lattice spacing along the reciprocal lattice vector defined by the Miller indices h, k, l . As will be discussed further in chapter 4, when the incident wavefunction satisfies the Bragg condition, the resulting forward-diffracted and Bragg-diffracted waves also satisfy the Bragg condition and get diffracted within the same crystal. The secondary diffraction generates a single crystal interference pattern known as the Pendelösung oscillation. Shown in Fig. 1.7a is a schematic of a NI based on Pendelösung oscillations, from a single crystal oriented in the Laue geometry [42, 43].

The forward-diffracted and the Bragg-diffracted waves (transmitted and reflected waves) propagate out of a single crystal as a superposition of two macroscopically separated components of a neutron wavefunctions. A second crystal can be used to recombine the wavefunctions, thereby realizing a double crystal interferometer in either the Laue or Bragg geometries [44, 45]. Schematic drawings of two crystal NI are shown in Figs. 1.7b and 1.7c. Of recent, they have been used to study deformation in crystals, and also in the search for the neutron electric dipole moment [46].

The commonly used perfect crystal interferometer is the three-blade NI in the Laue geometry [3]. It is analogous to the Mach-Zehnder interferometer in light optics and also inherits many features from x-ray interferometry. Made with three crystal blades, the first blade acts as a beam splitter and the middle blade as a lossy mirror to refocus the two components of the wavefunction onto the third crystal blade. Depending on the experiment, the mirror crystal can be implemented to achieve either the symmetric or the skew-symmetric NI. In the symmetric case, Fig. 1.8a, the neutron wavefunction on both arms reaches the mirror crystal at the same time. Meanwhile, in the skew-symmetric case, Fig. 1.8b, the mirror crystal is split into two blades located such that the components of the wavefunction on both arms reach it at different times [27, 47]. One of the advantages of the skew-symmetric NI over the symmetric NI is that it can accommodate a bigger sample which can be translated from one path to another without the need to rotate.

Over the years, other geometries of interferometers have been developed. The four-blade NI, shown in Fig. 1.8c, is similar to the three-blade NI, but differs in that the neutron wavefunction reaching the analyzer crystal is reflected twice without mixing at the crossing. In addition, the four-blade NI has been experimentally demonstrated to be immune to a low-frequency mechanical vibrational noise [6]. The five-blade NI, shown in Fig. 1.8d, can be converted into various geometries. One useful configuration is similar to the four-blade NI, but differs in that the wavefunctions interfere when they cross paths in the middle (see chapter 5). In Fig. 1.8e is a hybrid NI that can be converted into a three-blade and four-blade NIs. In Fig. 1.8f, is the six-blade double loop NI, which is a large area interferometer and has been used for probing the dynamical phase [48].

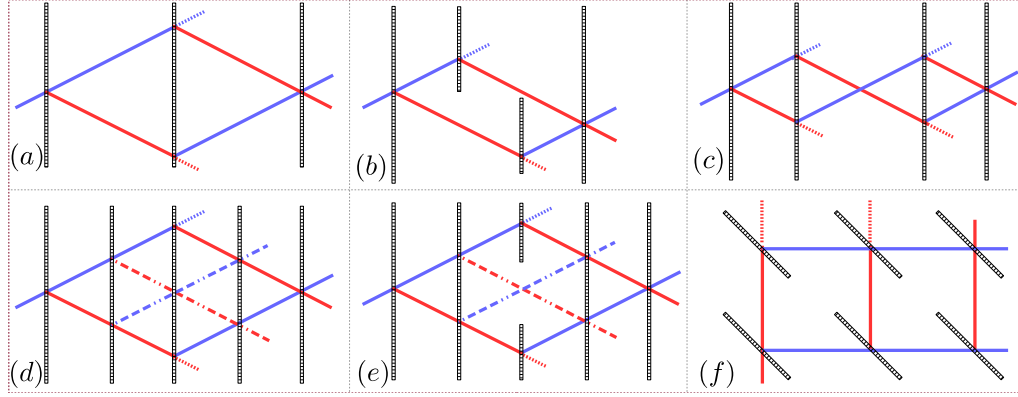


Figure 1.8: Schematics of Laue-type NIs. Shown in (a) is a symmetric three-blade NI. (b) is a skew symmetric three-blade NI is shown. It has a larger space to accomodate a bigger sample. (c) is a four-blade NI which is shown to refocus noise from mechanical vibration [6]. (d) is a multi-loop five-blade NI. It can be converted to three-blade and five-blade NIs. (e) is another design of the five-blade, which can be converted to the four-blade DFS and standard symmetric three-blade NIs. Finally, in (f) is the double loop interferometer, with six blades. It is a large area interferometer and has been used for probing the dynamical phase [48]

1.5 Operator representation

In the operator picture for neutron interferometry, the plane wave diffraction is formulated in terms of eigen-kets [49]. Figure 1.9 is a schematic of an incident wave coherently split into two states by a silicon crystal. These states, denoted by $|I\rangle$ for $k_{\parallel} > 0$, and $|II\rangle$ for $k_{\parallel} < 0$, form a basis for $SU(2)$. One representation is the eigenvectors of $\hat{\sigma}_z$ in the computational basis,

$$|I\rangle = \begin{pmatrix} 0 \\ 1 \end{pmatrix}, \quad \text{and} \quad |II\rangle = \begin{pmatrix} 1 \\ 0 \end{pmatrix}. \quad (1.33)$$

Since neutrons are from a single beam, the only choices of the input state to an NI is $|\Psi_{\text{in}}\rangle = |I\rangle$ or $|II\rangle$, which can be represented as a density matrix,

$$\rho = |\Psi_{\text{in}}\rangle\langle\Psi_{\text{in}}|. \quad (1.34)$$

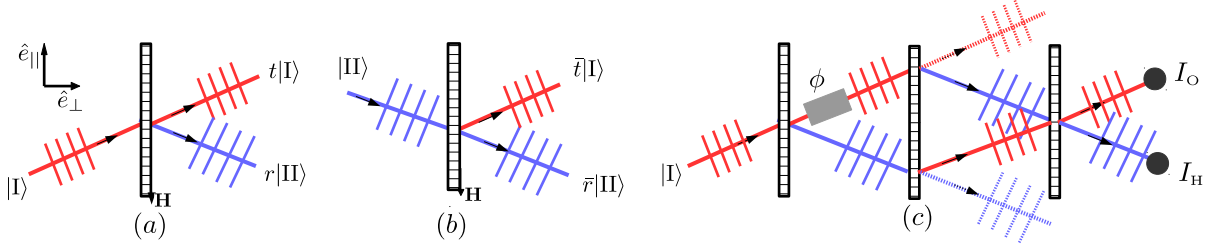


Figure 1.9: Operator formalism of a single crystal diffraction. (a) is the schematic of the evolution of $|I\rangle$, and (b) is the evolution of $|II\rangle$. A full sketch of the paths within a three-blade NI is shown in (c). The neutrons leaving after the middle crystal do not make it to O-beam or H-beam.

As a result, the input state for the path degree of freedom (DOF) is always pure. Depending on the type of crystal, neutrons are absorbed. For Si, the absorption cross-section for thermal neutrons is $\sigma_a = 0.17$ barns. This corresponds to a neutron transmission of 0.99 through a 10 mm thick sample of Si.

If we neglect the absorption, the transformation of the basis states under the crystal blade operator is a unitary operation. This unitary designated as U_B acts as:

$$U_B|I\rangle = t|I\rangle + r|II\rangle, \quad U_B|II\rangle = \bar{r}|I\rangle + \bar{t}|II\rangle,$$

where, t , is the transmission coefficient from down-to-up, and \bar{t} , is the transmission coefficient from up-to-down, and r and \bar{r} the similarly defined reflections. The 2×2 matrix representation of U_B is,

$$U_B = t|I\rangle\langle I| + r|II\rangle\langle I| + \bar{r}|I\rangle\langle II| + \bar{t}|II\rangle\langle II|$$

with, $\bar{t} = t^*$, $\bar{r} = -r^*$, and $|t|^2 + |r|^2 = 1$ the unitary conditions. The exact form of operator will be discussed in chapter 4. A phase flag, commonly made from a precisely machined plate of uniform density material, may be placed in the interferometer to induce a phase shift between the two paths, see Eq. 1.25. If phase difference induced by a sample in one path is $\phi = N\bar{b}\lambda D$ (see Fig. 1.9), the phase operator may be represented as,

$$U_\phi = e^{i\phi}|I\rangle\langle I| + |II\rangle\langle II|. \quad (1.35)$$

The middle crystal of the three-blade NI equally acts as a beam splitter, although from the geometry of the NI some neutrons leave the NI, Fig. 1.9. This is because no information encoded in the phases is lost to these neutrons that are usually not detected. By post-selection on neutron arriving at either the O-beam or H-beam, a unitary evolution description of the NI is obtained after re-normalization. The operator of the lossy mirror can be derived from U_B , as,

$$U_M = \Pi_O U_B \Pi_H + \Pi_H U_B \Pi_O = \bar{r}|I\rangle\langle II| + r|II\rangle\langle I| \quad (1.36)$$

where, Π_O and Π_H are corresponding projection operators given by,

$$\Pi_O = |I\rangle\langle I|, \quad \Pi_H = |II\rangle\langle II|, \quad (1.37)$$

when darkcounts resulting from the response of the detectors in the absence of the beam are neglected. The operator of the analyzer blade is the same as a beam splitter operator U_B , so the overall evolution of the state in an NI is given by,

$$\rho' = U_B U_M U_\phi U_B |\Psi_{\text{in}}\rangle\langle\Psi_{\text{in}}| U_B^\dagger U_\phi^\dagger U_M^\dagger U_B^\dagger. \quad (1.38)$$

In the case where the neutrons in both beams are detected at the exit of the interferometer, historically known as the the O-beam and H-beam (see Fig. 1.9), the unnormalized intensities averaged over a time period containing I_0 neutron are,

$$I_O = \text{Tr}[\rho' \Pi_O] = 2I_0 |tr\bar{r}|^2 (1 + \cos(\Delta\Phi)), \quad (1.39)$$

$$I_H = \text{Tr}[\rho' \Pi_H] = I_0 (|tr\bar{t}|^2 + |r\bar{r}r|^2 - 2|tr\bar{r}|^2 \cos(\Delta\Phi)), \quad (1.40)$$

where $\Delta\Phi = \phi + \phi_0$, and ϕ_0 is a constant phase resulting from any imbalance in the interferometer geometry. Also, the sum intensity is $I_O + I_H = \text{Tr}[\rho'] = I_0|r|^2$ and the neutrons escaping from the interferometer have intensities $I_0|t|^4$ and $I_0|rt|^2$ for the upper and lower paths, respectively. Using the projective value measure (PVM) and renormalizing the output intensity, we note that $\Pi_O + \Pi_H = \mathbb{1}$, the sum probabilities of detection on the O-beam and H-beam intensities is 1. This leads to a quantum information description of the second blade treated as a perfect mirror with operator O_M , given by;

$$O_M = e^{i \arg[r]} |II\rangle\langle I| - e^{-i \arg[r]} |I\rangle\langle II|. \quad (1.41)$$

In other words, the NI evolution of the state leads to an output state of,

$$\rho = U_B O_M U_\phi U_B |\Psi_{\text{in}}\rangle\langle\Psi_{\text{in}}| U_B^\dagger U_\phi^\dagger O_M^\dagger U_B^\dagger. \quad (1.42)$$

The average renormalized intensity at the O-beam and H-beam can be expressed as,

$$\overline{I}_O = \mathcal{A}_O \left(1 + \cos(\Delta\Phi)\right), \quad \text{and} \quad \overline{I}_H = \mathcal{B}_H - \mathcal{A}_O \cos(\Delta\Phi), \quad (1.43)$$

where,

$$\mathcal{A}_O = 2|tr|^2, \quad \mathcal{B}_H = |t|^4 + |r|^4, \quad \mathcal{A}_O + \mathcal{B}_H = 1. \quad (1.44)$$

In perfect crystal neutron interferometry experiments, self-interference occurs where at most a single neutron is present inside the interferometer at a given time. This is achieved thanks to the low intensity of neutrons through the interferometer, about 1 neutron per ms. At this rate, one neutron is detected at a time when the next is yet to be born.

1.6 Interferometry contrast

The contrast (analogous to the fringe visibility in optics) is commonly used to quantify the quality of the interference pattern. It can be expressed as,

$$\mathcal{V} = \frac{I_{\text{max}} - I_{\text{min}}}{I_{\text{max}} + I_{\text{min}}}, \quad (1.45)$$

where I_{max} and I_{min} are the maximum and minimum intensities of the interference pattern. In the ideal interferometry setting in Eq. (1.43), the contrasts for the O- and H-beams is $\mathcal{V}_O = 1$ and $\mathcal{V}_H = \mathcal{A}_O/\mathcal{B}_H$, respectively. In reality, the highest contrast is below 1. This is due to the presence of noise resulting from various environmental conditions and imperfections in making the NI. The loss of contrast can be viewed as a result of the loss of coherence.

In order to make a simple analogy between the contrast and the coherence function, we consider a wavepacket propagating through a three-blade NI with a material sample in one path. At the exit, each component of the wavepacket picks a phase $\Delta\Phi = \mathbf{k}\cdot\mathbf{\Delta}$ relative

to the reference beam with no sample. The intensities at the O-beam and H-beam may be expressed similar to Eqs. (1.39, 1.40) as,

$$I_{\text{O}} = \mathcal{A}_{\text{O}} \left(1 + |\Gamma(\Delta)| \cos(\arg[\Gamma(\Delta)]) \right), \quad (1.46)$$

$$I_{\text{H}} = \mathcal{B}_{\text{H}} - \mathcal{A}_{\text{O}} |\Gamma(\Delta)| \cos(\arg[\Gamma(\Delta)]). \quad (1.47)$$

With the coherence function expressed as,

$$\Gamma(\Delta) = \Gamma(\Delta, 0) = \int d\mathbf{k} p_k \exp(i\mathbf{k} \cdot \Delta), \quad (1.48)$$

where, $p_k = |\mu_{\mathbf{k}}|^2 |t\bar{r}|^2 / \mathcal{A}_{\text{O}}$. By comparison with Eq. 1.45, the contrasts in the O-beam and H-beam is related to the coherence function by,

$$\mathcal{V}_{\text{O}} = |\Gamma(\Delta)|, \quad \mathcal{V}_{\text{H}} = \mathcal{A}_{\text{O}} / \mathcal{B}_{\text{H}} |\Gamma(\Delta)|. \quad (1.49)$$

Thus, it is clear that the coherence in the O-beam is equal to that in the H-beam. However, the contrast in the O-beam is equal to the absolute value of the coherence function, but that of the H-beam is scaled by a factor $\mathcal{A}_{\text{O}} / \mathcal{B}_{\text{H}}$. Therefore, the contrast in an NI is equal to the absolute value of the coherence function only for a balanced NI.

1.7 Neutron detection

Neutron detection in perfect crystal neutron interferometry is mostly done with ^3He detectors. These detectors are typically thin walled, cylindrical, stainless steel containers of 2.5 cm in diameter pressurized to 10 bar of ^3He . During detection, the nuclear reaction,



takes place, with the energy released as the kinetic energy of the proton, p , and triton, ^3H . As these energetic particles propagate through the gas chamber, they create ion pairs that move to a thin anode/cathode wire producing an electrical signal. The signal is passed through an amplifier and an electronic pulse counter to generate a count. Figure 1.10 shows a typical circuit used for neutron detection.

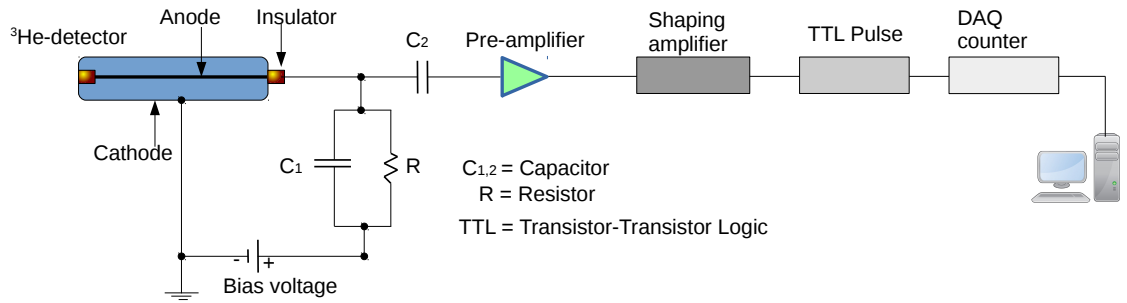
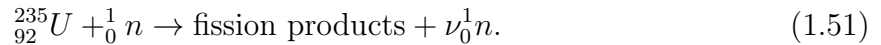


Figure 1.10: A schematic circuit used for neutron detection. After a nuclear reaction, the energetic fission products create a proton and triton pair that moves to the cathode and anode to ionize ^3He gas and generate an electric signal. The signal is then amplified and converted to a standard TTL pulse. The pulse is registered by a digital acquisition DAQ control board as a count. The DAQ is controlled via a computer.

Another type of detector is the fission chamber detector. They are used especially for monitoring fluctuations of the neutron beam. Also, they are usually designed in a uranium coated flat panel form for a large surface area of a cathode cylinder. Made from uranium-235 (U-235), fission chamber detectors are less efficient (about 0.1% or less), but can accept a high intensity beam compared to ^3He detectors. The neutrons in the beam undergo a nuclear reaction given by,



Among various types of fission products, the two products ${}_{36}^{92}\text{Kr}$ and ${}_{56}^{141}\text{Ba}$ for $\nu = 3$, carry energies of about 90 MeV and 65 MeV. As they travel through gas, the gaseous mixture (e.g methane/argon) along their path is ionized. Depending on their charge, the ion pairs travel to the cathode and anode producing a current that is digitized and displayed. Fission chambers typically don't use amplifiers as the signal produced is strong enough for detection.

Another class of detectors are those used especially in neutron imaging. They exploit the electronic excitations generated when a thermal neutron is captured and then a subsequent emission of energetic charged particles. The electrons created from ionization can generate further excitations in the material causing more electrons to be emitted. When

the electrons relax, they emit photons. These photons are then passed through photomultiplier tube or avalanche photodiode before being registered as counts. The details of these detectors will not be discussed here.

In polarized neutron experiments spin-dependent detection is commonly accomplished with polarized ^3He filter in combination with a neutron detector. The operation principles of a polarized ^3He filter is the large nuclear spin-dependence of neutron capture into the broad unbound resonance of the intermediate ^4He state [50]. The neutron capture cross-section σ_c for ^3He depends on the wavelength by $\sigma_c[\text{barns}] = 2962\lambda [\text{\AA}]$. In its design, the ^3He is filled in a 1.8 bar pressurized glass cell alongside Rubidium and nitrogen. The cell is polarized by the collision of ^3He atoms and rubidium in a process referred to as spin-exchange optical pumping [51]. In optical pumping, a circularly polarized infrared laser light that is tuned to the appropriate wavelength, is used to excite electrons in rubidium. Through collision, angular momentum is transferred from the rubidium electrons to the ^3He nuclei. Nitrogen serves as a quenching gas to prevent the fluorescence of ^3He , a process that would lead to depolarization. An ^3He polarization, P_{He} , of about 75% can be achieved [52]. Using these values and also ignoring the small scattering of the neutrons with spin-component parallel to the ^3He nuclear spin, the spin-dependent transmission of the neutron beam through the cell of length D , is given by,

$$T_{\pm} = (1/2)T_E \exp[-n_{\text{He}}D\sigma_{\pm}], \quad \text{where} \quad \sigma_{\pm} = \sigma_c(1 \mp P_{\text{He}}) \quad (1.52)$$

where \pm refers to neutron and ^3He nuclear spins parallel or anti-parallel, respectively. n_{He} is the ^3He atomic number density, T_E is the transmission of the cell glass window. The spin-dependent cross-sections are about $\sigma_+ = 876$ barns and $\sigma_- = 6131$ barns for thermal neutrons through helium with a polarization of 75%. The filtering efficiency of a ^3He cell target, during polarized neutron detection, is given by,

$$P = \frac{T_+ - T_-}{T_+ + T_-} = \tanh(-\sigma_c n_{\text{He}} D P_{\text{He}}). \quad (1.53)$$

The quantity $\sigma_c n_{\text{He}} D$ is often referred to as the opacity of the cell.

Chapter 2

A New Neutron Interferometry & Optical Facility at NCNR

2.1 Introduction

The Neutron Interferometer and Optics Facility (NIOF) is part of the cold stage instruments that are installed in the guide hall of NCNR. It is home to two neutron interferometry beamlines designated as NIOF and NIOFa, see in Fig. 2.1. The NIOFa beamline was added, during the 2010 yearlong reactor shut-down that saw the expansion of NCNR (see Fig. 2.1), to accommodate the high volume of experiments. This new facility, benefits from higher flux, improved neutron polarization capabilities, a designated cryostat for cold stage measurements, and an environmental temperature control. On the other hand, the facility may lack long-term phase stability as it is not fully isolated from the rest of the guide hall like the NIOF. To ensure temperature stability, we placed the NI crystal in a vacuum chamber, isolating from the environment [53]. NIOFa will focus on:- spin-based neutron interferometry, neutron spin manipulation, materials research, and quantum information science applications.

In this chapter, we present design features and characteristics of NIOFa, full description of which can also be found in article [7]. This chapter is structured as follows: The Sec. 2.2

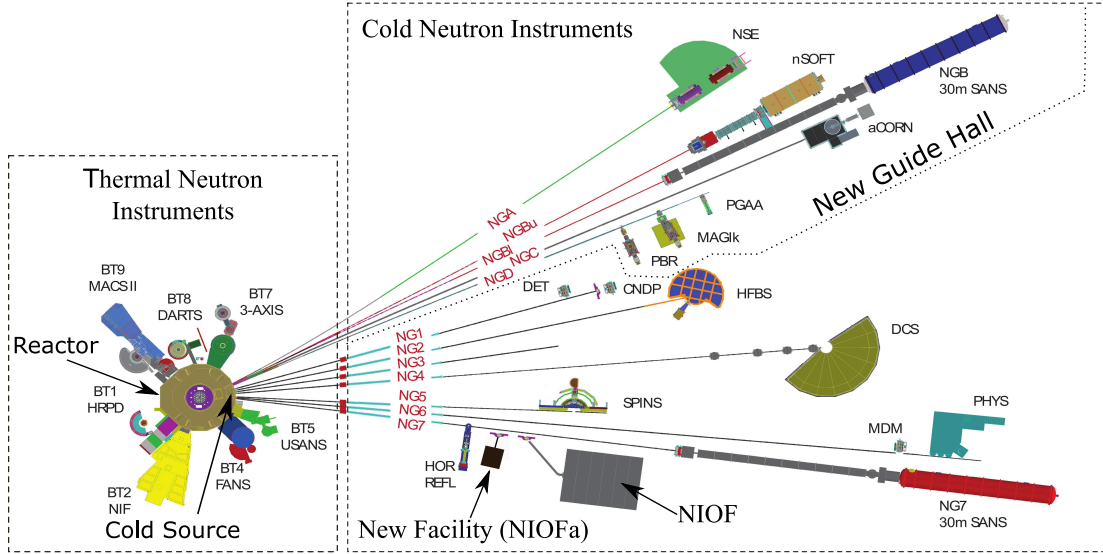


Figure 2.1: A simplistic layout of the NCNR showing the reactor core (purple) surrounded by high energy neutron instruments denoted by BT#. The next segment shows the cold source instruments, where the recently added beamline, NIOFa, resides just upstream of the existing beamline NIOF of the NG7 guide (see ref. [7]).

describes the NIOFa beamline followed by the neutron beam characteristics description in Sec. 2.3. Section 2.4 presents the wavelength measurement and Sec. 2.5 the contrast measurements followed by the polarization measurement in Sec. 2.6.

2.2 Description of NIOFa beamline

A layout of NIOFa beamline is presented in Fig. 2.2 (for a detailed schematic see ref. [7]). Neutrons extracted from NG7 by two pyrolytic graphite (PG) (002) monochromators, labelled Mon1 and Mon2, with lattice vector angular variation (otherwise called the mosaic) of 0.5° . PG crystals are locally perfect and imperfect over a long range due to a distribution in the reciprocal lattice vector. The neutron reflectivity of a mosaic crystal is greater than

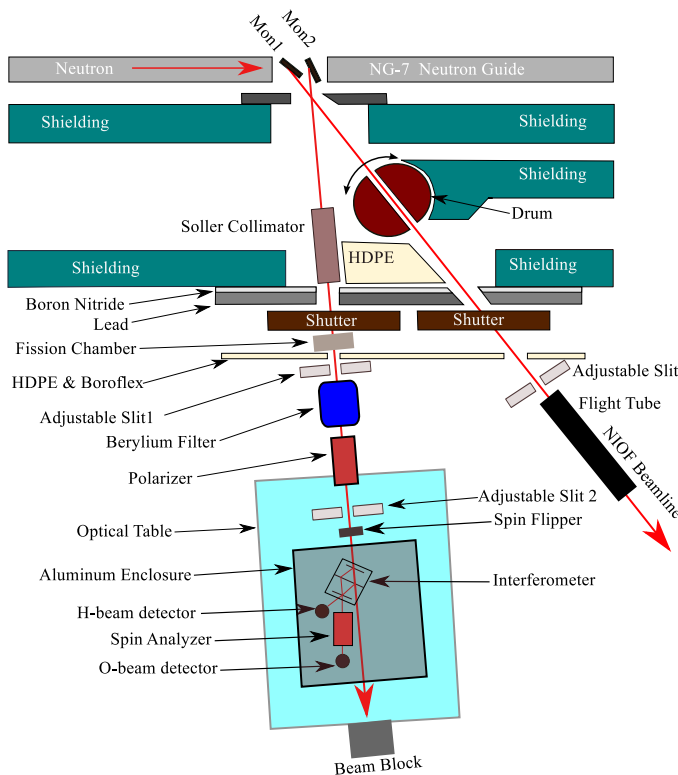


Figure 2.2: Schematic of the NIOFa beamline. A PG(002) silicon crystal (Mon2) extracts 4.4 \AA wavelength neutrons into the facility. The neutron beam passes through a set of devices including a collimator, fission chamber, beryllium filter, polarizer, and spin flipper before reaching the interferometer aluminum box enclosure. Shown also is a second monochromator Mon1 that reflects neutrons into the NIOF hutch (see ref. [7]).

that of a perfect crystal where the distribution of angular lattice parameter is zero. Mon2 reflects neutrons of wavelength 4.4 \AA to NIOFa, and Mon1 reflects neutrons to the NIOF beamline. Due to the orientation of Mon1 and Mon2, the two beams cross path. Mon2 is coupled to a nema true planetary gearhead¹ on a stage system with motors² that controls

¹model # NT17-100-H-34-615-557-D769

²Faulhaber model # AM1524-A-0.25-15.5-6 15/8 900:1

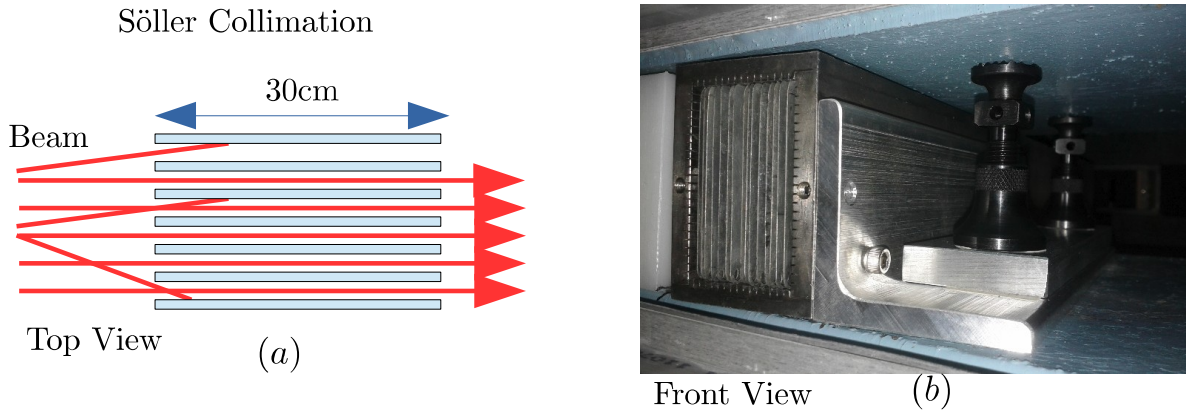


Figure 2.3: A sketch of a top view of a Söller collimator in (a) and a front view picture of it installed at the NIOFa beamline. Any neutron incident at an angle greater the allowed divergence of 0.2° is absorbed.

rotation and tilt, simultaneously. Rotation stages facilitate the monochromator Bragg scan, and the tilt stage assists in the optimization of the reflectivity.

A 41 cm gap exists between the two shielding walls and contains a 30 cm-long Söller collimator [54] to restrict the transverse horizontal beam divergence to 0.2° (see Fig. 2.3), with no effect on the beam divergence in the vertical direction. The internal plates of the Söller collimator are made with neutron absorbing gadolinium-coated blades oriented to absorb neutrons at angles greater than 0.2° . Downstream of the Söller collimator is a combination of 12 mm thick boron nitride and 76 mm thick lead that serves as an adjustable window for neutrons. A shutter is used to open and close the neutron window during operation. It is made from 12 mm thick boron-nitride, 1 mm thick cadmium, and 10 cm lead. The neutron source fluctuation is monitored with a fission chamber of detection efficiency 0.01% mounted after the shutter. On the downstream of the fission chamber is Slit1 made from two perpendicular pairs of boron-nitride. Slit1 can be translated and adjusted to any desired beam size. Located after Slit1 is a liquid nitrogen cold beryllium (Be) filter to remove undesired thermal neutrons from the beamline by scattering wavelengths $\lambda < 3.96 \text{ \AA}$ into the boron shielding. The Be crystal is cooled by liquid nitrogen to reduce the incoherent scattering cross-section due to phonon excitations, and improve the transmission

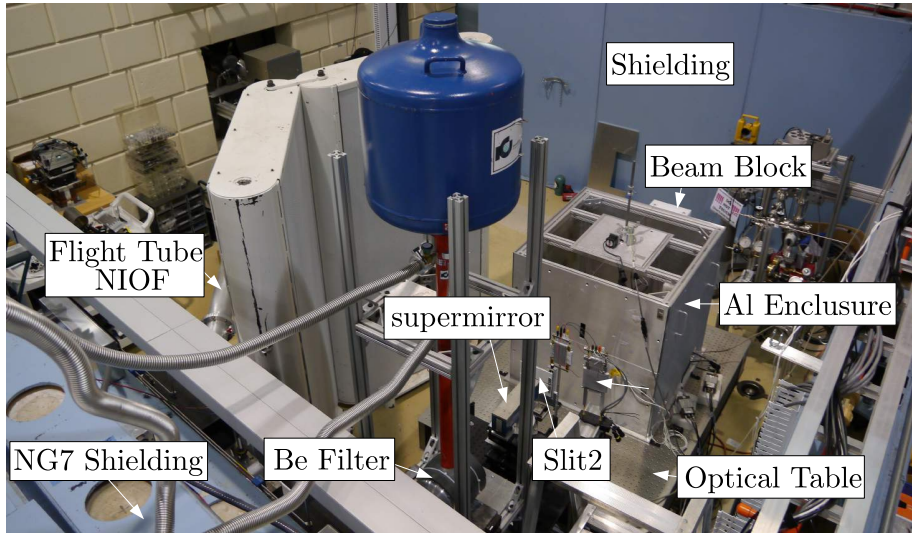


Figure 2.4: A real view of the NIOFa beamline looking from the guide.

of the 4.4 Å wavelength by about 15%.

Following the Be filter is a neutron spin polarizer. The later is made from a CoFeV-coated mirror and works in the transmission geometry by reflecting the undesired spin state out of the beam. The NIOFa is capable of achieving polarizations $P \geq 98\%$ for a beam polarized and analyzed with supermirrors (see Sec. 2.6). A second slit assembly, identical to Slit1 and labelled Slit2 is used downstream of the polarizer to limit the beam divergence. The combination of Slit1 and Slit2 generates a trapezoidal-distributed beam profile whose width depends on slit sizes and separation. Downstream from Slit2 is a precession coil spin rotator to flip the neutron's polarization.

After the spin flipper there is a 150 cm by 180 cm non-magnetic optical bench (Fig. 2.5) and a breadboard on which the interferometer is supported by a rotation stage³, transverse horizontal stage⁴ and transverse vertical stage⁵. The rotation stage is used to align the interferometer to the beam via Bragg scan, and the horizontal and vertical translation stages are used to locate the best operating spot, characterized by the highest contrast.

³PI Micos model # PRS-200 180:1 with SiGNUM Encoder

⁴Huber model # 5101.20

⁵Huber model # 5103.A20

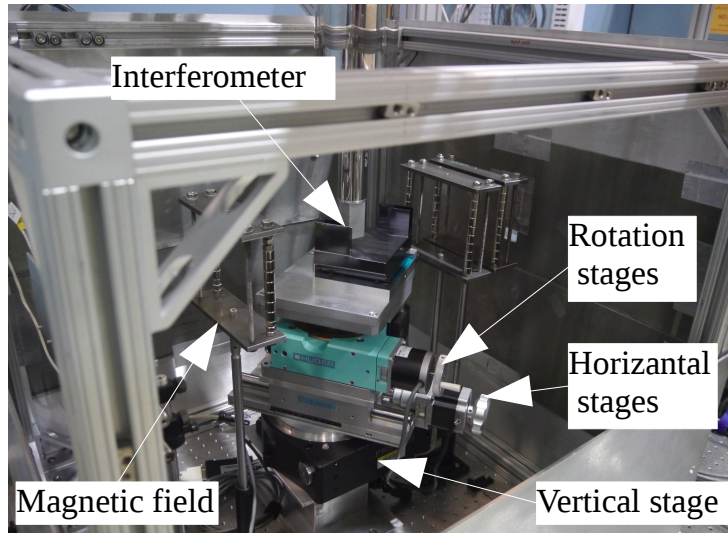


Figure 2.5: A real view of an interferometer on the NIOFa beamline.

The NI rests on felt cloth lining the aluminium mounting plate to avoid stress on the crystal blades. In polarized neutron interferometry, a spin analyzer is used for analyzing neutrons in the O-beam or H-beam. Detection is done with ^3He counters of 2.5 cm in diameter⁶ and filled with pressurized ^3He to 10 bar. After the detector, there is a beam block, made from a combination of high-density polyethylene coated boron nitride and lead. Most of the thermal neutrons go straight through the setup and captured by a beam block. The whole NI setup on the table is housed by an aluminium box $76 \times 76 \times 76 \text{ cm}^3$, to reduce phase instability due to thermal gradients. The box is thermally isolated from the table by a 3 mm thick piece of fibreglass, which is a poor heat conductor, and from stray neutrons by a cadmium lining on the interior surface.

2.3 Beam characteristics

The orientation of Mon2 determines the wavelength and the intensity of neutrons directed to the NIOFa beamline. Mon2 is first aligned to the beam optically and then a Bragg scan

⁶For the 25.4mm in diameter: GE Energy, model # RS-P4-0802-204

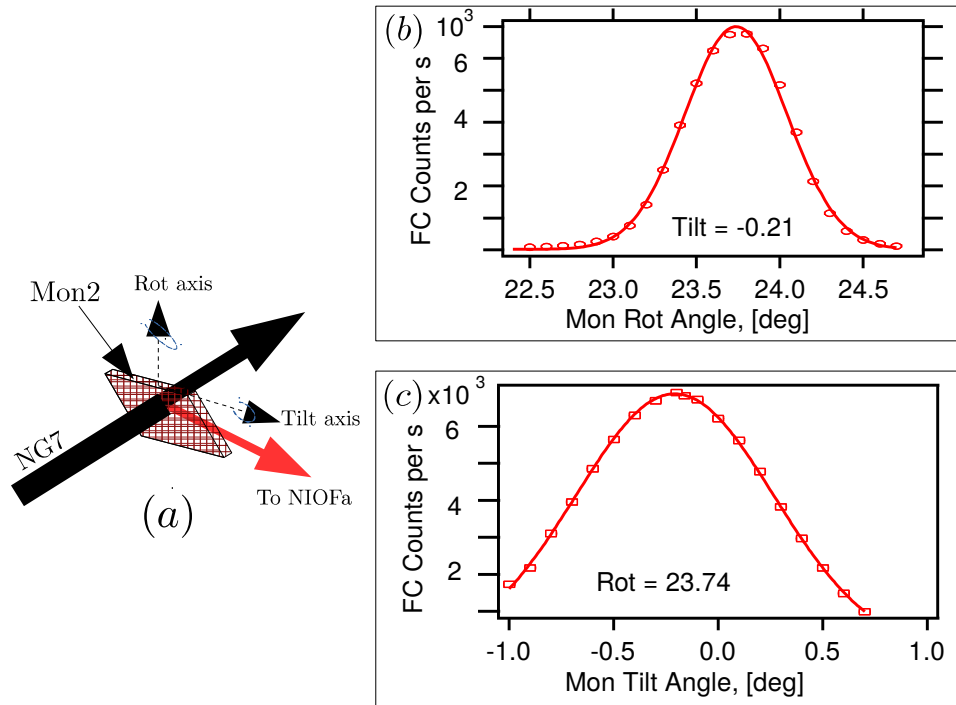


Figure 2.6: A Bragg angle scan of the monochromator PG crystal to determine the wavelength of the beamline. (a) is a schematic diagram of Mon2 reflecting neutrons from NG7. Mon2 is first aligned to the beam optically and then via a Bragg rotation scan around the crystallographic axis denoted by Rot axis. The experimental data from the NIOFa is shown in (b) with peak intensity at the Bragg angle. The full width at half maximum (FWHM) is related to the lattice vector spread of the PG crystal and the peak corresponds to $\lambda = 4.4 \text{ \AA}$. In (c) is the crystal tilt angle scan for optimizing the intensity.

is performed using motorized stages. The schematic of the setup is shown in Fig. 2.6a. The intensity of neutrons reflected from Mon2 against the angle of rotation is shown in Fig. 2.6b. The location of the peak intensity corresponds to the main wavelength, and the FWHM is related to the lattice vector spread of the PG crystal. With the PG set to the peak intensity location the intensity optimization scan against tilt is shown in Fig. 2.6c. At the NIOFa, the main neutron wavelength is 4.4 \AA and is closer to the peak of the Maxwell-Boltzmann distribution provided by the liquid hydrogen cold source leading to a

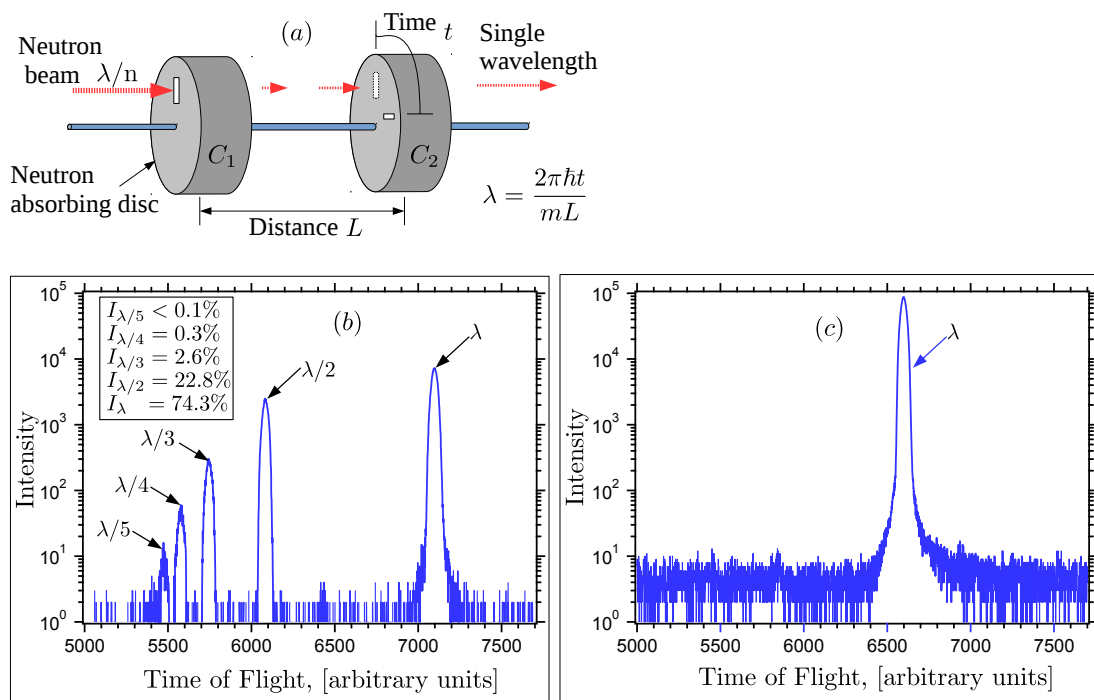


Figure 2.7: (a) a schematic diagram of neutron velocity selector disc choppers. It consists of a fixed disc C_1 (just a slit) and a rotating disc C_2 . By carefully choosing the rotation frequency and the separation, a particular wavelength can be selected. In (b), the spectrum for various neutron harmonics $\lambda = (4.4/n) \text{ \AA}$, with $n = 1, 2, 3, \dots$ measured using a disc chopper (a) prior to installing the beryllium filter. In (c), are measurements after the installation of the beryllium filter. Only the $\lambda = 4.4 \text{ \AA}$ neutrons remain. The measurements in (b) and (c) were carried under different measurement times and so the intensities and the time bins are different.

high neutron intensity.

The total number of neutrons going through a unit area per unit time is known as the flux, measured in neutrons $\text{cm}^{-2} \text{ s}^{-1}$. In the NIOFa beamline, the flux measured after Slit1 using a fission chamber with $32.6 \mu\text{g}$ of uranium is 3.56×10^6 neutrons $\text{cm}^{-2} \text{ s}^{-1}$. This flux is higher than the flux of 1.32×10^5 neutrons $\text{cm}^{-2} \text{ s}^{-1}$ measured after Mon1 on the NIOF beamline.

The neutron flux measured for both NIOFa and NIOF do not discriminate between the λ/n harmonics present in the beam. In order to quantify the beam, a disc chopper was used to measure the composition of the beam because it is capable of selecting neutrons according to their velocity. It is made from two consecutive discs with windows on one quadrant as shown in Fig. 2.7a. The first chopper (C_1) functions as a source slit by selecting a pulse beam with different energies, and the second chopper (C_2) which is opened at a well defined later time (due to its rotation) transmits only a single wavelength. The wavelength is related to the separation L and time t by $\lambda = 2\pi\hbar t(mL)^{-1}$.

Shown in Fig. 2.7a is the spectrum for various harmonics $\lambda = (4.4/n)$ Å, with $n = 1, 2, 3, \dots$, measured using a disc chopper, prior to installing the Be filter; the relative composition of the harmonics λ/n to the peak wavelength is 25%. With the Be filter, the intensity obtained using a disk chopper time-of-flight measurement is shown in Fig. 2.7b with no detectable λ/n and a reduced relative composition of the main wavelength to 62%. Note that the measurements are carried with different time windows.

2.4 Wavelength measurement

The wavelength measurement was carried out using a nearly perfect Si (111) crystal analyzer of dimensions $15 \times 40 \times 60$ mm³ oriented in the Laue geometry. The lattice vector spread of nearly perfect crystals is relatively broad compared to perfect crystals, but relatively small compared to a PG crystal. This allows for a greater reflected intensity than perfect crystals and a better resolution than PG crystals. The setup contains the crystal and three detectors labelled D_+ , D_- , and D_0 . Detector D_+ measures the intensity at an angle $+2\theta_B$ which correspond to the crystallographic orientation parallel to the monochromator; D_- is located at $-2\theta_B$ and correspond to the crystallographic orientation oriented anti-parallel. The direct beam detector D_0 is a monitoring detector to record the drop in the intensity of the transmitted beam when the crystal is oriented at the Bragg angle. The alignment of the analyzer crystal to the beam was done via a $2\theta_B$ scan (see Fig. 2.8a, a similar process as the monochromator) using a stage with a highly accurate encoder⁷. The

⁷Heidenhain model # RON 287 18000 lines per revolution

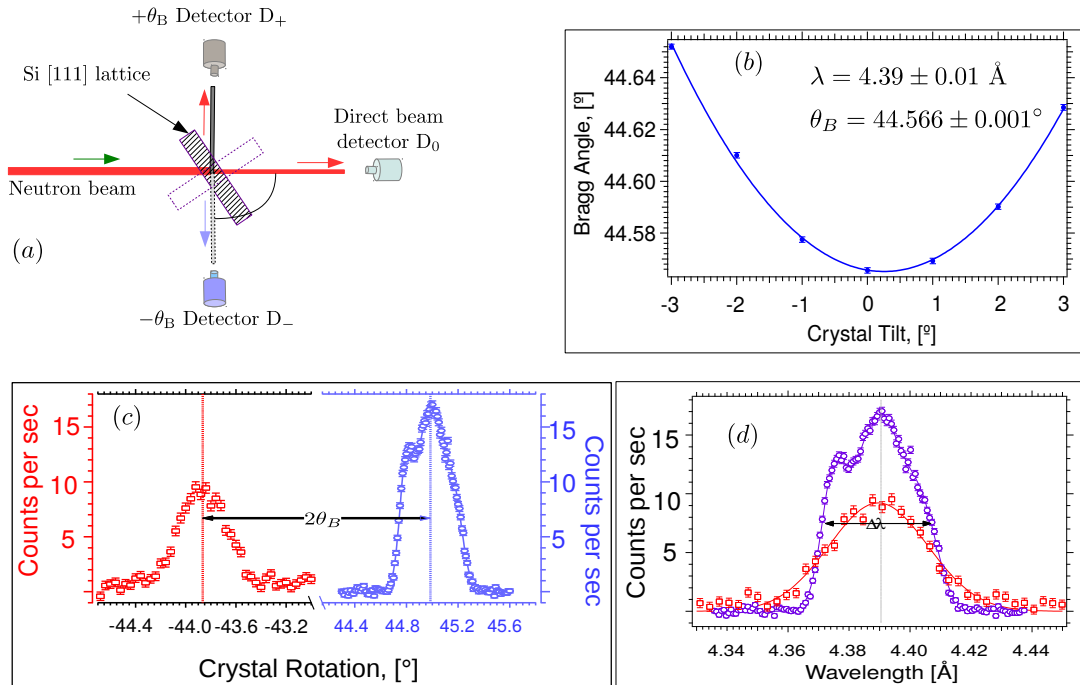


Figure 2.8: (a) Schematic setup for wavelength measurement, made up of a nearly perfect Si [111] crystal analyzer and three detectors. The crystal is rotated around the Bragg in two distinct orientations $\pm\theta_B$ in which neutrons are detected with detectors D_{\pm} , respectively. D_{\pm} are mounted at $\pm 2\theta_B$ to measure the reflected intensities in parallel and anti-parallel geometries, respectively. The monitor D_0 is located in the direct beam to measure the reduction in the neutron counts when the crystal is at the Bragg angle. (b) plot of the Bragg angle at various tilts is fitted to a second degree polynomial to determine the optimal tilt. (c) the intensity recorded by D_- (red squares) and D_+ (blue circles) versus the rotation angle, after background subtraction. The intensity in D_- is fit to a Gaussian and that in D_+ to a triple-peak Gaussian. These fits are shown in (d) with the same data in (c) plotted against the wavelength. The wavelength, calculated using the Bragg diffraction formula, corresponding to the peak and marked as a vertical line, is obtained to $\lambda = 4.389 \pm 0.009$ Å with $\Delta\lambda/\lambda \approx 0.8$ %, where $\Delta\lambda$ is the FWHM.

optimization of the Bragg angle performed via the crystal tilt scan is shown in Fig. 2.8b. The data is fit to a second degree polynomial to obtain the Bragg angle. The minimum of

the polynomial corresponds to the exact Bragg angle. Shown in Fig. 2.8c, is the intensity at D_- (red boxes) and D_+ (blue circles) against the Bragg angle after background counts are subtracted. The difference between the angles at which the peaks occur is $2\theta_B$. These angles are obtained by fitting the resulting data to a Gaussian, with the center representing the angle and the FWHM the error in the angle. The data on D_- was fit to a single Gaussian, while that in D_+ was fit to a triple-peak Gaussian. The fits are shown in Fig. 2.8d, which are the same data in (c) plotted against the wavelength, λ . The wavelength is calculated using the Bragg diffraction formula $\lambda = 2d \sin \theta$, with $\Delta\lambda$ defined as the FWHM of the resulting fit. The mean wavelength $\lambda = 4.389 \text{ \AA}$, is indicated by a vertical line and the wavelength is determined to be $\lambda = 4.389 \pm 0.009 \text{ \AA}$ with $\Delta\lambda/\lambda \approx 0.8 \%$.

2.5 Contrast measurement

The contrast measurements on the NIOFa was performed for two wavelengths, namely $\lambda = 2.2 \text{ \AA}$ and $\lambda = 4.4 \text{ \AA}$. The intensities of the O-beam and H-beam versus the NI rotation for $\lambda = 2.2 \text{ \AA}$ are shown in Fig. 2.9a and 2.9b, respectively. The line shows the fit to a Gaussian to obtain the peak at $\theta_B = 20^\circ$. Setting the NI angle to the peak intensity, the spot characterized by the highest contrast is determined by doing a contrast scan. This scan is achieved by introducing a phase flag in the interferometer and rotating to introduce a phase difference between the two paths.

At the NIOFs the phase flag is an optically flat piece of fused silica of dimension $5 \text{ cm} \times 5 \text{ cm} \times 0.15 \text{ cm}$ chosen so as to introduce a phase shift in both paths of an NI. By rotating the phase flag by an angle δ from its initial position parallel to the blades, a phase shift of

$$\begin{aligned} \Delta\phi(\delta) &= -Nb\lambda D \left[\frac{1}{\cos(\theta_B + \delta)} - \frac{1}{\cos(\theta_B - \delta)} \right] \\ &= -Nb\lambda D \left[\frac{2 \sin(\delta) \sin(\theta_B)}{\cos^2(\theta_B) - \sin^2(\delta)} \right] \end{aligned} \quad (2.1)$$

where b , N , and D are the scattering coherent length, number density, and thickness of the phase flag, respectively. An interaction to be probed with phase (ϕ_s) can be added,

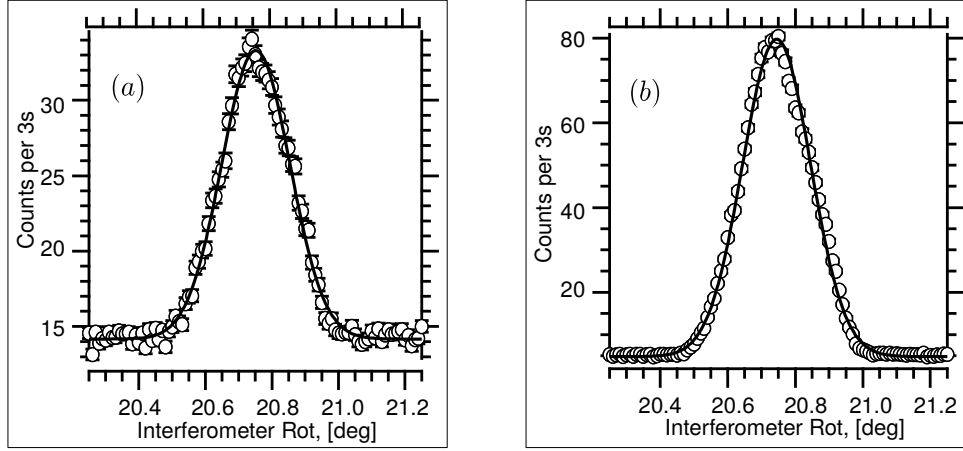


Figure 2.9: The interferometer Bragg angle scan with intensity recorded on the O-beam shown in (a) and that in the H-beam shown in (b) for $\lambda = 2.2 \text{ \AA}$. The data is fit to a Gaussian to obtain the peak at 20.75° .

and the total phase also include the intrinsic phase (ϕ_0) resulting from imperfections in the matching of the beam on the blades. Shown in Fig. 2.10a, is an interferometry setup to measure the phase shift due to a sample. In Fig. 2.10b is a real picture of the three-blade neutron interferometer that was used in the measurements. In Fig. 2.10c are interferograms for I_O (red circles) and I_H (blue squares) obtained by rotating a phase flag a few degrees, in the absence and presence of a neutron absorbing sample. The coefficients in the equations,

$$I_O = A_O \left(1 + \mathcal{V} \cos(\Delta\Phi) \right), \quad I_H = A_H - A_O \mathcal{V} \cos(\Delta\Phi). \quad (2.2)$$

are determine from the fit with total phase difference $\Delta\Phi = \Delta\phi(\delta) + \phi_s + \phi_0$. Because the sample has an absorption cross-section σ_a , the O-beam intensity may be expressed as,

$$I_O = A_O e^{-\frac{\sigma_a ND}{2}} \left[\cosh \left(\frac{\sigma_a ND}{2} \right) + \mathcal{V} \cos(\Delta\Phi) \right], \quad (2.3)$$

where $e^{-\sigma_a ND}$ is the absorption coefficient. An analogous but slightly complicated equation for I_H can be written by making use of the individual reflection and transmission coefficients of each of the blades.

The NIOFa optical table is mounted on vibration isolation legs to suppress vibrations

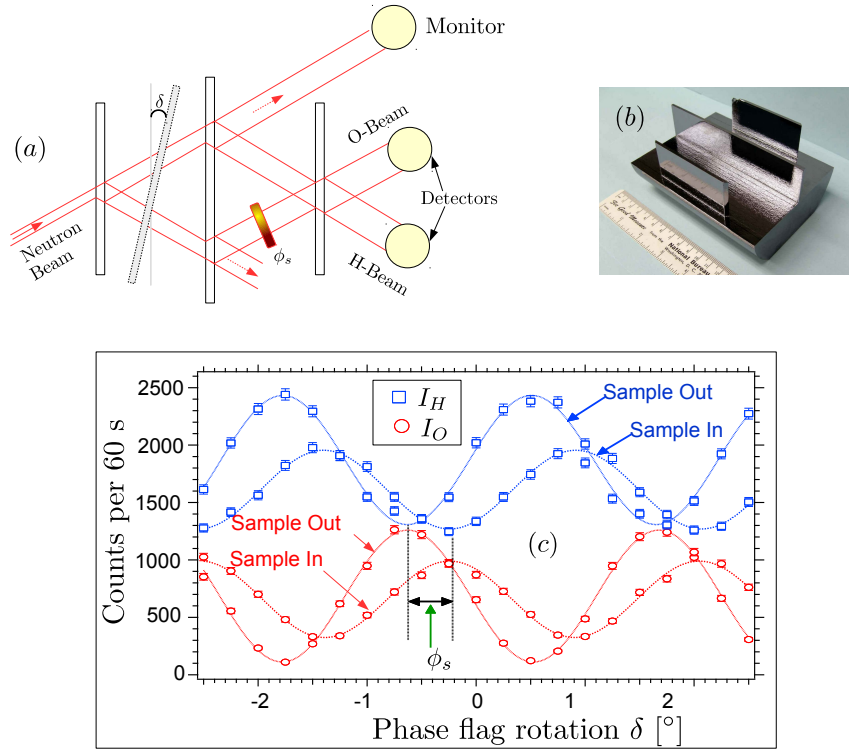


Figure 2.10: (a) An interferometry setup to measure contrast or extract the phase due to a sample. (b) A real picture of the three-blade neutron interferometer tested at the NIOFa. (c) An interferogram showing I_O (red circles) and I_H (blue squares) for sample in and out with line fit using Eq. 2.2. The interferogram indicates that the sample has an appreciable neutron scattering cross-section. The phase shift due to the sample ϕ_s is obtained by comparing the sample in (solid) and out (dotted) intensity patterns.

as low as 1 Hz. The table legs are equipped with an active support structure⁸ built on a piezoelectric (PZT) driven compensator system. When the table moves, the compensator system uses a feedback mechanism to balance the table by canceling the movement. However, this response might drive the table to a different position than its previous, leading to tiny unavoidable NI drifts around the center of the beam. The contrast was measured when the table is supported on various isolations including the PZT system, a pressure-driven

⁸TMC model # STACIS iX

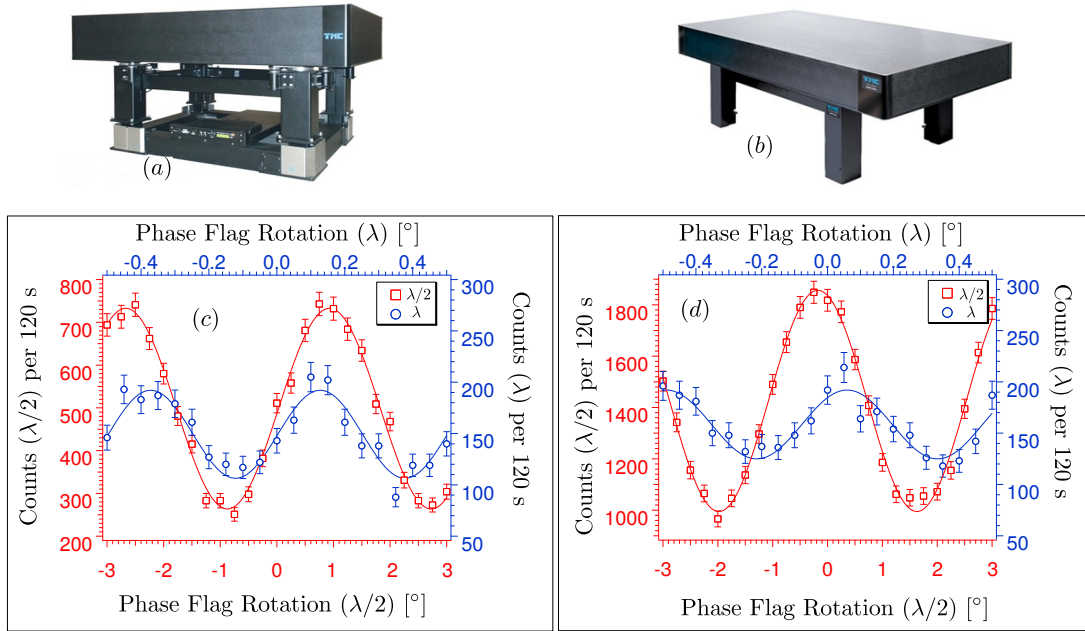


Figure 2.11: The O-beam intensities for two neutron wavelengths $\lambda = 2.2 \text{ \AA}$ (red squares) and $\lambda = 4.4 \text{ \AA}$ (blue circles). In (a), a picture of the table supported by PZT-control STACIS, and in (b) a picture of table supported by rubber pad fixed legs. In (c) are interferograms when the table is supported by STACIS with the PZT-control turned off. The contrast is 47% for $\lambda = 2.2 \text{ \AA}$ and 32% for $\lambda = 4.4 \text{ \AA}$. In (d) the contrast decreased to 30% for 2.2 \AA and 21% for 4.4 \AA for table resting on fixed rubber pad legs.

control⁹, an assembly of rubber pads. A picture of the table with PZT-control STACIS is shown in Fig. 2.11a and that with rubber pad fixed legs is shown in Fig. 2.11b. A contrast of $\mathcal{V} = 47\%$ for $\lambda = 2.2 \text{ \AA}$ and $\mathcal{V} = 32\%$ for $\lambda = 4.4 \text{ \AA}$ measured when the PZT-control of the STACIS system are turned off, but the table still retains some vibration isolation is shown in Fig. 2.11c. In Fig. 2.11d is the interferograms for a table supported by rubber pads with the contrast reducing to 30% for $\lambda = 2.2 \text{ \AA}$ and 21% for $\lambda = 4.4 \text{ \AA}$. In comparison with the NIOF beamline, this same NI can measure a contrast of about 85% at 2.71 \AA . Many factors may be responsible for the decrease in contrast. These may include

⁹model # PEPS II

mechanical vibration, temperature fluctuations and the beam divergence. A contrast of about 45% was observed for the 4.4 Å wavelength with a tiny beam size.

2.6 Neutron polarization

The NIOFa is primarily constructed for polarized neutron interferometry. The neutrons are polarized with double-V cavity supermirrors¹⁰, which use preferential reflection [23]. The polarization is manipulated with high efficiency using DC driven precession spin flippers [33, 34] and thin films [37]. The polarizer and analyzer at the NIOFa are specially designed supermirrors to reach neutron polarization $P \geq 98\%$ with a pencil size neutron beam of wavelength more than 2.0 Å [55]. Each supermirror (SM) is 30 cm long and 5 cm tall, and is divided into three identical 3 mm channels, each equipped with two double-sided coated SM plates which are mounted back-to-back in the shape of a V (see Fig. 2.12a), hence the name double-V. The design maximizes the neutron transport capabilities of the SM. On either sides of the channel there are neutron absorbing materials capturing neutrons of the opposite spin which are reflected from the CoFeV-coated mirror.

Figure 2.12 is a schematic setup for polarization measurement with two consecutive slits Slit1 and Slit2 for collimation, and a Be filter to remove shorter neutron wavelengths. Downstream of the Be filter is, a SM spin polarizer, a coil spin flipper, a spin analyzer, and a ³He counter. Slit1 and Slit2 are used to limit the transverse horizontal beam divergence since the measured polarization of the beam depends it. The Be filter is located before the SM polarizer to remove all the higher energy neutrons so that the optimization of the components is carried out with only the 4.4 Å wavelength. Slit2 can be located either downstream or up stream of the SM polarizer. The location downstream is suited for geometric reasons only.

The neutron spin flipper is a rectangular double coil DC spin flipper, see Fig. 2.12b. The inner coil is used to generate a compensating field and the outer coil to generate a field perpendicular to the neutrons flight path. The compensating field is tuned to exactly cancel the vertical guide field at the flipper location. A background magnetic field of about

¹⁰custom designed and made by SwissNeutronics

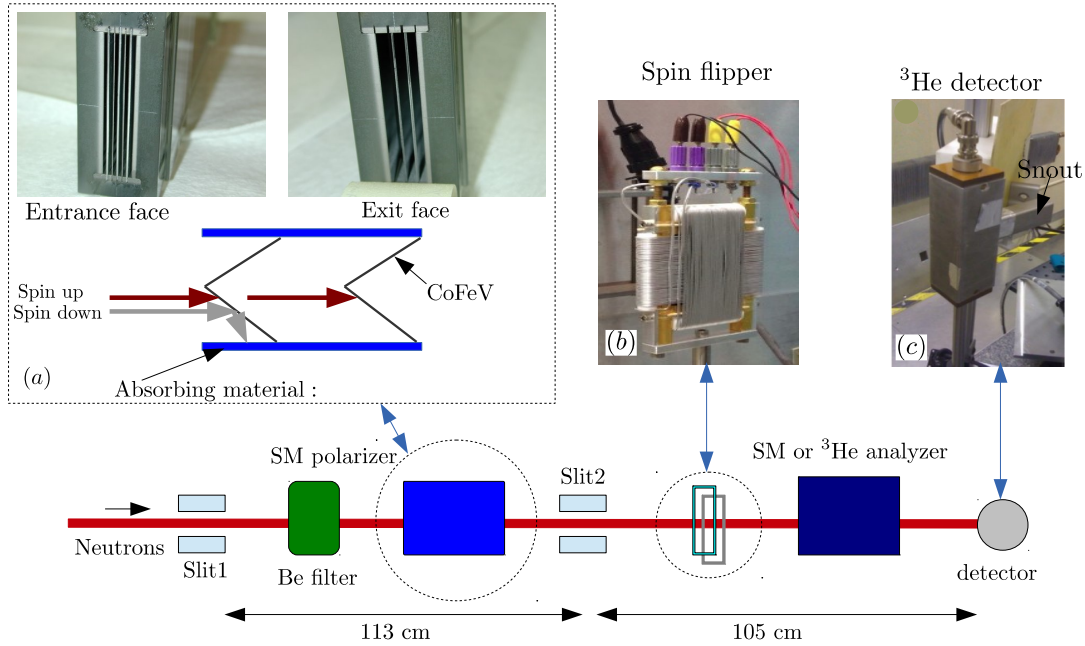


Figure 2.12: Schematic setup used to measure neutron polarization at the NIOFa. The components used are the two slits for collimation, a beryllium filter to remove shorter wavelengths. The polarizer, spin flipper and analyzer are the main components. The neutron beam is polarized with a SwissNeutronics double-V cavity supermirrors and analysed with either another double-V supermirror or polarized ^3He filter. A picture of the coil spin flipper used is shown in (b) and that of the ^3He counters are shown in (c).

8 Gauss was used. This field is far above the earth magnetic field to avoid depolarization. The optimization of the inner coil's field to the maximum flipping ratio, characterized by a π -flip, is shown in the bottom plot in Fig. 2.13. Also, the optimization of the outer coil's field to the maximum flipping ratio is shown in the top plot in Fig. 2.13. The flipping probability of our spin flippers is 0.99.

Prior to polarization measurements, the detector was aligned to an empty beam (no component present) by translating it and rotation it around the beam center. The linear scan, performed to locate the center of the beam is shown in Fig. 2.14a. On the detector rotation shown in Fig. 2.14b, there is a secondary peak resulting from background neutrons

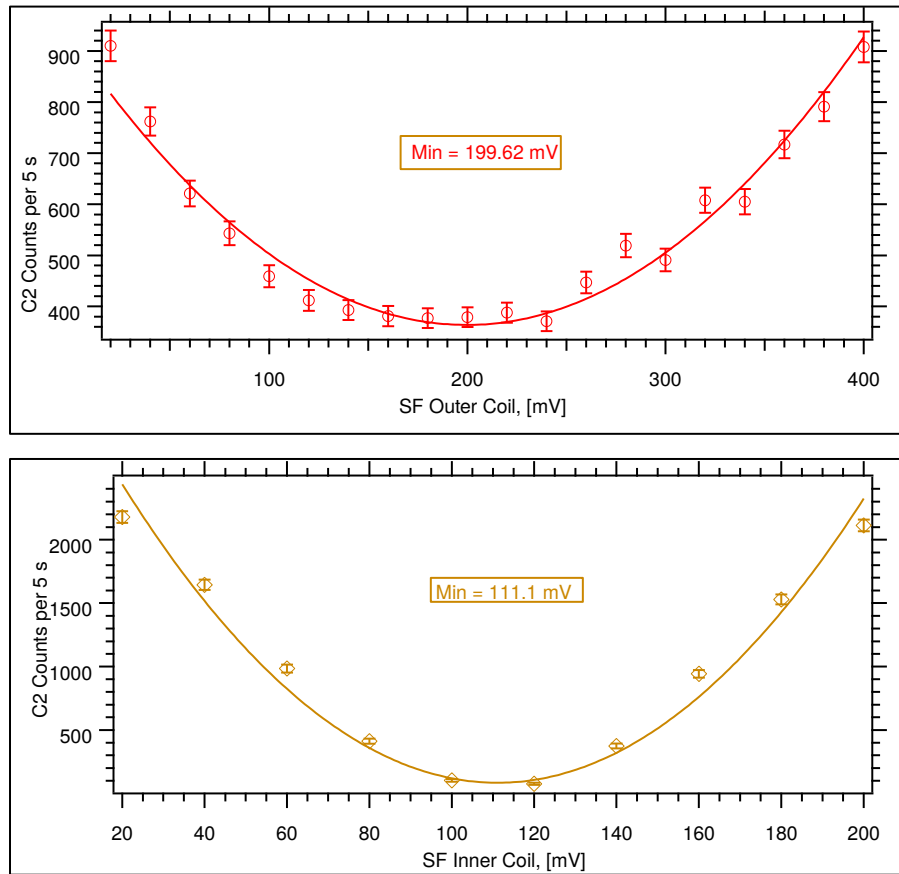


Figure 2.13: Experimental data for tuning the currents in the vertical and horizontal coils of the coil spin flipper shown in Fig. 2.12c.

streaming from the NG7 guide into the NIOFa beamline. For the mean time, the detectors are enhanced with snouts (to reduce background neutrons) and rotated to angles that exclude these neutrons. With a snout (see Fig. 2.12c), the beam profile is a trapezoidal distribution resulting from the convolution of the collimation slit and the detector snout. The polarizer and analyzer alignments are done in a similar fashion as the detector through a linear and a rotation scan.

The degree of neutron polarization P is determined from the flipping ratio expressed as $R = I_{\text{off}}/I_{\text{on}}$, where I_{off} and I_{on} denotes the neutron intensity recorded on the detector

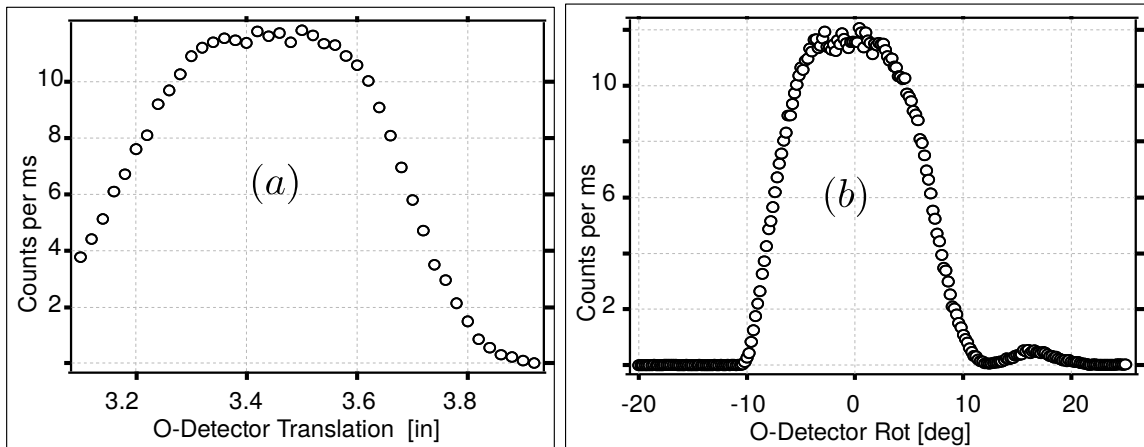


Figure 2.14: Detector linear and rotation scan for alignment during polarimetry. There is a secondary peak on detector rotation which comes from background neutrons streaming from the NG7 guide into the NIOFa beamline.

when the spin flipper is *on* and *off*, respectively. In the *off* state, the spin orientation of the neutron remains unchanged as it propagates between the polarizer and analyzer. On the other hand, when the flipper state is *on*, the neutron spin orientation is reversed between the polarizer and the analyzer. The flipping R is related to the polarizer efficiency P_n and flipper efficiency ϵ_F by

$$P = P_a \epsilon_F P_n = \frac{R - 1}{R + 1} \quad (2.4)$$

where P_a is the analyzer efficiency. Without the Be filter, the measured polarization was $\leq 90\%$, major reason being the presence of short wavelength neutrons that constitute $\sim 25\%$ of the beam, and also fall outside the polarizing SM range. After installing the Be filter, the neutron polarization increased to $\sim 98\%$, but strongly depends on the experimental settings such as a beam size, divergence, and polarizer orientation.

There are four double-V SM at the NIOFa each of which was characterized as a polarizer. The SM polarizing efficiencies were each measured using polarized ^3He cells in combination with a ^3He detector and with the flipper taken out of the beam. The polarization efficiencies for SMs designated as Cavity 1.1, 1.2, 2.1 and 2.2. are presented in

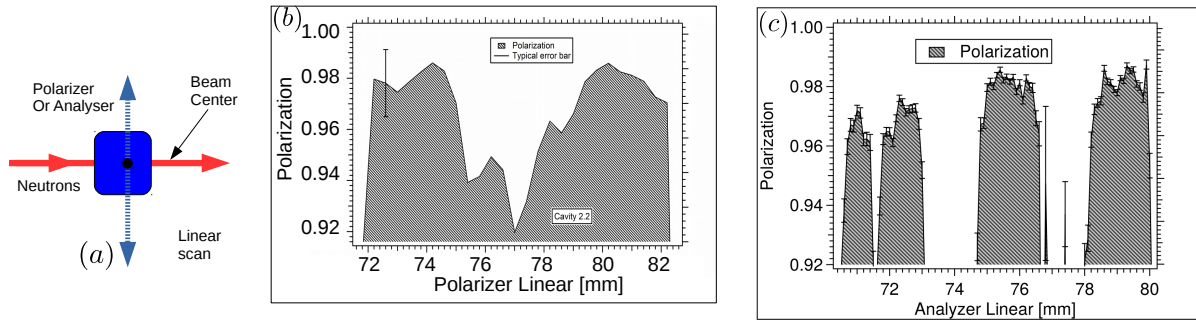


Figure 2.15: The spatial dependence of polarization of Cavity 2.2 supermirror for a fixed rotation angle. (a) is the schematic diagram of the polarizer linear scan setup. (b) is the polarization efficiency when Cavity 2.2 acts as a polarizer and (c) is the polarization efficiency when Cavity 2.2 acts as an analyzer.

Tab. 2.1¹¹ for different slit sizes. Because of the dependence of the polarization on beam size, a small beam of about $1.15 \times 13 \text{ mm}^2$ was used to measure the polarizing efficiency of each of the three channels of the SM (about 2.5 mm). For Cavity 1.2, the polarizations of $98.26 \pm 0.50\%$, $98.51 \pm 0.50\%$, $97.46 \pm 0.50\%$ were obtained for each of the channels.

¹¹* refers to measurements done with Syrah, and [†] are those done with Marverick cell

Slit[mm ²]	Cavity 1.1, [%]*	Cavity 1.2, [%] [†]	Cavity 2.1, [%]*	Cavity 2.2, [%]*
1.25x10	98.32	98.20	97.60	99.23
1.25x15	98.79	98.51	—	99.23
5x5	97.23	96.83	96.40	96.99
11.25x1.25	96.79	98.47	96.40	98.50
2.5x7.5	97.62	—	98.15	97.98

Table 2.1: Table shows polarization of each SM measured with polarized ³He cell as analyzer for various slit configurations. The beam used for these measurements has a uniform beam divergence for which Slit1 and Slit2 are same size.

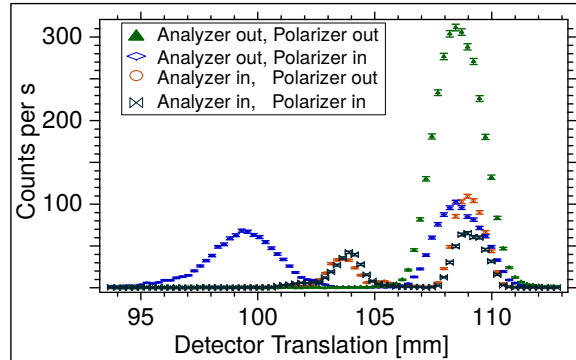


Figure 2.16: Plots showing the beam profile for the various combination of polarizer and analyzer, including when both are in and out of beam simultaneously. In the setup, the detector is translated along a direction perpendicular to the beam direction and results for various configurations obtained. It can be noted that when the SM polarizer and SM analyzer are out of the beam, there is just one peak. When wither the SM polarizer or SM analyzer are in the beam the beam is splitted in to two components. The splitting is likely caused by refraction from the double-Vs in each channel.

Because the polarization efficiencies of each of the SM channels differ, the dependence of the degree of polarization was measure with linear scans. A schematic setup for polarizer/analyzer transverse linear scan is shown in Fig. 2.15a. Figure 2.15 is the polarization versus translation linear scan when Cavity 2.2 acts as a polarizer (left) and analyzer (right). It is clearly noticeable that the linear position affects the performance thereby making it challenging to work with a wider beam as portions of the beam may carry different polarizations.

The beam emerging from either the polarizer/analyzer combination is split into various peaks, studied with a position sensitive detection realized by translating a detector with a $1 \times 8 \text{ mm}^2$ slit on the snout. In these measurements, collimator Slit1 was set to $1.25 \times 5 \text{ mm}^2$. For calibration purposes, the detector translation scan was first done (without the polarizer and the analyzer). Various SM polarizer/analyzer combination scan were performed and the data is shown in Fig. 2.16.

When a SM polarizer and SM analyzer are present on the beam, the beam splits into two peaks indicating that the two peaks coming out of the polarizer have polarization of the same sign. The cause of the splitting might be attributed to refraction from the edge of the double-Vs in each channel. A final study of the effect of the slit size on the polarization was done by keeping one slit fixed and changing the width of the other. It was observed that the polarization is strongly affected by the slit.

Chapter 3

Dynamical Diffraction in a Perfect Crystal Neutron Interferometer

3.1 Introduction

The theory of dynamical diffraction (DD) is a very successful theory; first formulated for x-rays [56, 10, 57] and later adapted for electrons [58] and neutrons [2, 59]. It describes the interaction of a particle with a periodic lattice which includes atomic crystal structures, nanometre scaled multi-layers, and self-assembly systems. Our main interest is in perfect periodic crystals although, the concepts presented here can be adapted to other periodic structures. According to the theory of DD, a plane wave incident at the Bragg condition generates four distinct wavefields inside the crystal. Two of the wavefields propagate along the direction of incidence and the other two propagate along the reflected direction. Despite being distinct wavefields, their wavevectors differ only slightly and so they interfere as they propagate through the crystal, generating most of the fine features of DD. At the exit surface of the crystal, the four waves recombine into two waves whose properties depend on the momentum at incidence and the nature of the lattice [60, 61, 62]. The diffracted waves propagate at a direction determined by the geometry of the crystal. The two common geometries are the Bragg geometry where both the incident and diffracted waves are on the same surface of the crystal, and the Laue geometry where they are on different surfaces.

An alternative theory to DD is the kinematical theory of diffraction. The theory of DD differs from the kinematical theory because it describes the approximate position of the diffraction peaks in reciprocal space while making corrections for refraction, interference, and multiple scattering. The validity of DD is commonly described as the *thick* crystal regime. This regime is when the crystal thickness is greater than the *extinction length*, and the beam divergence is greater than the Darwin width of the crystal. On the one hand, the Darwin width specifies the acceptance angle of an incident beam which has a finite divergence. On the other hand, the extinction length is the minimum thickness at which neutrons are completely reflected from the crystal. The DD effects are dominant in perfect crystal neutron interferometry. This is because, the NI blade thicknesses are orders of magnitude greater than the extinction length.

In previous DD work where the incident beam was assumed to have a broad wavelength distribution, the neutron intensity seems to be independent of the crystal thickness [63, 64, 65]. However, for highly monochromatic neutron beams realized using perfect crystal monochromators [43, 66], this assumption is not true. The result is that the intensity couples to the crystal thickness offering a possible control of the intensity via the thickness. In perfect crystal NI, monochromatic beams are inevitably used offering an opportunity to optimize the neutron intensity through an interferometer via the thickness.

In this chapter we present a brief description of the theory of DD, then provide simulations and experiments of the effect of thickness on the intensity of neutrons diffracted from a combination of perfect crystal beam splitters. In Sec. 3.2, we describe DD from a single crystal. In Sec. 3.3 we outline the effect of crystal thickness on the intensities at the exit of a three-blade NI together. In Sec. 3.4 the experimental procedure is presented, and in Sec. 3.5 the data collected are shown presenting experimental results. Finally, in Sec. 3.6 we present the data fitting procedure and then conclude in Sec. 3.7

3.2 Dynamical diffraction

Consider a plane wave component of a wavepacket, incident on a periodic silicon crystal of thickness z_0 , located at $\mathbf{r} = z\hat{e}_\perp$, see Fig. 3.1. The crystal is oriented in the Laue geometry

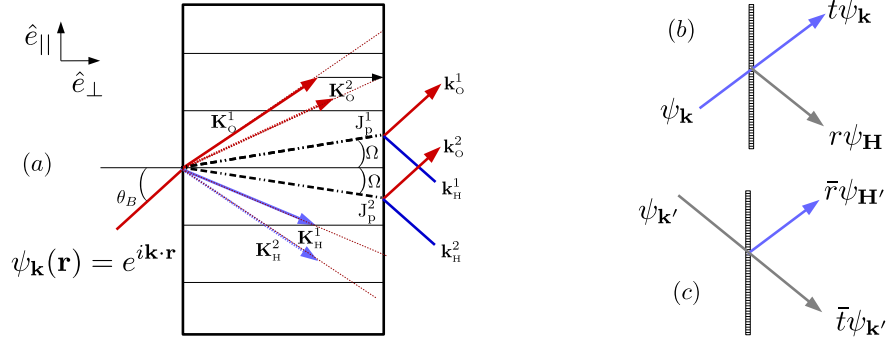


Figure 3.1: Illustration of Bragg diffraction in the Laue geometry. An incident wave at the Bragg angle is coherently split into two components, the forward diffracted with wavevector \mathbf{k}_o and the reflected wavevector \mathbf{k}_H which originate from the wavefield inside the crystal along branch 1 and 2. The current $J_p^{1,2}$ propagate at an angle Ω which is an amplification of the deviation $\delta\theta$. For Si [220], the amplification is $\tan\theta_B/\sigma_D \sim 10^6$. The diffraction of the two possible input waves is shown in (b) and (c).

with the crystallographic planes assumed to be perpendicular to the crystal surface. As a result, the incident wavevector can be represented as $\mathbf{k} = k_\perp \hat{e}_\perp + k_\parallel \hat{e}_\parallel$, where \hat{e}_\perp and \hat{e}_\parallel are unit vectors perpendicular and parallel to the crystal surface, respectively. The position representation of the steady state wavefunction is a sum over plane-waves,

$$\Psi(\mathbf{r}) = \int d\mathbf{k} \mu_{\mathbf{k}} \psi_{\mathbf{k}}(\mathbf{r}), \quad (3.1)$$

where, $\psi_{\mathbf{k}}(\mathbf{r}) = \exp(i\mathbf{k} \cdot \mathbf{r})$.

Inside the crystal, the wavefunction $\Psi(\mathbf{r})$ must satisfy the stationary state Schrödinger equation,

$$\left[-\frac{\hbar^2}{2m} \nabla^2 + V(\mathbf{r}) \right] \Psi(\mathbf{r}) = E\Psi(\mathbf{r}), \quad (3.2)$$

where $V(\mathbf{r})$ is the potential of the scattering centres. The total energy E of the particle inside the crystal is equal to the kinetic energy of the particle in free space, $E_0 = \hbar^2 k^2 / 2m$, where $k = |\mathbf{k}|$ and m is the mass particle. For a periodic crystal, $V(\mathbf{r}) = V(\mathbf{r} + \mathbf{R})$ where \mathbf{R} is the crystal translation vector. So the solutions to Eq. (3.2) are multiple scattered

Bloch waves which maybe expressed as [67],

$$\Psi_{\mathbf{K}}(\mathbf{r}) = u_{\mathbf{K}}(\mathbf{r}) \exp(i\mathbf{K} \cdot \mathbf{r}), \quad (3.3)$$

where \mathbf{K} is the wavevector of the neutron inside the crystal. The functions $u_{\mathbf{K}}(\mathbf{r})$ are periodic modulation functions with period \mathbf{R} . Because of the periodicity condition, the potential and the modulation functions maybe be rewritten as Fourier transforms,

$$V(\mathbf{r}) = \sum_{\mathbf{H}} v_{\mathbf{H}} e^{i\mathbf{H} \cdot \mathbf{r}}, \quad u(\mathbf{r}) = \sum_{\mathbf{H}} u_{\mathbf{H}} e^{i\mathbf{H} \cdot \mathbf{r}}, \quad (3.4)$$

where, $u_{\mathbf{H}}$ and $v_{\mathbf{H}}$ are Fourier coefficients, and $\mathbf{H} = h\mathbf{b}_1 + k\mathbf{b}_2 + l\mathbf{b}_3$ is the reciprocal lattice vector with Miller indices (h, k, l) . The vectors $\mathbf{b}_i = 2\pi\mathbf{a}_j \times \mathbf{a}_k / vol$ are reciprocal basis of the lattice spanned by the vectors \mathbf{a}_i and unit cell volume vol . Using Eqs. (3.2-3.4) and resetting the indices we obtain,

$$\sum_{\mathbf{H}} \left[\frac{\hbar^2}{2m} (\mathbf{K} + \mathbf{H})^2 - E \right] u_{\mathbf{H}} \exp^{i(\mathbf{K} + \mathbf{H}) \cdot \mathbf{r}} = - \sum_{\mathbf{H}\mathbf{H}'} v_{\mathbf{H}-\mathbf{H}'} u_{\mathbf{H}'} \exp^{i(\mathbf{K} + \mathbf{H}) \cdot \mathbf{r}}. \quad (3.5)$$

which is a set of linearly independent equations. They are satisfied for every \mathbf{r} leading to the Fourier coefficients which satisfy,

$$\left[\frac{\hbar^2}{2m} (\mathbf{K} + \mathbf{H})^2 - E \right] u_{\mathbf{H}} = - \sum_{\mathbf{H}'} v_{\mathbf{H}-\mathbf{H}'} u_{\mathbf{H}'}. \quad (3.6)$$

It is worth mentioning that no assumptions have been made so far about the physics, apart from the periodicity of the potential. In other words, Eq. (3.6) is the Fourier space representation of the Schrödinger equation in a periodic lattice. The coefficients $u_{\mathbf{H}}$ depend only on the displaced coefficients, $u_{\mathbf{H}'}$ and $v_{\mathbf{H}-\mathbf{H}'}$, for reciprocal lattice vectors \mathbf{H}' , allowing it to foresee the periodicity of the dispersion curves.

The coefficients can be rewritten as,

$$u_{\mathbf{H}} = - \frac{\sum_{\mathbf{H}'} v_{\mathbf{H}-\mathbf{H}'} u_{\mathbf{H}'}}{\left[\frac{\hbar^2}{2m} (\mathbf{K} + \mathbf{H})^2 - E \right]} \quad \text{for } E \neq \frac{\hbar^2}{2m} (\mathbf{K} + \mathbf{H})^2. \quad (3.7)$$

Using the Bragg condition for internal wavevectors $\mathbf{K}_{\mathbf{H}} = \mathbf{K} + \mathbf{H}$ and the fact that the neutron-nuclear interaction is extremely small ($V \ll E$) we can use Eqs. (3.6) and (3.7) to

conclude that only $v_{\mathbf{H}}$ with two energies E_K and E_{K_H} are strongly excited. In DD, this is commonly referred to as the two wave approximation, otherwise states as,

$$H = 0 : \quad \left(\frac{\hbar^2}{2m} K^2 - E \right) u_0 = -v_0 u_0 - v_{-\mathbf{H}} u_{\mathbf{H}}, \quad (3.8)$$

$$H \neq 0 : \quad \left(\frac{\hbar^2}{2m} K_H^2 - E \right) u_{\mathbf{H}} = -v_{\mathbf{H}} u_0 - v_0 u_{\mathbf{H}}, \quad (3.9)$$

or in matrix form,

$$\begin{pmatrix} E_K - \epsilon & v_{-\mathbf{H}} \\ v_{\mathbf{H}} & E_{K_H} - \epsilon \end{pmatrix} \begin{pmatrix} u_0 \\ u_{\mathbf{H}} \end{pmatrix} = 0, \quad (3.10)$$

where $E_K = \hbar^2 K^2/2m$, $E_{K_H} = \hbar^2 K_H^2/2m$, and $\epsilon = E - v_0$. The non-trivial solution obtained by setting the determinant to zero,

$$(E_K - \epsilon)(E_{K_H} - \epsilon) - v_{\mathbf{H}} v_{-\mathbf{H}} = 0. \quad (3.11)$$

is a quadratic equation in ϵ representing the energy dispersion. The solutions to this quadratic equation give the dispersion relations:

$$\epsilon_{1,2} = E_K + |v_{\mathbf{H}}| \left(\eta \pm \sqrt{\eta^2 + 1} \right), \quad (3.12)$$

with the dimensionless normalized energy parameter expressed as,

$$\eta = \frac{E_{K_H} - E_K}{2|v_{\mathbf{H}}|}, \quad (3.13)$$

whose significance will be explained later. The difference between the eigenvalue of the energy is

$$\Delta\epsilon = \epsilon_1 - \epsilon_2 = 2|v_{\mathbf{H}}| \sqrt{\eta^2 + 1}. \quad (3.14)$$

It is worth mentioning that far away from the Brillouin zone boundary $|E_{K_H} - E_K| \gg |v_{\mathbf{H}}|$, whereas on the boundaries $E_{K_H} - E_K = 0$ and this leads to the energy gap, $\Delta\epsilon = 2|v_{\mathbf{H}}|$.

The wavevectors inside the crystal associated with each of the kinetic energies $\epsilon_{1,2} = \hbar^2 K_{1,2}^2/2m$, maybe expressed as,

$$\mathbf{K}^{1,2} = K_{1,2\perp} \hat{e}_{\perp} + K_{1,2\parallel} \hat{e}_{\parallel}. \quad (3.15)$$

From the conservation of energy, the neutron wavevector parallel to the surface of the crystal is unchanged, i.e, $K_{1,2\parallel} = K_{\parallel} = k_{\parallel}$, while the normal components are, $K_{1,2\perp} \approx K_{\perp} \left[1 + \frac{|v_H|}{2E_{K\perp}} \left(\eta \pm \sqrt{\eta^2 + 1} \right) \right]$. Combining these components, we obtain,

$$\mathbf{K}^{1,2} = \mathbf{K} + \frac{\pi}{\Delta_H} \left(\eta \pm \sqrt{\eta^2 + 1} \right) \hat{e}_{\perp}, \quad (3.16)$$

where, Δ_H is the extinction length expressed as,

$$\Delta_H = \frac{\hbar^2 K_{\perp} \pi}{m|v_H|}. \quad (3.17)$$

Δ_H specifies the minimal thickness at which the energy of the incident wave is fully converted into the reflected wave, i.e total reflection. Inside the crystal, the eigenstates are doubly degenerate Bloch waves, giving rise to four excited waves; two waves propagating along the transmitted direction, with wavevectors $\mathbf{K}^{1,2}$, and two along the reflected direction with wavevectors $\mathbf{K}^{1,2} + \mathbf{H}$. The slight change in the wavevectors given by,

$$\Delta\mathbf{K} = \frac{2\pi}{\Delta_H} \sqrt{\eta^2 + 1}, \quad (3.18)$$

leads to a complicated mutual interference pattern known as the Pendellösung oscillations. The period of oscillations is Δ_H and it is sometimes referred to as the extinction length. Inside the crystal, there are two probability currents, denoted as $J_p^{1,2}$, which propagate at an angle Ω , see Fig. 3.1a. This angle is an amplification of $\delta\theta$ given by,

$$\Omega = \left(\frac{2E \sin^2 \theta_B}{|v_H|} \right) \delta\theta, \quad (3.19)$$

where for Si [220] at thermal neutrons $2E \sin^2 \theta_B / |v_H| \sim 10^6$.

To understand the Pendellösung oscillations, consider the case where the exact Bragg condition is satisfied ($\eta = 0$) so that $\mathbf{K}^{1,2} = \mathbf{K} \pm \frac{\pi}{\Delta_H} \hat{e}_{\perp}$. The standing wave inside the crystal is a sum of two excitations, one with nodes at the atomic planes and the other with nodes between the planes, and is given by [68],

$$\Psi_{\text{II}}(\mathbf{r}) = e^{i\mathbf{K}\cdot\mathbf{r}} \left[\cos \left(\frac{\pi z}{\Delta_H} \right) + i e^{-iHx} \sin \left(\frac{\pi z}{\Delta_H} \right) \right]. \quad (3.20)$$

The cosine term represents the component in the forward direction and the sine term represents the component in the reflected direction. The reflected component contains a phase $\exp(-i\pi Hx)$ that accounts for the location at which the wave is incident. As z changes, the waves oscillate between the forward and reflected directions, so that the thickness z_0 determines the ratio of the transmitted to the reflected intensity. For Silicon [111], the Pendellösung period $\lambda = 2.2 \text{ \AA}$ is $\Delta_H = 90.4 \mu\text{m}$ and for $\lambda = 4.4 \text{ \AA}$, it is $\Delta_H = 34.4 \mu\text{m}$. In order to preserve this interference, the dimensions of the interference system have to be accurate on a scale compatible to this length.

At the exit surface, due to the boundary conditions, the four waves recombine to form the transmitted wave denoted Ψ_O and the reflected wave denoted Ψ_H . Here O and H traditionally refer to the transmitted and reflected direction as defined by the reciprocal lattice vector \mathbf{H} . Using Eq. (3.1) we get,

$$\Psi_O(\mathbf{r}) = \int d\mathbf{k} \mu_{\mathbf{k}} t(\mathbf{k}) \psi_{\mathbf{k}}(\mathbf{r}), \quad \text{and} \quad \Psi_H(\mathbf{r}) = \int d\mathbf{k} \mu_{\mathbf{k}} r(\mathbf{k}) \psi_{\mathbf{k}}(\mathbf{r}). \quad (3.21)$$

The reflection (r) and transmission (t) coefficients for non-absorbing crystals are given by [3, 62],

$$t = e^{i\chi} \exp(-iA\eta) \left[\cos(A\sqrt{1+\eta^2}) + \frac{i\eta}{\sqrt{1+\eta^2}} \sin(A\sqrt{1+\eta^2}) \right], \quad (3.22)$$

$$r = e^{i\chi} \exp[i(-A\eta + 2A\eta z/z_0)] \left(\frac{v_H}{v_{-H}} \right) \frac{-i}{\sqrt{1+\eta^2}} \sin(A\sqrt{1+\eta^2}), \quad (3.23)$$

where $A = \pi D/\Delta_H$ is the dimensionless crystal thickness, and χ is the nuclear phase shift due to refraction given by,

$$\chi = D(K_{\perp} - k_{\perp}), \quad \text{where} \quad K_{\perp} = \sqrt{k_{\perp}^2 - 2mV/\hbar^2}, \quad (3.24)$$

χ is also present when the crystal is oriented outside the Bragg condition. In Fig. 3.1b, the transmission and reflection for a beam incident along $-\hat{e}_{\parallel}$ is denoted by \bar{t} and \bar{r} , respectively. It can be easily shown that (ref. chapter 4)

$$\bar{t} = t(-\eta) = t^*, \quad \bar{r} = r(-\eta) = -r^*. \quad (3.25)$$

We note here that the parameter $\eta = \eta(\delta\theta)$ characterizes the deviation (angular or momentum) from the exact Bragg condition, so that each component of the wavepacket have a unique transmission coefficient. η can manifest itself in different forms although, it is commonly used to denote the scaled angular or momentum deviation.

The reflection and transmission probabilities are given by,

$$p_r = |r|^2 = \frac{\sin^2\left(\frac{\pi z_0}{\Delta_H} \sqrt{1 + \eta^2}\right)}{1 + \eta^2}, \quad \text{and} \quad p_t = |t|^2 = \frac{\eta^2 + \cos^2\left(\frac{\pi z_0}{\Delta_H} \sqrt{1 + \eta^2}\right)}{1 + \eta^2}, \quad (3.26)$$

In the special case of zero beam divergence ($\eta = 0$), the transmitted and reflected probabilities at any thickness z are

$$p_t = |r|^2 = \sin^2\left(\frac{\pi z}{\Delta_H}\right), \quad \text{and} \quad p_r = |t|^2 = \cos^2\left(\frac{\pi z}{\Delta_H}\right). \quad (3.27)$$

The probabilities oscillate out of phase such that, at any instant, the ratio z/Δ_H determines the relative amplitudes of the wave in each direction. At the exit, the relative amplitudes in the forward and reflected directions are determined by z_0/Δ_H . These oscillation are explored in details in Chapter 4.

3.3 Three-blade neutron interferometer

A detail sketch of a three-blade perfect Si crystal NI, is shown in Fig. 3.2. It depict four waves leaving the NI into the O-beam detector D_O , H-beam detector D_H , transmitted-transmitted beam D_1 , and reflected-transmitted beam D_2 . Consider a wavefunction $|\Psi\rangle$ satisfying the Bragg condition of a three-blade NI. Without loss of generality the projected wavefunctions on the detectors D_1 , D_O , D_H , and D_2 are respectively,

$$\begin{aligned} |\Psi_1\rangle &= tt|\Psi\rangle, & |\Psi_O\rangle &= (tr\bar{r} + e^{i\Delta\Phi} r\bar{r}t) |\Psi\rangle, \\ |\Psi_2\rangle &= r\bar{t}|\Psi\rangle, & |\Psi_H\rangle &= (tr\bar{t} + e^{i\Delta\Phi} r\bar{r}r) |\Psi\rangle, \end{aligned} \quad (3.28)$$

where $\Delta\Phi$ is the total phase difference. It is a combination of the control phase from the phase flag and the constant phase from the offset between the two states. The probabilities

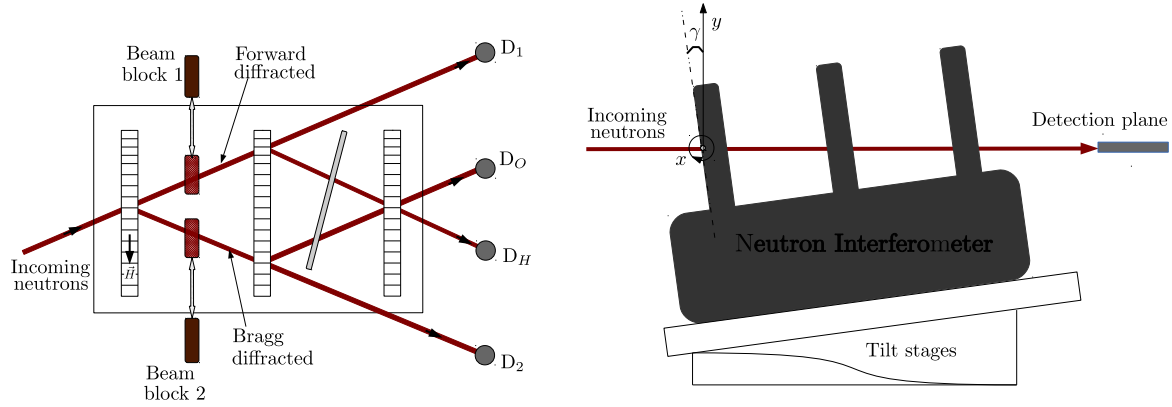


Figure 3.2: Schematic of the experimental setup at the NIOFa. Left figure shows the top view of the three-blade NI setup with four detectors D_1 , D_O , D_H , and D_2 placed in the beams at the NI exit. The component of the wavefunction arriving at detectors D_O and D_H has a phase difference, which can be varied by rotating the phase flag. Each beam path can be blocked using a cadmium plate to form a network of consecutive beam splitters. In order to vary the thickness of each of the beam splitters, the interferometer is tilted around the x -axis. On the right is the side view of the experimental setup diagram.

associated with each of the components are,

$$\begin{aligned}
 p_1 &= |t|^4, & p_O &= 2|r|^4|t|^2 \left(1 + \cos(\Delta\Phi)\right), \\
 p_2 &= |r|^2|t|^2, & p_H &= |r|^2|t|^4 + |r|^6 - 2|r|^4|t|^2 \cos(\Delta\Phi).
 \end{aligned}
 \tag{3.29}$$

The lack of a dependence on $\Delta\Phi$ indicates that there is no interference in the p_1 and p_2 terms. Therefore, the rotation of the phase flag does not affect these beams.

It is a common assumption in the theory in DD that the incident beam has a momentum spread significantly broader than the Darwin width. In addition to this assumption, if the crystal thickness is greater than the extinction length, then the detected intensity is independent of the thickness of the crystal [63, 64, 65]. However, in a perfect crystal NI, the first blade reduces the momentum spread of the beam input onto the second blade, which further narrows the width of the input onto the third blade. The resulting beam has a narrow spread and thus averaging over a spread equals to the Darwin width leads

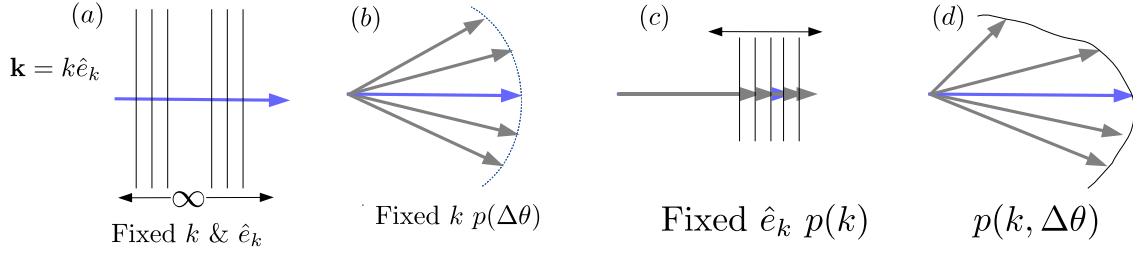


Figure 3.3: Illustration of the various wavevector deviation from the mean value (considered the center of the wavepacket or the exact Bragg wavevector). (a) when the deviation in magnetude and direction (angle) are both zero. (b) there is a deviation in angle but not magnetude, (c) there is a deviation is magnetude but not direction, while (d) illustrates deviation in both magetude and direction.

to intensities profiles that weakly couple to the thickness of the beam splitters. Although other possibilities exist as illustrated in Fig. 3.3, we are only interested in the case where there is an angular or wavelength divergence. In Fig. 3.3a you see a plane wave with no angular and no wavevector distribution. In Fig. 3.3b is a distribution with an angular and a fixed wavevector while in Fig. 3.3c is a distribution with a wavevector magnitude and no angular divergence. Finally in Fig. 3.3d there is both an angular and wavevector distribution.

3.3.1 Case of wavelength spread

When the incident beam is distributed in wavelength, $\lambda = 2\pi/k$, an average over the reduced length $A(\lambda) = \pi D/\Delta_H$ must be taken into account. This leads to the full average probability spectrum expressed as,

$$J_{nm} = \int_{-\infty}^{\infty} p_r(\eta)^n p_t(\eta)^m \left| \frac{dA}{d\lambda} \right| d\lambda = \int_{-\infty}^{\infty} p_r(\eta)^n [1 - p_r(\eta)]^m dA, \quad (3.30)$$

where the identity $p_t = 1 - p_r$ is used. The average are taken over the whole space because the Darwin width is very small. Applying this average to the probability densities

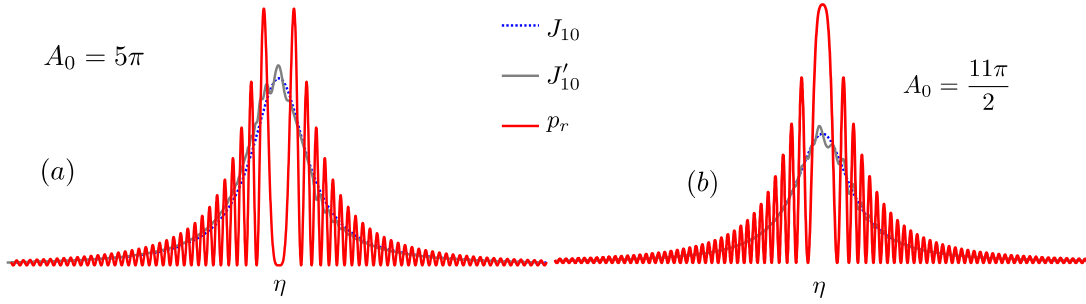


Figure 3.4: The Pendellösung oscillations. The averages of p_r , J'_{nm} and J_{nm} , are plotted against η for $A = 5\pi$ in (a) and $A = 11\pi/2$ in (b).

Eq. (3.29), we obtain

$$\begin{aligned} I_1(\eta) &= J_{02}, & I_o &= J_{21}(1 + \cos \phi), \\ I_2(\eta) &= J_{11}, & I_H &= J_{30} + J_{12} - J_{21} \cos \phi. \end{aligned} \quad (3.31)$$

The J_{nm} 's are obtained by replacing the integrals of the sinusoidal oscillations with the averages taken over A , given by $\langle \sin^2(\cdot) \rangle \rightarrow 1/2$, $\langle \sin^4(\cdot) \rangle \rightarrow 3/8$, and $\langle \sin^6(\cdot) \rangle \rightarrow 5/8$, to get for example,

$$J_{21}(\eta) = \frac{1 + 6\eta^2}{8(1 + \eta^2)^3}, \quad J_{10}(\eta) = \frac{1}{2(1 + \eta^2)}$$

Another formulation (best suited for perfect crystals monochromators and microradian collimation) is to take the average of the reduced length around the mean period of $A \pm \Delta A$, with beat frequency $\Delta A = 2\pi/(\eta + \sqrt{1 + \eta^2})$ to get,

$$J'_{nm} = \int_{\lambda - \Delta\lambda}^{\lambda + \Delta\lambda} p_r(\eta)^n p_t(\eta)^m \frac{1}{\Delta\lambda} \left| \frac{dA}{d\lambda} \right| d\lambda = \frac{1}{2\Delta A} \int_{A_0 - \Delta A}^{A_0 + \Delta A} p_r(\eta)^n [1 - p_r(\eta)]^m dA. \quad (3.32)$$

The deviation between the two averages is very small, and so each can be used interchangeably as the case may be. A comparison of J_{10} and J'_{10} is shown alongside the probability p_r in Fig. 3.4, and there is a significant agreement.

3.3.2 Case of angular spread

As mentioned earlier, when perfect crystal monochromators are used, it is realistic to ignore the wavelength distribution. On the other hand, it is extremely difficult to obtain a collimated beam with no angular divergence. We address the case where the incident beam is monochromatic but has angular spread. If a beam with only angular spread is incident onto a network of perfect crystal beam splitters so that it undergoes n reflections and m transmissions, the average intensity as a function of crystal thickness z_0 ,

$$\mathcal{J}_{nm} = \int_{-\infty}^{\infty} p_r(z_0)^n p_t(z_0)^m d\eta = \int_{-\infty}^{\infty} p_r(z_0)^n [1 - p_r(z_0)]^m d\eta, \quad (3.33)$$

where the integration is taken over all possible η 's. In experiments, the intensity \mathcal{J}_{nm} can be varied through two techniques. One technique varies the neutron wavelength for a fixed crystal thickness [43, 69], and the other varies the thickness of the crystal for a fixed wavelength [42, 70]. The method adopted here is that of changing the thickness of the crystal and maintaining the same wavelength. This was achieved by tilting the crystal around an axis parallel to the crystallographic plane, as shown in Fig. 3.2.

The intensities at the detectors obtained from the average of the probabilities in Eq. (3.29) over angular divergence are,

$$\begin{aligned} I_1(z_0) &= \mathcal{J}_{02}, & I_o(z_0) &= 2\mathcal{J}_{21} (1 + \cos \phi), \\ I_2(z_0) &= \mathcal{J}_{11}, & I_H(z_0) &= \mathcal{J}_{30} + \mathcal{J}_{12} - 2\mathcal{J}_{21} \cos \phi. \end{aligned} \quad (3.34)$$

It is possible to express \mathcal{J}_{nm} as a sum of reflections, \mathcal{J}_n , (where the zero is suppressed for brevity) only as $\mathcal{J}_{12} = \mathcal{J}_1 - \mathcal{J}_3$, $\mathcal{J}_{11} = \mathcal{J}_1 - \mathcal{J}_2$, $\mathcal{J}_{21} = \mathcal{J}_2 - \mathcal{J}_3$, and $\mathcal{J}_{12} = \mathcal{J}_1 - 2\mathcal{J}_2 + \mathcal{J}_3$. With the approximate intensity modulation function \mathcal{J}_{10} given by [71],

$$\mathcal{J}_1 \simeq \frac{\pi}{2} - \frac{1}{2} \sqrt{\frac{\Delta_H}{z_0}} \left[\cos \left(\frac{2\pi z_0}{\Delta_H} + \frac{\pi}{4} \right) + \frac{5}{16} \frac{\Delta_H}{\pi z_0} \sin \left(\frac{2\pi z_0}{\Delta_H} + \frac{\pi}{4} \right) \right] \quad (3.35)$$

and also

$$\begin{aligned} \mathcal{J}_2 &\simeq \frac{3\pi}{16} - \frac{1}{2} F'(z_0; 2, 16/13) + \frac{1}{32} F'(z_0; 4, 32/13), \\ \mathcal{J}_3 &\simeq \frac{15\pi}{128} - \frac{15}{32} F'(z_0; 2, 16/21) + \frac{3}{64} F'(z_0; 4, 16/21) - \frac{1}{288} F'(z_0; 6, 16/7). \end{aligned}$$

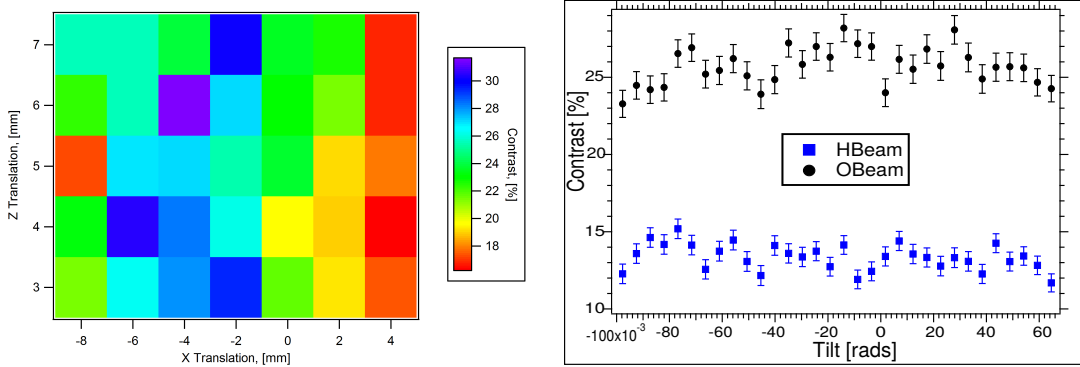


Figure 3.5: On the left, a colour representation of the contrast variation along the transverse vertical and transverse horizontal positions of the NI. On the right the contrast variation versus interferometer tilt γ for O- and H- beams (see Fig. 3.2 for the tilt geometry).

The function $F'(z_0; a, b)$ is defined as,

$$F'(z_0; a, b) = \sqrt{\frac{\Delta_H}{z_0}} \left[\cos \left(\frac{a\pi z_0}{\Delta_H} + \frac{\pi}{4} \right) + \frac{1}{b} \frac{\Delta_H}{\pi z_0} \sin \left(\frac{a\pi z_0}{\Delta_H} + \frac{\pi}{4} \right) \right], \quad (3.36)$$

which is true for $z_0/\Delta_H > 1$. Similar expressions can be obtained for higher order values of n and m , but their analytical forms are long and cumbersome. Because the intensities depend on the thickness, there is in principle a thickness z_0 for which $\mathcal{J}_{20} - \mathcal{J}_{30} = \mathcal{J}_{10}/2$, which effectively generates a balanced NI. This limit is however not achieved in our experiments due to geometric constraints.

3.4 Experimental procedure

An experiment was performed on the NIOFa beamline at the NCNR described in Chapter 2. In this experiment, the thickness of the NI was changed by tilting. The NI used was a three-blade Laue-type made from perfect crystal silicon with a blade thickness of 2.51 mm and a (111) crystallographic orientation. A detail sketch of the setup is shown in Fig. 3.2a. It shows movable pieces of cadmium to block either the transmitted beam or reflected beam after the first blade. Detectors D_O , D_H , D_1 , and D_2 are located on each

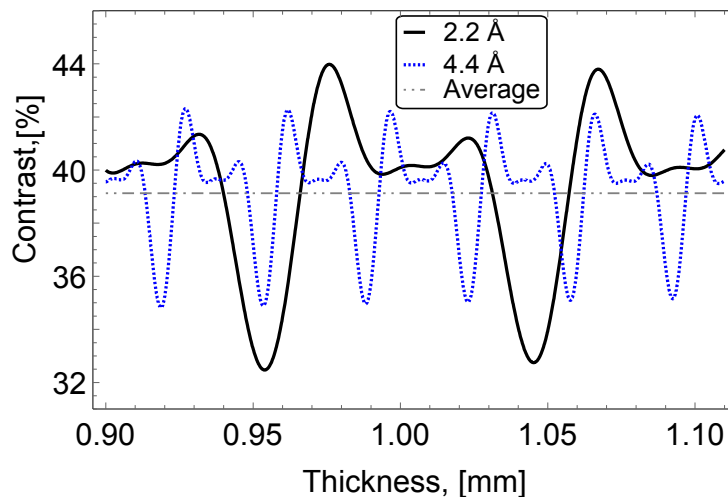


Figure 3.6: Simulations showing the variation of the contrast of the H-Beam with the blade thickness of a three-blade NI for a neutron wavelength of 2.2 Å and 4.4 Å. The horizontal line shows the contrast when integrated over a broad neutron wavelength distribution.

of the beams leaving the NI. They are large area detectors meant to detect the neutron beam in the experiment with a cross-section area of $5 \times 3.75 \text{ mm}^2$. The tilt geometry is shown in Fig. 3.2b. In order to ensure that the tilt does not affect the neutron wavelength selected, Bragg scans were done at three different tilt angles, $\gamma = -4^\circ, 0^\circ, 4^\circ$, for which no significant change in Bragg angle was observed.

After aligning the interferometer to the beam, a 2D contrast scan in the transverse vertical and horizontal directions was performed to find the position with highest contrast shown in Fig. 3.5 (left). With the interferometer at this position, a contrast scan against the NI tilt is shown Fig. 3.5 (right). For an ideal perfect crystal NI with blades of equal thickness, the O-beam is made up of a superposition of components of the same amplitude and so its contrast is expected to remain constant as the NI is tilted. However, some fluctuations attributed to phase drift arising from the difference in the thickness of various NI blades are observed. From the fabrication techniques, it is known that the thicknesses of the blades might differ by about $\pm 10 \mu\text{m}$. Because of this difference, possible features of DD might emerge. These effects were not studied in this chapter.

3.4.1 Contrast variation

The contrast of the H-beam depends on the thickness, z_0 , as,

$$\mathcal{V}(z_0) = \frac{2\mathcal{J}_{21}(z_0)}{\mathcal{J}_{30}(z_0) + \mathcal{J}_{12}(z_0)}. \quad (3.37)$$

Theoretically, it fluctuates around the value of 39.13% as the thickness increases, see page 284 of [16]. Simulations of the H-beam contrast versus the thickness is shown in Fig. 3.6 for the 2.2 Å and 4.4 Å neutron wavelengths. The plot shows some oscillations, although these were not observed in our experiments. These oscillations can be observed in beamlines with arcseconds divergence in wavevector spread. Obtained plots show that the thickness of the NI blades should be carefully considered when designing an interferometer. This is a result of the H-beam contrast difference with wavelength ($\Delta_H = 0.091$ mm for 2.2 Å, and $\Delta_H = 0.035$ mm for 4.4 Å).

3.5 Intensities from an interferometer

The experimental data and fit to the data collected from an NI (without beam blocks) illuminated with neutrons of wavelength $\lambda = 2.2$ Å are shown in Fig. 3.7. The intensity at the O-beam and H-beam against the tilt angle, γ , are shown in Figs. 3.7a and 3.7b, respectively. Also shown in Fig. 3.7c is the empty interferometer phase against the tilt and a fit to a linear equation $c_1 + c_2 \gamma$. This phase difference is obtained by rotating the phase flag and extracting the phase, for every γ . Also shown in Fig. 3.7d is the sum of the O-beam and H-beam intensity alongside a line of best fit given by,

$$I_o(z_0) + I_H(z_0) = \mathcal{J}_1. \quad (3.38)$$

It is clearly visible on the plots that the intensity changes with the thickness. Still the variation is very slow thus a high neutron counts is required.

In the study of two or more consecutive beam-splitting, a piece of cadmium was used to block one of the NI paths (see Fig. 3.2a). With beam block I inside the interferometer, no neutron is observed on detector D_1 . On the O-beam, the intensity corresponds to two

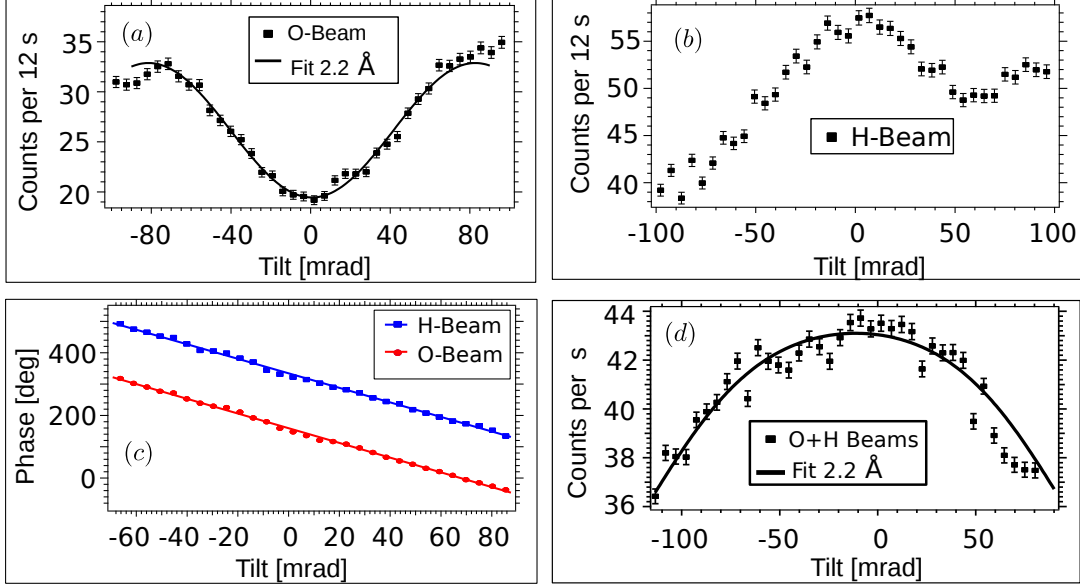


Figure 3.7: The O- and H-beam, the sum, and their phases obtained by tilting an NI without a phase flag. In (a) is plot of the experimental data and fit to the O-beam intensity for 2.2 Å wavelength. In (b), is the H-beam intensity for the same wavelength. In (c), is the phase of each of the beams fit to a linear equation $c_1 + c_2 \gamma$. In (d) is the the sum intensity (O+H) against the interferometer tilt (see Fig. 3.2).

reflections plus one transmission ($r\bar{r}t$) and on the H-beam to three reflections ($r\bar{r}r$). On detector D₂, the beam correspond to a reflection-transmission (rt). These intensities can be expressed as,

$$I_o(z_0) = \mathcal{J}_{21}, \quad I_H(z_0) = \mathcal{J}_{30}, \quad I_2(z_0) = \mathcal{J}_{11}. \quad (3.39)$$

The schematic setup for measuring these intensities is shown in Fig. 3.8(a). Experimental data and fit to the H-beam intensity is shown in Fig. 3.8. For neutrons with $\lambda = 2.2$ Å the intensity is shown in Fig. 3.8b and for neutron with $\lambda = 4.4$ Å the data is shown in Fig. 3.8c. Also shown is the data and fit to $I_2(z_0)$ in Fig. 3.8d only for neutrons with $\lambda = 4.4$ Å. Other possible configurations include the beam block in the reflected beam of the first blade, for which the O-beam intensity remains ($tr\bar{r}$) and the H-beam undergoes ($tr\bar{t}$) giving an intensity $I_H(z_0) = \mathcal{J}_{12}$.

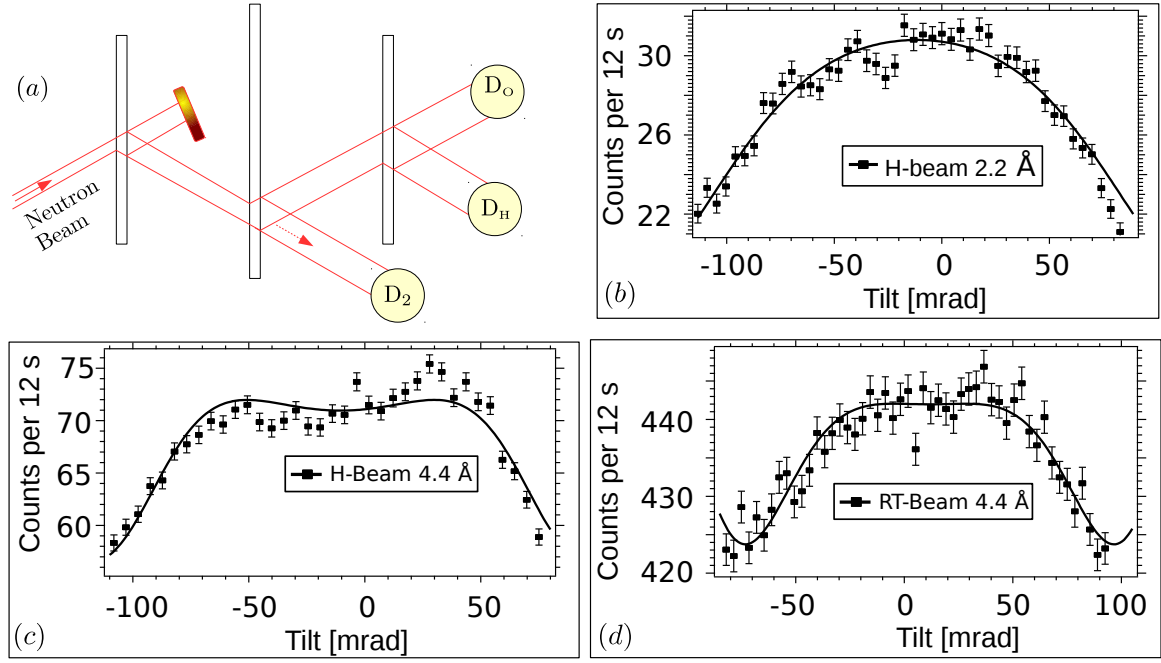


Figure 3.8: The schematic setup for measuring the H-beam intensity vs tilt angle for a neutron beam through three consecutive beam splitters is shown in (a). In (b) is the intensity for $\lambda = 2.2 \text{ \AA}$ and a fit using $A = 86.37$. In (c) is the intensity for $\lambda = 4.4 \text{ \AA}$ and a fit using $A = 227.03$. In (d), The experimental data and fit to the intensity on D_2 versus tilt angle $\lambda = 4.4 \text{ \AA}$.

3.6 Data analysis

For a [111] perfect silicon crystal the calculated values of the reduced length $A = \pi z_0 \Delta_H^{-1} = 86.86 \text{ rad}$ for $\lambda = 2.2 \text{ \AA}$ and $A = \pi z_0 \Delta_H^{-1} = 228.32 \text{ rad}$ for $\lambda = 4.4 \text{ \AA}$. Correspondingly, for the 2.2 \AA the Pendellösung period is $\Delta_H = 90.4 \mu\text{m}$ and for the 4.4 \AA , the Pendellösung period is $\Delta_H = 34.4 \mu\text{m}$. When the NI is tilted by γ , the blade thickness becomes $z = z_0 \sec(\gamma - \gamma_0)$, where z_0 is the thickness at zero tilt which is the offset angle γ_0 . The fit function to \mathcal{J}_1 as specified by theory is,

$$R_F^{(1)} = B_1 + B_2 \sqrt{\frac{\Delta_H \cos(\gamma - \gamma_0)}{4z_0}} \left(\cos[g(\gamma)] + \frac{5}{16} \frac{\Delta_H}{\pi z_0} \frac{\sin[g(\gamma)]}{\sec(\gamma - \gamma_0)} \right), \quad (3.40)$$

where B_1 and B_2 are constants to be determined, and $g(\gamma) = \left(\frac{2\pi z_0}{\Delta_H} \sec(\gamma - \gamma_0) + \frac{\pi}{4} \right)$. The fit to the sum intensity in Fig. 3.7d gave the values $B_1 = 3781 \pm 49$, $B_2 = 6275 \pm 705$, $\gamma_0 = -0.011 \pm 0.002^\circ$.

The values of $A = \pi z_0 \Delta_H^{-1}$ at zero tilt obtained by simultaneously fitting all the data from the various experimental configurations, gave the values $\pi z_0 \Delta_H^{-1} = 86.37 \pm 0.02$ for a wavelength of 2.2 Å and $\pi z_0 \Delta_H^{-1} = 226.75 \pm 0.02$ for a wavelength of 4.4 Å. The ratio $\Delta_H(2.2)/\Delta_H(4.4) = 2.625$, obtained from experiments, has a remarkable agreement with the calculated value $\Delta_H(2.2)/\Delta_H(4.4) = 2.628$.

The fit function to the O-beam intensity for the empty NI is,

$$I_F(\gamma) = B_1 + B_2 S_3 \left[\frac{2\pi z_0}{\Delta_H} \sec(\gamma - \gamma_0) \right] [1 + \cos(C_1 + C_2 \gamma)], \quad (3.41)$$

and is shown in Fig. 3.7a, with fit parameters $B_1 = 3287.5 \pm 38$, $B_2 = -2937 \pm 83$, $c_1 = -38.27 \pm 1.59$, and $c_2 = 6.31 \pm 0.06$.

3.7 Conclusion

We employed the technique of tilting the NI to study how the transmission and reflection coefficients can be controlled. The experimental results agree with the simulations for a crystal thickness of 2.51 mm, and neutron wavelengths of 2.2 Å and 4.4 Å. Having the ability to control the beam-splitting efficiencies, the intensity imbalance of the O-beam and H-beam may be controlled by designing an NI with no beam asymmetry. In the gravitational phase shift experiments [25], the NI was tilted to introduce a height difference between the two neutron paths in the NI, thereby introducing a gravitational phase shift. In a recent experiment (ref. [62]) a perfect crystal Si sample inside was tilted in an NI to probe the DD phases. The geometry of our experiment in Fig. 3.2b is different from that of these two experiment. These results could open up a way to customize the transmission and reflection coefficients for specific neutron wavelengths leading to an optimized NI.

Chapter 4

Quantum Information Approach to Dynamical Diffraction

4.1 Introduction

The theory of DD, as mentioned earlier, predicts many features of diffraction from periodic lattices; for example Pendellösung oscillations [43, 61], the extinction length and abnormal transmission [10] and the Borrmann effect [72]. DD theory is often approximated in the thick crystal regime by two waves emerging from the crystal, with one propagating along the incident wave direction called the transmitted or forward diffracted wave, and another propagating in the complementary direction called the reflected or Bragg diffracted wave. This treatment will be referred to as the standard theory of DD.

Although, the standard theory of DD has been very successful in explaining many diffraction phenomena, the mathematics can be quite cumbersome and involves solving the Schrödinger's equation for a lattice with Avogadro's number of interaction potentials. Even in the two-wave approximation, the standard theory of DD still uses many variable substitutions to make the formulae readable [3, 73, 74]. This lack of readability may end up obscuring very simple concepts.

Presented here is an alternative relatively simple treatment of DD that uses the language of quantum information (QI) to model a periodic lattice as a network of beam splitters. In this treatment, DD is considered as a coherent quantum effect arising from the interference of different paths taken by the wave as it passes through the lattice. While comparatively simple, this approach can accurately explain many effects of DD. We will consider beam profiles for DD through a single thick crystal, and show how it predicts the widening of the neutron beam profile. This widening is bounded by the outer path in the transmitted beam and the outer path in the reflected beam thereby forming a triangular region, known as the Borrmann triangle. The QI model also predicts the sinusoidal variations known as Pendellösung oscillations in the intensities of transmitted and reflected beams. The Pendellösung oscillations is a consequence of the energy transfer between the reflected and transmitted beams. Lastly, it is shown how this approach may be extended to multi-blade crystal devices, such as, three-blade NI.

Consider a neutron with wavefunction, $\Psi(\mathbf{r}) = \int d\mathbf{k} \mu_{\mathbf{k}} \psi_{\mathbf{k}}(\mathbf{r})$, (where $\psi_{\mathbf{k}}(\mathbf{r}) = e^{i\mathbf{k}\cdot\mathbf{r}}$ are a basis of plane-waves) diffracting off a silicon crystal. In the diffraction process, the wave inside the crystal is a superposition of two waves one along the direction of incidence, with wavevector \mathbf{K} , and the other along the reflected direction, with wavevector \mathbf{K}_H (see Fig. 3.1 in chapter 3). The wavefield at the exit surface of the crystal splits into the transmitted wave, which has undergone an even number of reflections, and the reflected wave, which has undergone an odd number of reflections. The difference in the number of reflections gives rise to a phase difference which lead to Pendellösung oscillations of energy exchange. For an incident plane wave satisfying exactly the Bragg condition on a crystal aligned to the origin, the two internal wavevectors $\mathbf{K} \pm \frac{\pi}{\Delta_H} \hat{e}_\perp$ correspond to a coherent superposition wavefunction inside the crystal given by,

$$\Psi_{\text{inside}}(\mathbf{r}) = e^{i\left(K_z - \frac{\pi}{\Delta_H}\right)z} \cos\left(\frac{\pi x}{d}\right) + ie^{i\left(K_z + \frac{\pi}{\Delta_H}\right)z} \sin\left(\frac{\pi x}{d}\right). \quad (4.1)$$

The cosine component is located at the lattice planes and the sine component is located between the lattice planes. The components of the wavevector along z are slightly different, resulting in a beating of the wave as it propagates through the crystal. For this reason the orientation of the wavefront oscillates periodically between the two directions.

According to DD, when a plane wave is incident on a non-absorbing crystal, for example

silicon (220), with $v_H/v_{-H} = 1$ and thickness D , the reflection (r) and transmission (t) coefficients for non-absorbing crystal are

$$t = e^{i\chi} e^{i\varphi} \cos \vartheta \qquad r = e^{i\chi} e^{-i\varrho} \sin \vartheta,$$

where,

$$\chi = D(K_{\perp} - k_{\perp}), \qquad \vartheta \equiv \arcsin \left[\frac{\sin[\Phi(\eta)]}{\sqrt{1 + \eta^2}} \right], \qquad (4.2)$$

$$\varrho \equiv -A\eta + 2A\eta z/D_0 + \pi/2, \qquad \varphi \equiv -A\eta + \arctan \left[\frac{\eta}{1 + \eta^2} \tan[\Phi(\eta)] \right], \qquad (4.3)$$

with $\Phi(\eta) = A\sqrt{1 + \eta^2}$, where, η quantifies the deviation from the Bragg condition. If the incident wavevector is in the complementary direction as shown in Fig. 1.9, the reflection and transmission amplitudes are denoted by \bar{r} and \bar{t} , respectively. The evolution can be written as an effective unitary operator of a 2×2 matrix, $U_{DD}(\varphi, \varrho, \vartheta)$, given by,

$$U_{DD}(\varphi, \varrho, \vartheta) = \begin{pmatrix} t & -r^* \\ r & t^* \end{pmatrix} = e^{i\chi} \begin{pmatrix} e^{i\varphi} \cos \vartheta & -e^{i\varrho} \sin \vartheta \\ e^{-i\varrho} \sin \vartheta & e^{-i\varphi} \cos \vartheta \end{pmatrix} \qquad (4.4)$$

Where we have used $\bar{t} = t^*$, and $\bar{r} = -r^*$. Under ideal conditions in DD (perfect monocrystalline crystal and no momentum spread and beam divergence) the parameters are $\varphi = 0$, $\varrho = \pi/2$, and $\vartheta = A$, giving rise to a constant unitary operator for the blade.

In Sec. 4.2, we extend the definition of the unitary operator to develop a QI model for DD.

4.2 Quantum information model

The process of DD through a perfect periodic non-absorbing crystal is a unitary evolution. In this work, we propose an alternative quantum information model for DD, based on the requirement that a crystal can be segmented into planes, with each acting as a unitary operator and the same unitary operator is repeatedly applied throughout the process. This is an operational approach that considers a coarse-graining of a thick perfect crystal

into a computationally tractable number of planes of logical scattering sites. Each of the logical scattering sites may be modelled as a general beam splitter that coherently splits an incoming wave into transmitted and reflected components. The choice of unitary depends on the number of planes in the coarse-graining, with the constraint that the phase of the wavefunction leaving the crystal does not wrap around in multiples of 2π . As the number of planes increase, so does the number of possible paths through the crystal for a given output component. This results in the widening of the matter wave beam profile, and the interference between the multiple paths reproduces many of the effects typically described by standard DD theory. The coarse-graining of scattering sites is necessary as there are an order of Avogadro's number of atoms corresponding to physical scattering sites in a perfect crystal. However, many DD features can be reproduced with only a modest number of coarse-grained scattering sites considered. This QI approach to DD is a quantum mechanical version of a Galton's board, that is one form of a discrete time quantum walk [75, 76, 77]. It is also related to the original proposal of DD by Darwin [78, 79] that involves breaking down the scattering media into layers, in conformation to the invariance principle in physics [61, 80].

4.2.1 Formalism of QI model for DD

In the QI model, it is also assumed that the scattering at each coarse-grained site is macroscopically distinct, similar to Bragg scattering and Bloch theory. This model also makes the assumption that the entire process of diffraction, through the crystal, is within the coherence length of the incoming wave.

The coarse-graining for a perfect crystal into scattering nodes is illustrated in Fig. 4.1. This coarse-graining procedure is performed in several steps. The crystal is segmented into planes, and each plane is further divided into *nodes*, creating a lattice where each node corresponds to a scattering site. Each node functions as a beam splitter with two input and output ports. The scattering action of an arbitrary node (denoted by j , which specifies the node's relative vertical location) may therefore be modelled as a unitary transformation, U_j , acting on the two-level system $\{|a_j\rangle, |b_j\rangle\} \in \mathbb{C}^2$ of the incident state. The collective action of all the nodes lead to a multiple scattering process that gives rise to quantum

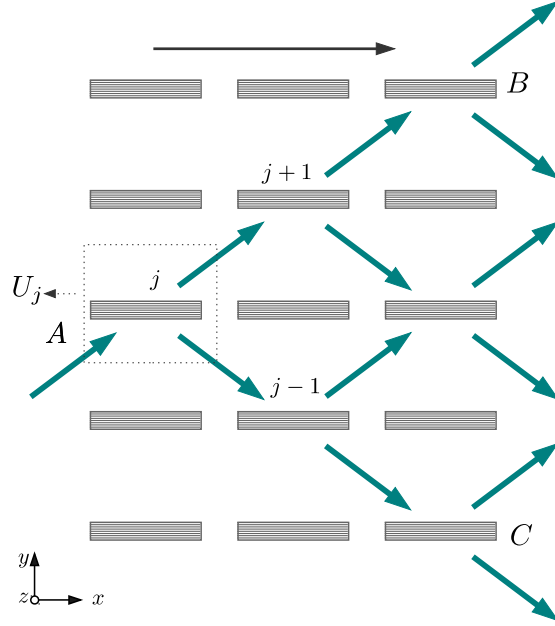


Figure 4.1: A perfect crystal decomposed into various scattering sites (nodes) shown as blocks. The incident wave is a single ray moving upward along AB and the direction AC is the reflected wave. The region ABC is the Borrmann triangle. At each node, the unitary operator U_j coherently splits the wave into two components; the transmitted and reflected. Repeated application of U_j generates the transmitted and reflected outputs of the crystal. Any ray of the transmitted beam has undergone an even number of reflections while those of the reflected beam have undergone an odd number of reflections.

interference effects. The unitary generating this multi-scattering process is denoted by, $\mathcal{U}(N) \in \mathcal{L}(\mathbb{C}^{2N})$, and its dimensions depend on the number of planes, N , considered in the coarse-grained approximation. The transmitted and reflected waves, denoted as $|\Psi^T\rangle$ and $|\Psi^R\rangle$, respectively, leaving the crystal surface and the corresponding intensities, depend on the parameters of $\mathcal{U}(N)$.

A ray is used to represent a single logical level of any wave, which may be modelled as a state vector $|a_j\rangle$ or $|b_j\rangle$, where the labels a and b refer to rays moving upwards (when $k_{||} > 0$) or downwards (when $k_{||} < 0$), respectively. Using $|a_j\rangle$ and $|b_j\rangle$ also reduces the ambiguity originating from the identification of transmitted wave and reflected wave, as

they depend on the type of input. The ray tracing approach is analogous to a path integral, and is used to illustrate some of the features of the wave leaving the crystal.

At the scattering site, the beams are coherently split according to the relation,

$$|a_j\rangle \mapsto t_a|a_{j+1}\rangle + r_a|b_{j-1}\rangle, \quad (4.5)$$

$$|b_j\rangle \mapsto r_b|a_{j+1}\rangle + t_b|b_{j-1}\rangle, \quad (4.6)$$

where, t_a, t_b, r_a , and r_b are complex transmission and reflection coefficients. For the scattering relation to be unitary, the conditions,

$$|t_a|^2 + |r_a|^2 = 1, \quad |t_b|^2 + |r_b|^2 = 1, \quad t_a \bar{r}_b + r_a \bar{t}_b = 0 \quad (4.7)$$

must be satisfied. A possible choice for these parameters is,

$$\begin{aligned} t_a &= e^{i\xi} \cos \theta, & t_b &= e^{-i\xi} \cos \theta, \\ r_a &= -e^{-i\zeta} \sin \theta, & r_b &= e^{i\zeta} \sin \theta, \end{aligned} \quad (4.8)$$

The parameters ξ, θ , and ζ maybe determined by two possible ways. The first is from experimental intensity profiles of the transmission and reflection beam. By mapping the intensities at node j and $j + 1$ at the exit surface to the position in the Borrmann fan, we could determine possible values of ξ, θ , and ζ . The second way to get these parameters is from the minimum thickness of a crystal, τ , for which the neutrons are all reflected given by $\tau/\Delta_H < 1/2$, where Δ_H is the Pendellösung length. By relating this standard DD formula to the model, we obtain that $\theta = \pi\tau/\Delta_H$, $\xi = 0$, and $\zeta = \pi$.

The unitary operator is then,

$$\begin{aligned} U_{j,\xi,\theta,\zeta} &= (e^{i\xi} \cos \theta |a_{j+1}\rangle - e^{-i\zeta} \sin \theta |b_{j-1}\rangle) \langle a_j| + (e^{i\zeta} \sin \theta |a_{j+1}\rangle + e^{-i\xi} \cos \theta |b_{j-1}\rangle) \langle b_j| \\ &= |a_{j+1}\rangle (e^{i\xi} \cos \theta \langle a_j| + e^{i\zeta} \sin \theta \langle b_j|) - |b_{j-1}\rangle (e^{-i\zeta} \sin \theta \langle a_j| - e^{-i\xi} \cos \theta \langle b_j|). \end{aligned} \quad (4.9)$$

It is evident that the action of $U_{j,\xi,\theta,\zeta}$ depends on the site that can be identified by j and τ . According to this, we define the state as a composition given by, $|j\rangle$ to,

$$|a_j\rangle \equiv |a\rangle \otimes |j\rangle, \quad \text{and} \quad |b_j\rangle \equiv |b\rangle \otimes |j\rangle, \quad (4.10)$$

such that the operation of the node is split into two parts; a part which only decides the direction of movement denoted, \mathbf{C} , and a part which does the movement, \mathbf{S}_τ . The *up* state $|\uparrow\rangle$ denotes the upward motion, while the *down* state, $|\downarrow\rangle$, denotes the downward motion. In addition, $\{|\uparrow\rangle, |\downarrow\rangle\} \in \text{SU}(2)$. The operator is then expressed as a product of $\mathbf{C} \otimes \mathbb{1}$ and \mathbf{S}_τ as,

$$U_{j,\xi,\theta,\zeta} = \mathbf{C} \otimes \mathbb{1} \cdot \mathbf{S}_\tau \quad (4.11)$$

where in the language of quantum walk the *shifting* operator, \mathbf{S}_τ , defined as,

$$\mathbf{S}_\tau = \sum_{j=1}^{\tau} |a_{j+1}\rangle\langle a_j| + |b_{j-1}\rangle\langle b_j| = \sum_{j=1}^{\tau} |a\rangle\langle a| \otimes |j+1\rangle\langle j| + |b\rangle\langle b| \otimes |j-1\rangle\langle j|, \quad (4.12)$$

is conditioned on the outcome of the *coin* operator, \mathbf{C} , defined such that

$$\begin{aligned} \mathbf{C} \otimes \mathbb{1} &= \sum_{j=1}^{\tau} |a_j\rangle \left(e^{i\xi} \cos \theta \langle a_j| - e^{i\zeta} \sin \theta \langle b_j| \right) + |b_j\rangle \left(e^{-i\zeta} \sin \theta \langle a_j| + e^{-i\xi} \cos \theta \langle b_j| \right), \quad (4.13) \\ &= \left[|a\rangle \left(e^{i\xi} \cos \theta \langle a| - e^{i\zeta} \sin \theta \langle b| \right) + |b\rangle \left(e^{-i\zeta} \sin \theta \langle a| + e^{-i\xi} \cos \theta \langle b| \right) \right] \sum_j |j\rangle\langle j|, \end{aligned}$$

with,

$$\mathbf{C} = \begin{pmatrix} e^{i\xi} \cos \theta & -e^{i\zeta} \sin \theta \\ e^{-i\zeta} \sin \theta & e^{-i\xi} \cos \theta \end{pmatrix}, \quad \mathbb{1} = \sum_j |j\rangle\langle j|. \quad (4.14)$$

$|j-1\rangle\langle j|$ and $|j+1\rangle\langle j|$ stand for the operators which are responsible for movement in the lower and upper positions of the lattice, respectively. The subscript j is dropped from the coin operator because it is independent of the location. In this parametrization, ξ and ζ are the phases of the transmitted and reflected beams, respectively, and $\theta/2$ is the rotation for a single node. In addition, θ determines the relative intensities of the reflected and transmitted beams from a single node.

Consider a normalized input state,

$$|\Psi_0\rangle = \alpha|\Psi_0^T\rangle + \beta|\Psi_0^R\rangle, \quad (4.15)$$

spanning multiple nodes, where the upward propagating $|\Psi_0^T\rangle$ and the downward propagating $|\Psi_0^R\rangle$ components are given by,

$$|\Psi_0^T\rangle = \sum_j \alpha_j |a_j\rangle, \quad |\Psi_0^R\rangle = \sum_j \beta_j |b_j\rangle. \quad (4.16)$$

From the normalization condition of $|\Psi_0\rangle$, $|\alpha|^2 + |\beta|^2 = 1$, we get

$$\sum_j |\alpha_j|^2 + \sum_j |\beta_j|^2 = 1. \quad (4.17)$$

The action of all the scattering nodes of a single vertical plane with M layers is given by,

$$\mathcal{U}_M |\Psi_0^T\rangle = \sum_{j \in T} \alpha_j \left(t_a |a_{j+1}\rangle + r_a |b_{j-1}\rangle \right) \quad (4.18)$$

$$\mathcal{U}_M |\Psi_0^R\rangle = \sum_{j \in R} \beta_j \left(r_b |a_{j+1}\rangle - t_b |b_{j-1}\rangle \right), \quad (4.19)$$

where, $\mathcal{U}_M = \sum_j U_j \in \mathbb{C}^{2M}$, so that the (unnormalized) transmitted and reflected beams are given by,

$$|\Psi_1\rangle = |\Psi_1^T\rangle + |\Psi_1^R\rangle \quad (4.20)$$

$$|\Psi_1^T\rangle = t_a \left(\sum_{j \in T} \alpha_j |a_{j+1}\rangle \right) + r_b \left(\sum_{j \in R} \beta_j |a_{j+1}\rangle \right), \quad (4.21)$$

$$|\Psi_1^R\rangle = r_a \left(\sum_{j \in T} \alpha_j |b_{j-1}\rangle \right) - t_b \left(\sum_{j \in R} \beta_j |b_{j-1}\rangle \right). \quad (4.22)$$

These states are then the input to the next plane. The appropriate normalization factor for the transmitted and reflected beams will depend on the reflection and transmission coefficients, and the resulting interference. Using these equations when the process is repeated until the last plane at the exit surface, the effective unitary, $\mathcal{U}(N)$, of a single blade at any time $\tau = M$, gives the state,

$$|\Psi_M\rangle = \mathcal{U}_M |\Psi_{M-1}\rangle = \prod_{k=1}^M \mathcal{U}_M |\Psi_0\rangle = \prod_{k=1}^M \sum_{j=1}^k U_j |\Psi_0\rangle, \quad (4.23)$$

In general, after propagating through a crystal segmented into N planes, the wavefunction is,

$$|\Psi_N\rangle = \mathcal{U}(N)|\Psi_0\rangle = |\Psi_N^T\rangle + |\Psi_N^R\rangle, \quad (4.24)$$

$$|\Psi_N^T\rangle = \sum_{j \in T} \alpha_j |a_j\rangle, \quad (4.25)$$

$$|\Psi_N^R\rangle = \sum_{j \in R} \beta_j |b_j\rangle, \quad (4.26)$$

where the expansion coefficients are given by,

$$\alpha_j = \langle a_j | \mathcal{U}(N) | \Psi_0 \rangle, \quad \text{and} \quad \beta_j = \langle b_j | \mathcal{U}(N) | \Psi_0 \rangle. \quad (4.27)$$

Using these equations, the effective unitary of a single blade $\mathcal{U}(N)$ based on the QI model may be represented by,

$$\mathcal{U}(N) = \prod_{\tau=1}^N \mathcal{U}_\tau = \prod_{\tau=1}^N \sum_{j=1}^{\tau} U_j. \quad (4.28)$$

If $|\psi_k\rangle$, $k = r, t$ is the two-level macroscopic orthonormal subspace for the presentation, the 2×2 form of the operator, $\mathcal{U}(N)$, may be represented as $\mathcal{U}(N) = \left(\mathcal{U}_{kk'} \right)$ where, $\mathcal{U}_{kk'} = \langle \psi_k | \mathcal{U}(N) | \psi_{k'} \rangle$. Relating to the above, for a crystal, a reasonable value of $N \sim 2D/\Delta_H$.

4.2.2 Example: 50:50 beam splitter

Here we apply the formalism to a particular case where each node acts as a 50:50 beam splitter. Consider the values of the parameters $\xi = 0$, $\theta = \pi/2$, and $\zeta = 0$, which sets the unitary U_j to the Hadamard matrix,

$$U_j = \frac{1}{\sqrt{2}} |a_{j+1}\rangle (\langle a_j | + \langle b_j |) + \frac{1}{\sqrt{2}} |b_{j-1}\rangle (\langle a_j | - \langle b_j |). \quad (4.29)$$

For an input state at not j on the entrance surface,

$$|\Psi_0\rangle = |\psi_j\rangle = \alpha_0 |a_j\rangle + \beta_0 |b_j\rangle, \quad (4.30)$$

the output from the single node is,

$$|\Psi_1\rangle = U_j|\psi_j\rangle = \left(\frac{\alpha_0 + \beta_0}{\sqrt{2}}\right)|a_{j+1}\rangle + \left(\frac{\alpha_0 - \beta_0}{\sqrt{2}}\right)|b_{j-1}\rangle. \quad (4.31)$$

Let's make a restriction to the case of a single input ray with $|\psi_j\rangle = |a_j\rangle$, that is $\beta_0 = 0$ and $\alpha_0 = 1$, so that

$$|\Psi_1\rangle = \frac{1}{\sqrt{2}}(|a_{j+1}\rangle + |b_{j-1}\rangle). \quad (4.32)$$

At the second vertical plane, the transmitted state, $|a_{j+1}\rangle$, becomes an input to a node with unitary U_{j+1} , and the reflected state, $|b_{j-1}\rangle$, becomes an input to a node with unitary U_{j-1} , such that,

$$U_{j+1}|a_{j+1}\rangle = \frac{1}{\sqrt{2}}(|a_{j+2}\rangle + |b_j\rangle), \quad U_{j-1}|b_{j-1}\rangle = \frac{1}{\sqrt{2}}(|a_j\rangle - |b_{j-2}\rangle), \quad (4.33)$$

leading to the state,

$$|\Psi_2\rangle = U_{j+1}U_{j-1}|\Psi_1\rangle = U_{j+1}U_{j-1}U_j|\Psi_0\rangle = \frac{1}{\sqrt{2}}(|\Psi_2^T\rangle + |\Psi_2^R\rangle), \quad (4.34)$$

where the transmitted beam, $|\Psi_2^T\rangle$, and reflected beam, $|\Psi_2^R\rangle$, each consists of two rays,

$$|\Psi_2^T\rangle = \frac{1}{\sqrt{2}}(|a_{j+2}\rangle + |a_j\rangle), \quad |\Psi_2^R\rangle = \frac{1}{\sqrt{2}}(|b_j\rangle - |b_{j-2}\rangle). \quad (4.35)$$

Appending an additional plane to make the three-plane case leads to three rays in each of the transmitted and reflected beams,

$$|\Psi_3\rangle = \sqrt{\frac{2}{3}}|\Psi_3^T\rangle + \frac{1}{\sqrt{3}}|\Psi_3^R\rangle \quad (4.36)$$

$$|\Psi_3^T\rangle = \frac{1}{\sqrt{6}}(|a_{j+3}\rangle + 2|a_{j+1}\rangle - |a_{j-1}\rangle) \quad (4.37)$$

$$|\Psi_3^R\rangle = \frac{1}{\sqrt{2}}(|b_{j+1}\rangle + |b_{j-3}\rangle). \quad (4.38)$$

Due to constructive and destructive interference of the state $|a_{j+1}\rangle$ and $|b_{j-1}\rangle$, two-third of the intensity is in the transmitted beam, and one-third in the reflected beam. Adding a

fourth plane gives,

$$|\Psi_4\rangle = \sqrt{\frac{3}{4}}|\Psi_4^T\rangle + \frac{1}{2}|\Psi_4^R\rangle, \quad (4.39)$$

$$|\Psi_4^T\rangle = \frac{1}{2\sqrt{3}}\left(|a_{j+4}\rangle + 3|a_{j+2}\rangle - |a_j\rangle + |a_{j-1}\rangle\right), \quad (4.40)$$

$$|\Psi_4^R\rangle = \frac{1}{2}\left(|b_{j+2}\rangle + |b_j\rangle - |b_{j-2}\rangle - |b_{j-4}\rangle\right). \quad (4.41)$$

With four planes and a 50:50 beam splitter we notice that the beam at the exit spreads unevenly due to interference.

In general, after propagating through a media with N vertical planes the transmitted and reflected components of the wavefunction are,

$$|\Psi_N^T\rangle = \sum_{j \in T} \alpha_j |a_j\rangle, \quad |\Psi_N^R\rangle = \sum_{j \in R} \beta_j |b_j\rangle, \quad (4.42)$$

where, in general, the probability amplitudes $\alpha_j \neq \beta_j$.

It is possible to use this QI model to extract information about parameters in DD experiments. This is captured by Eqs. (4.2) and (4.3) with functional dependence on ξ, ζ , and θ . Various applications of DD and choices of these parameters are considered in the next section.

The QI model can be used to derive results consistent with DD, examples include:

- Wavefield in the Borrmann triangle
- Integrated intensities after diffraction
- Pendellösung oscillations.

These are further discussed in Sec. 4.3. In addition, this approach provides a simple phenomenological way to study various types of noise processes considered in QI theory (such as dephasing), that may occur during a diffraction process due to variations in the parameters of individual scattering nodes when averaged across many particles. It is also simple to generalize this approach to predict the behaviour of multi-blade devices, such as neutron interferometers, which are discussed in Sec. 4.4.

4.3 Applications

In this section the QI model is applied to a few well-known phenomena in DD. Throughout this section, the state of the neutron at the input (node at $j = 0$) is,

$$|\Psi_0\rangle = |a_0\rangle,$$

which is a single ray propagating upwards. This scenario is depicted in Fig. 4.1.

4.3.1 Intensity profile of the Borrmann triangle

The first application considered is a simulation of the position dependent intensity profile for a single crystal. The spreading of the beam profiles caused by the crystal thickness is known as the *Borrmann fan*. The triangle formed by the outer edges of the transmitted beam, reflected beam, and the input point of a single ray is called the *Borrmann triangle*. In the QI model, it is given by the region ABC in Fig. 4.1. AB is along the transmitted wave direction and AC is along the reflected wave direction. As expected, the intensity profile of the transmitted and reflected beams exiting the crystal depends on both the number of planes considered in the model, and the transmission and reflection coefficients t_a, t_b, r_a , and r_b for a single node. The intensity spreading in the Borrmann triangle has been observed experimentally by scanning a slit, several microns wide, across the output surface of the crystal [43]. To study this in the QI model, the intensities at the output of the crystal are simulated for various values of θ . The transmitted and reflected probabilities at the output node j are given by,

$$\begin{aligned} p_j^T &= |\langle a_j | \mathcal{U}(N) | a_0 \rangle|^2, \\ p_j^R &= |\langle b_j | \mathcal{U}(N) | a_0 \rangle|^2. \end{aligned} \tag{4.43}$$

Figure 4.2 shows the reflected and transmitted intensity distributions of the exiting beam across the crystal surface for $N = 150$ and $\theta = \pi/8, \pi/4, \pi/3$, and $2\pi/5$. From the figure, it can be seen that the reflected beam has a symmetric profile with two intensity peaks at the edges of the Borrmann triangle. On the other hand, the transmitted beam is asymmetric, with the beam concentrated on one side of the Borrmann triangle. In addition, as $\theta \rightarrow \pi$,

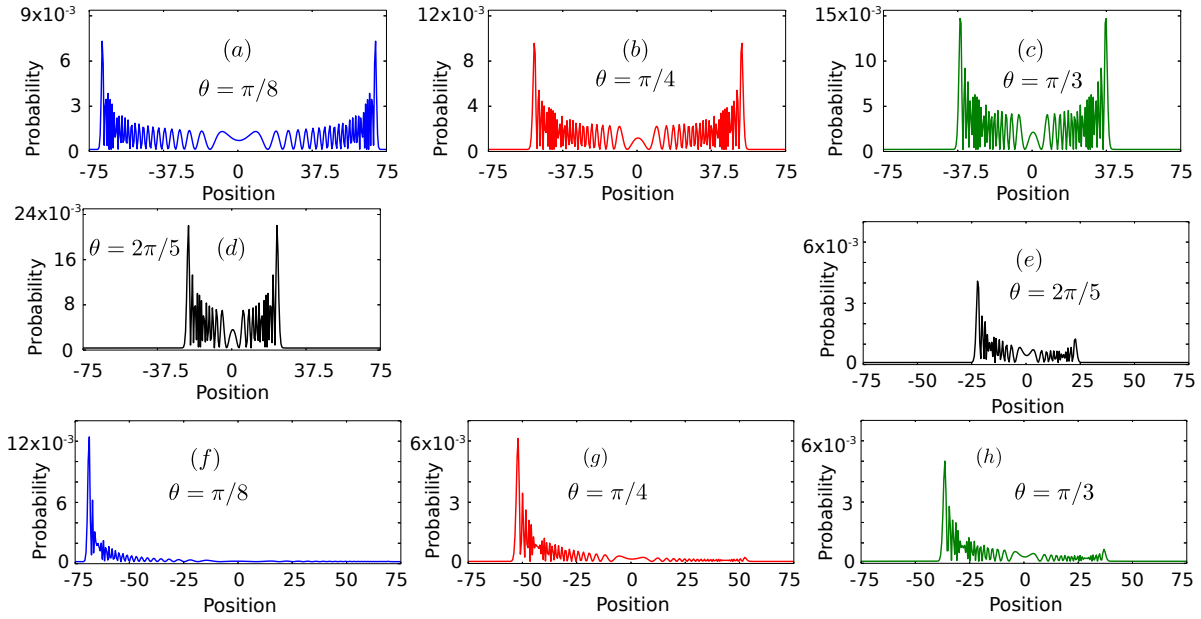


Figure 4.2: Simulated intensity profiles for the reflected beam (a)-(d) and transmitted beam (e)-(f) for a thick crystal modelled by $N = 150$ scattering planes, and for transmission and reflection coefficients $t = \cos \theta$, and $r = \sin \theta$, for values of $\theta = \pi/8, \pi/4, \pi/3$, and $2\pi/5$. The reflected intensities are symmetric with two peaks at the edges, while the transmitted intensities are asymmetric with a single peak at the outside. As $|t|$ approaches 1 the widths of both beams are compressed.

the width of the beam is reduced, leading to a profile with the intensity concentrated in the center of the Borrmann triangle. The data presented in Fig. 4.2, obtained with only a modest number of planes, are in good agreement with those obtained by the standard theory of DD and those observed experimentally.

4.3.2 Integrated intensities and Pendellösung oscillations

In the second application, the QI model is used to derive the integrated intensities of the output beam. The integrated intensities are obtained by summing over all the transmitted and reflected probabilities in the Borrmann triangle. For a wavefunction undergoing evolu-

tion under $\mathcal{U}(N)$, the relative integrated transmitted intensity and the relative integrated reflected intensity allows us to define the integrated transmission, I_T , and reflection, I_R , coefficients as,

$$I_T = \sum_j |\langle a_j | \mathcal{U}(N) | a_0 \rangle|^2, \quad (4.44)$$

$$I_R = \sum_j |\langle b_j | \mathcal{U}(N) | a_0 \rangle|^2. \quad (4.45)$$

The integrated transmission and reflection coefficients are known to undergo oscillations which are out of phase with each other, called *Pendellösung oscillations*. The phase difference is a result of the reflected beam undergoing an odd number of reflections and the transmitted beam undergoing an even number of reflections. When controlled, this periodic oscillation forms the basis for a single crystal NI. The integrated reflectivity was repeatedly observed in experiments where either the crystal thickness was varied [42, 70], or the neutron energy was varied [43].

In Fig. 4.3, the sum intensity is plotted against the N , for $\theta = \pi/16, \pi/8, \pi/4$, and $60\pi/111$. Figure 4.3e, is a magnified version of the reflected intensity shown in Fig. 4.3c. In addition, Fig. 4.3f, is the experimental observed integrated reflectivity of Bragg scattering in the Laue geometry (see Fig. 1 of ref. [42]. Copyright permission from Elsevier). In the special case of a 50:50 splitting, the normalized, integrated transmitted and reflected intensities converge to 0.65 and 0.35, respectively. In the limiting case $\theta \rightarrow \pi/2$, both the integrated reflected and transmitted intensities approach 1/2, as shown in a). There is a significant agreement between the results from experiments and the QI model.

In DD, the probability current inside the crystal propagates in two components. One centred on the atomic planes position and the other at the inter-planar position. As the wave propagates through the crystal, these currents constantly exchange energy with one another in a way that the total current is conserved. The energy exchange occurs in an oscillating manner, and is referred to as Pendellösung oscillation. In the standard theory of DD, Pendellösung oscillations are best represented by plotting the reflected or transmitted intensity as a function of the deviation from the Bragg condition (the parameter η is described in chapter 3).

In the simulation of the Pendellösung oscillations using the QI model, the output intensity is post-selected on a specific node, and the angle θ is varied to mimic the energy

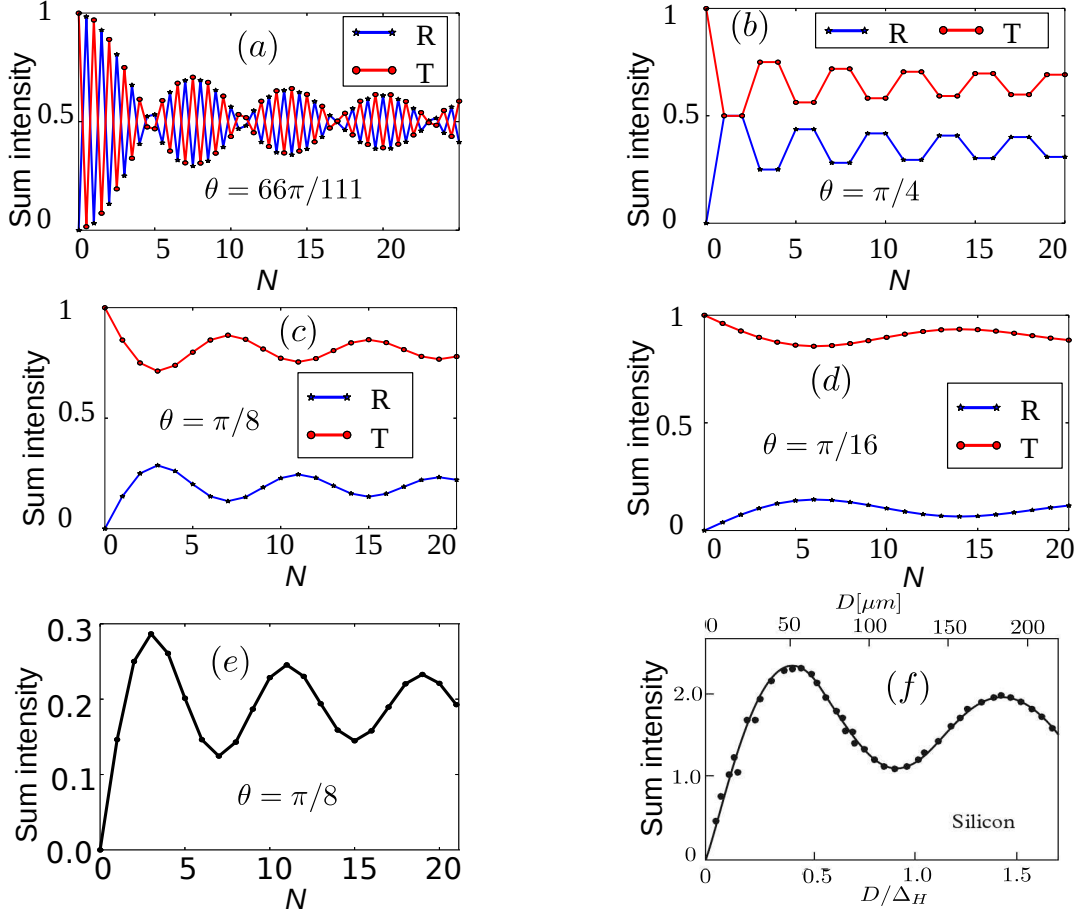


Figure 4.3: Transmitted and reflected intensities at the exit of a single coarse-grained crystal. Plots obtained with the QI model using node unitary operators $U_{0,0,\theta}$, for $\theta = \pi/16, \theta = \pi/8, \theta = \pi/4$, and $\theta = 60\pi/111$ are shown in (a), (b), (c) and (d), respectively. In (e) is a magnified version of the integrated reflectivity plot shown in (a). In (f) the measured integrated reflectivity of Bragg scattering in the Laue geometry Fig. 1 of ref. [42]. Copyright permission from Elsevier.

variation, while the number of planes N is fixed. This is illustrated on the left plot of Fig. 4.4 for $N = 50$, the unitary, $U_{j,0,0,\theta}$, and $\theta \in [0, \pi]$. In the simulations, the probability is post selected on node $j = 25$. In Fig. 4.4a is, the transmitted probability, Fig. 4.4b is the reflected probability and then their sum is plotted in Fig. 4.4c. Lastly, Fig. 4.4d is a

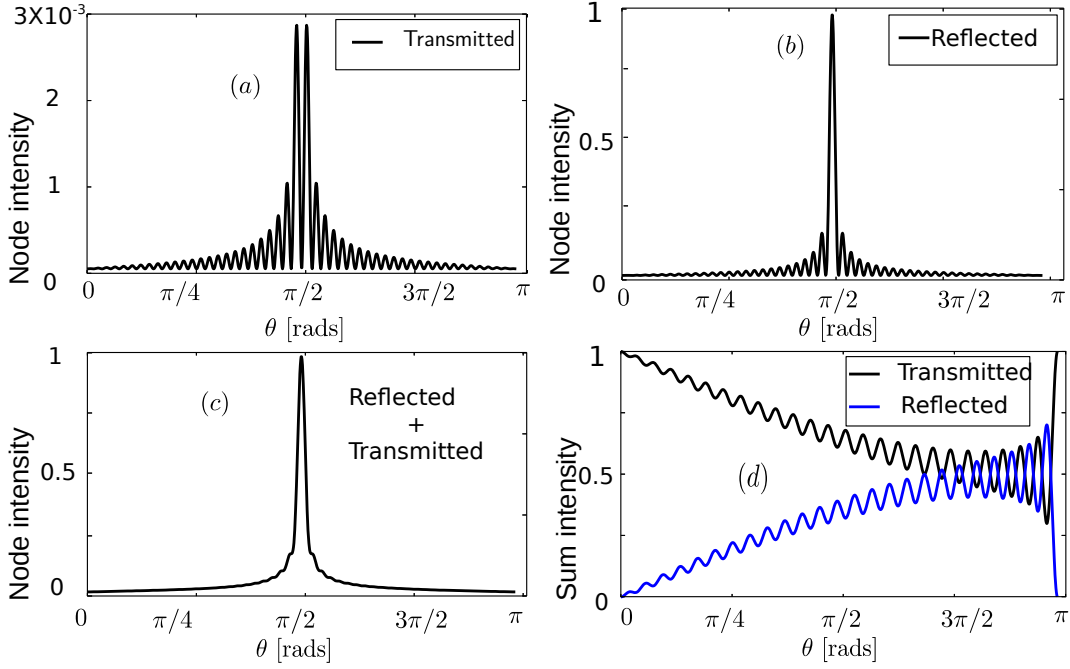


Figure 4.4: Plot of our simulated Pendellösung oscillation at the exit of the Borrmann fan. At node $j = 25$, and a blade with $N = 50$, a) and b) are the transmitted and reflected intensities, respectively, and c), is the sum each plotted against θ . The intensity conforms to the same effect derived from conventional dynamical diffraction theory. In d) the sum intensity, with the parameter θ , of the unitary U is shown. As $\theta \rightarrow \pi$, both the reflected and transmitted intensities approach $1/2$.

plot of the integrated intensity plotted against θ . These plots are consistent with the plots of the Pendellösung oscillations obtained from the standard DD theory. It can be noted that as $\theta \rightarrow \pi/2$, the integrated reflected and transmitted intensities both approach $1/2$.

4.4 Extension to a neutron interferometer

Here, the QI model of a single perfect crystal blade is extended to a three-blade perfect crystal NI. For a concise application of the standard theory of DD to a neutron interfer-

ometer, see refs. [81, 3]. The interferometer blades are of equal thickness. The first blade of the NI is identical to our single blade treatment and splits the neutron into the reflected and transmitted beams. The second NI blade splits the reflected and transmitted beams of the first blade each into two other transmitted and reflected beams so that a total of four beams emerge after the second blade. Only two of these make it to the last blade due to the geometry of the NI.

4.4.1 Beam profiles

The neutron beam profiles produced by the QI model for each of the eight beams in the three-blade NI are presented in Fig. 4.5. For the simulation the unitary operator at each node is $U_{j,0,0,\pi/4}$, and a coarse graining of $N = 100$ and $N = 1000$ is considered. If each blade of a three-blade neutron interferometer contains N -planes, then the output on the third blade has $3N$ -nodes, and hence the beam size increases at each blade. Note however, that the plotted profiles in the figure are normalized in width. By a normalized we mean that the horizontal axis is scaled so that the beams at each blade have the same size (this is just for convenience since the beam after the 3rd blade is three times the size of the beam after the first blade). We find that the simulations are in agreement with the profiles generated by the application of the standard theory of DD to an NI.

4.4.2 Output intensities

The QI model is applied to simulate the output integrated intensities of a three-blade NI. Consider projectors onto the O-beam, and the O-beam given by,

$$P_O = \sum_j |a_j\rangle\langle a_j|, \quad \text{and} \quad P_H = \sum_j |b_j\rangle\langle b_j|. \quad (4.46)$$

The unitary operator for the phase difference between the two macroscopic paths is,

$$U_z(\chi) = \exp \left[i\chi \sum_j (|a_j\rangle\langle a_j| - |b_j\rangle\langle b_j|)/2 \right]. \quad (4.47)$$

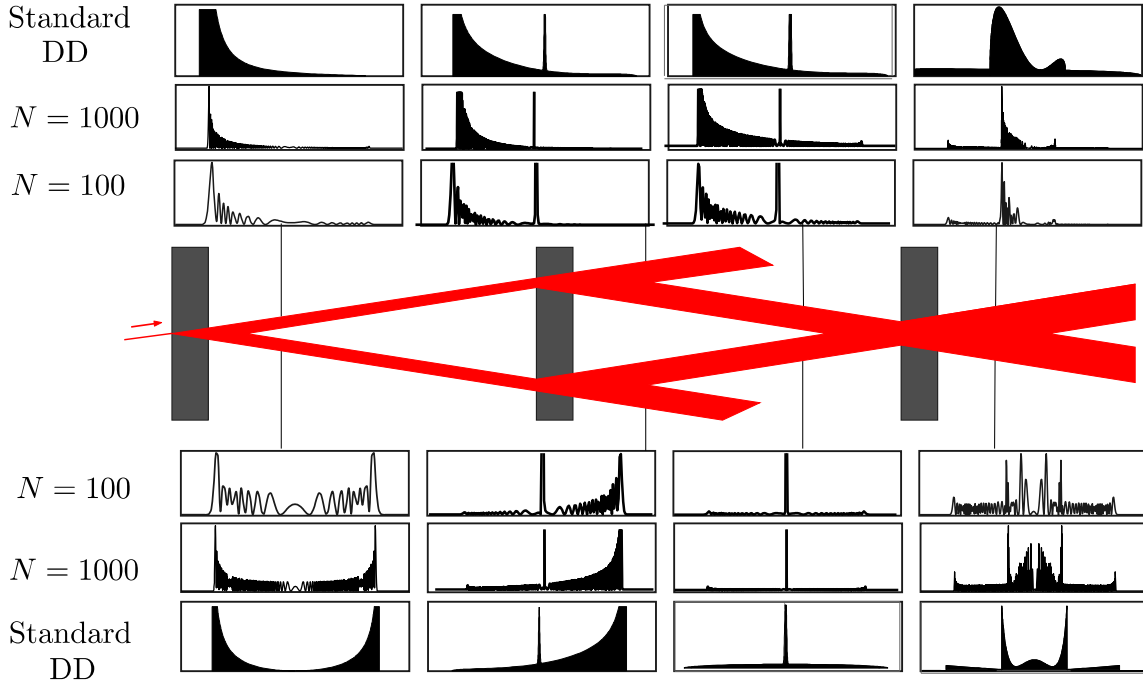


Figure 4.5: The various intensity profiles for a three-blade NI. The inteferometer geometry and the beam trajectories are shown in the middle. The two inner rows correspond to our simulated profiles with $N = 100$. The next two outer rows correspond to to our simulated profiles with $N = 1000$. And for comparison, in the two outermost rows, the intensity profiles obtained by standard theory of dynamical diffraction.

The rays along the each direction picks the same phase χ . Using the earlier notation where the operator of the first blade and last blade is U_B and the middle blade is U_M , the wavefunction at the output is,

$$|\Psi\rangle = U_B U_M U_z(\chi) U_B |\Psi_0\rangle. \quad (4.48)$$

Because no renormalization is performed yet, the operator of the middle blade is not a unitary. Explicitly, it can be represented by,

$$U_M = \sum_{ij} \left(\langle a_i | U_B | b_j \rangle | a_i \rangle \langle b_j | + \langle b_j | U_B | a_i \rangle | b_j \rangle \langle a_i | \right). \quad (4.49)$$

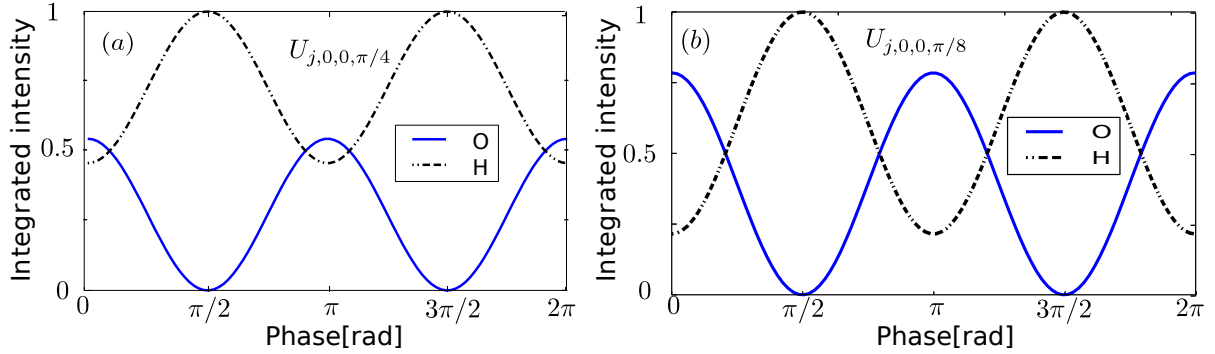


Figure 4.6: The intensity of the O-beam and H-beam against the phase difference χ between the two NI paths. $N = 100$. In (a) the node unitary operator is $U_{j,0,0,\pi/4}$ and in (b) it is $U_{j,0,0,\pi/8}$.

Upon projection, the O and H components of the wavefunction at the output can be written as,

$$|\Psi^O\rangle = \sum_j \psi_{j,\bar{r}rt} (e^{-i\chi/2} + e^{i\chi/2}) |a_j\rangle, \quad (4.50)$$

$$|\Psi^H\rangle = \sum_j (e^{-i\chi/2}\psi_{j,\bar{t}rt} + e^{i\chi/2}\psi_{j,r\bar{r}r}) |b_j\rangle. \quad (4.51)$$

with the probability amplitudes $\psi_{j,\bar{r}rt} = \langle a_j | U_B P_H U_M P_O U_B | \Psi_0 \rangle$, and $\psi_{j,\bar{t}rt}$ and $\psi_{j,r\bar{r}r}$ are similarly obtained. We note that the output based on the QI model can be compared to that of the standard DD in Eq. (1.43).

The sum intensity for O and H beams as a function of the phase difference between the paths is given by,

$$I_O = \mathcal{A}(1 + \cos \chi), \quad I_H = \mathcal{B} - \mathcal{A} \cos \chi, \quad (4.52)$$

with the coefficients,

$$\mathcal{A} = 2 \sum_j |\psi_{j,\bar{r}rt}|^2, \quad \text{and} \quad \mathcal{B} = \sum_j (|\psi_{j,\bar{t}rt}|^2 + |\psi_{j,r\bar{r}r}|^2). \quad (4.53)$$

The intensities at the output of the NI for the O and H beams are presented in Fig. 4.6 for $N = 100$ planes in each blade and the unitary $U_{j,0,0,\pi/4}$ at each node (note that $\theta = \pi/4$

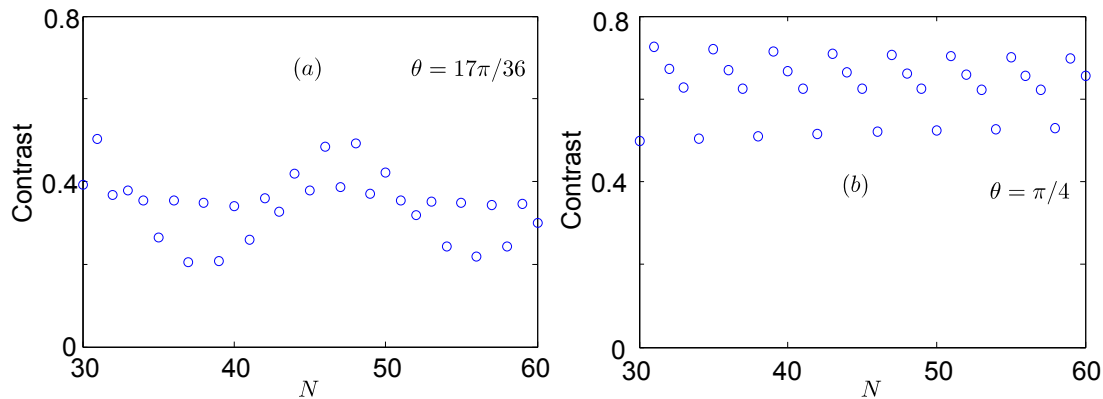


Figure 4.7: The contrast of the H-beam for a three-blade NI as a function of the number of planes in each blade N . In (a), the unitary operator for each node is $U_{j,0,0,17\pi/36}$, and in (b), the unitary operator is $U_{j,0,0,\pi/4}$.

corresponds to $t_a = r_a = 1/\sqrt{2}$. It is shown that the intensities of the output beams oscillate in a sinusoidal fashion and it can be seen that the intensity of the O -beam has a minimum at zero. The well known asymmetry known from interferometry can be seen on the H-beam, where the intensity never goes to zero.

4.4.3 Contrast

Under ideal conditions, the contrast of the H-beam using Eq. (4.52) is modulated by a function of the blade properties as it is not balanced. We therefore get $\mathcal{V}_H = \mathcal{A}/\mathcal{B}$, although the contrast of the O -beam is always 1. In experiments, the contrast is always below 1 due to various reasons such as NI impurities, blade imperfections, external vibrations, and thermal gradients. Figure 4.7 shows the contrast as a function of the number of planes obtained using the QI model where $\theta = 17\pi/36$. In the QI model, to obtain the contrast for a fixed number of planes, the phase difference between the two interferometer paths is varied over a full cycle and the maximum and minimum values are extracted. The standard theory of DD predicts that the contrast on the H-beam of a three-blade NI converges to 0.39 with the thickness of the blade [3]. With the QI model, if θ is increased, the contrast on the H-beam is reduced for a fixed number of planes. The 0.39 contrast obtained in the

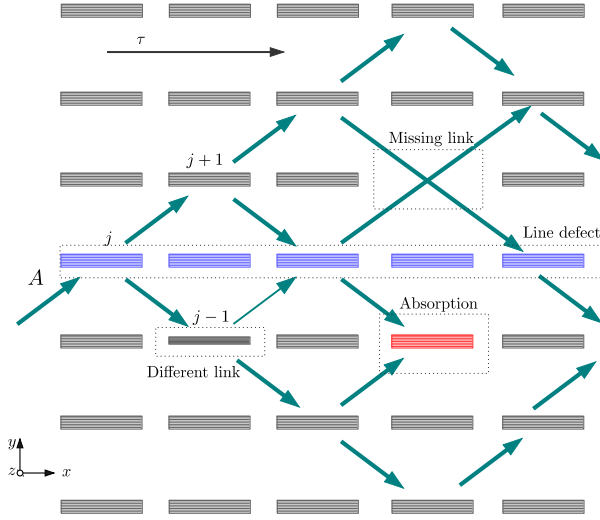


Figure 4.8: Depiction of various defects can be studied with the QI model of DD.

standard theory of DD could be reproduced in the QI model by using a suitable choice of θ that is close to $\pi/2$, corresponding to $t \rightarrow 0, r \rightarrow 1$. In this limit, the contrast converges to value approximately equal to that predicted by the standard theory of DD.

4.5 Further work and conclusion

In the future, the QI model will be applied to investigate decoherence during DD. Some specific cases are when the unitary U_j is different for various nodes, for example a missing link, a deformation in the periodic lattice, absorption, or isotopic concentration as illustrated on Fig. 4.8.

We have developed a QI model for DD and applied it to reproduce DD features such as the intensities in the Borrmann triangle and Pendellösung oscillation.

Chapter 5

Noise-Refocusing Five-blade Neutron Interferometer

5.1 Introduction

Perfect crystal neutron interferometry provides a powerful methodology for probing, with remarkable accuracy, the scattering coherence length of various samples [2, 3, 82]. However, as the neutron travels through the interferometer, it may couple to mechanical vibrations and pick up an undesired phase. The effect of mechanical vibrational noise is very drastic in the three-blade perfect crystal NI. As a measure to remove mechanical noise, isolation and control techniques have been developed by building vibration isolation systems that deal with low-frequency mechanical vibrational noise [5, 7, 83].

Of recent, the quest for noise-free neutron interferometry has motivated the design of the four-blade NI with a DFS [6, 84]. The information encoded in this DFS is free from low-frequency mechanical vibrational noise. In spite of its robustness to mechanical vibrational noise, we will show, in this chapter, that the four-blade NI is prone to the DD phase noise. DD phases result from variations in a blade's transmission amplitude (see Eq. 3.22). This can be caused by the finite angular and wavelength spreads resulting from the collimation and monochromation of the incident beam. For more details on DD phases

and some applications see ref. [62, 48]. It is therefore important that all NI geometries have the ability to refocus DD phases. We will also show that despite being affected by mechanical vibrational noise, the three-blade NI is capable of refocusing the DD noise. In order to eliminate the dynamical and mechanical noise, we propose a five-blade NI that is capable of refocusing low-frequency mechanical vibrational noise and DD noise.

This chapter is structured as follows: In Sec. 5.2, we present a brief overview of the the origin of the DD phase. It also include an analysis of the effect of the dynamical phase on the three-blade, four-blade and five-blade NIs. Next, Sec 5.3 is an analysis of the effects of a low-frequency external mechanical vibrational noise on the three interferometric geometries in terms of the coherence function [3, 18, 85, 86]. Lastly, in Sec. 5.4 is the conclusion and a highlight of future work with the proposed five-blade NI.

5.2 Dynamical phase

5.2.1 Interferometer geometries

The NI geometries considered are shown in Fig. 5.1. The analysis is carried out using the novel QI model of DD which is based on unitary evolution [11]. In each of the geometries considered in this section, the path degree of freedom (DOF) is a two-level system, which is defined by the momentum along the x -axis such that state $|I\rangle$ labels $k_x > 0$, and the state $|II\rangle$ labels $k_x < 0$.

The three-blade NI (see Fig. 5.1a) consists of three identical blades separated by the same distance L , with the second blade acting as a mirror to redirect the two paths to the third blade where they recombine and interfere. In the four-blade DFS NI (Fig. 5.1b), the situation is similar to the three-blade NI, with the difference that the two paths are redirected twice (with no mixing of states in the center of the interferometer) before reaching the last blade. The five-blade NI (Fig. 5.1c) can be thought of as two coupled three-blade NIs or a four-blade NI with the neutrons allowed to interfere on the additional blade in the middle. In all the interferometers considered, we ignore the neutrons that escape through the lossy mirror crystal by post-selecting on the neutrons that arrive at the detectors.

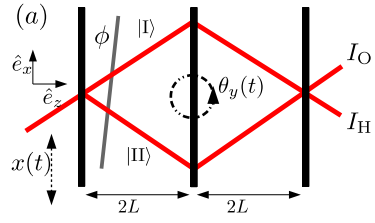
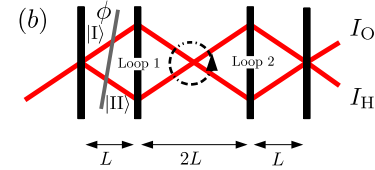
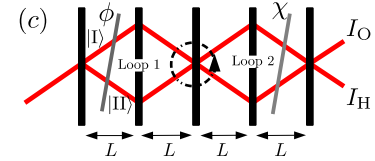
Geometry	$I_{\text{out}}/I_{\text{inc}}$	\mathcal{V}_{MV} ($\omega = 4.4$ Hz)	\mathcal{V}_{DD}
(a) 	0.5	0	1
(b) 	0.25	1	0.85
(c) 	0.25	0.83	1

Figure 5.1: Sketch of different 50:50 splitting NI geometries with phase flags producing phases ϕ and χ . The two detectors are O-detector (I_{O}) and H-detector (I_{H}). a) A symmetric three blade NI with phase flag ϕ and inter-blade distance $2L$. b) Four blade (DFS) NI with inter-blade distances: $L, 2L, L$. c) Five blade (double MZ loop) NI with blade separation L . The noise along the x-axis is $x(t)$, and along around the y-axis is $\theta_y(t)$. $I_{\text{out}}/I_{\text{inc}}$ is the ratio of the neutrons at the output $I_{\text{out}} = I_{\text{O}} + I_{\text{H}}$ to those at incidence I_{inc} . \mathcal{V}_{MV} and \mathcal{V}_{DD} are the fringe visibility with Z-noise ($\omega = 4.4$ Hz) and dynamical phase noise simulated for the DFS interferometer dimensions of [6], respectively.

Hence a simple renormalization, we treat the second blade as a perfect mirror.

5.2.2 Single blade unitary operator

Consider a schematic of DD from a single blade shown in Fig. 5.2 where two rays are incident; one at the Bragg angle θ_B and the other at an angle θ that is slightly off the Bragg angle by δ . The deviation from Bragg parameter is defined uniquely in terms of the

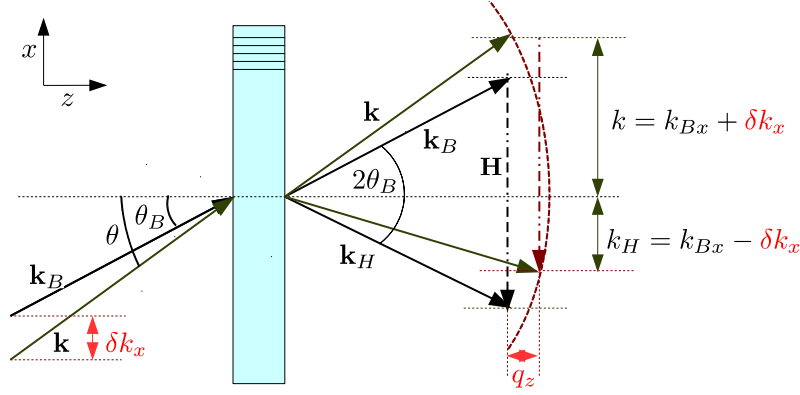


Figure 5.2: Bragg diffraction, in the symmetric Laue geometry showing incident and exit beams at perfect Bragg conditions (black). The corresponding profile for with a misset parameter δk_x is shown in red [68].

wavevector or the angle as,

$$\eta = -\frac{\delta k_x}{\sigma_{k_{Bx}}} = -\frac{k_x - \delta k_{Bx}}{\sigma_{k_{Bx}}} \quad \text{or} \quad \eta \approx -\frac{\delta\theta}{\sigma_D} = -\frac{\theta - \theta_B}{\sigma_D} \quad (5.1)$$

where,

$$\sigma_{k_{Bx}} = \frac{m|v_H|}{\hbar^2 k_{Bx}}, \quad \text{and} \quad \sigma_D = \frac{|v_H|}{E \sin(2\theta_B)} \quad (5.2)$$

are the momentum width and Darwin width of the crystal related by $\sigma_{k_{Bx}} = k_z \sigma_D$. k_x is the wavevector along the x -axis, and $k_{Bx} = H/2 = \pi/d$ is the exact Bragg vector with the crystallographic planes assumed perpendicular to the surface. The conservation of energy and the wavefunction continuity conditions lead to the incident wavevector and transmitted wavevector being identical to \mathbf{k} , while the reflected wavevector changes. The momentum transfer, $\hbar\vec{H}$, along the planes leads to $k_{Hx} = k_x - H$ and $k_{Hz} = \sqrt{k^2 - k_{Hx}^2}$, such that for a wave incident at an angle $\theta_B + \delta\theta$, one get,

$$\begin{aligned} \mathbf{k} &= k \sin(\theta_B + \delta\theta) \hat{e}_x + k \cos(\theta_B + \delta\theta) \hat{e}_z, \\ \mathbf{k}_H &\simeq -k \sin(\theta_B - \delta\theta) \hat{e}_x + k \cos(\theta_B - \delta\theta) \hat{e}_z. \end{aligned} \quad (5.3)$$

The deviation from the Bragg condition parameter changes sign, i.e, for an incident wave at an angle $\theta_B + \delta\theta$, the transmitted wave emerges at an angle $\theta_B + \delta\theta$ and the reflected at

an angle $\theta_B - \delta\theta$. As a result, $\delta\theta$ and δk_x changes sign after every reflection, leading to a corresponding change in the reflection and transmission coefficients (see Fig. 1.9) denoted by $\bar{r} = r(-\eta)$, $\bar{t} = t(-\eta)$, where, $\bar{r} = -r^*$, $\bar{t} = t^*$. DD from a single non-absorbing crystal can be abstracted as a rotation matrix,

$$U_B = \begin{pmatrix} e^{i\xi} \cos(\alpha/2) & ie^{-i\zeta} \sin(\alpha/2) \\ ie^{i\zeta} \sin(\alpha/2) & e^{-i\xi} \cos(\alpha/2) \end{pmatrix}, \quad (5.4)$$

where, $\xi(\eta) = \arg[t]$ and $\zeta(\eta) = \arg[r]$, satisfying the relations $\xi(-\eta) = -\xi(\eta)$ and $\zeta(-\eta) = -\zeta(\eta)$, are the phases of the transmitted and reflected waves, respectively. $\xi(\eta)$ is commonly referred to as the dynamical phase.

Due to symmetry, the Bragg diffraction is required to take the same form if the crystal is rotated by 180° . The consequence is that, the crystal blade operator can be expressed as a composite sequence of rotations

$$U_B = R_z(\xi)R_{xy}(\zeta, \alpha)R_z(\xi) \quad (5.5)$$

with the standard definitions of Bloch sphere rotations $R_z(\xi) = \exp(i\xi\sigma_z/2)$, $R_{xy}(\zeta, \alpha) = \exp(i\alpha(\cos(\zeta)\sigma_x + \sin(\zeta)\sigma_y)/2)$, where the Pauli matrices for the path are expressed as

$$\sigma_x = |I\rangle\langle II| + |II\rangle\langle I|, \quad \sigma_y = -i|I\rangle\langle II| + i|II\rangle\langle I|, \quad \sigma_z = |I\rangle\langle I| - |II\rangle\langle II|. \quad (5.6)$$

By definition, the dynamical phase is ξ , while the phase between the two paths in an interferometer is $\beta = \xi - \zeta$. We may limit the R_{xy} rotation to be along the σ_x , thereby effectively setting $\zeta = 0$. This is justified because $\zeta \ll \xi$ is a small linear contribution. This leads us to hypothesize a composite crystal blade operator [11]

$$U_B = R_z(\beta)R_x(\alpha)R_z(\beta). \quad (5.7)$$

From these relations, one can identify the relation to the dynamical diffraction variables as $\beta = \arg[t]$, $t = \cos(\alpha/2)$, and $r = \sin(\alpha/2)$. $\alpha \in [0, \pi]$ describing the transmission/reflection ratio, while β corresponds to the dynamical phase. When $\alpha = \pi/2$, the blade acts as a 50:50 beam splitter.

5.2.3 Three-blade neutron interferometer

In the composite rotation formalism, the operator of the first and last blades of a three-blade NI is, $U_B = R_z(\beta)R_x(\alpha)R_z(\beta)$. The operator of the middle blade which acts as a mirror to redirect the two paths onto the third blade is given by,

$$U_M = R_z(\beta)R_x(\pi)R_z(\beta) = R_x(\pi) = i\sigma_x. \quad (5.8)$$

With a phase difference ϕ between path I and path II (Fig. 5.1a), the NI operator is

$$\begin{aligned} U_{3\text{BNI}} &= U_B U_M R_z(\phi) U_B, \\ &= R_z(\beta)R_x(\alpha)R_x(\pi)R_z(\phi)R_x(\alpha)R_z(\beta), \end{aligned} \quad (5.9)$$

where, the simplification identity $R_x(\pi) = R_z(\beta)R_x(\pi)R_z(\beta)$ is used. Consider an input state $|I\rangle$ onto a three-blade NI with balanced beam splitters, $\alpha = \pi/2$. If the measurement PVM is $\{|I\rangle\langle I|, |II\rangle\langle II|\}$, we obtain the probabilities of detecting a neutron on the O-detector and H-detector,

$$p_o = \frac{1}{2}(1 + \cos \phi), \quad (5.10)$$

$$p_h = \frac{1}{2}(1 - \cos \phi). \quad (5.11)$$

Because these probabilities are independent of β , taking an average over different neutron instances leads to no loss in the contrast. Therefore, the three-blade NI is immune to the dynamical phase noise. This is also the case when $\alpha \neq \pi/2$.

5.2.4 Four-blade neutron interferometer

In the four-blade NI the operator of the first and fourth blades is $U_B = R_z(\beta)R_x(\alpha)R_z(\beta)$. The second and third blades act as mirrors U_M . With an initial state $|I\rangle$ and a phase difference ϕ between paths I and II (see Fig. 5.1b), the overall operator sequence for the four-blade NI is,

$$\begin{aligned} U_{4\text{BNI}} &= U_B R_x(\pi) R_x(\pi) R_z(\phi) U_B, \\ &= R_z(\beta) R_x(\alpha) R_z(2\beta) R_z(\phi) R_x(\alpha) R_z(\beta), \end{aligned} \quad (5.12)$$

where, the identity $\mathbb{1} = R_x(\pi)_x R(\pi)$ is used. When $\alpha = \pi/2$, the probabilities of detecting a neutron on the O-beam and H-beam are given by,

$$p_o = \frac{1}{2} \left(1 - \cos(\phi + 2\beta) \right), \quad (5.13)$$

$$p_H = \frac{1}{2} \left(1 + \cos(\phi + 2\beta) \right). \quad (5.14)$$

It is clear that the dynamical phase β is not refocused in the four-blade NI. When the detected intensity is averaged over different neutrons each with a different β , dephasing occurs. The dephasing leads to a reduction in the coherence by an amount dependence on the strength of the noise. The average normalized neutron intensities at the detectors is,

$$\overline{I_o(\phi)} = \frac{1}{2} \left(1 - \int d\beta p(\beta) \cos(\phi + 2\beta) \right), \quad (5.15)$$

$$\overline{I_H(\phi)} = \frac{1}{2} \left(1 + \int d\beta p(\beta) \cos(\phi + 2\beta) \right). \quad (5.16)$$

where $p(\beta)$ as the probability distribution. The intensity can be re-written as

$$\overline{I_o(\phi)} = \frac{1}{2} \left(1 - |\gamma| \cos(\phi + \arg \gamma) \right), \quad (5.17)$$

$$\overline{I_H(\phi)} = \frac{1}{2} \left(1 + |\gamma| \cos(\phi + \arg \gamma) \right), \quad (5.18)$$

where, $\gamma = \int d\beta p(\beta) e^{i2\beta}$, quantifies the effect of noise. Generally, when $\alpha \neq \pi/2$ we get,

$$\overline{I_o(\phi)} = \mathcal{B}_o - |\mathcal{A}_H| \cos(\phi + \arg[\mathcal{A}_H]), \quad (5.19)$$

$$\overline{I_H(\phi)} = \mathcal{B}_H + |\mathcal{A}_H| \cos(\phi + \arg[\mathcal{A}_H]), \quad (5.20)$$

where,

$$\mathcal{A}_H = \int p_H e^{i2\beta} \eta, \quad \mathcal{B}_H = \int p_H d\eta, \quad p_H = 2|tr|^2, \quad \mathcal{B}_o = \int (|t|^4 + |r|^4) d\eta.$$

If the four-blade NI is made from 1 mm thick Si blades in the (111) crystallographic orientation, and illuminated with neutrons of $\lambda = 2.71 \text{ \AA}$, the contrast $\gamma = \mathcal{A}_o/\mathcal{B}_H$ is about 80%. The extent to which the DD noise affects the coherence in a four-blade NI is not yet well quantified experimentally.

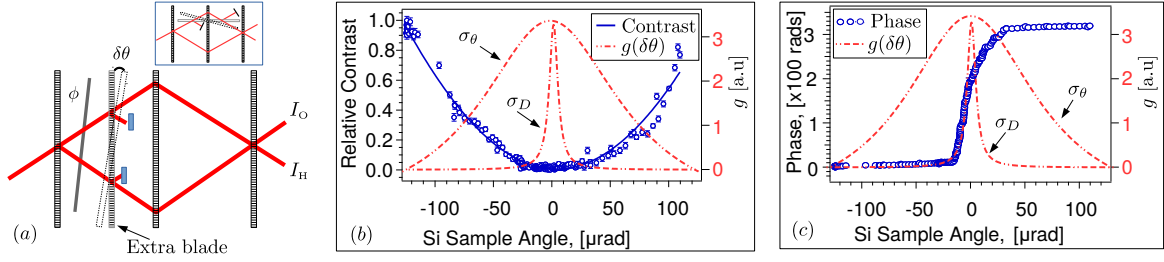


Figure 5.3: A 2 mm thick (111) Si crystal is added after the first blade of a three-blade NI and rotated around the Bragg angle. In (a) an additional blade of the same crystallographic orientation is added to a three-blade NI. An insert of an additional blade in the Bragg geometry is also shown. In (b), is the contrast and momentum distribution $p(\delta\theta)$ plotted against $\delta\theta$, and in (c), is the phase and $g(\delta\theta)$ plotted against $\delta\theta$. The Lorentzian distributions are a simulated one with a full width at half maximum (FWHM) given by Darwin width of the crystal $\sigma_D = 4.26$ μrad , and a fit to a Lorentzian distribution with FWHM of $\sigma_\theta = 69$ [μrad] extracted from the measured data. For more details on the data see the thesis [12, 87].

In a separate experiment, performed at the NCNR, to measure the neutron charge radius it was measured to which extent the contrast is affected by the dynamical phase (For more details see the thesis of M. Huber in ref. [87]) and the article [12]. The schematic of the setup is shown in Fig. 5.3a. In that experiment, a perfect Si crystal blade, of thickness 2 mm and crystallographic orientation [111], was added after the first blade of a three-blade neutron interferometer. When the crystal is aligned to the Bragg angle of the interferometer and the Bragg reflected beams are blocked, it replicates the dynamical phase that manifests itself in a four-blade NI. Using $\alpha = \pi/2$ the normalized output intensity at the O-beam in this case can be expressed as,

$$\overline{I_o(\phi)} = \mathcal{A}_o - |\mathcal{B}_o| \cos(\phi + \arg[\mathcal{B}_o]), \quad (5.21)$$

where as shown in [62],

$$\mathcal{A}_o = \int d\delta\theta g(\delta\theta), \quad \mathcal{B}_o = \int d\delta\theta g(\delta\theta)e^{i\beta}, \quad g(\delta\theta) = \frac{\sigma_\theta/\pi}{\sigma_\theta^2 + (\delta\theta - \delta\theta_0)^2}, \quad (5.22)$$

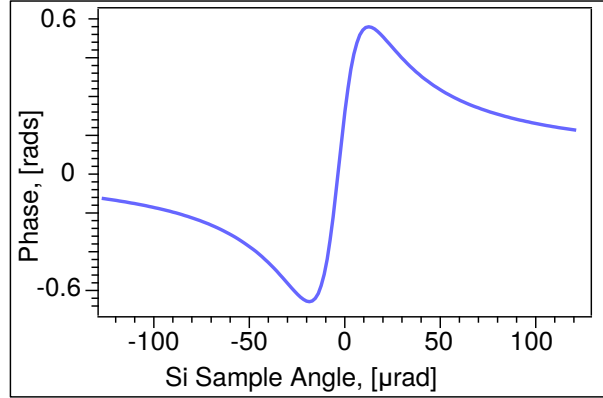


Figure 5.4: The DD phase extracted from the setup in Fig. 5.3, using a Lorentzian distribution FWHM $\sigma_\theta = 69$ [μrad]. This is a valid approach because the defocusing introduced by the crystal has no effect on the momentum distribution.

The average here is taken over $\delta\theta = \theta - \theta_B$ since $\beta = \beta(\delta\theta)$ is a function of the angular deviation, where θ_B is the Bragg angle. The measured contrast and phase against $\delta\theta$ are shown in Fig. 5.3b and Fig. 5.3c, respectively. Also shown is the simulated momentum distribution $g(\delta\theta)$ accepted by a single crystal, where the full width at half maximum (FWHM) is given by Darwin width of the crystal $\sigma_D = 4.26$ μrad . In addition, a fit to a Lorentzian distribution with FWHM of $\sigma_\theta = 69$ [μrad] extracted from the measured data.

The presence of the extra crystal in the three-blade NI also breaks the symmetry of the NI. The symmetry is in the distance separating the NI crystals. The result of this is that the beam arriving the third blade is partially defocused. The introduction of a defocusing is accompanied by a phase difference. This phase is extracted using the FWHM $\sigma_\theta = 69$ [μrad] of the measured data and plotted in Fig. 5.4. This is a valid approach because the defocusing introduced by the crystal has no effect on the momentum distribution. .

A similar experiment has since then been done, with the extra crystal blade oriented in the Bragg geometry [62]. The schematic setup is shown as an inset in Fig. 5.3a. In ref. [62] an analytical form of the contrast has been derived under the approximations listed below :

1. The total phase (DD and the nuclear) is $\Delta\Phi(\delta k) = \chi(1 + B/\delta k)$, for $\eta > 1$, where $B = |V_H|^2 m(V_0 \hbar^2 H^2)^{-1}$; and $\chi = D(K_\perp - k_\perp)$ is the nuclear phase,
2. $|t| = 1$ for the added blade since it cause a very small intensity reduction;
3. The momentum space distribution is assumed to be a Lorentzian

$$g(\delta k') = \frac{\sigma_k}{\pi(\sigma_k^2 + (\delta k' - \delta k)^2)}; \quad (5.23)$$

The combined conditions for a monocrystalline crystal and a beam misaligned from the Bragg condition of the crystal by $\delta k'$, the integrated intensity at the O-beam is,

$$\begin{aligned} \overline{I_o(\phi)} &= \int g(\delta k' - \delta k) \left(1 + \cos[\Delta\Phi(\delta k)]\right) d\delta k', \\ &= 1 + \exp\left(\frac{-B\sigma_k}{\delta k^2 + \sigma_k^2} |\chi|\right) \cos\left[\left(\frac{B\delta_k}{\delta k^2 + \sigma_k^2} + 1\right)\chi + \phi\right]. \end{aligned} \quad (5.24)$$

The measured phase χ_{meas} and the contrast \mathcal{V} vary as,

$$\mathcal{V} = \exp\left(\frac{-B\sigma_k}{\delta k^2 + \sigma_k^2} |\chi|\right) \quad \chi_{\text{meas}} = \left(\frac{B\delta_k}{\delta k^2 + \sigma_k^2} + 1\right)\chi, \quad (5.25)$$

where σ_k and δ_k are the width and center of the distribution, respectively, and χ is the nuclear phase from the Si crystal.

5.2.5 Five-blade neutron interferometer

The five-blade NI is similar to the four-blade NI but with an additional beam splitter blade in the middle. With a phase ϕ in the first loop and another phase χ in the second loop (see Fig. 5.1c), the combined operation of the interferometer is,

$$\begin{aligned} U_{5\text{BNI}} &= U_B R_z(\chi) R_x(\pi) U_B R_x(\pi) R_z(\phi) U_B, \\ &= R_z(\beta) R_x(\alpha) R_z(\chi) R_x(\alpha) R_z(\phi) R_x(\alpha) R_z(\beta). \end{aligned} \quad (5.26)$$

If the initial state is $|I\rangle$, and balanced beam splitters, the probability of detecting a neutron at the O-beam and H-beam are,

$$p_o = \frac{1}{4} \left(2 + \cos(\chi - \phi) - \cos(\chi + \phi)\right), \quad (5.27)$$

$$p_h = \frac{1}{4} \left(2 - \cos(\chi - \phi) + \cos(\chi + \phi)\right). \quad (5.28)$$

The probability is independent of β is an indication that the dynamical phase is refocused in the five-blade NI. The refocusing of the dynamical phases can also be understood in the sense of chirping. This means that the wavevectors that were travelling faster than the mean wavevector before the second blade (mirror) tend to travel slower than the mean wavevector after it and vice versa. With this concept in mind, the dynamical phase refocusing is similar to the principle of noise refocusing in nuclear magnetic resonance using Hahn echo and Carr-Purcell sequences [88, 89, 33].

5.3 Effects of mechanical vibration

The effect of mechanical vibrations in interferometry is commonly removed using vibration isolation systems, although, the effect of low-frequency vibration still persist. The four-blade NI has the experimentally demonstrated advantage, over the three-blade NI, of being robust against slow varying external mechanical vibrations. In this section, we adopt the vibration model in [84], that treats mechanical vibrational noise as sinusoidal oscillations of the form, $\zeta(t) = \zeta_0 \sin(\omega t + \varphi)$, where ζ_0 is the amplitude of the noise, ω is the frequency and $\varphi \in [0, 2\pi]$ is a random phase that considers different arrival times of the neutrons at the first blade. The effect of noise due to mechanical vibrations on the five-blade NI is presented in detail, and for completeness we also present previous results of the three-blade and four-blade NI.

Mechanical vibrations can cause a change in the momentum of the neutron. A change in momentum $\Delta \mathbf{p}$ gives rise to a phase difference, around any closed loop, given by

$$\Delta \Phi = \frac{1}{\hbar} \oint \Delta \mathbf{p} \cdot d\mathbf{s}. \quad (5.29)$$

In our model, the most significant effect comes from the linear vibration along the x -axis (X-noise) and NI rotations around the y -axis (Y-noise). The X-noise is that caused by the interferometer oscillations along the reciprocal lattice vector, while the Y-noise is that from rotations around the axis perpendicular to plane of interference. Using the form of the noise stated above, the X-noise and Y-noise can be modelled as $x(t) = x_0 \sin(\omega t + \varphi)$ and $\theta(t) = \theta_0 \sin(\omega t + \varphi)$ respectively, where x_0 and θ_0 are noise amplitudes. In general, the noise can have different frequencies.

5.3.1 X-Noise

The velocity of the incident neutron can be decomposed into two components (perpendicular and parallel to the reciprocal lattice vector), $\mathbf{v} = v_{\perp}\hat{e}_z + v_{\parallel}\hat{e}_x$. If the interaction of the neutron with the blade is modelled in a similar way to a ball bouncing off a hard surface, then the velocity along the z -axis is not affected while the velocity along the x -axis after the crystal is, $v_x = -v_{\parallel} + 2\dot{x}$, with $\dot{x} = dx/dt$. Assume that the neutron enters the interferometer at $t = 0$, then the phase shift around a three-blade NI loop, due to the changes in momentum along path I and path II is,

$$\Delta\Phi(\varphi) = \frac{32m}{\hbar}\tau^2[v_{\parallel} - u_x(0)]\dot{u}_x(0), \quad (5.30)$$

where $u_x(t) = \dot{x}(t)$, m is the mass of the neutron, $\tau = L/v_{\perp}$ and L is the inter-blade distances. For low frequency noise where $\omega\tau \ll 1$,

$$\Delta\Phi(\varphi) = \frac{32mv_{\parallel}x_0\tau^2}{\hbar}\omega^2 \sin \varphi, \quad (5.31)$$

since $v_{\parallel} \gg u_x(0)$. The probability of detecting a single neutron at the O-detector and H-detector is,

$$p_o = \frac{1}{2}\left(1 + \cos[\phi + \Delta\Phi(\varphi)]\right), \quad (5.32)$$

$$p_H = \frac{1}{2}\left(1 - \cos[\phi + \Delta\Phi(\varphi)]\right). \quad (5.33)$$

Each neutron arrives on the first blade at different time instances thereby picking up a different initial phase φ . Taking an average over a uniform probability distribution, $p(\varphi) = 1/2\pi$, the intensity at the O-beam detector as a function of the phase ϕ is,

$$\overline{I_o(\phi)} = \frac{1}{4\pi} \int_0^{2\pi} \left(1 + \cos[\phi + \Delta\Phi(\varphi)]\right) d\varphi = \frac{1}{2}\left(1 + |\gamma| \cos[\phi + \arg(\gamma)]\right), \quad (5.34)$$

where γ is the coherence function. γ is defined for statistically stable noise [71, 18] as

$$\gamma = \frac{1}{2\pi} \int_0^{2\pi} \exp[i\Delta(\varphi)] d\varphi. \quad (5.35)$$

For an interferometer with $L = 5$ cm, illuminated with wavelength 4.4 \AA , and noise with $x_0 = 0.1 \text{ \mu m}$ the coherence function for three-blade NI reduces to,

$$\gamma = J_0(\Omega\omega^2), \quad \text{with} \quad \Omega = \frac{32mv_{\parallel}x_0\tau^2}{\hbar}, \quad (5.36)$$

where J_0 is the zero order Bessel function of the first kind. For the O-beam of a three-blade NI, $|\gamma| = \mathcal{V}$. The plots of the intensity versus ϕ are shown in Fig. 5.5a for $\omega = 0, 100, 200$ Hz, and the plot of $|\gamma|$ against ω is shown in Fig. 5.5d. At the 100 Hz the intensity modulation depth is almost zero for three-blade NI.

In the four-blade NI the phase difference $\Delta\Phi_1$ in the first loop and $\Delta\Phi_2$ in the second loop are,

$$\Delta\Phi_1 = -\frac{4m\tau^2}{\hbar}[v_{\parallel} - u_x(0)][2\dot{u}_x(0) + \tau\ddot{u}_x(0)], \quad (5.37)$$

$$\Delta\Phi_2 = \frac{4m\tau^2}{\hbar}[v_{\parallel} - u_x(0)][2\dot{u}_x(0) + 7\tau\ddot{u}_x(0)]. \quad (5.38)$$

In the low frequency noise regime where $\omega\tau \ll 1$, the phase difference over the four-blade NI is,

$$\Delta\Phi(\varphi) = -\Delta\Phi_1 + \Delta\Phi_2 = \frac{24mv_{\parallel}x_0\tau^3}{\hbar}\omega^3 \cos\varphi. \quad (5.39)$$

At the exit, the probability of detecting a single neutron at the O-detector and H-detector in the four-blade NI is

$$p_o = \frac{1}{2}\left(1 - \cos[\phi + \Delta\Phi(\varphi)]\right), \quad (5.40)$$

$$p_h = \frac{1}{2}\left(1 + \cos[\phi + \Delta\Phi(\varphi)]\right). \quad (5.41)$$

Taking the average over the phase φ , and considering the fact that the H-beam in the four-blade NI carries the same phase information as the O-beam in the three-blade case, the intensity becomes

$$\overline{I_H(\phi)} = \frac{1}{4\pi} \int_0^{2\pi} \left(1 + \cos[\phi + \Delta\Phi(\varphi)]\right) d\varphi = \frac{1}{2} \left[1 + |\gamma| \cos(\phi + \arg \gamma)\right], \quad (5.42)$$

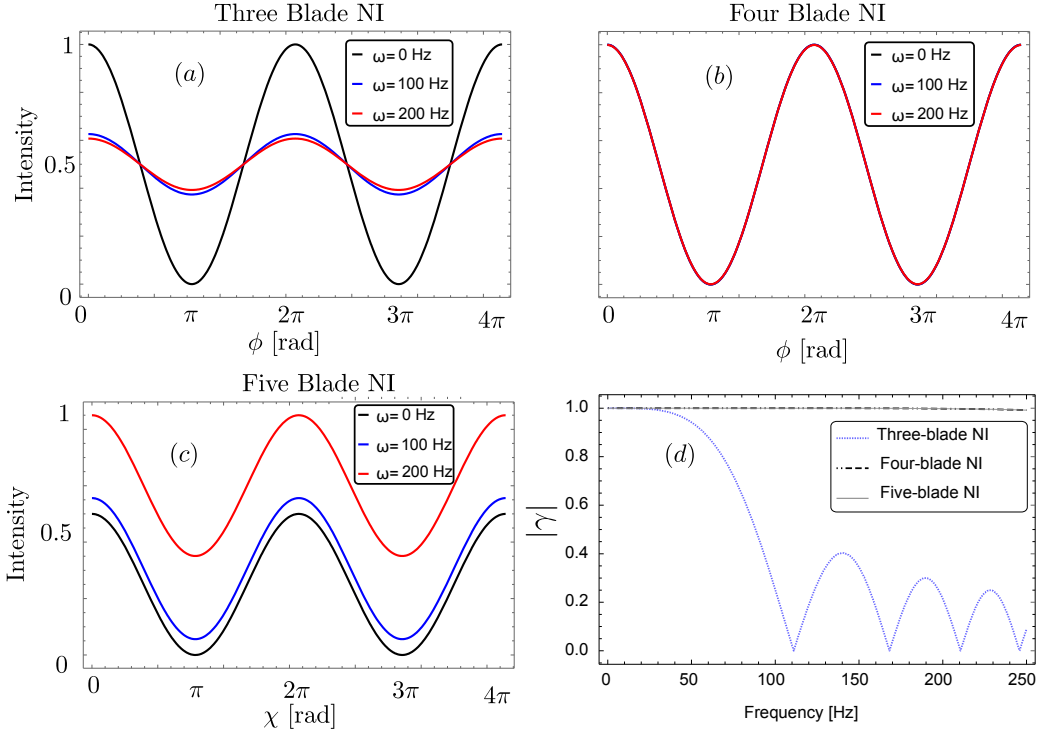


Figure 5.5: The intensity against phase for X-noise with $\omega = 0, 100$ and 200 Hz. In (a) is the O-beam intensity for the three-blade NI, in (b) is the H-beam intensity for the four-blade NI, and in (c) is the H-beam intensity for the five-blade NI. The oscillations in the three-blade NI are damped as the noise increases, while those for the four-blade are not. In the five-blade NI, the effect of noise leads to simply a DC shift. In (a) are the simulated variation of the absolute value of the coherence function γ against ω for the three-, four- and five-blade NIs. The interferometer separation between blades $L = 5$ cm, the neutron wavelength is 4.4 \AA . The noise-refocusing condition $\phi = -\chi + \pi$ is used in plot (d).

where, the coherence is

$$\gamma = J_0(\Omega\omega^3), \quad \text{with} \quad \Omega = \frac{24mv_{\parallel}x_0\tau^3}{\hbar}. \quad (5.43)$$

The intensity, as a function of ϕ , is shown in Fig. 5.5b for $\omega = 0, 100$, and 100 Hz. Also shown in Fig. 5.5d is a comparison of the variation of $|\gamma|$ with ω .

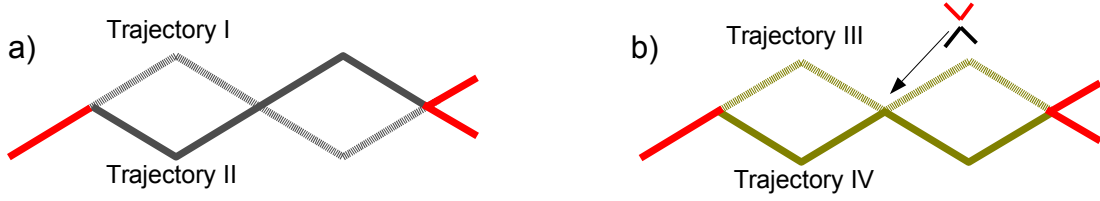


Figure 5.6: Sketches of the different paths, I, II, III and IV that leads to the output and contribute to the (a) symmetric and the (b) antisymmetric case.

In the case of the five-blade NI, the interferometer is first resolved into loops formed by the paths taken by the neutron from the first to the last blade. For simplicity, we split the four trajectories into two categories: the *symmetric* case and the *antisymmetric* case. The symmetric case contains the two paths corresponding to the middle blade acting as a perfect transmitter (see Trajectories I and II in Fig. 5.6a), and the antisymmetric case is where the middle blade acts as a perfect reflector (see Trajectories III and IV in Fig. 5.6b). It is worth noting that the symmetric case is identical to the four-blade NI. The phases loop 1 and loop 2, denoted by $\Delta\Phi_1$ and $\Delta\Phi_2$, respectively are,

$$\Delta\Phi_1 = -\frac{4m\tau^2}{\hbar}[v_{\parallel} - u_x(0)][2\dot{u}_x(0) + \tau\ddot{u}_x(0)], \quad (5.44)$$

$$\Delta\Phi_2 = \frac{4m\tau^2}{\hbar}[v_{\parallel} - u_x(0)][2\dot{u}_x(0) + 7\tau\ddot{u}_x(0)], \quad (5.45)$$

In the antisymmetric case, the phases in loop 1 and 2 denoted by $\Delta\Phi'_1$ and $\Delta\Phi'_2$ are,

$$\Delta\Phi'_1 = \Delta\Phi_1, \quad (5.46)$$

$$\Delta\Phi'_2 = -\frac{4m\tau^2}{\hbar}[v_{\parallel} - u_x(0)][2u_x(0) + 3\tau\ddot{u}_x(0)], \quad (5.47)$$

In the low frequency noise regime where $\tau\omega \ll 1$, the phase difference in both cases due to X-noise and can be represented as,

$$\Delta\Phi(\varphi) = \Delta\Phi_1 + \Delta\Phi_2 = \frac{24mv_{\parallel}x_0\tau^3}{\hbar}\omega^3 \cos \varphi, \quad \text{symmetric} \quad (5.48)$$

$$\Delta\Phi'(\varphi) = \Delta\Phi'_1 + \Delta\Phi'_2 = \frac{16mv_{\parallel}x_0\tau^2}{\hbar}\omega^2 \sin \varphi, \quad \text{antisymmetric.} \quad (5.49)$$

The phase difference from external vibrations along the x-axis almost cancel out in the symmetric case, but effectively doubles in the anti-symmetric loop. The phase in the antisymmetric loop is similar to that in the four-blade NI.

With a phase ϕ in the first loop and χ in the second (see Fig. 5.1c), the probability of detecting a single neutron at the O- and H- detectors in the five-blade NI are,

$$p_o = \frac{1}{4} \left(2 + \cos[\chi - \phi + \Delta\Phi(\varphi)] - \cos[\chi + \phi + \Delta\Phi'(\varphi)] \right), \quad (5.50)$$

$$p_H = \frac{1}{4} \left(2 - \cos[\chi - \phi + \Delta\Phi(\varphi)] + \cos[\chi + \phi + \Delta\Phi'(\varphi)] \right). \quad (5.51)$$

where, the symmetric, $\Delta\Phi(\varphi)$, and the antisymmetric, $\Delta\Phi'(\varphi)$, phase differences are those defined in Eqs. (5.48) and (5.49). The intensity in the H-beam obtained by taking an average over a uniform distribution in φ is given by,

$$\overline{I_H(\phi)} = \frac{1}{4\pi} \int_0^{2\pi} \left(2 - \cos[\chi - \phi + \Delta\Phi(\varphi)] + \cos[\chi + \phi + \Delta\Phi'(\varphi)] \right) d\varphi. \quad (5.52)$$

A plot of this intensity without noise ($\omega = 0$) is shown in Fig. 5.7a, and in Fig. 5.7b, the same intensity is plotted for noise with $\omega = 200$ Hz. The region through the 2D plots, where the oscillations are dampened, depicts the effect of noise. It is clearly visible on the plot that there are combinations of ϕ and χ for which the effect of noise is minimal. These include the lines $\phi = -\chi + \mu$, where μ is a constant. Along this set of lines the effect of noise results in a DC shift of the intensity profile with no effect on coherence. The 1-D plots in Fig. 5.5c illustrate the effect of noise with, $\omega = 0, 100$, and 100 Hz on the five-blade NI. At high frequencies, the intensity result in a DC shift, clearly visible on the plot.

The average intensity shown in Eq. (5.52) can be rewritten in terms of the coherence functions as,

$$\begin{aligned} \overline{I_H(\phi, \chi)} &= \frac{1}{4} \left(2 - \gamma_1 \cos(\chi - \phi) - \gamma_2 \sin(\chi - \phi) + \gamma_3 \cos(\chi + \phi) + \gamma_4 \sin(\chi + \phi) \right), \\ &= \frac{1}{4} \left(2 - |\gamma| \cos(\chi - \phi + \arg \gamma) + |\gamma'| \cos(\chi + \phi + \arg \gamma') \right). \end{aligned} \quad (5.53)$$

γ has a real and imaginary parts denoted as γ_1 and γ_2 , while γ' has a real and imaginary parts denoted respectively as γ_3 and γ_4 . The full expressions of the coherence function are,

$$\gamma = \frac{1}{2\pi} \int_0^{2\pi} \exp[i\Delta\Phi(\varphi)] d\varphi, \quad \gamma' = \frac{1}{2\pi} \int_0^{2\pi} \exp[i\Delta\Phi'(\varphi)] d\varphi \quad (5.54)$$

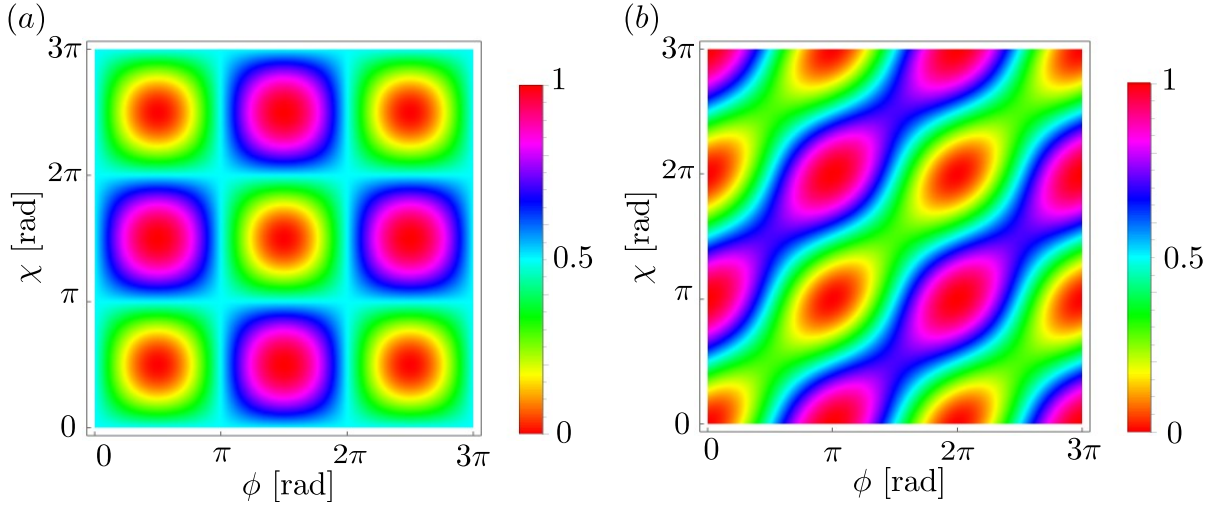


Figure 5.7: 2D plot of the intensity at the H-beam for a five-blade NI, as a function of the phase, ϕ in loop 1, and χ in loop 2 . (a) The plot without noise shows oscillations in 2D plot with (ϕ, χ) . (b) Shows the effect of noise with frequency $\omega = 200$ Hz. The interference pattern is dampened along some configurations of $(\phi$ and $\chi)$.

Using the phase difference due to X-noise, γ and γ' are real,

$$\gamma = J_0(\Omega\omega^3), \quad \text{with} \quad \Omega = \frac{24mv_{\parallel}x_0\tau^3}{\hbar} \quad (5.55)$$

$$\gamma' = J_0(\Omega'\omega^2), \quad \text{with} \quad \Omega' = \frac{16mv_{\parallel}x_0\tau^2}{\hbar}. \quad (5.56)$$

Under the condition $\phi + \chi = \pi$, the average intensities for the five-blade NI are,

$$\begin{aligned} \overline{I_{\text{H}}(\phi, \phi)} &= \frac{1}{4} \left[2 - J_0(\Omega'\omega^2) - |J_0(\Omega\omega^3)| \cos(2\phi - \arg(J_0(\Omega\omega^3))) \right], \\ \overline{I_{\text{O}}(\phi, \phi)} &= \frac{1}{4} \left[2 + J_0(\Omega'\omega^2) + |J_0(\Omega\omega^3)| \cos(2\phi - \arg(J_0(\Omega\omega^3))) \right]. \end{aligned} \quad (5.57)$$

The effect of noise is a DC shift or an additional background contribution of $1 - J_0(\Omega'\omega^2)$. Shown in Fig. 5.5c, the interference pattern is displaced along the vertical axis by $1 - J_0(\Omega'\omega^2)$ and the O-beam is displaced by the same amount below the maximum intensity of 1. Therefore, the coherence or the depth of the modulation, $|\gamma|$, remains the same despite a reduction in the contrast as defined in Eq. (1.45). The contrast for the five-blade

under this noise is

$$\mathcal{V} = \frac{|J_0(\Omega\omega^3)|}{2 - J_0(\Omega'\omega^2)}. \quad (5.58)$$

For Y-noise with an $\omega = 100$ Hz, the interferogram is offset by 0.2 which results in a relative contrast of about 82%. In Fig. 5.5d, a plot of $|\gamma|$ is compared with that for the three-blade and four-blade NIs. The five-blade NI is capable of refocusing low-frequency noise just as the four-blade DFS NI and the coherences in these two NIs only show some effects at frequencies above 250 Hz.

5.3.2 Y-noise

Consider the noise resulting from vibrations around the y-axis, modelled as $\theta(t) = \theta_0 \sin(\omega t + \varphi)$. Once again, assuming that a neutron beam is incident on the first blade at $t = 0$, the phase difference due to Y-noise in a three-blade NI using small angle approximations is

$$\begin{aligned} \Delta\Phi(\varphi) &= \frac{32m\tau}{\hbar}[v_{\parallel} - 2L\dot{\theta}(0)]L\dot{\theta}(0) = \frac{32mLv_{\parallel}\theta_0\tau}{\hbar}\omega \cos \varphi, \\ &= \frac{32mv_{\perp}v_{\parallel}\theta_0\tau^2}{\hbar}\omega \cos \varphi. \end{aligned} \quad (5.59)$$

Under the same conditions for a four-blade NI as the three-blade NI, the phase differences $\Delta\Phi_1$ in loop 1 and $\Delta\Phi_2$ in loop 2 are given by,

$$\Delta\Phi_1 = \frac{8m\tau}{\hbar}[v_{\parallel} - 2L\dot{\theta}(0)][L\dot{\theta}(0) - L\tau\ddot{\theta}(0)], \quad (5.60)$$

$$\Delta\Phi_2 = -\frac{8m\tau}{\hbar}[v_{\parallel} - 2L\dot{\theta}(0)][L\dot{\theta}(0) + 5L\tau\ddot{\theta}(0)], \quad (5.61)$$

The resulting phase difference reduces to,

$$\Delta\Phi(\varphi) = \Delta\Phi_1 + \Delta\Phi_2 = -\frac{48mv_{\perp}v_{\parallel}\theta_0\tau^3}{\hbar}\omega^2 \sin \varphi, \quad (5.62)$$

for low frequency vibrations.

In a similar approach as the X-noise, the phase difference for the five-blade NI is obtained by splitting it into loops. In the symmetric case, the phase difference, $\Delta\Phi_1$,

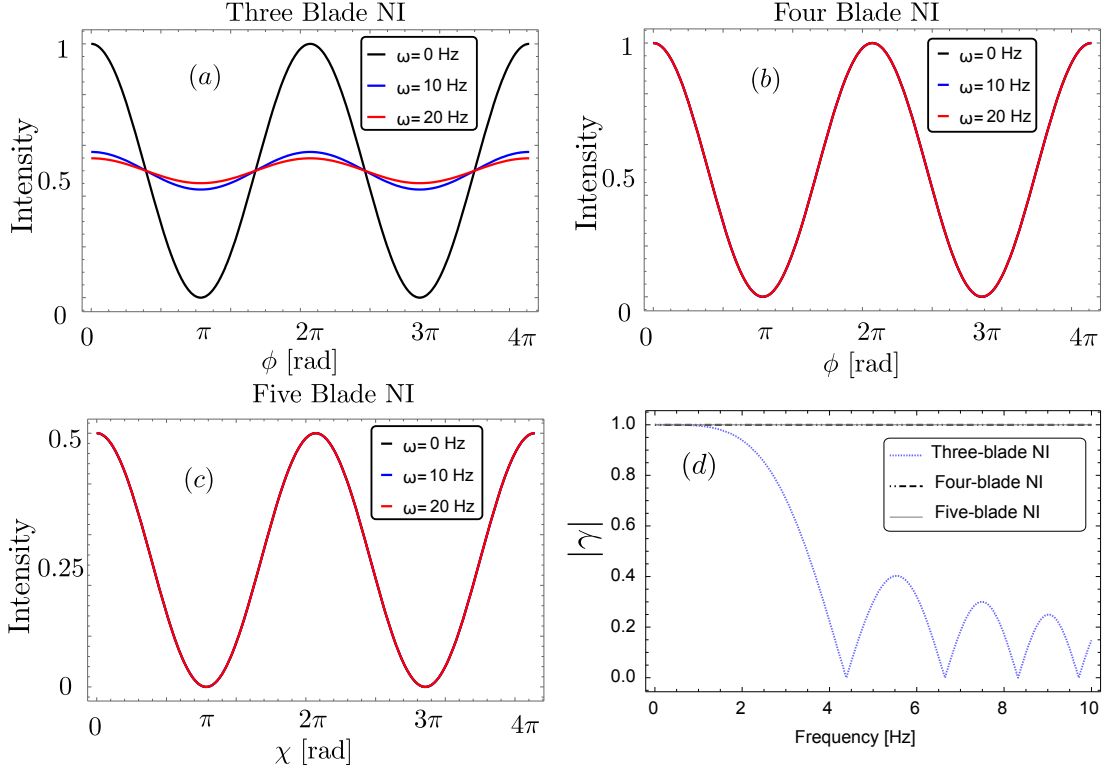


Figure 5.8: The intensity versus phase for Y-noise with $\omega = 0, 10, 20$ Hz. In (a), is the O-beam intensity against phase for the three-blade NI, in (b) is the H-beam intensity for the four-blade NI, and in (c) is the H-beam intensity for the five-blade NI. Similar to X-noise, the oscillations in the three-blade NI are damped as the noise increases, while those for the four-blade are not. The interferometer separation between blades $L = 5$ cm, the neutron wavelength is 4.4 \AA . In (c) are simulations of the variation of the absolute value of the coherence function, $|\gamma|$, with ω for each of the NIs. The coherence function of the four-blade and five-blade NIS remain unchanged at frequencies greater than 2 Hz while the three-blade NI is significantly affected. Note that the decoherence free condition from the configuration of the phase flags ϕ and χ is used.

acquired in loop 1 and $\Delta\Phi_2$ in loop 2 are,

$$\Delta\Phi_1 = \frac{8m\tau}{\hbar} [v_{\parallel} - 2L\dot{\theta}(0)][L\dot{\theta}(0) - L\tau\ddot{\theta}(0)], \quad (5.63)$$

$$\Delta\Phi_2 = -\frac{8m\tau}{\hbar}[v_{\parallel} - 2L\dot{\theta}(0)][L\dot{\theta}(0) + 5L\tau\ddot{\theta}(0)], \quad (5.64)$$

and those in loop 1 and loop 2 in the antisymmetric case are

$$\Delta\Phi'_1 = \Delta\Phi_1, \quad (5.65)$$

$$\Delta\Phi'_2 = \frac{8m\tau}{\hbar}[v_{\parallel} - 2L\dot{\theta}(0)][L\dot{\theta}(0) + L\tau\ddot{\theta}(0)], \quad (5.66)$$

At low frequencies, $\tau\omega \ll 1$, the phase differences in the five-blade NI resulting from the symmetric and the antisymmetric cases are

$$\Delta\Phi(\varphi) = \Delta\Phi_1 + \Delta\Phi_2 = -\frac{48mv_{\perp}v_{\parallel}\theta_0\tau^3}{\hbar}\omega^2 \sin\varphi, \quad \text{symmetric} \quad (5.67)$$

$$\Delta\Phi'(\varphi) = \Delta\Phi'_1 + \Delta\Phi'_2 = \frac{16mv_{\perp}v_{\parallel}\theta_0\tau^2}{\hbar}\omega \sin\varphi, \quad \text{antisymmetric.} \quad (5.68)$$

Just like the X-noise, the phase difference from external mechanical vibrations around the y-axis in the symmetric is the same as the four-blade (almost cancels out), and in the antisymmetric case it is similar to the three-blade case. The Y-noise can be refocused in a similar way as was done for the X-noise.

Let us consider again an NI with balanced beam splitters and vibrational noise with amplitude of $\theta_0 = 0.1 \mu\text{rads}$, on an NI of $L = 5 \text{ cm}$ illuminated with neutrons of $\lambda = 4.4 \text{ \AA}$. The O-beam intensity versus the phase for the three-blade and the H-beam intensity versus phase for the four-blade and five-blade NIs for Y-noise strengths of $\omega = 0, 10$ and 20 Hz are shown in Figs. 5.8 a, b and c respectively. The oscillations in the three-blade NI are damped as the noise increases, while those for the four-blade are not. In the five-blade, the effect of noise leads to a DC shift on the axis or effectively an additional background term. The coherence function of the various interferometers under the influence of Y-noise is plotted in Fig. 5.8d. Although the three-blade NI coherence function is strongly affected by noise, those of the four-blade and five-blade NIs remain unchanged.

It is worth noting that the noise refocusing ability of the five-blade NI goes beyond the symmetric noise which is refocused by the four-blade NI. If the noise is antisymmetric, the five-blade NI still retains the ability to refocus, but with the configuration changed from $\phi = -\chi + \mu$ to $\phi = \chi + \mu$. The four-blade DFS NI does not have the ability to refocus

this class of noise as the phase difference in two loops add up instead of cancelling. If the coherence function for a specific geometry is defined in general as,

$$\gamma = \langle \cos(\Phi + \nu\Phi) + i \sin(\Phi + \nu\Phi) \rangle, \quad (5.69)$$

$$= \int p(\Phi) \exp[i(\Phi + \nu\Phi)] d\Phi, \quad (5.70)$$

where the noise spectrum is $p(\Phi)$, and $\nu = \pm 1$. The coherence function can be calculated when the phase shift caused by noise (e.g vibration noise X, Y, etc) is known.

5.4 Future prospects and conclusion

The full five-blade NI is a multipath interferometer made up of multiple loops. This makes it possible to convert it to a number of interferometry geometries. Consider the full five-blade NI with phase differences $\chi_i, i = 1, \dots$ shown in Fig. 5.9 with the ability to convert to multiple NI geometries as shown in (a) to (k). For interferometry studies some of the geometries are redundant. However, for the study of DD the geometries can be used to study the behavior of the beams under the influence of the number of blades and the thickness. The geometries in Figs. 5.9c and 5.9k can be related to the Fransen interferometer in light optics. There is a possibility of three-loop interferometry in which the loops are of the same sizes and of different sizes. It is possible to explore a delay choice type experiments for neutron in this interferometer, as well as momentum squeezing.

We used the unitary operator approach of an interferometer blade to study the effect of dynamical phase on the three-blade, four-blade and five-blade NIs. It was shown that in spite it's robustness to external vibrational noise the four-blade NI is susceptible to the dynamical phase noise. The dynamical phase noise is refocused in the three-blade NI despite it susceptibility to the external mechanical vibrational noise. We then propose a design for a five-blade NI that is insensitive to both dynamical phase noise and low frequency vibration noise.

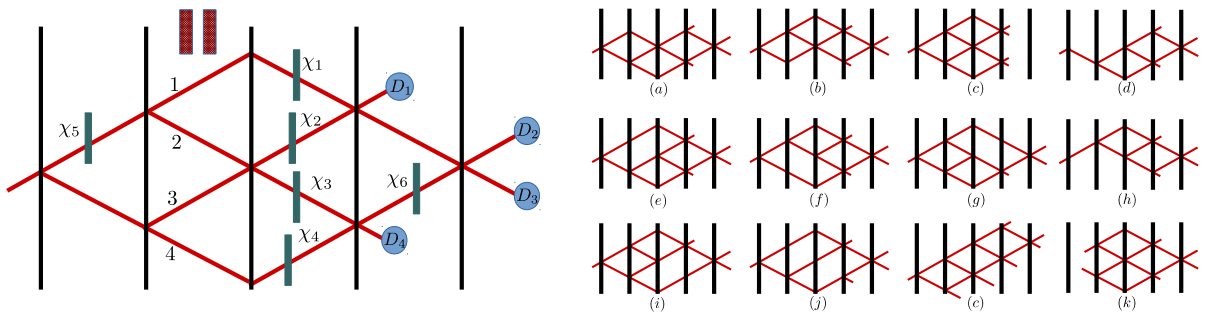


Figure 5.9: A schematic of a multipath five-blade NI. (a) to (k) are some possible configurations that could be used for in different studies.

Chapter 6

Spin-Orbit states of a neutron wavepacket

6.1 Introduction

In free space, matter waves may carry linear and angular (spin, orbital) momentum. Orbital angular momentum (OAM) states are characterized by a spatial-distribution helical wavefront of the form $e^{il\phi}$. OAM for photons was first recognized by Allen et al. [90], and since been experimentally observed with photons and electrons with numerous applications including quantum communication, imaging, resonators, quantum cryptography, QIP [91, 92, 93]. In this chapter, we focus on creating and manipulating OAM in a neutron wavepacket. Recently, it was demonstrated that neutrons can support OAM states by using a spiral phase plate to write a helical wavefront onto a neutron beam [94, 95]. In this realization, the OAM induced was an extrinsic property of the neutrons as opposed to the intrinsic property, where the whole beam propagates through the axis of the OAM inducing device. In effect, each neutron carries a well defined OAM that depends on the location of the wavepacket.

This chapter presents the methods of generation and detection of neutron orbital angular momentum states using a spiral phase plate, as well as the limitations due to the

off axis effects that result from the limited coherence length of the neutron wavepacket. It later proposes a method to prepare an entangled state between the orbital and spin states of a neutron and a Ramsey-fringe-type measurement, suggested as a method to verify the spin-orbit correlations.

This chapter is structured as follows: In Sec. 6.2, we present the basics of a wavefunction carrying OAM. Next, in Sec. 6.3, we identify how to generate OAM with a spiral phase plate and detect it using an NI. Further, in Sec. 6.4, we look at how to generate spin-orbit states with a magnetic quadrupole, and explore the entanglement. Subsequently, in Sec. 6.5, we discuss the Ramsey fringe experiment for OAM states generated by a quadrupole and a linear gradient. Finally, in Sec. 6.6, we discuss how to detect spin-orbit states in an NI.

6.2 Wavefunction

It is convenient to consider a neutron beam travelling along the z -direction, with momentum k_z , and the expectation values of momentum in the transverse plane equalling to zero such that, the mean wavevector is, $\mathbf{k} = (0, 0, k_z)$. Consider a wavepacket with momentum distribution along the x and y characterized by the standard deviations $\Delta k_{x,y}$, which are related to the spatial distribution by the minimum uncertainty relation. Under these conditions, the system can be treated in the paraxial approximation that uses $\partial^2/\partial_z^2 = k^2 + 2iz\partial/\partial_z$ to reduce the equation to the Helmholtz type. There is a mapping between the paraxial approximation Helmholtz equation and the Schrödinger equation of a quantum mechanical Harmonic Oscillator [96, 97]. As a result, the solution are the Laguerre-Gauss modes, known to possess discrete values of orbital angular momentum per unit energy [90].

The OAM operator in a cylindrical coordinate system is $\hat{L}_z = i\frac{\partial}{\partial\phi}$, and its eigenstates are a convenient basis for the neutron wavepacket when the standard deviations of momentum in the transverse directions are equal i.e $\sigma_x = \sigma_y \equiv \sigma_\perp$, where $\sigma_{x,y} = 1/(2\Delta k_{x,y})$ (not to be confused with Pauli operators $\hat{\sigma}_{x,y}$). In cylindrical symmetry, the separable neutron wavefunction is given by

$$\Psi(r, \phi, z) = \mathcal{R}(r)\Phi(\phi)\mathcal{Z}(z), \quad (6.1)$$

where $\mathcal{R}(r)$, $\Phi(\phi)$ and $\mathcal{Z}(z)$ the radial, azimuthal and longitudinal components of the wavefunction parametrized by $r = \sqrt{x^2 + y^2}$ and $\phi = \arctan(y/x)$. When propagating through space, the standard deviation of momenta in the transverse direction remains constant, so the transverse wavefunction, $\mathcal{R}(r)\Phi(\phi)$, is properly described in terms of the solutions to the 2D harmonic oscillator. In this chapter the longitudinal wavefunction, $\mathcal{Z}(z)$, is treated as a Gaussian wavepacket while the transverse is treated as solutions to the Hamiltonian;

$$H = -\frac{\hbar^2}{2m}\nabla^2 + \frac{1}{2}m\omega_{\perp}^2 r^2, \quad (6.2)$$

where \hbar is the reduced Planck's constant, m is the mass of the neutron, and $\nabla^2 = \frac{1}{r}\partial_r(r\partial_r) - \frac{1}{r^2}\partial_{\phi}^2$. The matter-wave oscillation frequency, ω_{\perp} , in the transverse direction is related to the neutron coherence length by,

$$\sigma_{\perp}^2 = \frac{\hbar}{2m\omega_{\perp}^2}. \quad (6.3)$$

The transverse Schrödinger equation defined using the Hamiltonian in Eq. (6.2), with a periodic orbital continuity condition, $\Phi(0) = \Phi(2\pi)$, has the solution $\Phi \sim e^{-i\ell\phi}$, where, $\ell \in \mathbb{Z}$ are orbital quantum numbers. In the radial direction, the solutions $\mathcal{R}(r)$ are the Laguerre-Gauss polynomials. The combined transverse and longitudinal solution is,

$$\psi_{n\ell}(r, \phi, z) = \frac{1}{\sigma_{\perp}} \sqrt{\frac{n!}{\pi(n + |\ell|)!}} \left(\frac{r}{\sigma_{\perp}}\right)^{|\ell|} e^{-\frac{r^2}{2\sigma_{\perp}^2}} \mathcal{L}_n^{|\ell|} \left(\frac{r^2}{\sigma_{\perp}^2}\right) e^{-i\ell\phi} \mathcal{Z}(z), \quad (6.4)$$

where, $n \in \mathbb{N}_0$ is the radial quantum number, and $\mathcal{Z}(z)$ is the wavefunction function along the z -axis. In the presence of an external magnetic field, the spin state contribute to the total wavefunction to constitute a basis state specified by,

$$\psi_{n\ell s}(r, \phi, z) = \frac{1}{\sigma_{\perp}} \sqrt{\frac{n!}{\pi(n + |\ell|)!}} \left(\frac{r}{\sigma_{\perp}}\right)^{|\ell|} e^{-\frac{r^2}{2\sigma_{\perp}^2}} \mathcal{L}_n^{|\ell|} \left(\frac{r^2}{\sigma_{\perp}^2}\right) e^{-i\ell\phi} \mathcal{Z}(z) \otimes |s\rangle, \quad (6.5)$$

that is an eigenstate with total energy,

$$E_T = \hbar\omega_{\perp}(2n + |\ell| + 1) + \frac{\hbar^2 k_z^2}{2m} + \vec{\mu} \cdot \vec{B}. \quad (6.6)$$

Our desired form to specify the basis states will be in the Dirac notation, which is,

$$|\psi_{n\ell s}\rangle = |n, \ell, s, k_z\rangle. \quad (6.7)$$

However, throughout this work, for any z , we will work exclusively with the transverse part of the basis function, denoted as $|n, \ell, s\rangle$, and with the transverse projection

$$\psi_{n\ell s}(\xi, \phi, z) = \mathcal{N} \xi^{|\ell|} e^{-\frac{\xi^2}{2}} \mathcal{L}_n^{|\ell|}(\xi^2) e^{-i\ell\phi} \otimes |s\rangle. \quad (6.8)$$

$|n, \ell, s\rangle \in \mathcal{H} = \mathcal{H}_R \otimes \mathcal{H}_O \otimes \mathcal{H}_S$, where R, O , and S stand for the radial, orbital and spin subspaces. The parameters $\xi = r/\sigma_\perp$, and $\mathcal{N} = \sqrt{\frac{n!}{\pi(n+|\ell|)!}}$, are such that the integration element will be $\xi d\xi$.

6.2.1 Basic characteristics of Laguerre-Gauss beams

Laguerre-Gauss (LG) are extensively studied in the optics literature, thus we will emphasize only those features we need.

- The LG represent wavepackets with Gaussian envelopes and constitute a complete, orthonormal set of modes, so that,

$$\langle p, m, s' | n, \ell, s \rangle = \delta_{pn} \delta_{m\ell} \delta_{s's}. \quad (6.9)$$

Any localized wavefunction can be represented as a superposition

$$|\Psi\rangle = \sum_{n\ell s} C_{n,\ell,s} |n, \ell, s\rangle, \quad \text{where} \quad C_{n,\ell,s} = \langle n, \ell, s | \Psi \rangle. \quad (6.10)$$

- LG modes with $\ell \neq 0$ contain a screw dislocation of the wavefront on the wavepacket axis, $\psi_{n\ell} \propto e^{i\ell\phi}$; in other words, they contain a phase vortex of strength, ℓ , at $r = 0$ and have a well-defined z -component of the OAM,

$$\hat{L}_z |n, \ell, s\rangle = \hbar \ell |n, \ell, s\rangle \quad (6.11)$$

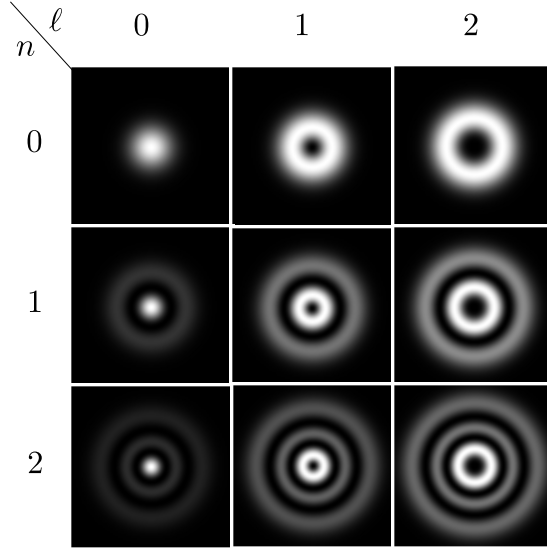


Figure 6.1: Beam profiles of the probability amplitude $|\psi_{n\ell}(\xi, \phi)|^2$ for combinations of $n = 0, 1, 2$ and allowed values $\ell = 0, \pm 1, \pm 2$.

- In cylindrical coordinates, the transverse probability density is,

$$\rho_{n\ell s}(r) = |\langle \xi, \phi | n, \ell, s \rangle|^2 = |\psi_{n\ell s}(\xi, \phi)|^2, \quad (6.12)$$

which for $\ell \neq 0$ represents $n + 1$ radial modes (concentric circles) which vanish at $r = 0$. To visualize this feature, various combinations of $n = 0, 1, 2$ and $\ell = 0, 1, 2$ are illustrated in Fig. 6.1, clearly showing that only beams with $\ell = 0$ have a non-zero intensity on the beam axis.

- If there is a term $e^{ik_z z}$ in the wavefunction, the mode carries linear momenta, $\hbar k_z$, per neutron, oriented along their propagation, with momentum density $\bar{P}_\ell(\xi)$, and probability current density $\bar{j}_\ell(\xi)$,

$$\bar{P}_\ell(\xi) = \hbar (k_z \hat{e}_z + \ell / \xi \hat{e}_\phi) \rho_\ell(\xi), \quad (6.13)$$

$$\bar{j}_\ell(\xi) = \bar{P}_\ell(\xi) / m. \quad (6.14)$$

The only dependence on ϕ is in the phase leading to the cylindrical symmetry of the complex amplitude about the beam axis. When $n = \ell = 0$, the mode is a Gaussian mode with complex amplitude independent of ϕ .

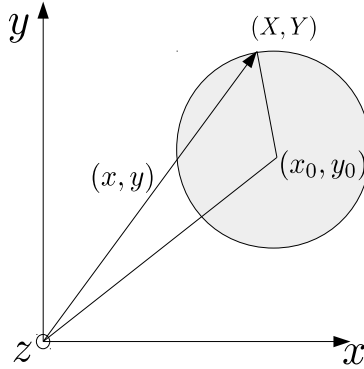


Figure 6.2: A neutron wavepacket with center (x_0, y_0) , propagating off the center of a phase inducing device with coordinate (x, y) . The neutron coordinate is (X, Y) .

6.2.2 Internal and external OAM

The internal OAM is an origin-independent angular momentum that can be associated with a helical phase over the neutron wavepacket carrying the same OAM. On the other hand, the external OAM is the origin-dependent angular momentum that can be associated to a neutron beam, this time with each constituent neutron wavepacket carrying a distinct OAM. As an example, when a spiral phase plate (SPP) is used to generate OAM, any wavepacket propagating through the axis gets a unique OAM as opposed to when the wavepackets is off-center. In the latter, a linear momentum in the tangential direction relative to the beam center is induced and it can be represented as a sum of multiple OAMs. We will commonly refer to the intrinsic OAM as *on-axis*, and the extrinsic OAM as *off-axis*.

We start by distinguishing the coordinates present: locations relative to the axis of the SPP are (x, y) and those relative to the center of the wavepacket are (X, Y) (see Fig. 6.2). In polar coordinates $x = \xi \cos \phi$, $y = \xi \sin \phi$ and $X = \rho \cos \varphi$, $Y = \rho \sin \varphi$. The center of mass coordinate of the wavepacket relative to the axis of the SPP is denoted by $x_0 = \xi_0 \cos \phi_0$ and $y_0 = \xi_0 \sin \phi_0$. Using the transformations above, any location on the wavepacket is related to the beam axis and beam center by, $(X, Y) = (x - x_0, y - y_0)$, such that, $\rho \cos \varphi = \xi \cos \phi - \xi_0 \cos \phi_0$ and $\rho \sin \varphi = \xi \sin \phi - \xi_0 \sin \phi_0$. Consider an incident

Gaussian state with no OAM relative to the wavepacket axis. The incident Gaussian wavefunction relative to the two coordinates is,

$$\psi_{in}(\rho, \varphi) = (1/\sqrt{\pi})e^{-\frac{\rho^2}{2}} = \psi_{00}(\rho, \varphi), \quad \text{wavepacket coordinates} \quad (6.15)$$

$$\psi_{in}(r, \phi; r_0, \phi_0) = (1/\sqrt{\pi})e^{-\frac{\xi^2 + \xi_0^2 - 2\xi\xi_0 \cos(\phi - \phi_0)}{2}}, \quad \text{SPP coordinates.} \quad (6.16)$$

Using the Jacobi-Anger transformation, Eq. (A.14), the input state can be rewritten as,

$$\psi_{in}(\xi, \phi; \xi_0, \phi_0) = \frac{1}{\sqrt{\pi}}e^{-\frac{\xi^2 + \xi_0^2}{2}} \sum_{\ell=-\infty}^{\infty} \mathcal{I}_{\ell}(\xi\xi_0) e^{i\ell(\phi - \phi_0)}. \quad (6.17)$$

A few things can be noted from this state. Despite carrying no harmonics, $\ell = 0$, around the center of the wavepacket, the state is composed of an infinite sum of harmonics relative to the axis of the SPP. Using the Laguerre-Bessel transform, Eq. (A.15), the input state can be represented in terms of the LG basis states as,

$$\psi_{in}(\xi, \phi) = \sum_{n=0}^{\infty} \sum_{\ell=-\infty}^{\infty} G_{n\ell}(\xi_0, \phi_0) \psi_{n\ell}(\xi, \phi), \quad (6.18)$$

where, we have defined the location dependent modulation function as,

$$G_{n\ell}(\xi_0, \phi_0) = \left(\frac{\xi_0^2}{4}\right)^{n + \frac{|\ell|}{2}} \frac{(-1)^n e^{\frac{\xi_0^2}{4} - i\ell\phi_0}}{\sqrt{n!(n + |\ell|)!}}, \quad (6.19)$$

for, $\xi_0 \neq 0$. In the on-axis case, $\xi_0 = \phi_0 = 0$, the input state reduces to,

$$\psi_{in}(\xi, \phi; 0) = \psi_{00}(\xi, \phi) = \psi_{00}(\rho, \varphi), \quad (6.20)$$

which is a state with a well defined OAM $\ell = 0$.

6.3 Generating OAM with a spiral phase plate

Here we analyze the action of an SPP in creating OAM. The spin component of the wavefunction as well as the z-component, will be ignored for now. An SPP is a material

with shape satisfying the equation of the thickness $h(\phi) = h_0 + h_s/(2\pi)\phi$, where ϕ is the azimuthal angle, h_0 is the base height, and h_s is the step height. As a result of the optical potential, a neutron propagating along the center of the SPP picks a phase,

$$\alpha(\phi) = \alpha_0 + q\phi, \quad (6.21)$$

where the uniform phase $\alpha_0 = -Nb_c\lambda h_0$ being the nuclear phase, with Nb_c the scattering length density of the material and λ the neutron wavelength. The topological charge (nothing to do with electronic charge) uniquely quantifies the nature of the singularity at the center of any SPP [98], and is generally defined as,

$$q = \frac{1}{2} \oint d\alpha(\phi). \quad (6.22)$$

When planar waves propagate through such a topology, the wavefronts become a $|q|$ intertwined helical surface, with the helicity or handedness, determined by the sign of q .

6.3.1 On-axis SPP

When a neutron propagates through the center of an SPP with topological charge q , the wavefunction is modified by $e^{iq\phi}$. Let us consider an input state with arbitrary, but well defined quantum numbers,

$$|\psi_{in}\rangle = |n_0, \ell_0\rangle, \quad (6.23)$$

through the center of an SPP. At the exit (we set $z = 0$ without loss of generality), the resulting wavefunction, $e^{iq\phi}|\psi_{in}\rangle$ is expanded in term of the basis functions as,

$$|\Psi_{\text{SPP}}\rangle = \sum_{n=0}^{\infty} \sum_{\ell=-\infty}^{\infty} C_{n,\ell} |n, \ell\rangle, \quad (6.24)$$

where the expansion coefficients are given by,

$$C_{n,\ell} = \int_0^{\infty} d\xi \int_0^{2\pi} d\phi \xi \langle n, \ell | \xi, \phi \rangle \langle \xi, \phi | \Psi_{\text{SPP}} \rangle. \quad (6.25)$$

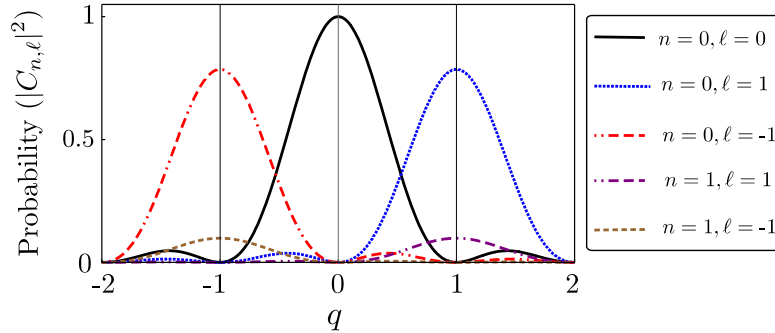


Figure 6.3: The probabilities for each of the $\ell = 0, 1, -1$ and $n = 0, 1$ states when a neutron wavepacket with no OAM ($n_0 = \ell_0 = 0$) passes through an SPP of topological charge q .

In most cases, OAM is generated from an incident state which carries no OAM, i.e $n_0 = \ell_0 = 0$, and so in that case we get,

$$C_{n,\ell} = \begin{cases} e^{iq\pi} \text{sinc}(q\pi) & \text{for } n = \ell = 0 \\ \frac{1}{\sqrt{n!(n+|\ell|)!}} \frac{|\ell|}{2} \Gamma\left(1 + \frac{|\ell|}{2}\right) e^{i(q-\ell)\pi} \text{sinc}[(q-\ell)\pi] & \text{otherwise} \end{cases}. \quad (6.26)$$

where Γ is the Gamma function, and $C_{n,\ell=0} \neq 0$ only for $n = 0$. Since q is a function of the parameters of the SPP, plotted in Fig. 6.3 are the probabilities for a combination of $n = 0, 1$ and $\ell = 0, 1, -1$ against the topological charge q . For $q = +1$, the state is,

$$|\Psi_{\text{SPP}}\rangle = \sum_{n=0}^{\infty} \sqrt{\frac{\pi}{16n!(n+1)!}} |n, 1\rangle.$$

Although the OAM is incremented by the topological charge, the radial quantum number of the outgoing wavepacket can take any allowed values, with the most probable one being $n = 0$, when $n_0 = \ell_0 = 0$. Helium-3 neutron detectors do not distinguish different quantum states (radial and orbital) and so the effect of measurement traces over the radial quantum number.

6.3.2 Off axis SPP

In most neutron beamlines, the coherence length is relatively small (1-100 nm) compared to the size of the SPP, which is the same size as the neutron beam (1 cm). As mentioned,

the state exiting the SPP has a tangential linear momentum, which can be represented as a sum over the basis states of the SPP axis or the internal OAM on the wavepacket axis, such that the resulting beam carries an external OAM. Consider a neutron wavepacket propagating parallel to the SPP axis, and displaced by ξ_0 , as shown in Fig. 6.2. A state $|\psi_{in}\rangle$ gets modified to $|\Psi_{\text{SPP}}\rangle = e^{iq\phi}|\psi_{in}\rangle$. Expanding in terms of the basis vector $\{\psi_{n\ell}(\rho, \varphi)\}$ of the center of the wavepacket, one obtains,

$$|\Psi_{\text{SPP}}\rangle = \sum_{n_r=0}^{\infty} \sum_{\ell=-\infty}^{\infty} C_{n,\ell}|n, \ell\rangle, \quad (6.27)$$

with the coefficients,

$$C_{n,\ell} = \int_0^{\infty} \int_0^{2\pi} \langle n, \ell|\rho, \varphi\rangle \langle \rho, \varphi|\Psi_{\text{SPP}}\rangle \rho d\rho d\varphi, \quad (6.28)$$

that satisfy the normalization condition $\sum |C_{n,\ell}|^2 = 1$. A major difference is that, unlike the on-axis, where $\phi = \varphi, \xi = \rho$, ϕ is function of the radial coordinate given by,

$$\phi(\rho, \varphi) = \tan^{-1} \left(\frac{\rho \sin \varphi + \xi_0 \sin \phi_0}{\rho \cos \varphi + \xi_0 \cos \phi_0} \right), \quad \xi(\rho, \varphi) = \rho^2 + \xi_0^2 + 2\rho\xi_0 \cos(\varphi + \phi_0). \quad (6.29)$$

In effect, the periodic linear relationship between ϕ and φ becomes sinusoidal. In this regard, the coefficients depend on the location of the input states and therefore are not guaranteed to be real, as in the on-center case. The mathematics is slightly simplified if we work with the axis of the SPP, namely $\rho d\rho d\varphi \rightarrow \xi d\xi d\phi$. The coefficients are,

$$C_{n,\ell} = \int_0^{\infty} \int_0^{2\pi} \langle n, \ell|\xi, \phi\rangle \langle \xi, \phi|\Psi_{\text{SPP}}\rangle \xi d\xi d\phi, \quad (6.30)$$

with explicit forms (using $\langle \xi, \phi|\Psi_{\text{SPP}}\rangle = \exp[-(\xi^2 + \xi_0^2 - \xi\xi_0 \cos(\phi - \phi_0))/2] / \sqrt{\pi}$) given by (see appendix),

$$C_{n,\ell} = e^{-\frac{\xi_0^2}{2}} e^{-i(\ell-q)\phi_0} \int_0^{\infty} \xi \mathcal{G}_{n,\ell}^{\ell-q}(\xi) d\xi, \quad (6.31)$$

where we define,

$$\mathcal{G}_{n,\ell}^m(\xi) = 2\sqrt{\frac{n!}{(n+|\ell|)!}} \xi^{|\ell|} e^{-\xi^2} \mathcal{L}_n^{|\ell|}(\xi^2) \mathcal{I}_m(\xi\xi_0), \quad (6.32)$$

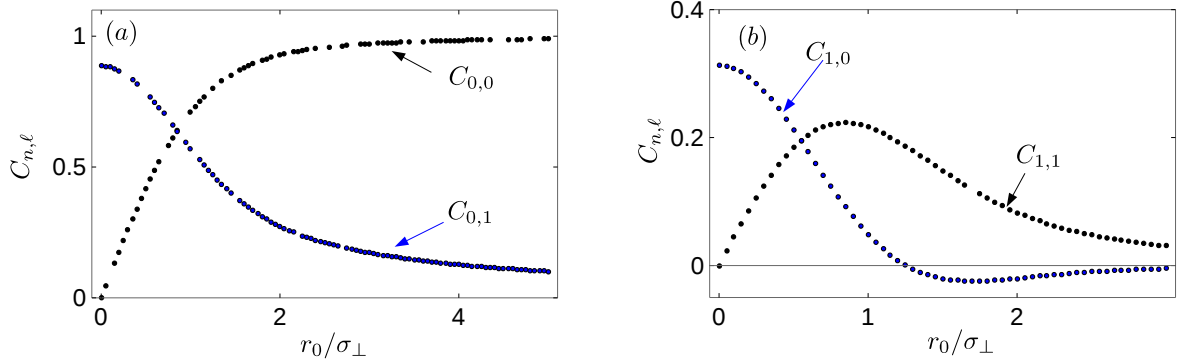


Figure 6.4: Coefficients of the $\ell = 0$ and $\ell = 1$ OAM for the $n = 0$ and $n = 1$ subspaces, for an input state $|0, 0\rangle$. Since the coefficients are complex, we plot for $\phi_0 = 0$.

which are coordinate invariant, as expected.

For an input state $|0, 0\rangle$, the coefficients versus the displacement of the wavepacket from the SPP axis are plotted in Fig. 6.4. Only the case for $\phi_0 = 0$, where the coefficients are real, is plotted. Figure 6.4a is the plots for $C_{0,0}$ and $C_{0,1}$, and Fig. 6.4b is the plots $C_{1,0}$ and $C_{1,1}$. These plots illustrate that the coefficient of the OAM term quickly falls off with the distance from the center i.e the most probable state changes, signifying the difficulty in generating OAM through the center. Since it is impossible to selectively address each of the OAM of given neutrons, we will characterize the average projected OAM onto the transverse plane.

6.3.3 Characterizing OAM using $\langle L_z \rangle$

As shown in the previous section, the probability amplitude of the most probable state decreases rapidly with the distance from the center of the SPP. The average projection of the OAM on the transverse plane can be used to quantify the quality of the wavefunction. Assuming the state is normalized, we get,

$$\bar{\ell} = \langle \Psi_{\text{SPP}} | \hat{L}_z | \Psi_{\text{SPP}} \rangle, \quad (6.33)$$

Since OAM is preserved upon the beam propagation [99], it can be calculated at an arbitrary plane, at $z = 0$, for example. Using Eqs. (6.3) and (6.31)

$$\bar{\ell} = \sum_{n=0}^{\infty} \sum_{\ell=-\infty}^{\infty} \ell |C_{n,\ell}|^2 = 2 \sum_{\ell=-\infty}^{\infty} \ell e^{-\xi_0^2} \int_0^{\infty} \xi e^{-\xi^2} \mathcal{I}_{\ell-q}^2(\xi\xi_0) d\xi. \quad (6.34)$$

It can be noticed that with the term $e^{-\xi_0^2}$, the average OAM decreases significantly from the contribution of the SPP when the wavepackets is far off the center.

6.3.4 Detection using a neutron interferometer

Due to the significant length scale difference between the coherent length and the SPP, OAM generated by an SPP is not directly detectable as all the neutrons are off the axis. Nevertheless, if the SPP is inserted in one arm of the three-blade NI, the beam OAM can be detected Fig. 6.5a. Consider a balanced NI with 50:50 beam splitters, a mirror, and a phase difference χ between the two paths. Denoting the states in the path degree of freedom by $|I\rangle$ and $|II\rangle$, and an incident state of $|\psi_{00}\rangle = |0, 0\rangle$, the neutron wavefunction inside the interferometer just before the third blade is,

$$|\Psi_{\text{NISPP}}\rangle = \frac{1}{\sqrt{2}} \left(|II\rangle |\Psi_{\text{SPP}}\rangle + e^{i\chi} |I\rangle |\psi_{00}\rangle \right). \quad (6.35)$$

After traversing a full three-blade neutron interferometer, the wavefunction becomes,

$$|\Psi_{\text{NISPPPO}}\rangle = \frac{|I\rangle}{2} \left(|\Psi_{\text{SPP}}\rangle + e^{i\chi} |\psi_{00}\rangle \right) + \frac{|II\rangle}{2} \left(|\Psi_{\text{SPP}}\rangle - e^{i\chi} |\psi_{00}\rangle \right). \quad (6.36)$$

The probability of detecting a neutron at the O-beam detector is $I_0 = |\langle I | \Psi_{\text{NISPPPO}} \rangle|^2$. Considering the fact that many neutrons arriving at the detector take different trajectories through the SPP, the average intensity on a 2D position sensitive detection at the output is a sum over these neutrons given by,

$$\overline{I_{2D}}(\xi, \chi, \phi) = \frac{1}{2} F(\xi, \phi) \left(1 + \cos(\chi + \ell\phi) \right). \quad (6.37)$$

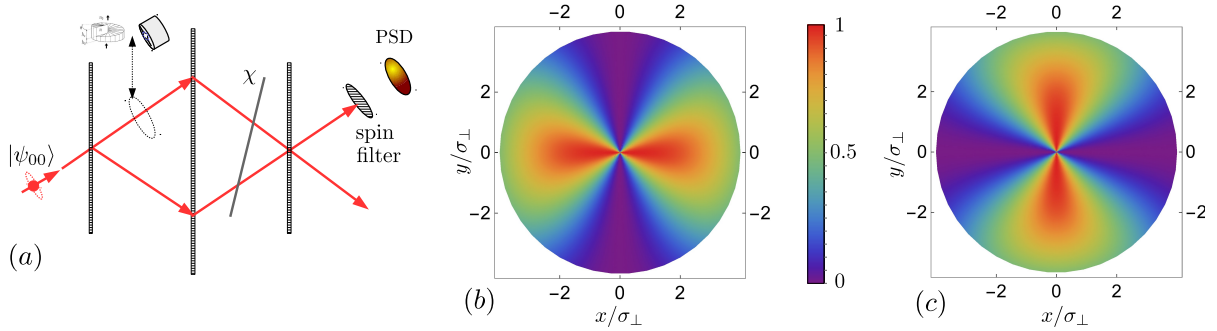


Figure 6.5: A schematic setup and a 2D plot of the intensity at the O-beam when a spiral phase plate (SPP) of topology ℓ is placed on one arm of a three-blade NI. In (a) is the schematic experimental setup showing the phase difference, χ , between the two paths. The incident state $|\psi_{00}\rangle$ carries no OAM. In (b) is the intensity distribution with $\chi = 0$ and $\ell = 2$, and in (c) is the intensity with $\chi = \pi/2$ and $\ell = 2$.

where the envelope function $F(\xi, \phi)$, over the area of radius R , is independent of ϕ , due to symmetry and is given by

$$F(\xi, \phi) = \frac{1}{\pi^2 R^2} \int_0^R \xi_0 d\xi_0 \int_0^{2\pi} d\phi_0 e^{-\xi^2 - \xi_0^2 + \xi \xi_0 \cos(\phi - \phi_0)} = \frac{2e^{-\xi^2}}{\pi R^2} \int_0^R \xi_0 d\xi_0 e^{-\xi_0^2} \mathcal{I}_0(2\xi \xi_0). \quad (6.38)$$

This intensity is that of a beam carrying OAM ℓ (relative to the axis of the SPP). In Fig. 6.5 are 2D intensity distributions for $\ell = 2$, for two values of χ . As χ changes, the OAM profile is rotated by an equivalent amount as shown in Fig. 6.5b for $\chi = 0$ and in Fig. 6.5c for $\chi = \pi/2$. The internal OAM from a SPP is extremely difficult to achieve in the case of a neutron beam. In the following sections we propose and analyse a method to create a neutron spin-orbit state over the coherence length of a neutron wavepacket.

6.4 Spin-orbit states of a neutron wavepacket

In order to generate the spin-orbit states, the spin independent SPP is replaced with a spatially dependent spin rotation. The OAM are generated as a result of the topological

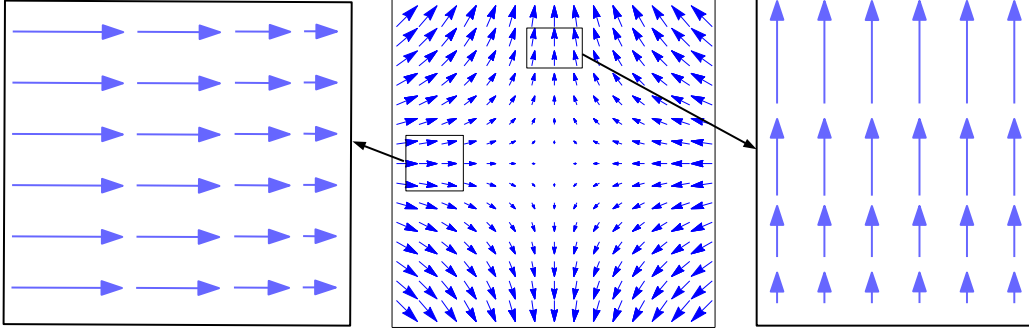


Figure 6.6: Vector plot of a quadrupole, with the region $x \gg y$ along the x -axis and $y \gg x$ along the y -axis shown. In these regions, the quadrupole behaves approximately as a linear magnetic gradient.

phase arising from the spin rotations induced by a quadrupole magnetic field. The resulting state is a spin-orbit state, as illustrated in the next subsection.

6.4.1 Generating operator for spin-orbit states

Consider a spin-polarized (along the z -axis) neutron wavepacket travelling through a quadrupole magnetic field geometry, Fig. 6.6, whose components satisfy, $\partial B_x/\partial y = -\partial B_y/\partial x$. In Cartesian coordinates, it is given by,

$$\mathbf{B} = |\nabla B| r (\cos(q\phi), \sin(q\phi), 0), \quad (6.39)$$

where $|\nabla B|$ is the quadrupole gradient, r is the distance from the quadrupole's center, and the topological charge $q = -1$. At a fixed radius, the magnetic field strength is a constant, but the orientation varies with the azimuthal direction. The Hamiltonian inside the quadrupole can be parametrized by,

$$H = \frac{1}{2} \gamma \hat{\boldsymbol{\sigma}} \cdot \mathbf{B}, \quad (6.40)$$

where $\gamma = 2\mu_n/\hbar$ is the gyromagnetic ratio of the neutrons, and $\hat{\boldsymbol{\sigma}}$ is the Pauli matrix vector (note: there is no relationship between $\hat{\boldsymbol{\sigma}}$ and σ_{\perp}). A more informative form of the

Hamiltonian is,

$$\begin{aligned}
H &= \frac{1}{2}\gamma|\nabla B|r\left(\hat{\sigma}_x \cos(q\phi) + \hat{\sigma}_y \sin(q\phi)\right), \\
&= \frac{1}{2}\gamma|\nabla B|r\left(\frac{\hat{\sigma}_x}{2}\left(e^{iq\phi} - e^{-iq\phi}\right) - i\frac{\hat{\sigma}_y}{2}\left(e^{iq\phi} + e^{-iq\phi}\right)\right), \\
&= \frac{1}{2}\gamma|\nabla B|r\left(\hat{\ell}_+\hat{\sigma}_+ + \hat{\ell}_-\hat{\sigma}_-\right),
\end{aligned} \tag{6.41}$$

where, ℓ_+ is the raising and ℓ_- is the lowering operator for OAM, and $\hat{\sigma}_+$ and $\hat{\sigma}_-$ are conditional spin-flipping operators. Their explicit forms are,

$$\hat{\sigma}_+ = \frac{1}{2}(\hat{\sigma}_x + i\hat{\sigma}_y), \quad \hat{\sigma}_- = \frac{1}{2}(\hat{\sigma}_x - i\hat{\sigma}_y), \tag{6.42}$$

$$\hat{\ell}_+ = e^{-iq\phi}, \quad \hat{\ell}_- = e^{+iq\phi}. \tag{6.43}$$

The operators ℓ_{\pm} and $\hat{\sigma}_{\pm}$ provide a clear relationship between the spin orientation of the incident neutron and the resulting OAM of the output state through the spin-orbit component $\hat{\ell}_+\hat{\sigma}_+ + \hat{\ell}_-\hat{\sigma}_-$.

Consider a quadrupole of length D , then the time spent by the neutron inside the quadrupole is $t_Q = Dv_z^{-1}$, where $v_z = 2\pi\hbar m^{-1}\lambda^{-1}$ is the velocity of the neutron. Ignoring the scattering effect, and the change of direction of the center of the wavepacket (Stern-Gerlach effects), the unitary operator is

$$\begin{aligned}
U_Q &= \exp\left[i\frac{\gamma|\nabla B|rD}{2v}(\hat{\sigma}_x \cos \phi - \hat{\sigma}_y \sin \phi)\right], \\
&= \cos\left(\frac{\pi r}{2r_c}\right)\mathbb{1} + i\sin\left(\frac{\pi r}{2r_c}\right)(\hat{\ell}_+\hat{\sigma}_+ + \hat{\ell}_-\hat{\sigma}_-).
\end{aligned} \tag{6.44}$$

We have conveniently re-parametrized the operator using the transverse radius r_c at which the spin state is reversed on passing through the length of the quadrupole, $\gamma|\nabla B|r_c D/v_z = \pi$. The action of the quadrupole operator is simply to increment the orbital state, and equipping the radial quantum number with information about the number of spin rotations along that direction.

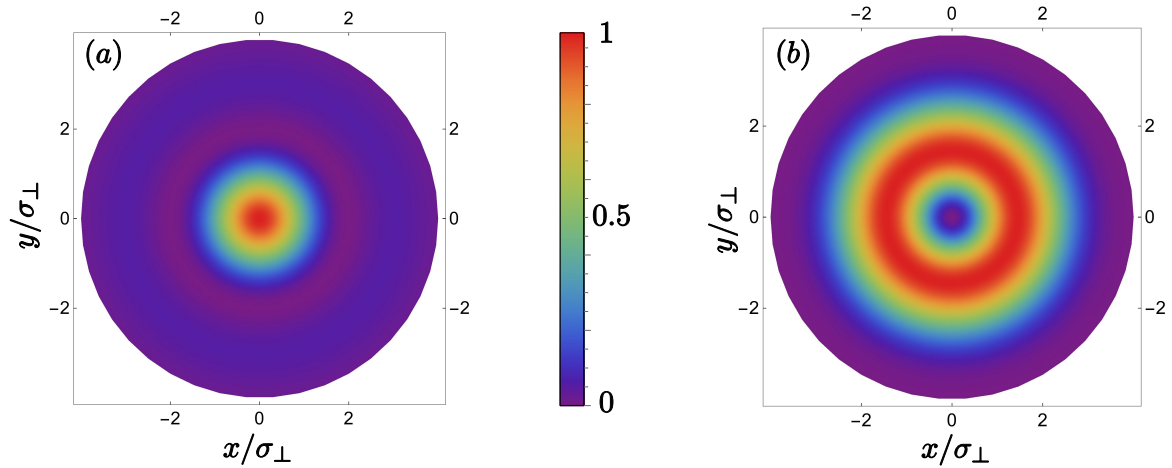


Figure 6.7: 2D intensity of the neutron after a single quadrupole. (a) the component with no OAM, $\ell = 0$ and (b) the component with OAM, $\ell = 1$. In the plots, the coherence length $\sigma_{\perp} = 2$, and $r_c/\sigma_{\perp} = 1$.

6.4.2 On-axis spin-orbit states

As in the case of an SPP, consider the case where an arbitrary spin up polarized basis state, $|\psi_{in\uparrow}\rangle = |n_0, \ell_0, \uparrow\rangle$, is incident through the center of a quadrupole. As mentioned above, the quantities k_z , and Δ_z , defining the wavefunction are all conserved upon propagation through a quadrupole magnetic field so that the state emerging (ignoring the z component) is,

$$|\Psi_Q\rangle = \cos\left(\frac{\pi r}{2r_c}\right) |n_0, \ell_0, \uparrow\rangle + ie^{i\phi} \sin\left(\frac{\pi r}{2r_c}\right) |n_0, \ell_0, \downarrow\rangle. \quad (6.45)$$

This state is spin coupled to the OAM state, which we refer to subsequently as spin-orbit. With a spin filter after a quadrupole, the position sensitive intensities for each of the spin states for $\ell = 0$ and $\ell = 1$ are,

$$I_{\downarrow, \ell=1} = \frac{e^{-\xi^2}}{\pi} \sin^2\left(\frac{\pi\sigma_{\perp}\xi}{2r_c}\right), \quad \text{and} \quad I_{\uparrow, \ell=0} = \frac{e^{-\xi^2}}{\pi} \cos^2\left(\frac{\pi\sigma_{\perp}\xi}{2r_c}\right) \quad (6.46)$$

The intensities are shown in Fig. 6.7 with spin up in (a) and spin down in (b). The spin-down intensity is zero at the origin, as a result of the geometry of the magnetic field. The

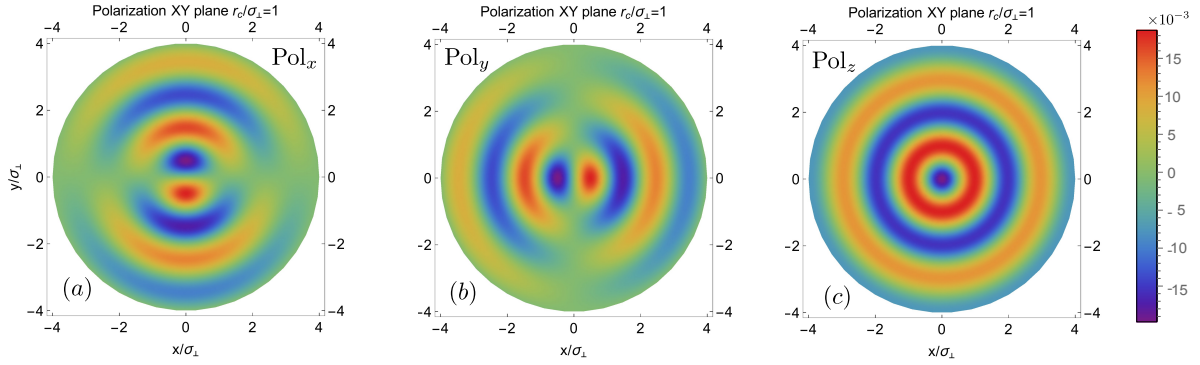


Figure 6.8: 2D plot of the components of polarization along the x-axis (a), along the y-axis (b), and along the z-axis, for $r_c = \sigma_\perp = 4$.

integrated intensities are,

$$\begin{aligned}
 I_\uparrow &= 2 \int_0^\infty \xi e^{-\xi^2} \cos\left(\frac{\pi\sigma_\perp\xi}{2r_c}\right)^2 d\xi = 1 - \frac{\pi\sigma}{2r_c} \mathcal{F}\left(\frac{\pi\sigma_\perp}{2r_c}\right), \\
 I_\downarrow &= 2 \int_0^\infty \xi e^{-\xi^2} \sin\left(\frac{\pi\sigma_\perp\xi}{2r_c}\right)^2 d\xi = \frac{\pi\sigma}{2r_c} \mathcal{F}\left(\frac{\pi\sigma_\perp}{2r_c}\right),
 \end{aligned} \tag{6.47}$$

where \mathcal{F} is the Dawson function [100].

One interesting quantity to consider is the polarization. The polarization gives the component of the spin orientation in each of the x, y, z -axes is expressed as,

$$\text{Pol}_j = \langle \Psi_Q | \sigma_j | \Psi_Q \rangle, \tag{6.48}$$

where $j \in \{x, y, z\}$. Density plots of the polarization along each x-, y- and z-axis are shown in Figs. 6.8a, b, and c, respectively, for $r_c = \sigma_\perp = 4$

The state in Eq. (6.45) can be expanded in the basis functions as

$$|\Psi_Q\rangle = \sum_{n=0}^{\infty} \sum_{\ell=-\infty}^{\infty} \left(C_{n,\ell,\uparrow} |n, \ell, \uparrow\rangle + i C_{n,\ell,\downarrow} |n, \ell, \downarrow\rangle \right), \tag{6.49}$$

where the expansion coefficients are,

$$\begin{aligned}
 C_{n,\ell,\uparrow} &= \langle n, \ell, \uparrow | \Psi_Q \rangle = \langle n, \ell, \uparrow | \cos(\pi r/2r_c) | n_0, \ell_0, \uparrow \rangle = \langle n | \cos(\pi r/2r_c) | n_0, \rangle \delta_{\ell\ell_0} \\
 &= \delta_{\ell\ell_0} \int_0^\infty G_{n,\ell_0}^{n_0,\ell_0}(\xi) \cos\left(\frac{\pi\sigma_\perp}{2r_c}\xi\right) \xi d\xi
 \end{aligned} \tag{6.50}$$

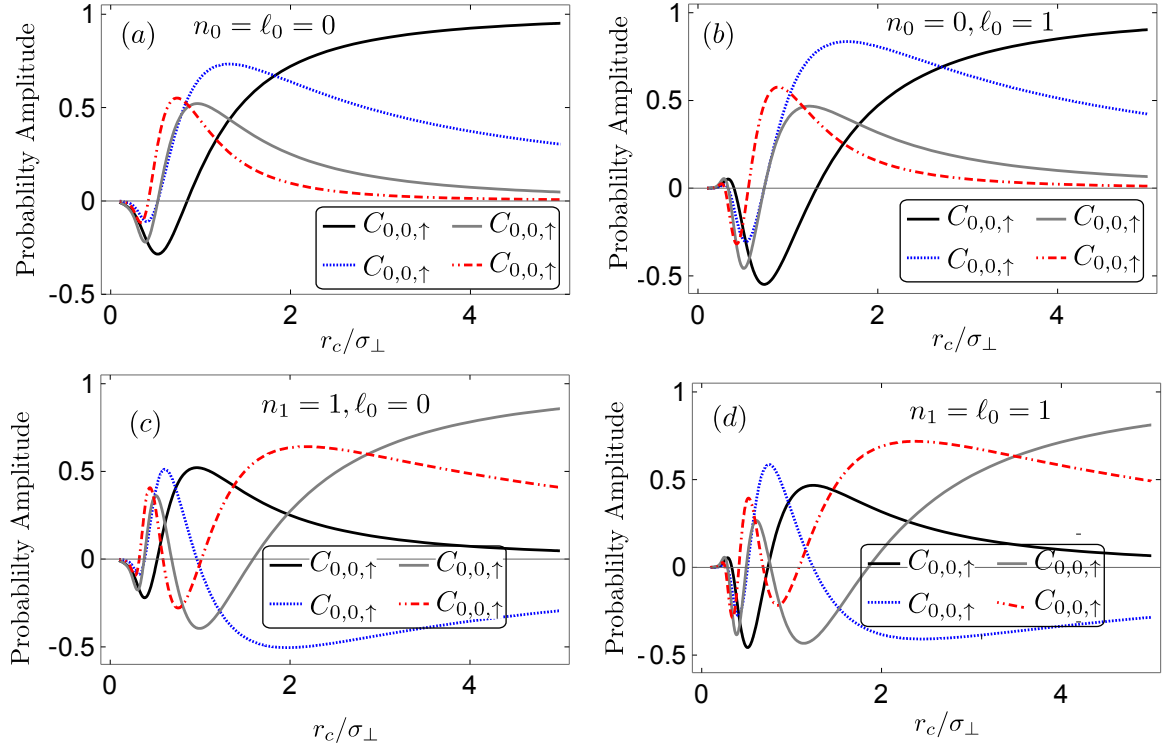


Figure 6.9: The coefficients $C_{n,0,\uparrow}$ and $C_{n,1,\downarrow}$ of the spin-orbit state for the $n = 0$ and $n = 1$ subspaces. The plots are for various inputs states $n_0, \ell_0 \in \{0, 1\}$.

$$\begin{aligned}
C_{n,\ell,\downarrow} &= \langle n, \ell, \downarrow | \Psi_Q \rangle = \langle n, \ell, \downarrow | \sin(\pi r/2r_c) | n_0, \ell_0 + 1, \downarrow \rangle = \langle n | \sin(\pi r/2r_c) | n_0 \rangle \delta_{\ell, \ell_0 + 1} \\
&= \delta_{\ell, \ell_0 + 1} \int_0^\infty G_{n, \ell_0 + 1}^{m_0, \ell_0}(\xi) \sin\left(\frac{\pi \sigma_\perp}{2r_c} \xi\right) \xi d\xi,
\end{aligned} \tag{6.51}$$

where,

$$G_{p,m}^{n,l}(\xi) = 2 \sqrt{\frac{p!n!}{(p+|m|)!(n+|l|)!}} \xi^{|m|+|l|} e^{-\xi^2} \mathcal{L}_p^{|m|}(\xi^2) \mathcal{L}_n^{|l|}(\xi^2). \tag{6.52}$$

The sum selects $\ell = \ell_0$ for the spin-up coefficients, and $\ell = \ell_0 + 1$ for the spin-down coefficients, leading to,

$$|\Psi_Q\rangle = \sum_{n=0}^{\infty} \left(C_{n,\ell_0,\uparrow} |n, \ell_0, \uparrow\rangle + i C_{n,\ell_0+1,\downarrow} |n, \ell_0 + 1, \downarrow\rangle \right). \tag{6.53}$$

Similar to the SPP, the coefficients $C_{n,\ell_0,\uparrow}$ and $C_{n,\ell_0+1,\downarrow}$ are real for all values of r_c/σ_\perp . The ratio r_c/σ_\perp quantifies the action of the quadrupole on the neutron wavepacket of transverse coherent length σ_\perp . The strong quadrupole fields regime corresponds to $r_c \rightarrow 0$ and the weak quadrupole regime to $r_c \rightarrow \infty$. Figure 6.9 shows the various coefficients for the specific subspaces for an input state $|n_0, \ell_0, \uparrow\rangle$, with $n_0, \ell_0 \in \{0, 1\}$. It can be shown that the normalization condition

$$\sum_n (|C_{n,\ell_0,\uparrow}|^2 + |C_{n,\ell_0+1,\downarrow}|^2) = 1, \quad (6.54)$$

holds. For the proof, see the appendix.

In the case where a wide neutron beam is considered, most of the neutrons are off-center and in a similar way as the SPP, the off-axis state of a neutron through the magnetic quadrupole is,

$$|\Psi_Q\rangle = \sum_{n,\ell} \left(C_{n,\ell,\uparrow} |n, \ell, \uparrow\rangle + iC_{n,\ell,\downarrow} |n, \ell, \downarrow\rangle \right), \quad (6.55)$$

with the coefficients,

$$C_{n,\ell,\uparrow} = e^{-\frac{\xi_0^2}{2}} e^{-i\ell\phi_0} \int_0^\infty \mathcal{G}_{n,\ell}^\ell(\xi) \cos\left(\frac{\pi\sigma_\perp}{2r_c}\xi\right) \xi d\xi, \quad (6.56)$$

$$C_{n,\ell,\downarrow} = e^{-\frac{\xi_0^2}{2}} e^{-i(\ell-1)\phi_0} \int_0^\infty \mathcal{G}_{n,\ell}^{\ell-1}(\xi) \sin\left(\frac{\pi\sigma_\perp}{2r_c}\xi\right) \xi d\xi. \quad (6.57)$$

The coefficients in this case are not real, and depend on the location of the center of the wavepacket ξ_0, ϕ_0 of the neutron.

6.4.3 Charactering spin-orbit states via entanglement

A useful measure of entanglement, for a bipartite quantum system, is the concurrence [101, 102, 103], which is equal to 1 when the entanglement is maximum, and 0 when the state is separable. For a bipartite mixed state, ρ_{SO} , the concurrence is given by,

$$\mathcal{C}(\rho_{SO}) = \max\{0, \lambda_1 - \lambda_2 - \lambda_3 - \lambda_4\}, \quad (6.58)$$

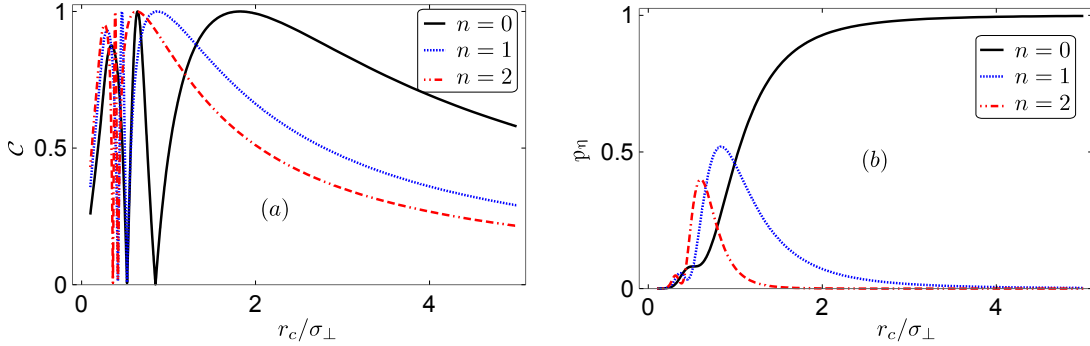


Figure 6.10: (a) Concurrence of the spin-orbit state for the filtered $n = 0, 1, 2$ subspaces and (b) the corresponding probabilities of the filtered spin-orbit $n = 0, 1, 2$.

where the λ_i 's are the eigenvalues, sorted in descending order of the density matrix, $\sqrt{\sqrt{\rho_{SO}}(\sigma_y \otimes \sigma_y)\rho_{SO}^*(\sigma_y \otimes \sigma_y)\sqrt{\rho_{SO}}}$, and ρ_{SO}^* is the complex conjugate of ρ_{SO} . For a pure state, $\rho_{SO} = |\psi_{SO}\rangle\langle\psi_{SO}|$, Eq. (6.58) reduces to,

$$\mathcal{C}(|\psi_{SO}\rangle) = \sqrt{2(1 - \text{Tr}[\rho_S^2])}, \quad (6.59)$$

where $\rho_S = \text{Tr}_O[|\psi_{SO}\rangle\langle\psi_{SO}|]$, is the reduced density matrix obtained by tracing over the subsystem S (or equivalently, tracing over subsystem O).

Let us first consider the entanglement of the spin-orbit neutron state in the case where we filter out a single radial quantum number $n = \eta$. With the current coherent length, the neutron intensity and the field gradients at our setup, filtering a particular radial subspace is extremely difficult to achieve. However, if there are other ways to realize it, we obtain the renormalized pure spin-orbit state ;

$$|\psi_\eta\rangle = \frac{1}{\sqrt{p_\eta}} \left(C_{\eta,\ell_0,\uparrow} |\ell_0 \uparrow\rangle + C_{\eta,\ell_0+1,\downarrow} |\ell_0 + 1 \downarrow\rangle \right), \quad (6.60)$$

where p_η are the probabilities of the wavepacket being in the $n = \eta$ subspace given by,

$$p_\eta = C_{\eta,\ell_0,\uparrow}^2 + C_{\eta,\ell_0+1,\downarrow}^2. \quad (6.61)$$

The concurrence of $|\psi_\eta\rangle$, and the probability p_η , are shown in Fig. 6.10 for the $n = 0, 1, 2$ radial subspaces. The concurrence of the spin-orbit state obtained by passing through a

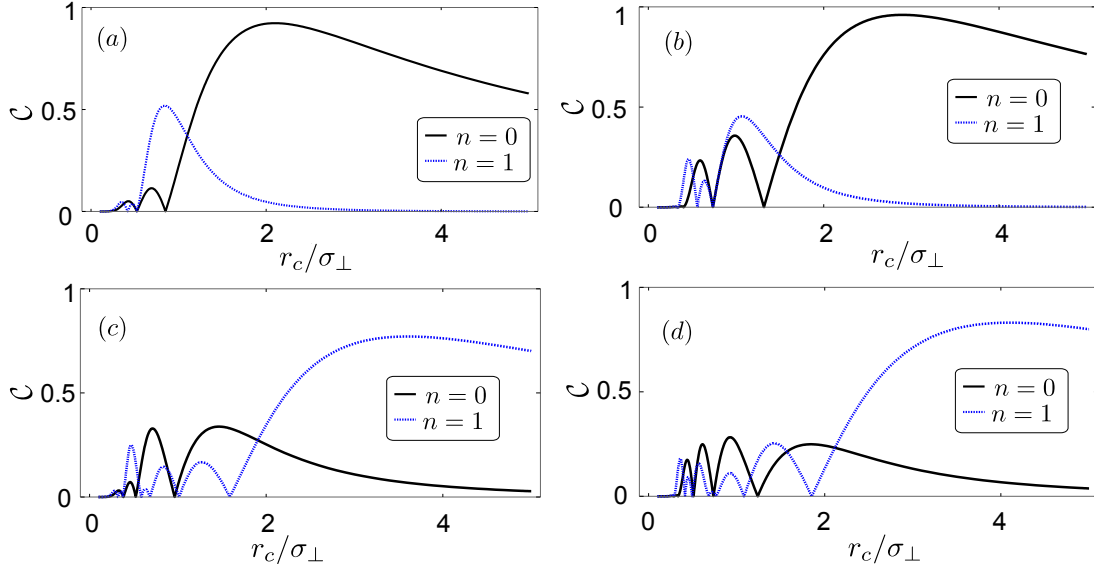


Figure 6.11: Concurrence of the spin-orbit state projected to the $n = 0$ and $n = 1$ subspaces for various inputs. The input is $|0, 0, \uparrow\rangle$ in (a), in (b), the input is $|0, 1, \uparrow\rangle$, in (c), the input is $|1, 0, \uparrow\rangle$, in (d), the input is $|1, 1, \uparrow\rangle$.

quadrupole is maximized for the $n = 0$ radial subspace, where the spin-flip ratio $r/\sigma_{\perp} = 1.82$. In other cases, we considered different input states. Figure 6.11 illustrates the concurrences of the $n = 0, 1$ subspaces for an input state $|0, 0, \uparrow\rangle$ in (a), $|0, 1, \uparrow\rangle$ in (b), $|1, 0, \uparrow\rangle$ in (c), and $|1, 1, \uparrow\rangle$ in (d)

In the second case, we assume that the neutron capture cross-section of the detector to be independent of the n subspace such that the spin-orbit density matrix obtained by tracing over the radial degree of freedom from Eq. (6.53) is,

$$\rho_{SO} = \sum_{n=0}^{\infty} \left(C_{n,0,\uparrow}^2 |0, \uparrow\rangle\langle 0, \uparrow| + iC_{n,0,\uparrow}C_{n,1,\downarrow} |0, \uparrow\rangle\langle 1, \downarrow| - iC_{n,0,\uparrow}C_{n,1,\downarrow} |1, \downarrow\rangle\langle 0, \uparrow| + C_{n,1,\downarrow}^2 |1, \downarrow\rangle\langle 1, \downarrow| \right). \quad (6.62)$$

This reduced state is not a pure state as $\text{Tr}[\rho_{SO}^2] \neq 1$, as seen in Fig. 6.12a. The concurrence of the mixed spin-orbit state as given by Eq. (6.58) is plotted in Fig. 6.12b. We find that the maximum value of concurrence is $\mathcal{C}(\rho_{SO}) = 0.97$, and it occurs at $r_c/\sigma_{\perp} = 1.82$. Hence

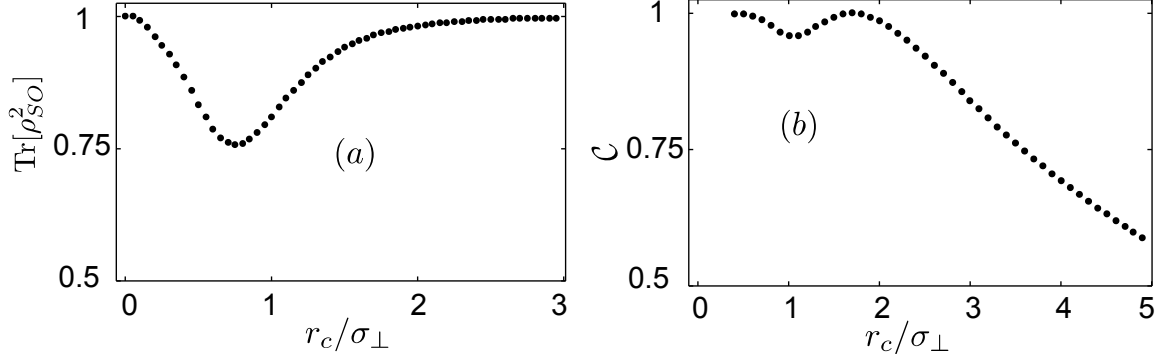


Figure 6.12: (a) $\text{Tr}[\rho_{SO}^2]$ against the r_c/σ_\perp . (b) The concurrence in the spin-orbit states after ρ_{SO} in Eq.6.62.

even after averaging over all radial subspaces, the spin-orbit state is still highly entangled.

6.4.4 Expectation of \hat{L}_z

For an incident state $|0, 0, \uparrow\rangle$ in the on-axis and off-axis case the expectation value $\langle L_z \rangle$ of the state generated by the quadrupole is,

$$\ell = \langle \Psi_Q | \hat{L}_z | \Psi_Q \rangle = \begin{cases} \frac{\pi\sigma}{2r_c} \mathcal{F}\left(\frac{\pi\sigma_\perp}{2r_c}\right) & \text{for } \xi_0 = 0 \\ 2 \sum_m \ell e^{-\xi_0^2} \int_0^\infty \xi e^{-\xi^2} \mathcal{I}_{m-1}^2(\xi\xi_0) \sin^2\left(\frac{\pi\sigma_\perp}{2r_c}\xi\right) d\xi & \text{otherwise} \end{cases} \quad (6.63)$$

A plot of the expectation value $\langle L_z \rangle$ against r_c/σ_\perp is shown in Fig. 6.13. The expectation value decreases both with the strength of the magnet and with the distance off the axis.

6.5 Ramsey-type experiment with spin-orbit states

6.5.1 Spin-Orbit generated from a quadrupole

To experimentally implement this proposal, two quadrupole magnets are constructed from specially orientated discrete NdFeB magnets. A 10-cm-long quadrupole with a gradient

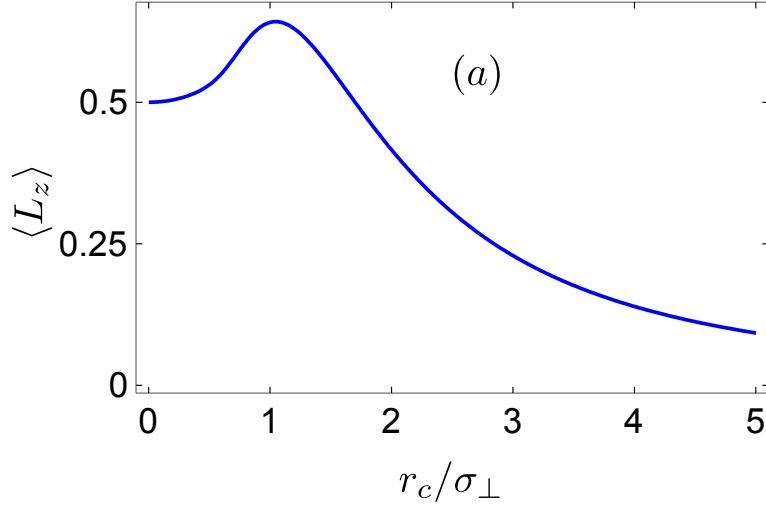


Figure 6.13: Numerical simulation of the on-axis expectation value L_z against the strength of the quadrupole r_c/σ_\perp .

of 13.8 T/cm would be required to satisfy the $r_c = 1.82\sigma_\perp$ condition for neutrons with a typical transverse coherence length of $\sigma_\perp = 100$ nm and a wavelength of 2.71 Å. With NdFeB of a surface field of strength 0.7 T, this gradient corresponds to an inner quadrupole gap of around 1 mm and length 10 cm. Under these experimental conditions, concurrences of 1 and 0.77 are obtained in the filtered subspaces $n = 0$ and 1 in Eq. (6.60) and a value of 0.97 in the trace state in Eq. (6.62).

The Ramsey-type experiment [104] provides a test of the spin-orbit preparation. In the experimental setup, we require a polarized neutron beam, two quadrupoles and a solenoid in between them, see Fig. 6.14. The solenoid provides a uniform magnetic field along the spin quantization axis and introduces a phase shift, β , in the spin degree of freedom through $U_z = \exp(\beta\hat{\sigma}_z/2)$. The second quadrupole can be rotated by angle θ , so that when its magnetic fields are anti-parallel to the first quadrupole, it acts as an inverse operator of the first quadrupole, such that,

$$U_{Q2} = \cos\left(\frac{\pi r}{2r_c}\right) \mathbb{1} + i \sin\left(\frac{\pi r}{2r_c}\right) (e^{-i\theta} \hat{\ell}_+ \hat{\sigma}_+ + e^{i\theta} \hat{\ell}_- \hat{\sigma}_-). \quad (6.64)$$

With the setup shown in Fig. 6.14, when the input state is $|\psi_{00\uparrow}\rangle = |0, 0, \uparrow\rangle$, the state at

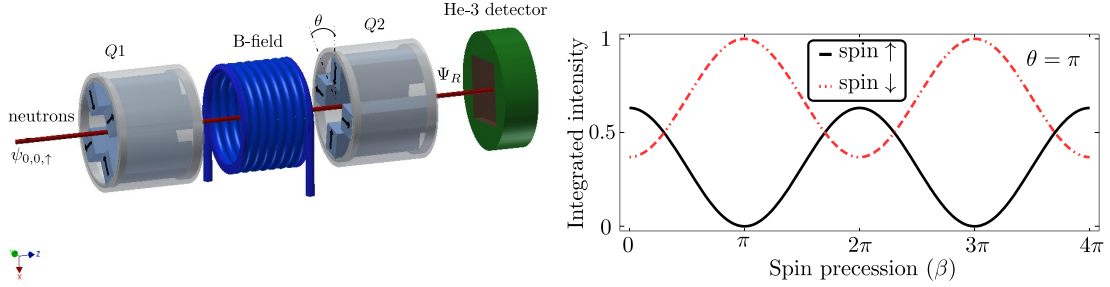


Figure 6.14: On the left is the schematic setup for the spin-orbit Ramsey-type experiment. The arrows on the magnets depict the quadrupole geometry. On the right is the integrated intensity at the output for the spin up and spin down neutrons as a function of the spin precession (β) inside the solenoid. The rotation of the second quadrupole is set to $\theta = \pi$. An identical plot can be obtained when $\beta = \pi$ and the quadrupole rotation is varied. This behavior is an indication of the correlation between the spin and OAM such that a phase induced by the spin rotation can be compensated by the rotation of the quadrupole.

the exit (with the global phase $e^{i\theta/2}$ excluded) is,

$$\begin{aligned}
 |\Psi_R\rangle &= U_{Q2}(\theta)U_z(\beta)U_Q|\psi_{00\uparrow}\rangle \\
 &= \left[\cos\left(\frac{\pi r}{r_c}\right) \cos\left(\frac{\beta - \theta}{2}\right) + i \sin\left(\frac{\beta - \theta}{2}\right) \right] |\psi_{00\uparrow}\rangle + i \sin\left(\frac{\pi r}{r_c}\right) \cos\left(\frac{\beta - \theta}{2}\right) e^{i\phi} |\psi_{00\downarrow}\rangle
 \end{aligned}$$

The integrated intensities at the output are,

$$\bar{I}_{\uparrow}(\beta, \theta) = 1 - \frac{\pi\sigma_{\perp}}{r_c} \mathcal{F}\left(\frac{\pi\sigma_{\perp}}{r_c}\right) \cos^2\left(\frac{\beta - \theta}{2}\right), \quad \bar{I}_{\downarrow}(\beta, \theta) = 1 - \bar{I}_{\uparrow}(\beta, \theta) \quad (6.65)$$

where $\mathcal{F}(\pi\sigma_{\perp}/r_c)$ is the Dawson function. These intensities show the same behaviour if β and θ are interchanged, indicating that the spin rotation can be compensated by rotation of the orbital state; a signature of spin-orbit correlation. On the right plot in Fig. 6.14 is the spin-dependent integrated intensity for β , varied with $\theta = \pi$, and with $r_c/\sigma_{\perp} = 1.82$. Note that the amplitude of the oscillations of the integrated intensity is not 1 because the spin-orbit state obtained by tracing the radial degree of freedom is not pure. Shown in Fig. 6.15 is a 3D plot of the spin up intensity for $r_c/\sigma_{\perp} = 1.82$.

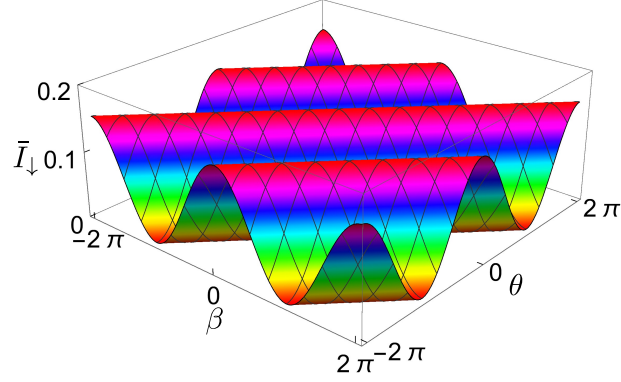


Figure 6.15: 3D plot of the integrated intensity at the output for the spin down neutrons as a function of β and θ . The phase induced by the spin rotation can be compensated by the rotation of the quadrupole.

When the center of the incident wavepacket, $|\Psi_{in}\rangle$, is off-axis, Eq. (6.16), the state at the exit of a Ramsey setup is,

$$|\Psi_R\rangle = \left[\cos\left(\frac{\pi r}{r_c}\right) \cos\left(\frac{\beta - \theta}{2}\right) + i \sin\left(\frac{\beta - \theta}{2}\right) \right] |\Psi_{in, \uparrow}\rangle - i e^{i\phi} \cos\left(\frac{\beta - \theta}{2}\right) \sin\left(\frac{\pi r}{r_c}\right) |\Psi_{in, \downarrow}\rangle. \quad (6.66)$$

After filtering the spin selection, the integrated intensity for spin down is

$$\bar{I}_{\downarrow}(\beta, \theta; \xi_0, \phi_0) = G(\xi_0) \cos^2\left(\frac{\beta - \theta}{2}\right), \quad (6.67)$$

where, the intensity modulation function,

$$G(\xi_0) = 2e^{-\xi_0^2} \int_0^{\infty} \xi e^{-\xi^2} \mathcal{I}_0(2\xi_0\xi) \sin^2\left(\frac{\pi\sigma_{\perp}\xi}{r_c}\right) d\xi. \quad (6.68)$$

Over an area of the quadrupole $\pi\xi_c^2$ selected around the axis gives an amplitude,

$$\bar{G}(r_c/\sigma_{\perp}) = \frac{2}{\xi_c^2} \int_0^{\xi_c} d\xi_0 \xi_0 G(\xi_0) = \begin{cases} \frac{1}{2} & \text{for } \xi_c \rightarrow \infty \\ \frac{\pi\sigma_{\perp}}{r_c} \mathcal{F}\left(\frac{\pi\sigma_{\perp}}{r_c}\right) & \text{for } \xi_c \rightarrow 0 \end{cases} \quad (6.69)$$

This illustrates that, the modulation envelope is independent of the ratio r_c/σ_\perp for large slit radii resulting in an oscillating intensity, with a maximum at $1/2$. In this regime, it is not possible to distinguish the effect of a strong and weak quadrupole. The intensity obtained is statistically equivalent to the one obtained by averaging over the neutrons arriving randomly at any location ξ_0, ϕ_0 . With this in mind, we designed a way to generate OAM around the center of mass of each neutron, a concept that is equivalent to neutrons propagating through the center of the quadrupole.

6.5.2 Spin-orbit generated from linear gradients

The challenge of focusing neutrons on the axis of the magnetic quadrupole leads us to a different process of generating OAM using two magnetic gradients. Two field gradients, one along the x-axis, and one along the y-axis when combined generate a state that is approximately similar to that generated by a quadrupole. The action of each linear gradient is translationally periodic. So by replacing the quadrupole with two linear gradients, we avoid the problem of the origin. A composition of the two gradients,

$$U_x = e^{i\frac{\pi r}{2r_c} \cos \phi \sigma_x}, \quad \text{and} \quad U_y = e^{-i\frac{\pi r}{2r_c} \sin \phi \sigma_y}, \quad (6.70)$$

can be understood via the BCH expansion

$$U_y U_x = e^{-i\frac{\pi r}{2r_c} \sin \phi \sigma_y} e^{i\frac{\pi r}{2r_c} \cos \phi \sigma_x} = e^{i\frac{\pi r}{2r_c} (\hat{\ell}_+ \hat{\sigma}_+ + \hat{\ell}_- \hat{\sigma}_-) + i\frac{\pi^2 r^2}{4r_c^2} \sin(2\phi) \sigma_z + \dots}, \quad (6.71)$$

and noticing that, to first order expansion in r/r_c , the double gradient behaves like a quadrupole. The state generated by the two gradients is similar to that generated by a single quadrupole when higher order terms are ignored.

Figure 6.16 illustrates the generation of OAM using two linear gradients where G_1 and G_2 are magnetic field gradients. The incident neutron, polarized along the z-axis, is represented as a ring for convenience. The spin orientation after the first field gradient is shown with part of the ring state pointing along the y-axis. In the second field, oriented along the y-axis, the same process is repeated so the resulting state is approximated to an OAM state. The intensity for spin up and spin down after a pair of linear gradients with $r_c/\sigma_\perp = 1$ is shown in Fig. 6.16b and c, respectively.

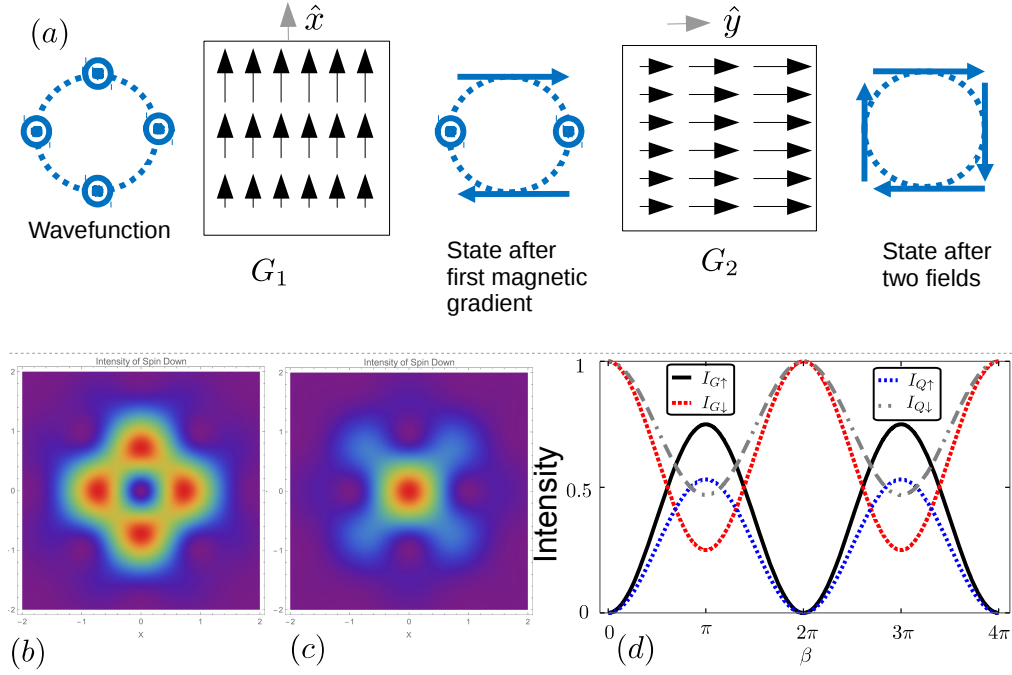


Figure 6.16: Generating OAM using two linear gradients. G_1 is a field gradient along the x -axis, and G_2 along the y -axis. The neutron is depicted as a ring with the incident state polarized along the z -axis. After G_1 , the spin that experience the same field are left in the same configuration (unchanged in this setup). In G_2 , the same process is repeated. 2D intensity of the neutron after a pair of linear gradients, (a) is the spin down and (b) is the the spin up for $r_c/\sigma_\perp = 1$. (d) Ramsey fringe pattern for a pair of quadrupoles compared to two pairs of linear gradients and they show a significant agreement.

In the proposed implementation, the gradients are realized by a quadrupole far off the center. The field of a quadrupole is,

$$\mathbf{B} = |\nabla B| r (\cos \phi, -\sin \phi, 0) = \begin{cases} |\nabla B| r \cos \phi & \text{for } \phi \rightarrow 0 \\ -|\nabla B| r \sin \phi & \text{for } \phi \rightarrow \pi/2 \end{cases}, \quad (6.72)$$

and is plotted in Fig. 6.6, with regions of the field shown at $x \gg y$ along the x -axis and $y \gg x$ along the y -axis. In these regions, the quadrupole is approximated to a linear gradient.

The fidelity of the state in this case is simply the overlap between the state generated from a quadrupole and that from two linear gradients can be used to quantify the deviations. We instead focus on the Ramsey fringe intensity for a pair of quadrupoles and two pairs of linear gradients. With the flipping radius $r_c/\sigma_\perp = 1$, and the background field parameter β varied, the intensity is shown in Fig. 6.16d.

6.6 Spin-orbit states in a neutron interferometer

Consider a quadrupole on one arm of a balance three-blade NI. Denoting the states in the path degree of freedom by $|I\rangle$ and $|II\rangle$ and incident state of $|\psi_{00\uparrow}\rangle = |0, 0, \uparrow\rangle$, the neutron wavefunction inside the interferometer just before the third blade is,

$$|\Psi_{\text{NIQ}}\rangle = \frac{1}{\sqrt{2}} \left(|I\rangle |\Psi_Q\rangle + e^{i\chi} |II\rangle |\psi_{00\uparrow}\rangle \right), \quad (6.73)$$

where χ is the phase difference between the two arms of the NI, and $|\Psi_Q\rangle$ is the quadrupole state given in Eq. (6.53). Upon traversing a full interferometer, the wavefunction at the output is,

$$|\Psi_{\text{NIQO}}\rangle = \frac{|I\rangle}{2} \left(|\Psi_Q\rangle + e^{i\chi} |\psi_{00\uparrow}\rangle \right) + \frac{|II\rangle}{2} \left(|\Psi_Q\rangle - e^{i\chi} |\psi_{00\uparrow}\rangle \right). \quad (6.74)$$

Given that the topological charge of the quadrupole is $\ell = 1$, the unfiltered intensity at the O-beam is

$$\overline{I_{2D}}(\xi, \chi, \phi) = \frac{F(\xi, \phi)}{2} \left[1 + \cos \left(\frac{\pi \sigma_\perp \xi}{2r_c} \right) \cos \chi \right], \quad (6.75)$$

contains a radial dependence modulation, but not the orbital, with $F(\xi, \phi)$ given earlier in Eqn. (6.38). It is possible to insert a spin flipper in the arm of the NI that doesn't contain the quadrupole. In this case, the unfiltered intensity at the O-beam,

$$\overline{I_{2D}}(\xi, \chi, \phi) = \frac{F(\xi, \phi)}{2} \left[1 + \sin \left(\frac{\pi \sigma_\perp \xi}{2r_c} \right) \sin(\chi + \phi) \right], \quad (6.76)$$

is dependent on the orbital state. Figure 6.17 is the 2D intensity distribution with spin flip (a) and without spin flip (b). Other configurations are possible with spin filters.

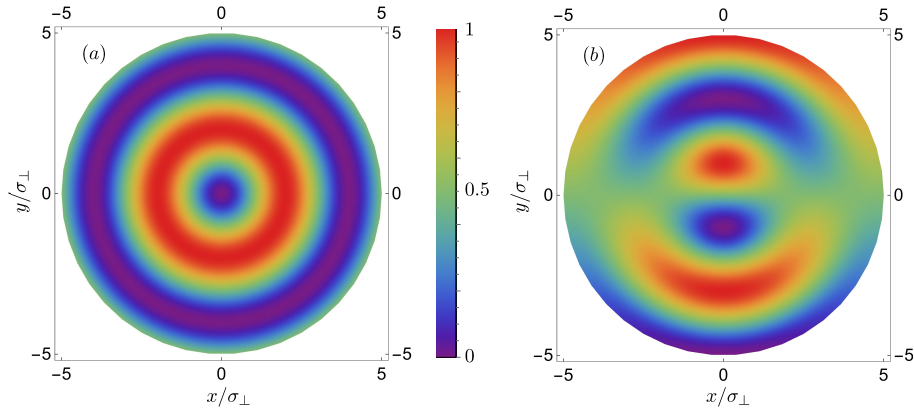


Figure 6.17: 2D intensity distribution at the unfiltered O-beam of an NI relative to the center of symmetry of the quadrupole, when a spin polarized neutron is incident into the interferometer. In (a), there is no spin flipper on one arm of the interferometer while in (b), there is a spin-flipper in the arm that doesn't contain the quadrupole.

6.7 Conclusion

We propose a method for preparing spin-orbit states of neutron wave packets that uses a quadrupole magnetic field. We also demonstrated that the spin-orbit state would be entangled, and that this entanglement is maximized for certain values of the coherence length and quadrupole-magnetic-field strength. A Ramsey fringe experiment on the spin-orbit states is also presented.

Chapter 7

Conclusion and Future Prospects

Conclusion

In chapter 2, we presented a description of the NIOFa beamline recently installed in the guide hall of the NCNR. This beamline is designed to work with a DFS NI but the four-blade DFS interferometer used to demonstrate the proof of concept of refocusing mechanical vibrational noise is not compatible with the beamline wavelengths. However, a three-blade symmetric NI has a measured contrast of about 40%.

Significant progress was made to improve temperature stability. A vacuum chamber got tested and showed to achieve a temperature stability of 3mdeg/hr. Furthermore a temperature control box equipped with thermal sensors and heaters to reduce temperature fluctuations to about mK is being tested. With a combination of both methods, the whole assembly is expected to significantly improve the phase stability, thus the contrast.

There are plans to probe material samples on the NIOFa beamline have been made. Most of these measurements will require polarized neutron and a low temperature facility. NIOFa has achieved a neutron polarization of about 98% with a broad-wavelength neutron beam. Despite the significance of that achievement, and because of high polarization requirements for some experiments, there is current work aimed at improving the neutron

polarization to about 99.9% for a neutron beam with broader wavelength and bigger divergence. A cold stage cryostat, capable of reaching temperatures of about 10K, has now been installed for low-temperature measurements.

In chapter 3, we also presented a brief overview of the theory of DD, then some experimental results to show the effect of DD in a three-blade NI. This include controlling the neutron intensity variation at the output of a multiblade device. Since intensity couples to interferometer thickness, the thickness plays an important role in determining the contrast of an unbalanced beam made from a superposition of waves with different amplitudes.

In chapter 4, we discussed the development of an alternative approach to the theory of DD based on unitary evolution in real space. Later on, this new approach is applied to better understand the origin of DD features including the Pendellösung oscillations, beam profiles, and the sum intensity in the Borrmann triangle. It is also extended to the interferogram and contrast of a three-blade NI. Further, our method may be applied to the two-blade and four-blade NIs as well as in the study of finer details of DD without reference to parameters such as the particle wavelength, crystallographic orientation and the interferometer geometry. In addition, it can be applied to the germanium neutron interferometer bearing higher neutron absorption than silicon.

In chapter 5, we showed that noise from the dynamical phase affects a four-blade NI but not a three-blade. According to the theory of DD, the waves emerging from a single crystal has a phase gradients induced by the momentum distribution of the incident beam when extended to an NI. In order to remove the momentum phase gradients, we proposed a five-blade NI design that are robust against both dynamical phase noise and low frequency mechanical vibrational noise. The noise formalism is done with the coherence function and can be generalized to any neutron interferometer geometry, to electrons and atomic interferometers.

In the quest to create an NI, which incorporates spin and orbital states, we propose a method for preparing spin-orbit states of a neutron wave packets using quadrupole magnetic field. We theoretically demonstrated the entanglement in the spin-orbit state and proposed a Ramsey-type experiment between the spin and orbit states. A successful realization of the spin-orbit states will provide an opportunity to use neutron interferometry as a probe

of chiral and helical materials. For example, these unique spin-orbit coupled states may be used to study chiral magnetic materials, spinwaves, and skyrmions.

Future prospects

- The neutron interferometry setup will be adapted to work with a cold stage cryostat, capable of reaching temperatures of about 5K. Low temperature measurements of correlated magnetic system could then be carried out.
- The QI model applied to variations in coherence effect as a function of the transverse beam mismatch in a four-blade NI will be employed. This formulation has the potential to reveal some information that will assist in the design of a four-blade NI refocussing DD phase.
- The QI model will be applied to study various DD features from imperfect and deformed crystal interferometers. This includes near-perfect crystals and pyrolytic graphite.
- Characterization of the five-blade NI will be done by measuring the contrast in each of the loops in the NI. A study of the beam distribution will also help us understand the ratio of neutron living each blade. Measurements of the effect of mechanical vibration noise on a five-blade NI will be done. Further opportunities are:
- Experimentation of higher order interference in a five-blade NI with multiple beams; This is related to the Born's rule.
- Calculations and experiments of the change in the capture cross-section when a neutron carrying OAM propagate through a material like boron and beryllium.
- Generation of OAM states in a lattice using linear gradients, and using it to study skyrmion lattice that are topological phases of matter.

References

- [1] Daniel M. Greenberger. The neutron interferometer as a device for illustrating the strange behavior of quantum systems. Rev. Mod. Phys., 55:875–905, Oct 1983.
- [2] Varley F. Sears. An Introduction to the Theory of Neutron Optical Phenomena and their Applications. Oxford University Press, New York, 1989.
- [3] H. Rauch and S. A. Werner. Neutron Interferometry: Lessons in Experimental Quantum Mechanics. Clarendon Press, 2000.
- [4] Martin Sudo. Quantum Interferometry in Phase Space. Springer, 2006.
- [5] M. Arif, D. E. Brown, G. L. Greene, R. Clothier, and K. Littrell. Multistage position-stabilized vibration isolation system for neutron interferometry. Vibr. Monit. Cont., 2264(1):20–26, 1994.
- [6] D. A. Pushin, M. G. Huber, M. Arif, and D. G. Cory. Experimental Realization of Decoherence-Free Subspace in Neutron Interferometry. Phys. Rev. Lett., 107:150401, 2011.
- [7] C. B. Shahi, M. Arif, D. G. Cory, T. Mineeva, J. Nsofini, D. Sarenac, C. J. Williams, M. G. Huber, and D. A. Pushin. A new polarized neutron interferometry facility at the ncnr. Nucl. Instrum. Meth. Phys. Res. Sec. A, 813:111 – 122, 2016.
- [8] C. W. Clark, R. Barankov, M. G. Huber, M. Arif, D. G. Cory, and D. A. Pushin. Controlling neutron orbital angular momentum. Nature, 525:504–506, 2015.

- [9] J. Nsofini, D.n Sarenac, C. J. Wood, D. G. Cory, M. Arif, C. W. Clark, M. G. Huber, and D. A. Pushin. Spin-orbit states of neutron wave packets. Phys. Rev. A, 94:013605, Jul 2016.
- [10] B. W. Batterman and H. Cole. Dynamical diffraction of x rays by perfect crystals. Rev. Mod. Phys., 36:681–717, Jul 1964.
- [11] J. Nsofini, K. Ghofrani, D. Sarenac, D. G. Cory, and D. A. Pushin. Quantum-information approach to dynamical diffraction theory. Phys. Rev. A, 94:062311, Dec 2016.
- [12] J. Nsofini, D. Sarenac, K. Ghofrani, M.G. Huber, M. Arif, D. G. Cory, and D.A. Pushin. Noise refocusing in a five-blade neutron interferometer. arXiv, 2016.
- [13] E. Rutherford. Nuclear constitution of atoms. Pro. Roy. Soc., 97(686):374–400, 1920.
- [14] J. Chadwick. Possible existence of a neutron. Nature, 129:312, 1932.
- [15] L. deBroglie. Researches on the quantum theory. PhD thesis, Paris University, 1924.
- [16] H. Rauch and S. A. Werner. Neutron Interferometry: Lessons in Experimental Quantum Mechanics, Wave-Particle Duality, and Entanglement. Oxford University Press, 2nd edition, 2015.
- [17] K. A. Olive and Particle Data Group. Review of particle physics. Chin. J. Phys. C, 38(9):090001, 2014.
- [18] E. Wolf. Theory of Coherence and Polarization of Light. Cambridge Press, Cambridge, 2007.
- [19] Eugene Feenberg. The scattering of slow electrons by neutral atoms. Phys. Rev., 40(1):40–54, Apr 1932.
- [20] J. Schwinger. On the polarization of fast neutrons. Phys. Rev., 73:407–409, Feb 1948.
- [21] L. Foldy. The electron-neutron interaction. Phys. Rev., 83:688–688, Aug 1951.

- [22] J. Byrne. Neutron, nuclei and matter. IOP Publication, 1994.
- [23] O. Schaerpf. Properties of beam bender type neutron polarizers using supermirrors. Physica B: Condensed Matter, 156:639 – 646, 1989.
- [24] H. Rauch, A. Zeilinger, G. Badurek, A. Wilfing, W. Bauspiess, and U. Bonse. Verification of coherent spinor rotation of fermions. Phys. Lett., A54(6):425 – 427, 1975.
- [25] R. Colella, A. W. Overhauser, and S. A. Werner. Observation of gravitationally induced quantum interference. Phys. Rev. Lett., 34(23):1472–1474, Jun 1975.
- [26] S. A. Werner, J. L. Staudenmann, and R. Colella. Effect of earth’s rotation on the quantum mechanical phase of the neutron. Phys. Rev. Lett., 42(17):1103–1106, Apr 1979.
- [27] A. Cimmino, G. I. Opat, A. G. Klein, H. Kaiser, S. A. Werner, M. Arif, and R. Clothier. Observation of the topological aharonov-casher phase shift by neutron interferometry. Phys. Rev. Lett., 63(4):380–383, Jul 1989.
- [28] B. E. Allman, A. Cimmino, A. G. Klein, G. I. Opat, H. Kaiser, and S. A. Werner. Scalar Aharonov-Bohm experiment with neutrons. Phys. Rev. Lett., 68(16):2409–2412, Apr 1992.
- [29] A. G. Wagh, V. C. Rakhecha, J. Summhammer, G. Badurek, H. Weinfurter, B. E. Allman, H. Kaiser, K. Hamacher, D. L. Jacobson, and S. A. Werner. Experimental separation of geometric and dynamical phases using neutron interferometry. Phys. Rev. Lett., 78:755–759, Feb 1997.
- [30] A. Zeilinger, R. Gähler, C. G. Shull, W. Treimer, and W. Mampe. Single- and double-slit diffraction of neutrons. Rev. Mod. Phys., 60:1067–1073, Oct 1988.
- [31] H. Maier-Leibnitz and T. Springer. Ein interometer für langsame neutronen. Z. Phys., 167:386, 1962.
- [32] A. G. Klein and S. A. Werner. Neutron optics. Rep. Prog. Phys., 46(3):259, 1983.

- [33] F. Mezei. The principles of neutron spin echo. Springer, Dresden, 1980.
- [34] S. Sponar, J. Klepp, G. Badurek, and Y. Hasegawa. Zero-field and larmor spinor precessions in a neutron polarimeter experiment. Phys. Lett. A, 372(18):3153 – 3156, 2008.
- [35] F. Li, S. R. Parnell, W. A. Hamilton, B. B. Maranville, T. Wang, R. Semerad, D. V. Baxter, J. T. Cremer, and R. Pynn. Superconducting magnetic wollaston prism for neutron spin encoding. Rev. of Sci. Instrum., 85(5), 2014.
- [36] H. Funahashi, T. Ebisawa, T. Haseyama, M. Hino, A. Masaike, Y. Otake, T. Tabaru, and S. Tasaki. Interferometer for cold neutrons using multilayer mirrors. Phys. Rev., A54(1):649–651, Jul 1996.
- [37] M. O. Abutaleb, D. A. Pushin, M. G. Huber, C. F. Majkrzak, M. Arif, , and D. G. Cory. Design of remnant magnetization fecov films as compact, heatless neutron spin rotators. Appl. Phys. Lett., 101:182404, 2012.
- [38] H. Weinfurter, G. Badurek, and H. Rauch. Improved performance of neutron spin flip devices. Physica B, 156-96157:650 – 652, 1989.
- [39] S. Sponar, J. Klepp, R. Loidl, K. Durstberger-Rennhofer, H. Geppert, G. Badurek, H. Rauch, and Y. Hasegawa. Triple entanglement in neutron interferometric and polarimetric experiments. J. Phys.: Conf. Series, 340(1):012044, 2012.
- [40] A. I. Ioffe. The diffraction optics of very cold neutrons. Physica B: Condensed Matter, 174(1):385 – 395, 1991.
- [41] G. van der Zouw. Gravitational and Aharonov-Bohm Phases in Neutron Interferometry. PhD thesis, Wien University, 200.
- [42] D. Sippel, K. Kleinstuck, and G. E. R. Schulze. Pendellosungs interferenzen mit thermischen neutronen an sieinkristallen. Phys. Lett., 14(3):174 – 175, 1965.
- [43] C. G. Shull. Observation of pendellösung fringe structure in neutron diffraction. Phys. Rev. Lett., 21:1585–1589, Dec 1968.

- [44] A. Zeilinger, C. G. Shull, J. Arthur, and M. A. Horne. Bragg-case neutron interferometry. Phys. Rev. A, 28:487–489, Jul 1983.
- [45] S. Kikuta, I. Ishikawa, K. Kohra, and S. Hoshino. Studies on dynamical diffraction phenomena of neutrons using properties of wave fan. J. Phys. Soc. Jpn, 39(2):471–478, 1975.
- [46] V.V Fedorov and V.V Veronin. Neutron diffraction and optics of a noncentrosymmetric crystal. new feasibility of a search for neutron edm. arXiv, 2005.
- [47] K. C. Littrell, B. E. Allman, and S. A. Werner. Two-wavelength-difference measurement of gravitationally induced quantum interference phases. Phys. Rev. A, 56:1767–1780, Sep 1997.
- [48] M. Zawisky, J. Springer, and H. Lemmel. High angular resolution neutron interferometry. Nucl. Instrum. Meth. Phys. Res. Sec. A, 634:S46 – S49, 2011.
- [49] D. A. Pushin. Coherent control of neutron interferometry. PhD thesis, MIT, 2006.
- [50] M. Batz, S. Baeler, W. Heil, E. W. Otten, D. Rudersdorf, J. Schmiedeskamp, Y. Sobolev, and M. Wolf. Helium 3 spin filter for neutrons. J Res Natl Inst Stand Technol, 110:293–298, May 2005.
- [51] T. G. Walker and W. Happer. Spin-exchange optical pumping of noble-gas nuclei. Rev. Mod. Phys., 69:629–642, Apr 1997.
- [52] W C Chen, T R Gentile, C B Fu, S Watson, G L Jones, J W McIver, and D R Rich. Polarized 3 he cell development and application at nist. Journal of Physics: Conference Series, 294(1):012003, 2011.
- [53] P. Saggiu, T. Mineeva, M. Arif, D. G. Cory, R. Haun, B. Heacock, M. G. Huber, K. Li, J. Nsofini, D. Sarenac, C. B. Shahi, V. Skavysh, W. M. Snow, S. A. Werner, A. R. Young, and D. A. Pushin. Decoupling of a neutron interferometer from temperature gradients. Review of Scientific Instruments, 87(12):123507, 2016.

- [54] C. J. Carlile, P. D. Hey, and B. Mack. High-efficiency soller slit collimators for thermal neutrons. J. Phys. E, 10(5):543, 1977.
- [55] Swissneutronics supermirror manual. <http://www.swissneutronics.ch/?id=24>.
- [56] W. H. Zachariasen. Theory of X-ray Diffraction in Crystals. Wiley, New York, 1945.
- [57] R. W. James. In Frederick S. and D. Turnbull, editors, The Dynamical Theory of X-Ray Diffraction, volume 15 of Sol. State Phys., pages 53 – 220. Academic Press, 1963.
- [58] M. Takeda. A simplified method for electron dynamical diffraction with crystal symmetry considerations. physica status solidi (a), 101(1):25–36, 1987.
- [59] H. Rauch and D. Petrascheck. Neutron diffraction. Top. Curr. Phys., 6(3):303, 1978.
- [60] A. Zeilinger. General properties of lossless beam splitters in interferometry . Am. J. Phys., 49(3):882, 1981.
- [61] Yu.G. Abov, N.O. Elyutin, and A.N. Tyulyusov. Dynamical neutron diffraction on perfect crystals. Phys. Atomic Nucl., 65(11):1933–1979, 2002.
- [62] H. Lemmel. Influence of bragg diffraction on perfect crystal neutron phase shifters and the exact solution of the two-beam case in the dynamical diffraction theory. Acta Crystallogr. Sec. A, 69(5):459–474, Sep 2013.
- [63] J. Demarco and R. Weiss. The integrated intensities of perfect crystals. Acta Crystallogr., 19(3):68, 1964.
- [64] H. Lemmel and A. G. Wagh. Phase shifts and wave-packet displacements in neutron interferometry and a nondispersive, nondefocusing phase shifter. Phys. Rev. A, 82:033626, Sep 2010.
- [65] D. Petrascheck and R. Folk. Theory of symmetric Ill interferometer with arbitrary absorption. Phys. Stat. Sol., 34(3):147, 1976.

- [66] S. Abbas, A. G. Wagh, M. Strobl, and W Treimer. First observation of neutron deflections by single crystal prisms. J. Phys., 251(1):012073, 2010.
- [67] N. W. Ashcroft and N. D. Mermin. Solid state physics. Saunders College Publishing, New York, 1976.
- [68] Hartmut Lemmel. Dispersion cancellation in a triple laue interferometer. J. Opt., 16(10):105704, 2014.
- [69] T. Dombek, R. Ringo, D. D. Koetke, H. Kaiser, K. Schoen, S. A. Werner, and D. Dombek. Measurement of the neutron reflectivity for bragg reflections off a perfect silicon crystal. Phys. Rev. A, 64:053607, Oct 2001.
- [70] V. A. Somenkov, S. S. Shilstein, N. E. Belova, and K. Utemisov. Observation of dynamical oscillations for neutron scattering by ge crystals using the inclination method. Solid State Commun., 25(8):593–595, 1978.
- [71] D. Petrascheck and H. Rauch. Multiple laue rocking curves. Acta Crystallogr., A40(3):445–450, 1984.
- [72] G. Borrmann. Die absorption von rontgenstrahlen imfall der interferenz. Z. Phys., 127(4):297–323, 1950.
- [73] H. Lemmel. Dynamical diffraction of neutrons and transition from beam splitter to phase shifter case. Phys. Rev. B, 76:144305, Oct 2007.
- [74] M. Utsuro and V. K. Ignatovich. Handbook of Neutron Optics. Wiley-VCH, 2012.
- [75] D. Bouwmeester, I. Marzoli, G. P. Karman, W. Schleich, and J. P. Woerdman. Optical galton board. Phys. Rev. A, 61:013410, Dec 1999.
- [76] Y. Aharonov, L. Davidovich, and N. Zagury. Quantum random walks. Phys. Rev. A, 48:1687–1690, Aug 1993.
- [77] S. Venegas-Andraca. Quantum walks: a comprehensive review. Quantum Information Processing, 11(5):1015–1106, 2012.

- [78] C. G. Darwin. Xxxiv. the theory of x-ray reflexion. Phil. Magazine Series 6, 27(158):315–333, 1914.
- [79] C. G. Darwin. Xcii. the reflexion of x-rays from imperfect crystals. Phil. Magazine Series 6, 43(257):800–829, 1922.
- [80] V. A. Ambartsumyan. Leading of Invariance Principle in Radiative Transport Theory. Akad. Nauk Arm. SSR, Yerevan, 1981.
- [81] U. Bonse and H. Rauch. Neutron Interferometry. Oxford University Press, Oxford, UK, 1979.
- [82] G. L. Squires. Introduction to Theory of Thermal Neutron Scattering. Cambridge University Press, Cambridge, 1978.
- [83] D. A. Pushin, M. G. Huber, M. Arif, C. B. Shahi, J. Nsofini, C. J. Wood, D. Sarenac, and D. G. Cory. Neutron interferometry at the national institute of standards and technology. Adv. High Energy Phys., Feb 2015.
- [84] D. A. Pushin, M. Arif, and D. G. Cory. Decoherence-free neutron interferometry. Phys. Rev. A, 79(5):053635, 2009.
- [85] D. Petrascheck. Coherence lengths and neutron optics. Phys. Rev. B, 35:6549–6553, May 1987.
- [86] H. Rauch, H. Wolwitsch, H. Kaiser, R. Clothier, and S. A. Werner. Measurement and characterization of the three-dimensional coherence function in neutron interferometry. Phys. Rev. A, 53:902–908, Feb 1996.
- [87] M. G. Huber. Precision measurement of neutron-matter interactions using neutron interferometry. PhD thesis, Tulane University, 2008.
- [88] E. L. Hahn. Spin echoes. Phys. Rev., 80:580–594, Nov 1950.
- [89] H. Y. Carr and E. M. Purcell. Effects of diffusion on free precession in nuclear magnetic resonance experiments. Phys. Rev., 94:630–638, May 1954.

- [90] L. Allen, M. W. Beijersbergen, R. J. C. Spreeuw, and J. P. Woerdman. Orbital angular momentum of light and the transformation of laguerre-gaussian laser modes. Phys. Rev. A, 45:8185–8189, Jun 1992.
- [91] Alison M. Yao and Miles J. Padgett. Orbital angular momentum: origins, behavior and applications. Adv. Opt. Photon., 3(2):161–204, Jun 2011.
- [92] Juan P. T. and Lluís T. Twisted Photons: Applications of Light with Orbital Angular Momentum. Wiley-VCH, March 2011.
- [93] V. Grillo, L. Marrucci, E. Karimi, R. Zanella, and E. Santamato. Quantum simulation of a spin polarization device in an electron microscope. New J. Phys., 15(9):093026, 2013.
- [94] C. W. Clark, R. Barankov, M. G. Huber, D. G. Cory, and D. A. Pushin. Controlling neutron orbital angular momentum. Nature, 525:504–506, Sep 2015.
- [95] R. W. Boyd. Neutrons with a twist. Nature, 525:462–464, Sep 2015.
- [96] G. Nienhuis and L. Allen. Paraxial wave optics and harmonic oscillators. Phys. Rev. A, 48:656–665, Jul 1993.
- [97] O. Steuernagel. Equivalence between focused paraxial beams and the quantum harmonic oscillator. Am. J. Phys., 73(7):625–629, 2005.
- [98] J. F. Nye and M. V. Berry. Dislocations in wave trains. Procs R. Soc. London, Sec. A, 336(1605):pp. 165–190, 1974.
- [99] S. N. Khonina, V. V. Kotlyar, V. A. Soifer, P. Pääkkönen, J. Simonen, and J. Turunen. An analysis of the angular momentum of a light field in terms of angular harmonics. J. Mod. Optics, 48(10):1543–1557, 2001.
- [100] F. Olver, D. Lozier, R. Boisvert, and C. Clark. NIST Handbook of Mathematical Functions. NIST, MD, 2010.
- [101] W. K. Wootters. Entanglement of formation of an arbitrary state of two qubits. Phys. Rev. Lett., 80:2245–2248, Mar 1998.

- [102] P. Rungta, V. Bužek, Carlton M. Caves, M. Hillery, and G. J. Milburn. Universal state inversion and concurrence in arbitrary dimensions. Phys. Rev. A, 64:042315, Sep 2001.
- [103] S. Albeverio and S. Fei. A note on invariants and entanglements. J. Opt. B, 3(4):223, 2001.
- [104] N. F. Ramsey. A molecular beam resonance method with separated oscillating fields. Phys. Rev., 78:695–699, Jun 1950.

Appendix A

A.1 Selected Publications

1. **J. Nsofini**, D. Sarenac, K. Ghofrani, M.G. Huber, M. Arif, D. G. Cory and D.A. Pushin. Noise refocusing in a five-blade neutron interferometer, [arXiv:1704.03589](#), (April 2017).
2. P. Saggi, T. Mineeva, M. Arif, D. Cory, R. Haun, B. Heacock, M. Huber, K. Li, **J. Nsofini**, D. Sarenac, C. Shahi, V. Skavysh, W. Snow, S. Werner, A. Young, and D. Pushin. Decoupling of a Neutron Interferometer from Temperature Gradients, [Rev. Sci Instrum](#), *87*, 123507, (Dec 2016).
3. **J. Nsofini**, K. Ghofrani, D. Sarenac, D. G. Cory, and D. A. Pushin. Quantum information approach to dynamical diffraction theory. [Phys. Rev. A](#), *94*, 062311, (Dec 2016).
4. **J. Nsofini**, D. Sarenace, C. J. Wood, D. G. Cory , M. Arif, C. W. Clerk, M. G. Huber and D. A. Pushin. Spin-Orbit States of Neutron Wavepackets. [Phys. Rev. A](#), *94*, 013605, (Jul 2016).
5. C. B. Shahi, M. Arif, D. G. Cory, T. Mineevag, **J. Nsofini**, et. al. A new polarized neutron interferometry facility at the NCNR. [Nucl. Instrum. Methods Phys. Research A](#), 0168-9002 (Jan 2016).

6. K. Li, M. Arif, D. G. Cory, R. Haun, B. Heacock, M. G. Huber, **J. Nsofini**, et al. Neutron limit on the strongly-coupled chameleon field. [Phys. Rev. D 93, 062001 \(March 2016\)](#).
7. S. A. Owerre and **J. Nsofini**. Antiferromagnetic molecular nanomagnets with odd-numbered coupled spins. [Europhys. Lett., 110, 47002 \(May 2015\)](#).
8. S. A. Owerre and **J. Nsofini**. A toy model for quantum spin Hall effect. [Solid State Commun., 218, 35-39 \(Sep 2015\)](#).
9. D. A. Pushin, M. G. Huber, M. Arif, C. B. Shahi, **J. Nsofini**, C. J. Wood, D. Sarenac, and D. G. Cory. Neutron Interferometry at the National Institute of Standards and Technology. [Adv. High Energy Phys., 2015, 687480 \(2015\)](#).

A.2 Important mathematical relations

$$\int_0^{2\pi} e^{i(n-m)\phi} d\phi = \begin{cases} 2\pi e^{i(n-m)\pi \frac{\sin[(n-m)\pi]}{(n-m)\pi}} & \text{for } n-m \in \mathbb{R} \\ 2\pi & n-m \in \mathbb{Z} \end{cases} \quad (\text{A.1})$$

$$e^{z \cos \phi} = \sum_{m=-\infty}^{\infty} \mathcal{I}_m(z) e^{im\phi}, \quad (\text{A.2})$$

$$\int_0^{\infty} \xi^{\gamma-1} e^{-\xi} \mathcal{L}_n^{\mu}(\xi) d\xi = \frac{\Gamma(\gamma)\Gamma(1-\gamma+\mu+n)}{n!\Gamma(1-\gamma+\mu)}, \quad \gamma > 0 \quad (\text{A.3})$$

$$\delta(t, x) = e^{-t^\alpha} \sum_p \frac{p!}{(p+\alpha)!} \mathcal{L}_p^{|\alpha|}(t) \mathcal{L}_p^{|\alpha|}(x) \quad (\text{A.4})$$

$$2e^{-\xi^2} \int_0^{\infty} e^{-x^2} \mathcal{I}_0(2\xi x) x dx = 1 \quad (\text{A.5})$$

$$2 \int_0^\infty e^{-\xi^2} \mathcal{I}_n(\xi x) \mathcal{I}_n(\xi y) \xi d\xi = e^{\frac{x^2+y^2}{4}} \mathcal{I}_n\left(\frac{xy}{2}\right) \quad \text{for } \text{Re } n > -1 \quad (\text{A.6})$$

$$2e^{-\xi^2} \int_0^\infty e^{-x^2} \sum \mathcal{I}_n^2(\xi x) x dx = 1 \quad (\text{A.7})$$

$$\sum \mathcal{I}_n(\xi^2) = e^{\xi^2} \quad (\text{A.8})$$

A.3 Coefficients of a an SPP

On-axis:

Consider an input state $|n_0, \ell_0\rangle$ on a topological charge of an SPP, $q \in \mathbb{R}$, and $\psi_{n\ell s}(\xi, \phi, z) = \mathcal{N} \xi^{|\ell|} e^{-\frac{\xi^2}{2}} \mathcal{L}_n^{|\ell|}(\xi^2) e^{-i\ell\phi}$, we get expansion coefficients of the output as

$$\begin{aligned} C_{n,\ell} &= \int_0^\infty d\xi \int_0^{2\pi} d\phi r \langle n, \ell | \xi, \phi \rangle \langle \xi, \phi | \Psi_{\text{SPP}} \rangle = \int_0^\infty \int_0^{2\pi} \psi_{n_0, \ell_0}(\xi, \phi) e^{iq\phi} \psi_{n\ell}^*(\xi, \phi) \xi d\xi d\phi \\ &= \int_0^\infty d\xi \xi G_{n,\ell}^{n_0, \ell_0}(\xi) \frac{1}{2\pi} \int_0^{2\pi} e^{i(\ell_0+q-\ell)\phi} d\phi, \quad \text{with,} \quad G_{p,m}^{n,\ell}(\xi) = 2\pi \psi_{pm}(\xi, 0) \psi_{n\ell}(\xi, 0) \\ &= e^{i(\ell_0+q-\ell)\pi} \frac{\text{sin}[(\ell_0+q-\ell)\pi]}{(\ell_0+q-\ell)\pi} \int_0^\infty d\xi \xi G_{n,\ell}^{n_0, \ell_0}(\xi) \end{aligned}$$

where we have used the integral Eq. (A.1), and

$$G_{p,m}^{n,\ell}(\xi) = 2 \sqrt{\frac{p!n!}{(p+|m|)!(n+|\ell|)!}} \xi^{|m|+|\ell|} e^{-\xi^2} \mathcal{L}_p^{|m|}(\xi^2) \mathcal{L}_n^{|\ell|}(\xi^2) \quad (\text{A.9})$$

For an incident state with no OAM $|\psi_{in}\rangle = |0, 0\rangle$,

$$C_{n,\ell} = \int_0^\infty d\xi \xi G_{n,\ell}^{0,0}(\xi) = \begin{cases} e^{iq\pi} \text{sinc}(q\pi) & \text{for } n = \ell = 0 \\ \frac{1}{\sqrt{n!(n+|\ell|)!}} \frac{|\ell|}{2} \Gamma\left(1 + \frac{|\ell|}{2}\right) e^{i(q-\ell)\pi} \text{sinc}[(q-\ell)\pi] & \text{otherwise} \end{cases},$$

by making use of the LG normalization integral identity in Eq. (A.3).

Off-axis in terms of SPP coordinate:

The expansion coefficients are from $\psi_{in} = \sum_{l=-\infty}^{\infty} \frac{1}{\sqrt{\pi}} e^{-\frac{\xi^2 + \xi_0^2}{2}} I_l(\xi \xi_0) e^{il(\phi - \phi_0)}$, and $e^{iq\phi} \psi_{in}$ as

$$C_{n,\ell} = \int_0^\infty d\xi \int_0^{2\pi} d\phi r \langle n, \ell | \xi, \phi \rangle \langle \xi, \phi | \Psi_{\text{SPP}} \rangle$$

Using the Jacobi-anger transform in Eq.(A.2), and also (A.1), we get for $\xi_0 \neq 0$, $\phi_0 \neq 0$

$$\begin{aligned} C_{n,\ell} &= 2e^{-\frac{\xi_0^2}{2}} \int_0^\infty \xi d\xi e^{-\frac{\xi^2}{2}} \sum_{m=-\infty}^{\infty} \mathcal{I}_m(\xi \xi_0) \psi_{n\ell}^*(\xi, 0) \frac{1}{2\pi} \int_0^{2\pi} d\phi e^{im(\phi - \phi_0)} e^{iq\phi} e^{-il\phi} \\ &= e^{-\frac{\xi_0^2}{2}} \sum_{m=-\infty}^{\infty} \int_0^\infty d\xi \xi \mathcal{G}_{n,\ell}^m(\xi, \xi_0) e^{-im\phi_0} \frac{1}{2\pi} \int_0^{2\pi} d\phi e^{i(m+q-\ell)\phi} \\ &= e^{-\frac{\xi_0^2}{2}} \begin{cases} \sum_{m=-\infty}^{\infty} e^{-im\phi_0} e^{i(m+q-\ell)\pi \frac{\sin[(m+q-\ell)\pi]}{(m+q-\ell)\pi}} \int_0^\infty d\xi \xi \mathcal{G}_{n,\ell}^m(\xi, \xi_0) & \text{for } m+q-\ell \in \mathbb{R} \\ e^{-il\phi_0} \int_0^\infty d\xi \xi \mathcal{G}_{n,\ell}^{q-\ell}(\xi, \xi_0) & \text{for } m+q-\ell \in \mathbb{Z} \end{cases}, \end{aligned}$$

where another function is defined as

$$\mathcal{G}_{p,m}^\ell(\xi, \xi_0) = 2 \sqrt{\frac{p!}{(p+|m|)!}} \xi^{|m|} e^{-\xi^2} \mathcal{L}_p^{|m|}(\xi^2) \mathcal{I}_\ell(\xi \xi_0) \quad (\text{A.10})$$

Normalization:

The normalization condition of the OAM states of an SPP can be shown using the coefficients in Eq. (6.31) as follows for the integer case.

$$\begin{aligned} \sum_{n,\ell} |C_{n,\ell}|^2 &= e^{-\xi_0^2} \int_0^\infty d\xi \int_0^\infty d\zeta \xi \zeta \sum_{n,\ell} \mathcal{G}_{n,\ell}^{q-\ell}(\xi, \xi_0) \mathcal{G}_{n,\ell}^{q-\ell}(\zeta, \xi_0) \\ &= 4e^{-\xi_0^2} \sum_\ell \int_0^\infty d\xi \int_0^\infty d\zeta \xi \xi^{|\ell|} e^{-\xi^2} \zeta \zeta^{-|\ell|} \delta(\zeta^2, \xi^2) \mathcal{I}_{\ell-q}(\xi \xi_0) \mathcal{I}_{\ell-q}(\zeta \xi_0) \quad \text{Eq. (A.4)} \end{aligned}$$

where we have used:

$$\begin{aligned} \sum_{n,\ell} \mathcal{G}_{n,\ell}^{q-\ell}(\xi, \xi_0) \mathcal{G}_{n,\ell}^{q-\ell}(\zeta, \xi_0) &= \sum_n \frac{4n!}{(n+|\ell|)!} \xi^{|\ell|} e^{-\xi^2} \zeta^{|\ell|} e^{-\zeta^2} \mathcal{L}_n^{|\ell|}(\xi^2) \mathcal{L}_n^{|\ell|}(\zeta^2) \mathcal{I}_{\ell-q}(\xi \xi_0) \mathcal{I}_{\ell-q}(\zeta \xi_0) \\ &= 4 \xi^{|\ell|} e^{-\xi^2} \zeta^{-|\ell|} \mathcal{I}_{\ell-q}(\xi \xi_0) \mathcal{I}_{\ell-q}(\zeta \xi_0) \delta(\zeta^2 - \xi^2) \quad \text{using Eq. (A.4),} \end{aligned}$$

Using the property of delta function,

$$\delta(\xi^2, \zeta^2) = \frac{1}{2|\zeta|} \left(\delta(\xi - \zeta) + \delta(\xi + \zeta) \right) = \frac{1}{2\zeta} \delta(\xi - \zeta) \quad \text{for } \xi, \zeta > 0 \quad (\text{A.11})$$

we obtain

$$\sum_{n,\ell} |C_{n,\ell}|^2 = 2e^{-\xi_0^2} \int_0^\infty d\xi \xi e^{-\xi^2} \sum_\ell \mathcal{I}_{\ell-q}^2(\xi\xi_0) = 1 \quad \text{using Eq. (A.7).}$$

A.4 Input state expanded in to the LG basis

A wave packet located off axis with its center located at a $x_0 = r_0 \cos \phi_0, y_0 = r_0 \sin \phi_0$ can be represented similarly to eqn. 6.15 as

$$\psi_{in}(x, y) = N e^{-(x-x_0)^2 - (y-y_0)^2}, \quad \text{cartesian coordinates} \quad (\text{A.12})$$

$$\psi_{in}(\xi, \phi) = N e^{-\xi^2 - \xi_0^2 + 2\xi\xi_0 \cos(\phi - \phi_0)}, \quad \text{polar coordinates} \quad (\text{A.13})$$

where $\xi = \sqrt{x^2 + y^2}, \phi = \arctan(y/x)$, and $N = 1/\sqrt{\pi}$. Using the Jacobi-Anger transform and the Bessel to Laguerre relation

$$e^{z \cos \phi} = \sum_{l=-\infty}^{\infty} \mathcal{I}_l(z) e^{il\phi}, \quad (\text{A.14})$$

$$\mathcal{I}_l(z) = \left(\frac{z}{2}\right)^l \frac{e^{-t}}{\Gamma(l+1)} \sum_{p=0}^{\infty} \frac{\mathcal{L}_p^{|l|}(-z^2/4t)}{p+l C_p p!}, \quad (\text{A.15})$$

where, $p+l C_p = (p+l)!/l!$ for positive l and arbitrary t , the incident beam off axes can be represented as a spectral decomposition of Laguerre-Gauss modes. Eqn. (A.13) becomes

$$\psi_{in}(\xi, \phi) = \frac{1}{\sqrt{\pi}} e^{-\frac{\xi^2 + \xi_0^2}{2}} \sum_{l=-\infty}^{\infty} I_l(\xi\xi_0) e^{il(\phi - \phi_0)}. \quad (\text{A.16})$$

Making a choice of $t = -\xi_0^2/4$ the expansion of the associated Bessel becomes

$$I_l(\xi\xi_0) = \left(\frac{\xi\xi_0}{2}\right)^l \frac{e^{\frac{\xi_0^2}{4}}}{\Gamma(l+1)} \sum_{p=0}^{\infty} \frac{\mathcal{L}_p^{|l|}(\xi^2)}{p+l C_p p!}, \quad (\text{A.17})$$

$$= \left(\frac{\xi\xi_0}{2}\right)^l e^{\frac{\xi_0^2}{4}} \sum_{p=0}^{\infty} \frac{\mathcal{L}_p^{|l|}(\xi^2)}{(p+l)!}. \quad \text{for } l \in \mathbb{Z}, \Gamma(l+1) = l! \quad (\text{A.18})$$

Eq. (A.16) can be re-expressed as:

$$\psi_{in}(\xi, \phi) = \sum_{p=0}^{\infty} \sum_{l=-\infty}^{\infty} \left(\frac{\xi_0^2}{4}\right)^{p+\frac{|l|}{2}} e^{\frac{\xi_0^2}{4}} \cdot \frac{(-1)^p}{\sqrt{\pi}(p+|l|)!} e^{-\frac{\xi^2}{2}} \xi^{|l|} \mathcal{L}_p^{|l|}(\xi^2) e^{il(\phi-\phi_0)}. \quad (\text{A.19})$$

Making a choice of normalized LG beams basis of

$$\psi_{pl}^{LG}(\xi, \phi) = \sqrt{\frac{p!}{\pi(p+|l|)!}} \xi^{|l|} e^{-\frac{\xi^2}{2}} \mathcal{L}_p^{|l|}(\xi^2) e^{il\phi}, \quad (\text{A.20})$$

the off-axis beam input state becomes

$$\psi_{in}(\xi, \phi) = \sum_{p=0}^{\infty} \sum_{l=-\infty}^{\infty} (-1)^p \left(\frac{\xi_0^2}{4}\right)^p \frac{\left(\frac{\xi_0^2}{4}\right)^{\frac{|l|}{2}} e^{\frac{\xi_0^2}{4}}}{\sqrt{p!(p+|l|)!}} \psi_{pl}^{LG}(\xi, \phi - \phi_0, 0). \quad (\text{A.21})$$

This is a combination of two Laguerre-Gauss basis. The coordinates can be interchanged giving rise to two orbital momenta states define relative to two origins one along the axis of the SPP $(0, 0)$, and the other around the neutron center r_0, ϕ_0 . The OAM around the center of the neutron is polynomial modulated Laguerre-Gauss

$$\psi_{0l} = N_0 \left(\frac{\xi_0}{2}\right)^{|l|} e^{\frac{\xi_0^2}{4}} \quad (\text{A.22})$$

and it in turn modulate the OAM about the axis of the SPP. The normalization factor is $N_0 = \sqrt{2^{l-1}/(\pi l! \sigma_{\perp})}$.

$$\psi_{in}(\xi, \phi) = \sum_{p=0}^{\infty} \sum_{l=-\infty}^{\infty} A_{pl}(\xi_0, \phi_0) \psi_{pl}^{LG}(\xi, \phi - \phi_0, 0), \quad (\text{A.23})$$

where we have defined the location dependent modulated Gaussian as:

$$A_{pl}(\xi_0, \phi_0) = \left(\frac{\xi_0^2}{4}\right)^{p+\frac{|l|}{2}} \frac{(-1)^p e^{\frac{\xi_0^2}{4}}}{\sqrt{p!(p+|l|)!}} \quad (\text{A.24})$$

Upon taking diffraction into account, we can express $\sigma_{\perp} = \sigma_{\perp}(z)$ at any point z along the z -axis. We can note from the state in Eq. A.23 that the state at incidence carries infinite sum of OAM as a result of it proximity.

Propagating through a phase plate of topological charge q the state at the exit is

$$\Psi_{\text{SPP}}(\xi, \phi, 0) = \psi_{in}(\xi, \phi) e^{iq\phi} \quad (\text{A.25})$$

$$= \sum_{p=0}^{\infty} \sum_{l=-\infty}^{\infty} A_{pl}(\xi_0) \psi_{pl}(\xi, \phi - \phi_0) e^{iq\phi}, \quad (\text{A.26})$$

which can be expressed as a linear combination of the basis as

$$\Psi_{\text{SPP}}(\xi, \phi, 0) = \psi_{in}(r, \phi) e^{iq\phi} \quad (\text{A.27})$$

$$= \sum_{p=0}^{\infty} \sum_{l=-\infty}^{\infty} A_{pl}(\xi_0) e^{-il\phi_0} \sum_{n=0}^{\infty} \sum_{m=-\infty}^{\infty} C_{nm}^{pl} \psi_{nm}(\xi, \phi) e^{im\phi}, \quad (\text{A.28})$$

where

$$\begin{aligned} C_{nm}^{pl} &= \int_0^{\infty} \xi d\xi \int_0^{2\pi} d\phi \psi_{pl}(\xi, \phi) \psi_{nm}(\xi, \phi)^* e^{iq\phi} = \int_0^{\infty} d\xi \xi G_{n,m}^{p,l}(\xi) \frac{1}{2\pi} \int_0^{2\pi} e^{i(l+q-m)\phi} d\phi, \\ &= \begin{cases} e^{i(l+q-m)\pi} \frac{\sin[(l+q-m)\pi]}{(l+q-m)\pi} \int_0^{\infty} d\xi \xi G_{n,m}^{p,l}(\xi) & \text{for } l+q-m \in \mathbb{R} \\ \int_0^{\infty} d\xi \xi G_{n,m}^{p,l}(\xi) \delta(l+q-m) & \text{for } l+q-m \in \mathbb{Z} \end{cases}. \end{aligned} \quad (\text{A.29})$$

A.5 On-axis quadrupole

The output state is from a quadrupole when an input state if $|\psi_{0,0,\uparrow}\rangle = |n_0, \ell_0, \uparrow\rangle$ can be rewritten as an expansion to the basis function as

$$|\Psi_Q\rangle = \cos\left(\frac{\pi r}{2r_c}\right) |\psi_{0,0,\uparrow}\rangle + ie^{i\phi} \sin\left(\frac{\pi r}{2r_c}\right) |\psi_{0,0,\downarrow}\rangle = \sum_{n,\ell} |n\rangle \left(C_{n,\ell,\uparrow} |\ell, \uparrow\rangle + iC_{n,\ell,\downarrow} |\ell, \downarrow\rangle \right),$$

where,

$$\begin{aligned} C_{n,\ell,\uparrow} &= \int_0^{\infty} dr \int_0^{2\pi} d\phi \xi \langle n, \ell | \xi, \phi \rangle \langle \xi, \phi | \Psi_Q \rangle = \langle n, \ell, \uparrow | \cos(\pi r/2r_c) | n_0, \ell_0, \uparrow \rangle \\ &= \langle n | \cos(\pi r/2r_c) | n_0, \rangle \delta_{\ell\ell_0} = \delta_{\ell\ell_0} \int_0^{\infty} G_{n,\ell_0}^{n_0,\ell_0}(\xi) \cos\left(\frac{\pi\sigma_{\perp}}{2r_c}\xi\right) \xi d\xi \end{aligned} \quad (\text{A.30})$$

$$\begin{aligned}
C_{n,\ell,\downarrow} &= \int_0^\infty dr \int_0^{2\pi} d\phi \xi \langle n, \ell | \xi, \phi \rangle \langle \xi, \phi | \Psi_Q \rangle = \langle n_r, \ell, \downarrow | \sin(\pi r/2r_c) | n_0, \ell_0 + 1, \downarrow \rangle \\
&= \langle n | \sin(\pi r/2r_c) | n_0 \rangle \delta_{\ell, \ell_0 + 1} = \delta_{\ell, \ell_0 + 1} \int_0^\infty G_{n, \ell_0 + 1}^{n_0, \ell_0}(\xi) \sin\left(\frac{\pi \sigma_\perp}{2r_c} \xi\right) \xi d\xi \quad (\text{A.31})
\end{aligned}$$

where

$$G_{p,m}^{n,l}(\xi) = 2 \sqrt{\frac{p!n!}{(p+|m|)!(n+|l|)!}} \xi^{|m|+|l|} e^{-\xi^2} \mathcal{L}_p^{|m|}(\xi^2) \mathcal{L}_n^{|l|}(\xi^2) \quad (\text{A.32})$$

Using the coefficients above, the states above can be represented as

$$|\Psi_Q\rangle = \sum_n |n\rangle \left(C_{n, \ell_0, \uparrow} |\ell_0 \uparrow\rangle + i C_{n, \ell_0 + 1, \downarrow} |\ell_0 + 1, \downarrow\rangle \right), \quad (\text{A.33})$$

The coefficients are all real and normalized, i.e

$$\sum_n \left(C_{n, \ell_0, \uparrow}^2 + C_{n, \ell_0 + 1, \downarrow}^2 \right) = 1 \quad (\text{A.34})$$

Proof:

Define an arbitrary coefficient

$$T_{p,m}^{n,l} = \int_0^\infty G_{p,m}^{n,l}(\xi) F(\xi) \xi d\xi, \quad \text{where, } F(\xi) = \sin\left(\frac{\pi \sigma_\perp}{2r_c} \xi\right) \text{ or } \cos\left(\frac{\pi \sigma_\perp}{2r_c} \xi\right),$$

so that that the sum over p ,

$$\sum_p |T_{p,m}^{n,l}|^2 = \sum_p \int_0^\infty d\xi \int_0^\infty d\zeta G_{p,m}^{n,l}(\xi) G_{p,m}^{n,l}(\zeta) \xi F(\xi) \zeta F(\zeta). \quad (\text{A.35})$$

Using Eq. (A.32), one gets

$$\begin{aligned}
\sum_p G_{p,m}^{n,l}(\xi) G_{p,m}^{n,l}(\zeta) &= \sum_p \frac{4p!n!}{(p+|m|)!(n+|l|)!} \xi^{|m|+|l|} e^{-\xi^2} \zeta^{|m|+|l|} e^{-\zeta^2} \mathcal{L}_p^{|m|}(\xi^2) \mathcal{L}_p^{|m|}(\zeta^2) \mathcal{L}_n^{|l|}(\xi^2) \mathcal{L}_n^{|l|}(\zeta^2) \\
&= \frac{4n!}{(n+|l|)!} \xi^{|m|+|l|} e^{-\xi^2} \zeta^{-|m|+|l|} \mathcal{L}_n^{|l|}(\xi^2) \mathcal{L}_n^{|l|}(\zeta^2) \delta(\zeta^2 - \xi^2) \quad \text{using Eq. (A.4),}
\end{aligned}$$

such that in combination with the delta function decomposition Eq. (A.11), we get

$$\sum_p |T_{p,m}^{n,l}|^2 = \frac{2n!}{(n+|l|)!} \int_0^\infty d\xi \xi^{2|l|} e^{-\xi^2} \mathcal{L}_n^{|l|}(\xi^2)^2 \xi F(\xi)^2. \quad (\text{A.36})$$

Noting that this relation is independent of m , the normalization condition becomes,

$$\begin{aligned} \sum_n |C_{n,\ell_0,\uparrow}|^2 + \sum_n |C_{n,\ell_0,\downarrow}|^2 &= \frac{2n_0!}{(n+|\ell_0|)!} \int_0^\infty d\xi \xi^{2|\ell_0|} e^{-\xi^2} \mathcal{L}_n^{|\ell_0|}(\xi^2)^2 \xi \left(\sin^2(\cdot) + \cos^2(\cdot) \right), \\ &= \frac{n_0!}{(n_0+|\ell_0|)!} \int_0^\infty \xi^{|\ell_0|} e^{-\xi} \mathcal{L}_{n_0}^{|\ell_0|}(\xi)^2 d\xi = 1 \quad \text{LG normalization} \end{aligned}$$

A.6 Non expanded input state in to the LG basis

Consider the input wavepacket with no OAM, polarized along the z -axis, and located at (r_0, ϕ_0) i.e Gaussian modulation $\psi_{in} = \frac{1}{\sqrt{\pi}} e^{-\xi^2 - \xi_0^2 + 2\xi\xi_0 \cos(\phi - \phi_0)}$ which we denote as $|\psi_{in}, \uparrow\rangle$. The output state of a quadrupole is

$$|\Psi_Q\rangle = \cos\left(\frac{\pi r}{2r_c}\right) |\psi_{in}, \uparrow\rangle + i e^{i\phi} \sin\left(\frac{\pi r}{2r_c}\right) |\psi_{in}, \downarrow\rangle = \sum_{nl} \left(C_{n,\ell,\uparrow} |n, \ell, \uparrow\rangle + i C_{n,\ell,\downarrow} |n, \ell, \downarrow\rangle \right)$$

where, $C_{n,\ell,\uparrow} = \int_0^\infty dr \int_0^{2\pi} d\phi r \langle n, \ell | r, \phi \rangle \langle r, \phi | \Psi_Q \rangle$ using the Jacobi-anger transform in Eq. (A.2), we get

$$\begin{aligned} C_{n,\ell,\uparrow} &= \frac{e^{-\frac{\xi_0^2}{2}}}{\sqrt{\pi}} \int_0^\infty \xi d\xi \int_0^{2\pi} d\phi e^{-\frac{\xi^2}{2}} \sum_{m=-\infty}^\infty \mathcal{I}_m\left(\frac{r r_0}{\sigma_\perp^2}\right) \cos\left(\frac{\pi \sigma_\perp \xi}{2r_c}\right) \psi_{nl}^*(r, 0) e^{im(\phi - \phi_0)} e^{-i\ell\phi} \\ &= 2\sqrt{\pi} e^{-\frac{\xi_0^2}{2}} \sum_{m=-\infty}^\infty \int_0^\infty \xi d\xi e^{-\frac{\xi^2}{2}} \mathcal{I}_m(\xi \xi_0) \cos\left(\frac{\pi \sigma_\perp \xi}{2r_c}\right) \psi_{nl}^*(\xi, 0) e^{-im\phi_0} \frac{1}{2\pi} \int_0^{2\pi} d\phi e^{i(m-\ell)\phi} \\ &= e^{-\frac{\xi_0^2}{2}} \sum_{m=-\infty}^\infty \int_0^\infty \xi d\xi \mathcal{G}_{n,\ell}^m(\xi, \xi_0) \cos\left(\frac{\pi \sigma_\perp \xi}{2r_c}\right) e^{-im\phi_0} \frac{1}{2\pi} \int_0^{2\pi} d\phi e^{i(m-\ell)\phi} \\ &= e^{-\frac{\xi_0^2}{2}} \begin{cases} \sum_{m=-\infty}^\infty e^{-im\phi_0} e^{i(m-\ell)\pi \frac{\sin[(m-\ell)\pi]}{(m-\ell)\pi}} \int_0^\infty d\xi \xi \mathcal{G}_{n,\ell}^m(\xi, \xi_0) \cos\left(\frac{\pi \sigma_\perp \xi}{2r_c}\right) & \text{for } m - \ell \in \mathbb{R} \\ e^{-i\ell\phi_0} \int_0^\infty d\xi \xi \mathcal{G}_{n,\ell}^\ell(\xi, \xi_0) \cos\left(\frac{\pi \sigma_\perp \xi}{2r_c}\right) & \text{for } m - \ell \in \mathbb{Z} \end{cases}, \end{aligned} \tag{A.37}$$

In a similar fashion, $\xi_0 = r_0/\sigma_\perp$. In a similar way

$$\begin{aligned}
C_{n,\ell,\downarrow} &= \frac{e^{-\frac{\xi_0^2}{2}}}{\sqrt{\pi}} \int_0^\infty \xi d\xi \int_0^{2\pi} d\phi e^{-\frac{\xi^2}{2}} \sum_{m=-\infty}^\infty \mathcal{I}_m(\xi\xi_0) \sin\left(\frac{\pi\sigma_\perp\xi}{2r_c}\right) \psi_{n\ell}^*(r, 0) e^{im(\phi-\phi_0)} e^{i(1-\ell)\phi} \\
&= e^{-\frac{\xi_0^2}{2}} \begin{cases} \sum_m e^{-im\phi_0} e^{i(m-\ell+1)\pi\frac{\sin[(m-\ell+1)\pi]}{(m-\ell+1)\pi}} \int_0^\infty d\xi \xi \mathcal{G}_{n,\ell}^m(\xi, \xi_0) \cos\left(\frac{\pi\sigma_\perp\xi}{2r_c}\right) & \text{for } m-\ell \in \mathbb{R} \\ e^{-i(\ell-1)\phi_0} \int_0^\infty d\xi \xi \mathcal{G}_{n,\ell}^{\ell-1}(\xi, \xi_0) \cos\left(\frac{\pi\sigma_\perp\xi}{2r_c}\right) & \text{for } m-\ell \in \mathbb{Z} \end{cases}
\end{aligned} \tag{A.38}$$

where

$$\mathcal{G}_{p,m}^\ell(\xi, \xi_0) = 2\sqrt{\frac{p!}{(p+|m|)!}} \xi^{|m|} e^{-\frac{\xi^2}{2}} \mathcal{L}_p^{|m|}(\xi^2) \mathcal{I}_\ell(\xi\xi_0) \tag{A.39}$$